University *of* Leicester

Photometric Variability and Rotation in Magnetic White Dwarfs

Katherine Anne Lawrie

Supervisor:

Matthew Burleigh

Thesis to be submitted for the degree of

Doctor of Philosophy

at the University of Leicester

X-ray & Observational Astronomy Group

Department of Physics and Astronomy

University of Leicester

April 2013

Declaration

I hereby declare that no part of this thesis has been previously submitted to this or any other University as part of the requirement for a higher degree. The work described herein was conducted by the undersigned except for contributions from colleagues as acknowledged in the text.

Katherine Lawrie
April 2013

Photometric Variability and Rotation in Magnetic White Dwarfs

Katherine Anne Lawrie

ABSTRACT

This thesis explores the photometric variability in isolated magnetic white dwarfs (MWDs) to search for spin periods. Approximately 40% of MWDs exhibit photometric modulations as the star rotates due to the effects from a strong magnetic field or star spots. A sample of 77 MWDs is studied to discover periods on timescales of minutes to one week. Well-defined periods are determined in 12 MWDs, with periods of roughly an hour to a few days, and variability with poorly constrained periods is found in a further 13 stars. MWD spin periods can provide important constraints for their post main-sequence evolution and formation, and in particular, potential information on the influence magnetism plays on the mass and angular momentum loss of the evolving star. A correlation has emerged between the spin period and magnetic field strength and temperature, suggesting hotter MWDs spin faster and have higher field strengths, characteristics possibly associated with MWDs that might have formed in binary mergers.

A similar investigation is carried out on longer timescales (months – years) for ten single MWDs, which are stable on short timescales but were previously found to display modulations between observing seasons. However, no significant variability is detected in the sample, although G 240-72 may display variations over months.

Finally, the spin period evolution over $\sim$ 20 years is studied in the hot, massive, highly magnetic, rapidly rotating MWD, RE J0317-853. A rate of period change is measured as $\dot{P} = (9.6 \pm 1.4) \times 10^{-14}$ s/s which is most likely due to the orbital motion of the wide binary pair of RE J0317-853 and LB 9802. Spin-down from magnetic dipole radiation is ruled out as a possible mechanism. Periodic variations in the expected arrival times of maximum flux tentatively suggest a low-mass planetary companion may be orbiting RE J0317-853.

Publications

Work in this thesis has been published in the following papers:

Chapter 2 –
"Photometric Variability and Rotation in Magnetic White Dwarfs",
Lawrie K. A., Burleigh M. R., Brinkworth C. S., Marsh T. R., Hodgkin S. T., Baker D. E. A., Cossins P., Littlejohns O. M., Scott A. E., Steele P. R., 2013, *in preparation*

"Photometric Variability of Magnetic White Dwarfs",
Lawrie K. A., Burleigh M. R., Brinkworth C. S., Marsh T. R., Hodgkin S. T., Baker D. E. A., Cossins P., Littlejohns O. M., Scott A. E., Steele P. R., 2013, in '*18th European White Dwarf Workshop*,' eds. Krzesiński J., Stachowski G., Moskalik P., Bajan K., ASP Conference Proceedings, Vol. 469. San Francisco: Astronomical Society of the Pacific., p.429

Chapter 3 –
"SDSS J000555.90−100213.5: a hot, magnetic carbon-dominated atmosphere WD rotating with a 2.1 day period",
Lawrie K. A., Burleigh M. R., Dufour P., Hodgkin S. T., 2013, MNRAS *in press*, arXiv:1305.2219

Chapter 4 –
"Photometric Variability and Rotation in Magnetic White Dwarfs",
Lawrie K. A., Burleigh M. R., Brinkworth C. S., Marsh T. R., 2010, in '*17th European White Dwarf Workshop*,' eds. Werner K., Rauch T., AIP Conference Proceedings, Vol. 1273, p. 91

Chapter 5 –
"Detecting the Orbital Motion of RE J0317−853 and LB 9802",
Lawrie K. A., Burleigh M. R., Barlow B. N., O'Donoghue D., Barstow M. A., Marsh T. R., Kilkenny D., Worters H., 2013, in '*18th European White Dwarf Workshop*,' eds. Krzesiński J., Stachowski G., Moskalik P., Bajan K., ASP Conference Proceedings, Vol. 469. San Francisco: Astronomical Society of the Pacific., p.385

The method used in Chapter 2 has been published in the following papers:

"Measuring the rotational periods of isolated magnetic white dwarfs",
Brinkworth C. S., Burleigh M. R., Lawrie K. A., Marsh T. R., Knigge C., 2013, ApJ, *in press*

"NLTT 5306: the shortest period detached white dwarf+brown dwarf binary",
Steele P. R., Saglia R. P., Burleigh M. R., Marsh T. R., Gänsicke B. T., Lawrie K., Cappetta M., Girven J., Napiwotzki R., 2013, MNRAS, 429, 3492

"WD0837+185: The formation and Evolution of an Extreme Mass-ratio White-dwarf-Brown-dwarf Binary in Praesepe",
Casewell S. L., Burleigh M. R., Wynn G. A., Alexander R. D., Napiwotzki R., Lawrie K. A., Dobbie P. D., Jameson R. F., Hodgkin S. T., 2012, ApJ, 759, L34

Acknowledgments

To start, thank you to my supervisor, Matt Burleigh, for your guidance over the years; for initiating me into the mysteries of observing and the techniques of operating the INT in La Palma and the 1.0m telescope in South Africa. There are many memories, especially from observing trips, that will stay with me forever.

I am indebted to numerous people around the world who have been observing and collecting data for me. This research wouldn't have been possible without you. Many thanks to Brad Barlow for all your help, support and enthusiasm with the O – C project. It has been a joy to get to know Amy, Vicky, Owen, Suzy, Nathan, Andrew, David, Chris, Andreas, Charly (and Rich), Lucy and Peter, who have made the hard work more enjoyable with their good humour. I thank you and wish you all great success in the future!

A special thank you to three inspirational women who I've had the honour of working with: Carolyn Brinkworth, Sarah Casewell and Francesca Faedi. You have all provided support and encouraging words as well as showing your passion for science. It's easy to forget the point sometimes, so thank you for reminding me. Sarah, you have become a colleague and friend. We have shared many important moments over the last three years and as we move forward with our lives, I will miss sharing an office with you.

Last, but certainly not least: none of this would have been possible without the love and continual support of my Mother and Pelham. I cannot fully express my deep gratitude for such acts of support as keeping me company on skype into the small hours of the morning while I've been observing; for listening to my frustration when I couldn't get a code to work or when a telescope was uncooperative; and for ensuring there was always a generous supply of hugs and chocolate.

I am very lucky to have in my life such wonderful people who have been a part of this journey and believed in me.

Thank you!

For my Mother

Contents

List of Tables

List of Figures

1

Introduction

This thesis investigates the photometric variability of isolated magnetic white dwarfs and their rotation periods. In this chapter, I introduce the topic of white dwarfs and their basic structure, how they form and evolve, and how they are classified. In addition, I discuss the origin of magnetism in white dwarfs, how their field strengths can be measured and some of their unique characteristics, such as their apparent higher than average masses and their photometric variability, that can be used for determining rotation periods. Spin periods of magnetic and non-magnetic white dwarfs can provide important constraints for their post main-sequence evolution and formation, and more specifically probe the influence that magnetism has on the stars' mass and angular momentum loss. Furthermore, the rotation and physical properties of magnetic white dwarfs can give insight into the understanding of the origin of the magnetic fields in white dwarfs, linking with the formation of cataclysmic variables and the double-degenerate progenitor channel for Type Ia supernovae.

1.1 White Dwarfs

White dwarfs are essentially dying stars: the end point of stellar evolution for stars with initial masses less than 8 solar masses ($M_\odot$). They are the most common stellar remnant, with approximately 98% (Wood 1992) of all stars ending their lives as white dwarfs. They typically have radii similar to the Earth's, with masses around 0.6 $M_\odot$, which range from as low as $\approx 0.17 M_\odot$ (Kilic et al. 2007; Kawka & Vennes 2009; Hermes et al. 2012) up to a maximum mass of $\approx 1.4 M_\odot$, the Chandrasekhar limit. These properties make white dwarfs very dense objects $\sim 10^9$ kg/m^3 (in contrast the density at the core of the Sun is $\sim 1.5 \times 10^5$ kg/m^3).

The Discovery of White Dwarfs

The first white dwarf was discovered in 1783 by Friedrich W. Herschel orbiting the bright main-sequence star 40 Eridani, along with another companion in a triple system, although it was not recognised as a white dwarf at the time. A spectrum of the faint companion 40 Eri B, taken by Henry N. Russell, Edward C. Pickering and Williamina Fleming in 1910, later revealed it to have a spectral type expected for an A-type star. Similarly, Adams (1915) was most surprised when a spectrum of Sirius B indicated it was also a hot, blue-white star, nearly three times hotter and almost 1,000 times fainter than its host star Sirius A. Both stars, with low luminosities and high temperatures, are located in the lower left corner of the Hertzsprung-Russell diagram, which had previously been unoccupied. This was an unexpected result as hot stars were supposed to have a higher luminosity than cooler stars of the same size, and therefore 40 Eri B and Sirius B would have to be 100 times smaller than the Sun, implying they have enormous densities.

The first isolated white dwarf was later discovered by Adriaan Van Maanen in 1917. By the 1950s, more than one hundred white dwarfs had been confirmed (Luyten 1950), and thanks to surveys, such as the Sloan Digital Sky Survey (SDSS), the latest white dwarf catalogue based on the SDSS data release 7 has identified nearly 20,000 white dwarfs (Kleinman et al. 2013).

The Basic Structure of White Dwarfs

A white dwarf has an electron degenerate core, which accounts for 99.99% of its mass and is surrounded by a thin non-degenerate atmosphere, usually of hydrogen or helium. The core is a plasma of degenerate electrons, and carbon and oxygen ions, leftover from the progenitor star's helium burning phase. White dwarfs cool at a roughly constant radius throughout their lifetime, since the electron degeneracy pressure is only weakly dependent on temperature. From the Pauli Exclusion Principle, no two electrons can share the same energy state. Therefore, as the electron density increases with the contracting star, the electrons must occupy higher available energy states. Once all the states are filled and the electrons can no longer be compressed together, a pressure is created, known as the electron degeneracy pressure. Fowler (1926) demonstrated that this degenerate pressure could maintain hydrostatic equilibrium in white dwarfs against gravitational collapse. The structure and unique characteristics of white dwarfs are dictated by its electron degenerate matter.

Chandrasekhar (1931) determined that degenerate objects, such as white dwarfs, have an inverse mass-radius relationship $R \propto M^{-1/3}$, from equating the gravitational potential energy to the energy from electron degeneracy pressure. This implies that the more massive the degenerate object, the smaller its radius will become. However, this degeneracy pressure will only prevent the star from collapsing under its own gravitational force for white dwarfs with masses below a certain limit. He determined the maximum mass for a non-rotating body that can be supported by electron degeneracy pressure from gravitational collapse, as $\approx 1.4M_{\odot}$, known as the Chandrasekhar limit. Stars more massive than this limit can no longer support themselves against gravity and will collapse to neutron stars or black holes.

1.1.1 White Dwarf Formation

Low to intermediate mass stars with initial masses $\leq 8M_{\odot}$ will evolve into white dwarf stars at the end of their lives (Weidemann & Koester 1983). A star, such as our Sun, spends the majority of its lifetime on the main-sequence where it burns hydrogen into helium in its core by nuclear fusion, producing energy. This process produces sufficient pressure to keep the star in hydrostatic equilibrium, maintaining a roughly constant radius, and preventing the star from collapsing under its gravitational force. A more massive star will have a higher gravity and thus will burn its hydrogen fuel faster, illustrating that more massive stars will have shorter lives on the main-sequence than less massive stars. For example, a star like our Sun (with a mass of $1M_{\odot}$) will be on the main sequence for ~10 billion years, while a star ten times more massive ($10M_{\odot}$) will spend only 30 million years on the main sequence. Eventually, all main-sequence stars exhaust their hydrogen supply in the core, leaving behind a helium core, at which point hydrogen burning in the core ceases. Since the equilibrium is no longer being maintained, the helium core starts to cool, causing the pressure to fall and consequently the stellar core to collapse (Schönberg & Chandrasekhar 1942).

The typical evolutionary path for stars with an initial mass between $\sim 0.8-8M_{\odot}$ is shown in Figure 1.1 on a Hertzsprung-Russell (H-R) diagram. Hydrogen burning continues in the shell around the core, while the contracting stellar core converts the gravitational energy into thermal energy, causing the temperature in the core to increase and thus increasing the temperature of the surrounding material. The additional heat source accelerates the hydrogen burning in the shell and the helium from the inner shell falls inward to the core, causing the luminosity of the star to increase massively (~100 times its previous luminosity). The mass of the core increases, causing further contraction and increasing the temperature. The outer envelope is then forced to expand, to compensate for the increased heat in the core, where the star then becomes cooler and less dense. The drop in temperature causes a convection zone to develop in the envelope, allowing more hydrogen to move up to the burning shell. At this point, the star is known as a “red giant” and is located on the Red Giant Branch (RGB), as indicated in Figure 1.1.

As the shell continues to burn hydrogen, the amount of helium in the core increases, causing it to contract further until the temperature and density are high enough to ignite helium burning in the core. Helium begins fusing, producing carbon and oxygen, via the triple-α process. With the onset of helium burning, the core contraction ceases. The core then expands and the rate of burning in the helium core and hydrogen shell slows down, resulting in the atmosphere shrinking quickly. The star is now located on the Horizontal Branch, where it is known as a “sub-giant”.

Once the helium in the centre is exhausted, the core contracts again until it is halted by electron degeneracy pressure. The layers surrounding the core get hotter, due to the core contracting, allowing helium burning to start in the shell. Again, the release of energy from the helium shell burning is enormous (like the earlier hydrogen shell burning) and the star’s atmosphere expands, where the star enters a second red giant phase, known as the Asymptotic Giant Branch (AGB). At this point, the star comprises a carbon-oxygen core, helium and hydrogen burning shells, all surrounded by a hydrogen envelope. The expansion of the star causes the outer hydrogen-burning shell to cool, becoming inactive for the meantime. As the star evolves along the AGB phase and the helium becomes exhausted in the helium burning shell, the outer layers collapse, re-igniting the hydrogen shell. This shell burning causes further helium to fall onto the depleted helium burning shell underneath, resulting in a series of “helium-shell flashes” and thermal pulses. The outer stellar atmosphere is then later ejected as a Planetary Nebula. During this time, the star moves horizontally from right to left on the H-R diagram, as the core contracts at a constant luminosity until it is prevented from further collapse by electron degeneracy pressure. The temperature increases from 5,000 K to >100,000 K and its surface gravity increases. The lifetime of the Planetary Nebula is short, and within ~100,000 years it dissipates and is no longer visible. The remaining core, known as a “white dwarf”, is then left to cool and fade.

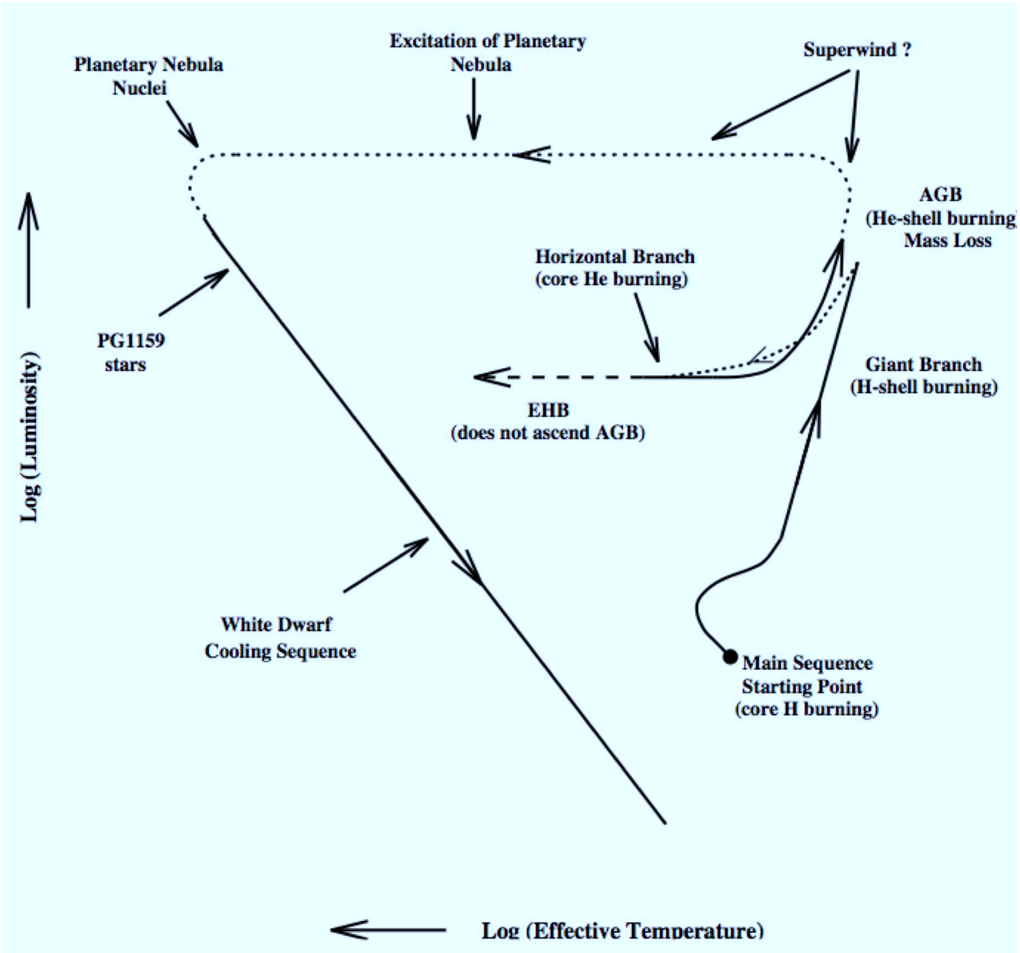

Figure 1.1: The evolutionary path for an intermediate mass star from the main-sequence to the white dwarf cooling sequence on the Hertzsprung-Russell diagram (from Marsh 1995).

Low mass stars that reach the Horizontal Branch, and which are capable of burning helium in their cores but do not have sufficient mass in the envelope to support helium burning in the shell, are unable to ascend the AGB. Instead, these stars move along the Extended Horizontal Branch (EHB), contracting at a constant luminosity until degeneracy pressure dominates, halting their collapse. Here, the degenerate stars are known as “subdwarfs”.

For very low mass stars ($< 0.5M_{\odot}$), the core does not have sufficient energy to ignite helium burning and therefore the white dwarf remnant will have a core mainly composed of helium. However, the evolutionary timescale for this to occur by single star evolution is longer than the age of the Universe (Laughlin et al. 1997); therefore the helium white dwarfs that do exist must have been created from a binary mass transfer (Liebert et al. 2004). In this case, most of the progenitor star's mass is stripped by its binary companion before helium burning can start in the core.

At the other end of the spectrum, massive main-sequence stars with initial masses up to $10.5 M_{\odot}$ (Iben et al. 1997) may be able to ignite carbon burning in the core once helium burning ceases, resulting in oxygen-neon-magnesium core white dwarfs, although there is considerable uncertainty where this occurs in the mass range. Furthermore, for stars with high initial masses, the carbon burning in the core may be the beginning of successive nuclear reactions (that are highly dependent on the mass of the star), leading to the evolutionary paths for creating neutron stars or black holes.

1.1.2 White Dwarf Classification

The core of a white dwarf is typically composed of carbon and oxygen, surrounded by a thin helium envelope and then a thin outer layer of hydrogen. Heavy elements in the atmosphere quickly sink downwards due to the white dwarfs' high surface gravity, leaving behind atmospheres dominated by the lightest elements, hydrogen or helium (Schatzman 1958; Fontaine & Michaud 1979). The presence and strength of absorption lines in the spectra of white dwarfs are used to classify the stars. The system currently used for classification was first introduced by Sion et al. (1983) and is shown in Table 1.1 (with a few modifications). The uppercase "D", at the start, stands for the degenerate nature of white dwarfs, followed by the second letter corresponding to the primary spectroscopic features in the optical spectrum. Subsequent letters can be included to denote secondary spectral features, which appear in order of dominance. Finally, a temperature index (from 0 to 9) is calculated by dividing 50,400 K by the effective temperature of the white dwarf (although it is not normally used when referring to the class of a white dwarf). For example, a hydrogen dominated white dwarf showing Zeeman split hydrogen lines due to a magnetic field, with an effective temperature of 10,000 K, can be denoted as DAH5 (where the "H" indicates it is magnetic without a detected polarisation, see Table 1.1). Approximately 80% of white dwarfs are hydrogen-rich atmosphere DAs and ~18% are helium-rich atmosphere DBs, with the remainder making up the more exotic types, such as those with carbon-dominated atmospheres (DQs) or those with metal polluted atmospheres (DAZ/DZs).

Table 1.1: White dwarf spectral classifications.

Class	Approximate Temperature Range (K)	Spectral Characteristics
H-rich		
DA	6,000–100,000	Balmer lines only, no He or metal features
DAO	>45,000	Balmer lines and weak HeII features
He-rich		
DO	45,000–100,000	Strong HeII lines, some HeI or H present
DB	12,000–30,000*	HeI lines, no H or metal features
DBA	12,000–30,000	HeI lines, weak Balmer lines present
C-rich		Carbon features (atomic or molecular)
Hot DQ	18,000–24,000	Atomic CII lines
Warm DQ	12,000–18,000**	Atomic CI lines, sometimes with Swan bands
DQ	6,000–12,000	C_2 Swan bands
Cool WDs		
DZ	<6,000†; 10,000‡	Metal lines only, no H or He
DC	<6,000†; 10,000‡	Continuous spectrum, no lines deeper than 5%

Additional		Secondary Feature
P		Magnetic with detectable polarisation
H		Magnetic without detectable polarisation
V		Variable
E		Emission lines present
d		Debris Disc

* Some "hot" DB white dwarfs have been discovered in the "DB gap" with 30,000 K < $T_{\rm eff}$ < 45,000 K (Kleinman et al. 2004; Eisenstein et al. 2006).
** Recently discovered by Dufour et al. (2013) in the SDSS DR7 catalogue.
† For a hydrogen-rich atmosphere.
‡ For a helium-rich atmosphere.

1.1.3 White Dwarf Evolution

As white dwarfs age, cool and dim, their evolution follows a relatively simple cooling track on a timescale on the order of 10^9 years. However, as Table 1.1 shows, there is a variety of WD spectral types, some of which occur at different stages along the evolutionary sequence. Standard stellar evolution predicts ∼80% of white dwarfs form carbon-oxygen cores with hydrogen envelopes, while the remainder have helium envelopes.

The evolution of hydrogen-dominated atmosphere DA white dwarfs appears straightforward. White dwarfs maintain pure hydrogen atmospheres as they cool until the temperature becomes low enough that convection zones develop ($T_{\rm eff} \sim 14{,}000$ K, Bergeron et al. 1995). In most cases, the convection zone is too shallow to cause significant amounts of helium and carbon to be dredged up to pollute the photosphere.

The evolution of helium-dominated atmosphere white dwarfs is, however, more complex. These stars are thought to undergo a late helium flash at the end of the AGB phase, burning the remaining hydrogen in the envelope and mixing the core materials and the helium layer. The star then begins to cool and the carbon and oxygen precipitate below the photosphere due to the high surface gravity, leaving behind a hot, helium-dominated atmosphere DO white dwarf. As the star cools further, any remaining traces of hydrogen in the atmosphere move to the surface, resulting in the star appearing as a DA white dwarf with a thin hydrogen atmosphere layer. This transition accounts for the apparent absence of helium atmosphere DO or DB white dwarfs with effective temperatures in the range of $30,000 - 45,000$ K (referred to as the "DB gap", Liebert et al. 1986). However, Kleinman et al. (2004) reported tentative detections for hot DBs in the "DB gap". These were later followed up and confirmed by Eisenstein et al. (2006), who also compared the ratio of DA stars to DBs over a range of temperatures, and indeed found the "DB gap" is deficient in helium atmosphere stars. With further cooling ($T_{\rm eff} < 30,000$ K), the developing convection zone mixes the massive helium layer underneath, bringing it to the surface, where the star is, once again, observed as a helium-dominated DB or DBA white dwarf.

Then, at effective temperatures of ~12,000 K, carbon from the core is brought upward to the photosphere by deep convection zones, creating a cool, carbon-rich DQ white dwarf (Pelletier et al. 1986; Dufour et al. 2005).

The carbon-dominated hot DQ white dwarfs are thought to have a similar evolutionary track as the helium-dominated white dwarfs (Dufour et al. 2008b) but instead experience a more violent late helium flash, burning both the hydrogen and helium layers, leaving behind an atmosphere composite mixture of carbon and oxygen. The white dwarf then re-appears as a hot DQ along the sequence at $T_{\rm eff} \sim 24{,}000$ K, when the carbon convection zone dilutes the thin helium layer. This is outlined in more detail in Chapter 3.

Ultimately, all white dwarfs cool to a point where no spectral features can be identified at optical wavelengths, where they become known as DC white dwarfs. Overall, this is a simplified version of white dwarf evolution, does not account for all the specific spectral types and assumes no binary interaction has occurred.

1.2 Magnetic White Dwarfs

The possibility that white dwarfs could possess large magnetic fields was first suggested by Blackett (1947), following the discovering of a magnetic field of ~1500 G in an Ap main-sequence star (78 Vir, Babcock 1947), assuming the magnetic flux could be conserved during stellar evolution. However, magnetism in an isolated white dwarf was not detected until the 1970s when Kemp et al. (1970) first detected strong circular polarisation at a level of 1–3% for the white dwarf, Grw+70°8247. Subsequent discoveries soon followed of the highly magnetic white dwarfs G 195-19 (Angel & Landstreet 1971) and GD 229 (Swedlund et al. 1974), with large polarisation measurements of ~1% and 1 – 4% respectively. For comparison, the Sun has an average magnetic field strength of ~1 G (or 10^{-4} Tesla, T).

Since then, observations and surveys, including the SDSS, have detected several hundred (>500) isolated white dwarfs with magnetic field strengths ranging from a few kG up to 1000 MG (Kleinman et al. 2013; Kepler et al. 2013; Külebi et al. 2009; Kawka et al. 2007; Vanlandingham et al. 2005; Gänsicke et al. 2002; Wickramasinghe & Ferrario 2000). Kleinman et al. (2013) recently found that ∼3% of the white dwarfs in the SDSS DR7 catalogue have magnetic fields $\gtrsim$2 MG, although this fraction is expected to be higher when white dwarfs with weaker field strengths are included. Using spectropolarimetry of 10 white dwarfs together with previous investigations (Aznar Cuadrado et al. 2004), Jordan et al. (2007) estimated 11 − 15% of white dwarfs have kilo-Gauss field strengths, while Kawka & Vennes (2012), in contrast, found 5 ± 2% of white dwarfs have field strengths $\lesssim$100 kG. In the Solar neighbourhood (within 13 pc of the Sun), Kawka et al. (2007) estimate the incidence of magnetism is as high as 21 ± 8%, while Liebert, Bergeron & Holberg (2003) and Giammichele et al. (2012) found that ≈10% of white dwarfs within 20 pc of the Sun have magnetic fields.

1.2.1 Methods for Measuring Magnetism in White Dwarfs

There are four main techniques for determining the magnetic field strength in white dwarfs. These are briefly summarised in the following section but are beyond the scope of this work. A more detailed review of these methods can be found in Wickramasinghe & Ferrario (2000).

Zeeman Spectroscopy

The presence of a magnetic field affects the electron energy levels in atoms and causes each spectral absorption feature to split into a distinctive triplet. The magnetic field has no influence on the wavelength of the central π component of the Zeeman triplet, but the two wing σ components are shifted, with one shifted to a longer wavelength (σ^-) and the other shifted to a shorter wavelength (σ^+). The strength of the magnetic field can be determined from the degree of separation between the central component and the wings

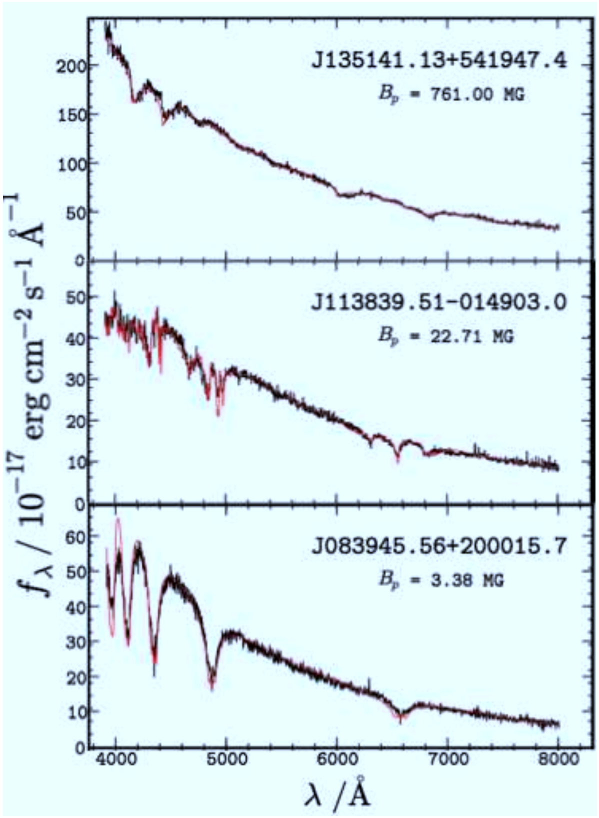

Figure 1.2: Example SDSS spectra of three magnetic white dwarfs taken from Külebi et al. (2009) of comparable effective temperatures ($T \sim 10,000$ K) with three different magnetic field strengths. The red line is the best-fitting dipole model. For the weakest field strength ($B = 3$ MG, *lower panel*), the Zeeman splitting is concentrated to the core of the spectral lines, whereas for the intermediate field strength ($B = 22$ MG, *middle panel*), the Zeeman splitting of the spectral lines covers a much broader wavelength. For the strongest magnetic field ($B = 761$ MG, *top panel*), no Zeeman splitting is detectable and the hydrogen lines are almost unrecognisable in comparison to the spectra at weaker field strengths.

($\pi - \sigma$). Zeeman splitting should be detectable for white dwarfs with fields $\gtrsim$1 MG. This method was first successfully utilised by Angel et al. (1974), who discovered resolvable Zeeman splitting of the hydrogen lines in the white dwarf GD90, with a magnetic field of 9 MG. Figure 1.2 shows three example spectra of magnetic white dwarfs covering a range of magnetic field strengths at 3 MG, 22 MG and 760 MG, illustrating the how the Zeeman splitting of the lines changes for different field strengths.

Zeeman Spectropolarimetry

An electron in an atom can be modelled as a linear harmonic oscillator. In the presence of a magnetic field, the electron precesses about the field and can be described as a combination of a linear oscillator along the field (π component), a circular oscillator rotating in the same manner as a free electron in the magnetic field (σ^+ component) and another circular oscillator rotating in the opposite direction (σ^- component). The polarisation and intensity of these three components can be used to determine not only the magnetic field strength, but also the direction of the field in the star. The σ components will be circularly polarised when observed along the direction of the magnetic field, linearly polarised when viewed perpendicular to the field and elliptically polarised when viewed at all other angles. The π component will be observed as linearly polarised at all viewing angles, apart from when it is viewed along the field, where no intensity will be detected. Spectropolarimetry is crucial for detecting low field strengths ($\lesssim$1 MG), where the spectral resolution of the spectrum is insufficient to resolve the individual Zeeman components, as the opposite circular polarisations can be measured for the σ^+ and σ^- components in the wings of the triplet. This method has been used to measure field strengths as small as a few kilo-Gauss (e.g. Aznar Cuadrado et al. 2004; Jordan et al. 2007; Kawka & Vennes 2012).

Magnetic Field Broadening

The positions, strengths and polarisations of the Zeeman split line components are strongly dependent on the magnetic field strength and its direction, which are expected to vary over the stellar surface of a white dwarf. The field spread over the visible surface can cause broadening of the spectral lines, known as “magnetic field broadening”. The width of the component due to the spread in the field can then be used to estimate the magnetic field strength. An additional line broadening effect occurs in the presence of an electric field, referred to as “Stark broadening”, caused by the splitting of the spectral lines. For weak magnetic field strengths ($\lesssim$1 MG), the Stark broadening of the spectral features is the dominant effect, making the Zeeman splitting undetectable (Moran et al. 1998).

Continuum Polarisation

A magnetic field influences the absorption and scattering processes in the stellar continuum and consequently leads to atmospheric opacities dependent on the magnetic field and its polarisation (known as magnetic dichroism). Therefore, the presence of a magnetic field can be determined from the degree of polarisation of the observed light from the white dwarf, while the field strength can be estimated from the ratio of linear to circular polarisation. For example, the polarisation is mostly linear for frequencies below the cyclotron resonance frequency (for $B \gtrsim 200\,\mathrm{MG}$ for optical wavelengths), and mainly circular for frequencies above the cyclotron resonance frequency (for $B \lesssim 200\,\mathrm{MG}$ for optical wavelengths, Martin & Wickramasinghe 1982). This method of detecting and characterising the magnetic field is particularly useful for white dwarfs with the highest field strengths, where the spectral features have been washed out and cannot be identified. Variations in the continuum brightness with changing field strength and direction can also be utilised to measure the spin periods of single magnetic white dwarfs (see Chapter 2 and Brinkworth et al. 2013).

1.2.2 The Origin of the Magnetic Fields

Magnetism in white dwarfs could have formed from two possible channels: either a single star evolution or from a binary merger. The magnetic fields may be fossil remnant fields from their main-sequence progenitor stars or may be generated through a dynamo process in the common envelope phase of the post main-sequence evolution during the merger of a binary. The population of magnetic white dwarfs is most likely a mixture from the two formation mechanisms.

Single Star Evolution

Early detections of magnetism in white dwarfs (e.g. Angel et al. 1981) led to the natural conclusion that the magnetic field was a fossil remnant from the white dwarf's progenitor main-sequence star. Since the chemically peculiar main-sequence Ap and Bp stars are the only main-sequence stars with significant field strengths, ranging from $\sim 10^2 - 10^4$ G, they were generally assumed to be the progenitors of magnetic white dwarfs. Zeeman spectropolarimetry observations of these stars has shown that all Ap and Bp stars appear to be magnetic (Aurière et al. 2007). Assuming the magnetic flux is conserved during the star's contraction in the post main-sequence evolution ($R_i^2 B_i = R_{WD}^2 B_{WD}$), weak and undetectable main-sequence magnetic fields could become observable at the white dwarf stage. The field strengths of Ap/Bp stars scale appropriately to the field strengths observed for the high-field magnetic white dwarfs, with fields of ~1 to 1000 MG, and consequently, provided a natural progenitor link to the high-field magnetic white dwarfs. This hypothesis was supported when only ~5% of white dwarfs were thought to be magnetic; Angel et al. (1981) claimed that the observed space density of the high-field magnetic white dwarfs was consistent with the space densities of the Ap/Bp stars as their progenitors. However, with the increasing numbers of spectropolarimetric and spectroscopic surveys, Kawka et al. (2007) found the incidence of magnetism among the stellar population, within 13 pc of the Sun, to be 21±8%, therefore illustrating that the Ap/Bp stars were unlikely to be the only progenitor stars of the high-field magnetic white dwarfs. Additionally, if the low-field magnetic white dwarfs are considered (Aznar Cuadrado et al. 2004; Jordan et al. 2007; Kawka & Vennes 2012), the possibility of the Ap/Bp stars being the sole progenitors becomes increasingly remote. Wickramasinghe & Ferrario (2005) thus explored other scenarios to explain the observed mass and field distributions of the high-field magnetic white dwarfs, where the progenitors are not limited to groups of main-sequence stars that are currently labelled as magnetic. They suggested that if ~40% of main-sequence stars that are more massive than ~4.5 $M_\odot$ have magnetic fields of 10 – 100 G, which is below the current detection level for most stars, then the mass distribution and observed percentage of high-field magnetic white dwarfs could be naturally explained (Wickramasinghe & Ferrario 2005). To account for the incidence of low-field magnetic white dwarfs, Wickramasinghe & Ferrario (2005) suggest that their progenitors may mainly be F stars; a different progenitor than for the high-field magnetic white dwarfs. However, a model for the origin of magnetic fields in white dwarfs also needs to account for the occurrence of the observed higher-than-average mass in the high-field magnetic white dwarfs (Wickramasinghe & Ferrario 2005).

Findings from Dobbie et al. (2013) regarding double-degenerate systems (consisting of a high-field magnetic white dwarf) are compatible with the "fossil field" hypothesis. Dobbie et al. (2013) observed newly resolved components of two hot, double-degenerate systems, where each system consists of a hydrogen-rich, non-magnetic white dwarf and a hydrogen-rich high-field magnetic white dwarf at wide separations (>100 AU). The parameters derived for the magnetic white dwarfs suggest their progenitors were perhaps early-type stars of $M_{\rm init} > 2M_{\odot}$, indicating a late B spectral type, where the incidence of magnetism is at its highest along the main sequence (Ferrario & Wickramasinghe 2005). They note, however, that the formation of high-field magnetic white dwarfs from close binary interactions cannot be ruled out.

If the magnetism in white dwarfs originates from the evolution of single magnetic main-sequence stars, then the same fraction of magnetic white dwarfs in detached binary systems might be expected. However, in the SDSS observations up to DR3, Liebert et al. (2005) noticed that no magnetic white dwarf was found in a detached binary with a main-sequence star. More recently, Rebassa-Mansergas et al. (2012) also found no magnetic white dwarfs in detached binary systems with main-sequence stars amongst a sample of 2248 such binaries. This contrasts with the high proportion (~25%, Wickramasinghe & Ferrario 2000) of magnetic white dwarf primaries in close interacting accreting systems (magnetic cataclysmic variables, CVs). The absence of magnetic white dwarfs in detached binary systems, combined with their much higher occurrence (~25%) in close interacting binaries, perhaps indicates that the origin of strong magnetic fields may be a product of some part of the binary evolution and has a close link with the formation of CVs.

Merger Evolution

Consequently, this led Tout et al. (2008) to propose that the progenitors of single high-field magnetic white dwarfs have a binary star origin where the stellar cores merge in a common envelope. As the giant star fills its Roche lobe, the unstable mass transfer between the two cores leads to a envelope surrounding both the degenerate core and its companion (most likely an unevolved, lower mass main-sequence star). Within the common envelope the cores spin inwards, and energy and angular momentum are transferred outwards to the envelope. Differential rotation occurs in the common envelope as the cores move closer together and their orbital period decreases. In the presence of differential rotation and convection in the common envelope a stellar magnetic dynamo is generated. The magnetic field can penetrate the surface of the core and as it later cools and contracts, the field becomes frozen in the core. If the cores are closer at the end of the common envelope evolution, the differential rotation in the common envelope is greater, and therefore a stronger magnetic field is expected (Tout et al. 2008). As a result, the stars that merge will appear from the common envelope phase with the strongest magnetic fields, while magnetic CVs will be the result of those systems that almost merged in the common envelope. This hypothesis assumes that any fossil magnetic field present in the binary system will either be destroyed in the common envelope phase or act as a seed field for the magnetic dynamo.

As the star emerges from the common envelope phase it should rotate rapidly, but then spin down quickly due to magnetic braking within $10^4 - 10^5$ years (Tout & Pringle 1992). Furthermore, once the giant envelope dissipates the high-field magnetic white dwarf is no longer expected to rotate quickly. As a result, this mechanism accounts for the “slow rotator” magnetic white dwarfs with suspected periods of $\gtrsim$100 years, but not for the stars with rapid rotation periods (e.g. SDSS J2257+0755 with $P \approx 1354$ s, Chapter 2).

However, simulations have since shown that while strong field strengths may be transferred to the degenerate core, once the common envelope is ejected, the magnetic field decays rapidly and is quickly lost (Potter & Tout 2010). Therefore, this mechanism could produce weaker magnetic fields, but far more energy than the system could yield would be required to generate the strongest white dwarf field strengths. As an exception to this, Potter & Tout (2010) also noted that some particular orientations of the magnetic dynamo could produce stronger magnetic fields.

Similarly, García-Berro et al. (2012) show that high-field magnetic white dwarfs can be created from the merger of two degenerate cores. Their simulations indicate that magnetic fields on the order of 10^7 G, comparable to field strengths for high-field magnetic white dwarfs, can be produced by a stellar dynamo in a hot, convective, and differentially rotating corona in the outer layers of the remnant, following the merging of double-degenerate cores. Simulations by Lorén-Aguilar et al. (2009) yield high field strengths of $\sim 10^{10}$ G, demonstrating that the energy available in the convective corona is sufficiently large to produce strong magnetic fields. Even if the efficiency of converting the total energy in the convective shell to magnetic energy is as low as 0.1%, the field strengths are still comparable to those of typical high-field magnetic white dwarfs ($\sim 10^7$ G). Furthermore, García-Berro et al. (2012) claim their model also accounts for the wide variety of spin periods observed for high-field magnetic white dwarfs (i.e. both slow and fast rotators), from the angle between the magnetic axis and rotation axis. For example, a magnetic white dwarf will rapidly spin-down (becoming a slow rotator) on short timescales by magnetic dipole radiation if the rotation and magnetic axes are not aligned, while the magnetic white dwarf will remain a fast rotator if the axes are near alignment.

The merger hypothesis may explain the deficiency of high-field magnetic white dwarfs in detached binary systems with late-type main-sequence stars, and their abundance in interacting CVs.

1.2.3 Mass Distribution

In general, magnetic white dwarfs are thought to have higher masses than the average mass of their non-magnetic counterparts. This could indicate that magnetic white dwarfs either evolve from more massive main-sequence progenitor stars, or that they are more massive due to a binary merger (or both). High-field magnetic white dwarfs form the majority of the known magnetic white dwarfs and, as a group, have a higher mean mass of $\sim 0.93 M_\odot$ (Liebert et al. 2003) than their non-magnetic counterparts, which have a mean mass of $\sim 0.58 M_\odot$ (Bergeron et al. 1992). To account for the higher mean mass, high-field magnetic white dwarfs could have more massive progenitors on average than the non-magnetic white dwarfs.

The distribution of magnetic white dwarfs shown in Figure 1.3 (created using the magnetic white dwarf catalogue listed in Table A.1) peaks at masses of $0.5 - 0.6 M_\odot$, comparable to the mean mass of non-magnetic white dwarfs at $\sim 0.6 M_\odot$ (e.g. Bergeron et al. 1992; Liebert, Bergeron & Holberg 2005; Kepler et al. 2007). However, a considerable fraction of the magnetic white dwarf population also appears to have masses of $\sim 0.9 M_\odot$. This bimodal distribution may be indicative of the field strengths of the magnetic white dwarfs, where the low-field stars have masses in the range from 0.5 to 0.6 $M_\odot$ (Jordan et al. 2007) and formed from single star evolution, similar to their non-magnetic counterparts, while the high-field stars have higher masses of $0.8 - 1.0 M_\odot$ and evolved either from single or binary star evolution. The high-field magnetic white dwarfs could have evolved from different, more massive progenitor stars, in comparison to the progenitors of the weaker field white dwarfs: Wickramasinghe & Ferrario (2005) proposed that the progenitors of the low-field magnetic white dwarfs may be F stars, whereas the progenitors of high-field magnetic white dwarfs could be larger A/B stars. Therefore, a relationship between the magnetic field strength and white dwarf mass may be expected, and may provide useful insight into the progenitors of magnetic white dwarfs (explored in further detail in Chapter 2). Alternatively, the magnetic field may inhibit the mass and angular momentum loss during the post main-sequence evolution, hence leaving behind a higher mass white dwarf, perhaps also meaning that magnetic stars have a different initial-final mass relation. Observations of white dwarfs in clusters provide a unique opportunity to test this relationship and the influence of magnetism. So far, only one magnetic white dwarf has been discovered in a cluster, which is WD 0836+201[1] (EG59) in the Praesepe cluster. The

[1]Casewell et al. (2009) warns this star has been mislabelled in previous work (e.g. Claver et al. 2001;

magnetic white dwarf has an estimated mass of $0.82 \pm 0.05 M_{\odot}$ (Külebi et al. 2009), while the non-magnetic white dwarfs in the cluster have an average mass of $0.77 M_{\odot}$ (calculated from the masses listed in Casewell et al. 2009). The magnetic white dwarf lies slightly above the rest of the Praesepe white dwarfs in the initial mass – final mass plot for the cluster (see Fig. 7 in Casewell et al. 2009).

Finally, the magnetic white dwarfs in the high-mass tail of the distribution ($> 1.2 M_{\odot}$) may be merger products, of which some may have resulted from a double-degenerate merger. These stars could potentially provide important model constraints for the progenitor masses required for the formation of some Type Ia supernovae via the double-degenerate channel, while the numbers of high-field magnetic white dwarfs may help resolve the discrepancy between predicted and observed Type Ia supernovae rates, and bring them in closer agreement (Ruiter et al. 2009). The mass distribution for high-field magnetic white dwarfs may also further the understanding of the circumstances for the failed Type Ia supernovae, which produce white dwarfs. For example, if RE J0317-853 formed from a double-degenerate merger ($M \sim 1.35 M_{\odot}$), it may have narrowly missed becoming a Type Ia supernova.

Mass estimates have been made for few magnetic white dwarfs. For low-field stars, their masses can be determined from spectral fitting of atmospheric models, where a zero magnetic field is assumed. However, this cannot be achieved accurately for high-field magnetic white dwarfs, where spectral features can be affected by the presence of a magnetic field, and thus modelled inappropriately. Parallax measurements from *Gaia* will be revolutionary, allowing mass estimates to be determined for the entire sample of magnetic white dwarfs. An accurate parallax π (in arcseconds) for white dwarfs from *Gaia* will yield a measurement of the distance (in parsecs) to the star since $d = 1/\pi$. The luminosity of the star is determined using the distance to the white dwarf and its apparent magnitude. The radius of the star can then be estimated using Stefan-Boltzmann's law (assuming the

Dobbie et al. 2006) and should not be confused with WD 0837+199 (EG61).

star emits black body radiation),

$$L = 4\pi R^2 \sigma T^4, \tag{1.1}$$

where L is the star's luminosity, R is the radius of the star, σ is the Stefan-Boltzmann constant and T is the effective temperature of the star. In combination with spectroscopic observations, a comparison between an observed spectrum of a white dwarf and model atmospheres gives an estimate of the white dwarf's surface gravity $\log g$ and effective temperature T. The width of the spectral lines depends on the density of the star's atmosphere, and therefore the surface gravity. Assuming, the core is degenerate, the theoretical mass-radius relation can be utilised to determine the mass of the white dwarf for a particular core composition (but this approach cannot be used to test the mass-radius relation). Alternatively, the estimate for the surface gravity and radius can be used to calculate the mass using $M = gR^2/G$, without requiring the mass-radius relation. Provencal et al. (1998) outlined different methods for determining white dwarf masses using *Hipparcos* parallaxes.

The ability to accurately determine masses of magnetic white dwarfs will be hugely significant in determining whether there are two distinct progenitor populations making up the magnetic white dwarf sample, the influence of magnetism during the post main-sequence evolution, and if there is a relationship between the mass and field strength.

1.2.4 Field Distribution & Structure

The field structure of magnetic white dwarfs is typically modelled with an offset dipole structure, where the dipole is shifted from the centre along the dipole axis, rather than with a centred dipole model. Evidence of Zeeman splitting in spectroscopic observations suggests that magnetic white dwarfs have complex non-dipolar fields (Wickramasinghe & Ferrario 2000). For example, Külebi et al. (2009) modelled spectra of 141 DAH magnetic

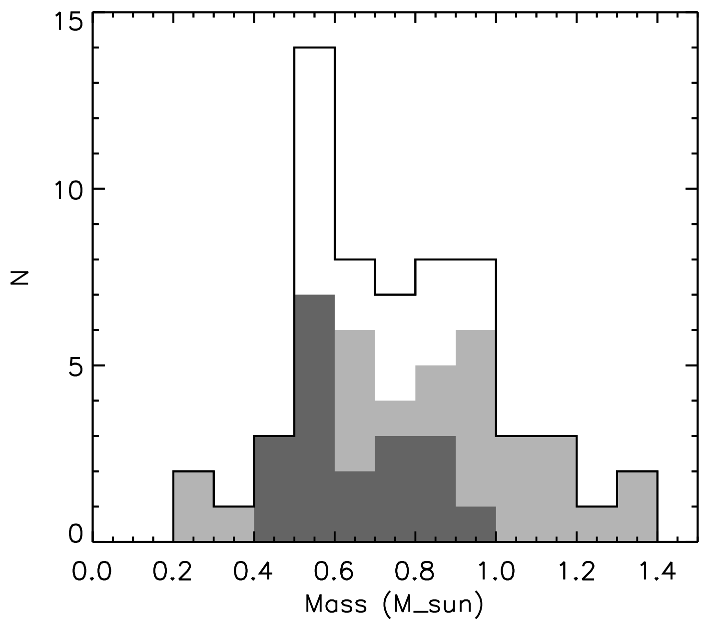

Figure 1.3: Mass distribution of magnetic white dwarfs listed in the catalogue in Table A.1 (black outline). The darker shaded region is the mass distribution of the low-field magnetic white dwarfs ($B < 1$ MG) and the lighter shaded region is the mass distribution of the high-field magnetic white dwarfs ($B > 1$ MG). The mass distribution of the high-field stars covers a wider range of masses than the low-field magnetic white dwarfs. Note – There is one magnetic white dwarf that is included in the overall distribution, but not in the separate distributions with magnetic field, as it has an unknown field strength.

white dwarfs from the SDSS, and found that, in all cases, the offset dipole models yielded significantly better fits than the centred dipole models. In addition, they found appropriate model fits could not be obtained for the magnetic white dwarfs with the highest field strengths, indicative of a more complicated field structure. Using flux and circular polarisation spectroscopy, Euchner et al. (2005) performed a Zeeman tomographic analysis and revealed that HE 1045-0908 has a complex field structure, dominated by a quadrupole with additional dipole and octupole contributions.

The offset dipole model is not suitable in all cases, and for WD 1953-011 (Maxted et al. 2000) and PG 1031+234 (Latter et al. 1987), the spectra can be modelled with a spot-like field enhancement, where the spectra at some phases is fit with a centred dipole model but at other phases requires a much stronger field strength.

1.2.5 Rotation Periods & Variability

Conservation of angular momentum as the core contracts during the post main-sequence evolution suggests white dwarfs should rotate rapidly, near their break-up value, similar to neutron stars. Assuming a simple spherical rotating star, with a typical mass of $M = 0.6M_{\odot}$ and radius of $R = 0.009R_{\odot}$, the break-up velocity equates to $\approx 3.5 \times 10^6$ m/s and a rotation period of 11 s. No spin periods of white dwarfs have ever been measured as fast as their break-up value, indicating there must be significant angular momentum loss during the post main-sequence evolution, with angular momentum efficiently transferred from the core to the outer envelope (as proposed by Spruit 1998, 2002). Spruit (1998) suggested that if the magnetic field locks the white dwarf to the envelope, the angular momentum would be lost quickly, yielding slow rotators. Meanwhile, King et al. (2001) proposed that double-degenerate mergers may cause white dwarfs to be spun up, producing rapid rotators ($P \sim$ minutes). Magnetic white dwarfs may also rotate more slowly than their non-magnetic counterparts, as the magnetic field could cause magnetic braking as the star evolves. Observations show that isolated non-magnetic and magnetic white dwarfs are both generally slow rotators. For example, Heber et al. (1997) estimated upper limits for the projected rotational velocities of a sample of DA white dwarfs using the narrow Hα line cores. They found that none of the projected velocities or upper limits exceeded 60 km/s, and were consistent with rotation periods greater than one hour. Although their sample covered a broad range of masses with a mean of $\approx 0.6M_{\odot}$, they concluded that isolated DA white dwarfs are slow rotators, regardless of mass.

Non-Magnetic White Dwarfs

Rotation velocities can be estimated for non-magnetic white dwarfs using the spectral line cores in high-resolution spectroscopic observations, and are found to have periods up to ~1 day (e.g. Heber et al. 1997; Koester et al. 1998; Karl et al. 2005; Berger et al. 2005). However, these measurements often only provide upper limits, as the spectral lines usually suffer from considerable broadening due to the strong gravitational field. Pulsating white dwarfs also appear to consistently have rotation periods of ~1 day (Kawaler 2004), measured from rotational splittings in the pulsations, which typically have oscillation modes of 140 − 4000 s (Winget & Kepler 2008; Hermes et al. 2012).

Magnetic White Dwarfs

Rotation periods of magnetic white dwarfs can be measured through variability in spectroscopic, polarimetric and photometric observations. Rotation in a magnetic white dwarf was first discovered by Angel & Landstreet (1971) in G 195-19, from measuring periodic variations in its circular polarisation. Since their discovery, well-constrained spin periods have been determined for 32 magnetic white dwarfs using the variations in their polarisation, spectra and photometry with time. Known rotation periods for magnetic white dwarfs range from 725 s (for RE J0317-853, Barstow et al. 1995; Ferrario et al. 1997a) up to 17.9 days (for KUV 813-14, Schmidt & Norsworthy 1991). There is a subset of five highly magnetic white dwarfs thought to be very slow rotators with periods greater than 100 years (West 1989), as no variability has been detected in their spectral or polarisation observations taken over decades; however, the absence of variability could also be due to a rotationally symmetric magnetic field geometry. Rotating magnetic white dwarfs provide a unique opportunity to better understand the rotational behaviour of the whole population of white dwarfs, and thus the mechanisms required for angular momentum loss during post main-sequence evolution. Ferrario & Wickramasinghe (2005) suggested that the rotation periods measured for magnetic white dwarfs appear to be divided into three sub-groups: very slow, highly magnetised rotators with long periods of 100 years; intermediate rotators with periods of approximately hours to days; and strongly magnetised fast rotators. However, these divisions are only a result of observations and it is unknown whether they are even real sub-groups, caused by different evolutionary paths and underlying physical processes. Ferrario & Wickramasinghe (2005) revealed there may be a relationship between the magnetic field strength and the rotation period, where the larger the magnetic field, the longer the spin period, for the high-field magnetic white dwarfs that formed by single star evolution (discussed further in Chapter 2). It is likely that the magnetic white dwarfs consist of two populations: those from a single star evolution and those resulting from a binary star merger, suggesting there may be a wide variety of rotation periods exhibiting different characteristics and relationships with their physical parameters, depending on their evolutionary path.

Variability

Spectral variability can be observed from changes in the Zeeman split components, caused by changes in the magnetic field strength. Approximately 40% of magnetic white dwarfs show signs of photometric variability as the star rotates (Brinkworth et al. 2013, and see Chapter 2). Photometric modulations can be exhibited in high-field magnetic white dwarfs due to the effects of magnetic dichroism: the dependence of the continuum opacity on the surface field strength (Ferrario et al. 1997a). For example, RE J0317-853 shows photometric fluctuations of ∼10% at optical wavelengths as it rotates, perhaps due to the effects of magnetic dichroism (Ferrario et al. 1997a), where its field strength varies between $180 - 800\,\mathrm{MG}$ across the surface (Burleigh et al. 1999).

However, photometric variability has also been observed for the cool, low-field magnetic white dwarfs ($T < 12,000\,\mathrm{K}$), where the modulations have been attributed to star spots on the surface of the white dwarf in a partially convective atmosphere, analogous to Sun spots (Brinkworth et al. 2004, 2005). Star spots on the surface are caused by the suppression of convection in the stellar atmosphere due to the magnetic field. These star spots are cooler and therefore darker than the surrounding atmosphere. As the star rotates and the spot moves in and out of view, fluctuations are observed in the star's brightness. White dwarfs become fully radiative at effective temperatures higher than $12,000 - 14,000\,\mathrm{K}$ for DA white dwarfs and $27,000 - 29,000\,\mathrm{K}$ for DBs (e.g. Winget & Kepler 2008 and references therein), and therefore magnetic white dwarfs below these temperature ranges will have at least partially convective atmospheres, capable of forming star spots. This effect is observed for WD 1953-011 ($T_{\mathrm{eff}} \approx 8000\,\mathrm{K}$, $B \approx 70\,\mathrm{kG}$), which exhibits sinusoidal variability of ≈2% peak-to-peak amplitude with a period of 1.44 days, due to the presence of a star spot covering ∼10% of the surface (Maxted et al. 2000; Brinkworth et al. 2005). Photometric variability is not expected to be observed for magnetic white dwarfs with high effective temperatures and low-field strengths, as they are too hot to have a convective atmosphere in which star spots can form, and have field strengths too weak for dichroism to have an effect. However, in Chapter 2, four magnetic white dwarfs with these characteristics are found to display photometric modulations, showing there must be another mechanism causing the variability that has not yet been explored. The photometric fluctuations exhibited by some white dwarfs can also be used as a method for identifying previously undetected magnetic fields. Holberg & Howell (2011) found unusual photometric variations of $\approx$5% peak-to-peak amplitude, with a period of 6.1375 h for a hot white dwarf in the *Kepler* field. Later, high signal-to-noise spectra revealed the presence of a magnetic field.

Photometric variability is also observed on short timescales by pulsating white dwarfs. Pulsations are detected in instability strips along the white dwarf cooling track. Hydrogen-rich DA white dwarfs pulsate in a temperature region between $10,850-12,270$ K (referred to as DAVs or ZZ Ceti stars), while the instability region for helium-rich DB stars (the DBVs or V 777 Her stars) is between $22,000-29,000$ K. For hot pre-white dwarf PG 1159 stars, with mixtures of helium, carbon and oxygen in their atmospheres (the DOVs or GW Vir stars), the region lies between $75,000 - 170,000$ K (see Winget & Kepler 2008, and references therein, and Fontaine & Brassard 2008 for reviews). A fourth instability strip lies around temperatures of 20,000 K for hot carbon-dominated atmosphere DQ white dwarfs (Fontaine, Brassard & Dufour 2008; Dufour et al. 2008b, and see Chapter 3). The fluctuations in brightness arise at the temperature region where the atmosphere evolves from being radiative to convective, i.e. between partial ionisation and recombination in the atmosphere, which excites low-order non-radial g-mode pulsations across the instability strip.

In summary, white dwarfs appear to have rotation periods around a day, while periods for magnetic white dwarfs seem to have a wider distribution. This may be indicative of the influence of the magnetic field on the white dwarf, and the role it plays during the white dwarf formation and evolution. Precise measurements of rotation periods for a large sample of magnetic white dwarfs are required to test theories of mass and angular momentum loss during the post main-sequence evolution, and to inform formation and evolutionary scenarios that can explain their generally longer than expected spin periods.

1.3 Structure of Thesis

This thesis comprises six chapters. In the following chapter, I present optical time-series observations of a sample of magnetic white dwarfs to obtain spin periods using their photometric variability. Chapter 3 discusses, in more detail, one of the interesting variable magnetic white dwarfs (a hot, carbon-dominated atmosphere magnetic white dwarf) identified in Chapter 2, which shows modulations on a timescale of days. Observations from a long term monitoring campaign of magnetic white dwarfs searching for rotation periods on a timescale of months are shown in Chapter 4. In Chapter 5, I present an "Observed minus Calculated" analysis (O – C), using nearly 20 years of observations, of the exceptional magnetic white dwarf RE J0317−853, and explore the possible causes for a rate of period change ($\dot{P}$) in the O – C diagram. Finally, Chapter 6 contains concluding remarks and outlines future projects on magnetic white dwarf research.

2

Photometric Variability and Rotation in Magnetic White Dwarfs

In this chapter, I present results from a survey of 77 magnetic white dwarfs (MWDs) to search for photometric variability and determine their rotation periods. The sample consists of 24 bright ($V < 16$), isolated MWDs and 53 MWDs ($r' < 18.5$) discovered spectroscopically by the Sloan Digital Sky Survey (SDSS). The 2.5 m Isaac Newton Telescope in La Palma is used to obtain photometric light curves for each target. Well-defined periods of variability are determined in 12 isolated MWDs (16% of the sample), while variability with poorly constrained periods is found in a further 13 stars (17%). A period of $7.72^{+0.58}_{-0.42}$ days is detected for LHS 5064, the second longest period measured for an isolated MWD. Where periods of variability are determined, the magnetic field strength, temperature, mass and cooling age are compared to search for correlations between the parameters. A relationship is detected between the spin period and field strength and temperature, suggesting hotter MWDs spin faster and have higher magnetic fields, characteristics associated with MWDs possibly forming in mergers. However, the sample is small and thus conclusions on the correlations between parameters are limited.

2.1 Background

Prior to this investigation, rotation periods had been measured for 23 MWDs (not including the "slow rotators"), of which 10 were found through photometric variations, with spin periods mostly of a few hours to days (e.g. Brinkworth et al. 2004, 2005, 2013; Holberg & Howell 2011). As discussed in Chapter 1, the photometric variability is believed to be caused by different mechanisms depending on the temperature and magnetic field strength of the star. Generally, the modulations in brightness are thought to occur with the rotation of the star, with the exception of some carbon-dominated hot DQ WDs, which appear to exhibit non-radial pulsations on short timescales up to $\sim 1000\,$s (explored in Chapter 3).

A larger sample of well-determined spin periods for MWDs provides the opportunity to search for correlations between intrinsic physical parameters of MWDs and their spin periods. If relationships exist between properties, there is the potential to better understand the evolution and formation of MWDs, the influence of magnetism on the post main-sequence evolution, and how they compare with the non-magnetic white dwarf population.

2.2 Observations

A sample of 77 MWDs was observed photometrically with the Isaac Newton Telescope (INT) in six runs[1] in 2-8 March 2009, 17-23 October 2009, 3-9 March 2010, 10-12 February 2011, 4-7 July 2011 and 27 March - 2 April 2012. One target was additionally observed in May 2010. The sample consisted of 24 bright ($V < 16$), isolated MWDs (selected from the 65 listed in Wickramasinghe & Ferrario 2000; see Table 2.1) and 53 MWDs ($r' < 18.5$) discovered spectroscopically in the SDSS (Table 2.2). The bright

[1] I was an observer for the March 2010 run, and the observer and principal investigator for runs in February 2011, July 2011 and March 2012.

MWDs were observed in the Harris V filter, apart from three targets, which were taken in the SDSS r' filter (KUV 03292+0035, HE 0330-0002 and LHS 2229). The observations of the SDSS MWDs were taken in the SDSS r' filter, except for SDSS J1250+1549 which was taken in the SDSS z' and i' band. Exposure times ranged from 5 to 60 s for the bright MWDs, depending on the magnitude of the target and the weather conditions. Exposure times for the SDSS MWDs ranged from 30 to 180 s. The observing strategy was developed to search for both short term (minutes – hours) and long term (days) variability. Each star was observed repeatedly for at least 30 minutes, then an hour later, three hours later, a day later and 5 – 7 days later. This also helped to break period aliases due to the time sampling.

Isaac Newton Telescope (INT)

The 2.5 m INT is part of the Isaac Newton Group, located at the Roque de los Muchachos Observatory in La Palma, Spain. The Wide Field Camera (WFC) was used on the INT and mounted at prime focus. The WFC instrument offers the ability to achieve high-resolution, deep wide-field optical imaging. For the purpose of this survey, it meant that a sufficient number of stable comparison stars for the differential photometry analysis were in the field-of-view. The INT WFC is a mosaic of four thinned 2k×4k pixel CCDs, with a total field-of-view of $34 \times 34\,\mathrm{arcmin}^2$ at 0.33 arcsec/pixel. The coordinates of the target were positioned in the centre of CCD four.

The Sloan Digital Sky Survey (SDSS)

The SDSS is a redshift survey that uses multi-filter imaging and spectroscopy to observe, primarily, galaxies and quasars. It began in 2000 and uses a dedicated a 2.5 m wide-angle telescope at Apache Point Observatory in New Mexico and can image 1.5 square degrees of the sky at a time. The SDSS telescope uses the drift scanning technique for observations, where the telescope is kept stationary and stars are imaged in small strips on the sky, as they move across the focal plane of the CCD, as the Earth rotates. In this configuration, the telescope shutter stays open and reads out continuously. This method maintains consistent astrometry over the widest possible field and the precision is unaffected by telescope tracking errors. Even though the main science objectives of the SDSS have not been stellar astronomy, it has been vital to the development and progression of the field of white dwarfs. Prior to the SDSS, just 65 isolated MWDs were known (Wickramasinghe & Ferrario 2000). Since the SDSS started, more than 200 isolated MWDs have been catalogued (see Table A.1), with field strengths ranging from 10 kG up to 1000 MG (Gänsicke et al. 2002; Schmidt et al. 2003; Vanlandingham et al. 2005; Külebi et al. 2009), and the latest WD SDSS DR7 catalogue has identified more than 500 possible isolated MWDs (Kepler et al. 2013).

The Catalina Sky Survey (CSS)

The Catalina Sky Survey (CSS) started in 1998, with the aim of searching for near-Earth objects (NEOs) and, in particular, potentially hazardous asteroids. In addition, the Catalina Real-time Transient Survey (CRTS) searches for optical transients in the data (e.g. Drake et al. 2009). CSS utilises three telescopes: a 1.5 m and a 0.68 m located in the Catalina Mountains in Arizona and a 0.5 m telescope at Siding Spring Observatory in Australia. All telescopes are mounted with the same CCD technology, which has a field-of-view of 8 square degrees. On a clear night, the main 1.5 m Catalina telescope covers up to ∼1200 square degrees of sky. Observations of a specific field are repeated four times at regular intervals over ∼30 minutes, with exposures of 30 s, allowing for variations on timescales of minutes to years to be investigated. Each of the stars in the sample (listed in Tables 2.1 and 2.2) were checked for possible observations by the Catalina Sky Survey.

Table 2.1: List of 24 bright MWDs (from the 65 listed in Wickramasinghe & Ferrario 2000) observed with the INT between March 2009 and March 2012. N is the total number of observations taken for that object. WD age is the cooling age only and does not include the main-sequence lifetime.

Target	WD	Epoch	V (mag)	N	B_p (MG)	$T_{\rm eff}$ (K)	M ($M_\odot$)	WD Age (Gyr)	$P_{\rm lit}$	CSS data?	Refs
LHS 1038	0009+501	Oct 2009	14.4	78	0.295	6540	0.74	2.97	8.02 ± 0.19 h	no	1,2
G 158−45	0011−134	Oct 2009	15.9	105	16.7	6010	0.71	3.65	11 h – 1 d	yes	2,3
PG 0136+251	0136+251	Oct 2009	16.1	90	≤0.1	39640	1.20	0.75		yes	4,5
MWD 0159−032	0159−032	Oct 2009	17.1	43	6	26000				yes	6
KPD0253+5052	0253+508	Oct 2009	15.2	48	13-14	15000			3.79 ± 0.05 h	no	7,8
LHS 5064	0257+080	Oct 2009	15.9	57	0.090	6680	0.57	1.60	9 h – 6 d	yes	9,10,2,11
KUV 03292+0035	0329+005	Oct 2009	16.7	44	13.13	15500				yes	12,13
HE 0330−0002	0330−000	Oct 2009	16.9	35	849	7000				yes	12,14,13
LHS 1734	0503−174	Oct 2009	16.0	55	7.3	5300	0.37	1.86		yes	15,2
G 99−37	0548−001	Mar & Oct 2009	14.6	152	7.3	6070	0.69	3.90	4.117 h	yes	16,17,2,18
G 99−47	0553+053	Mar & Oct 2009	14.1	320	20	5790	0.71	4.11	0.97 h	no	19,2,18
GD 77	0637+478	Mar 2010	14.8	10	1.2	14870	0.69			no	20,21
G 234−4	0728+642	Mar 2009 & 2010	16.3	54	0.0396	4500	0.58	7.58		yes	3,22,23
GD 90	0816+376	Oct 2009	15.6	42	9	14000	0.60	0.47		yes	24,25
LB 8915	0853+163	Mar 2010 & Feb 2011	15.8	42	0.75-1	24000			2 h – 1 d	yes	26,11
G 195−19	0912+536	Mar 2009 & 2010	13.8	73	~100	7160	0.75	2.54	1.33 d	no	27,2,28
LHS 2229	1008+290	Mar 2012	17.5	81	~100	4600				yes	29
PG 1015+014	1015+014	Mar 2012	16.3	126	50-90	10000	1.15		98.7 min	yes	30,31,32,33,11
GD 116	1017+366	Mar 2012	16.0	69	65	16000				yes	34
LHS 2273	1026+117	Mar 2009	16.5	61	18	7160	0.59	1.51	35 – 45 min	yes	10,11
HE 1043−0502	1043−050	Mar 2010	17.1	13	~820	~15000				yes	35,14
HE 1045−0908	1045−091	Mar 2009	16.7	15	16	10000			2.7 h	yes	36
SBS 1349+5434	1349+545	Mar 2009 & Jul 2011	16.4	68	761	11000				yes	12,37,38
PG 2329+267	2329+267	Oct 2009	15.3	69	2.3	11730	1.18	2.04		yes	39,5

Table 2.1: *continued*

REFERENCES.— (1) Valyavin et al. 2005; (2) Bergeron et al. 2001; (3) Putney 1997; (4) Schmidt et al. 1992; (5) Liebert, Bergeron & Holberg 2005; (6) Achilleos et al. 1991; (7) Achilleos & Wickramasinghe 1989; (8) Friedrich et al. 1997; (9) Koester et al. 2009; (10) Bergeron et al. 1997; (11) Brinkworth et al. 2013; (12) Külebi et al. 2009; (13) Schmidt et al. 2003; (14) Schmidt et al. 2001; (15) Bergeron et al. 1992; (16) Vornanen et al. 2010; (17) Dufour, Bergeron & Fontaine 2005; (18) Bues & Pragal 1989; (19) Putney & Jordan 1995; (20) Schmidt, Stockman & Smith 1992; (21) Giovannini et al. 1998; (22) Holberg, Bergeron & Gianninas 2008; (23) Sion et al. 2009; (24) Angel et al. 1974; (25) Limoges & Bergeron 2010; (26) Wesemael et al. 2001; (27) Angel 1977; (28) Angel et al. 1972; (29) Schmidt et al. 1999; (30) Euchner et al. 2006; (31) Liebert, Bergeron & Holberg 2003; (32) Wickramasinghe & Cropper 1988; (33) Schmidt & Norsworthy 1991; (34) Saffer et al. 1989; (35) Wickramasinghe et al. 2002; (36) Euchner et al. 2005; (37) Vanlandingham et al. 2005; (38) Liebert et al. 1994; (39) Moran et al. 1998.

Table 2.2: List of 53 SDSS MWDs observed with the INT between October 2009 and March 2012. N is the total number of observations taken for that target.

SDSS Target	WD	Epoch	r' (mag)	N	B_p (MG)	$T_{\rm eff}$ (K)	CSS data?	Ref
SDSS J000555.91−100213.4	0003−103	Oct 2009	18.11	27	1.47	19420	yes	1,2,3
SDSS J001742.44+004137.4	0015+004	Oct 2009	17.21	40	8.3	15000	no	1
SDSS J002129.00+150223.7	0018+147	Oct 2009	17.97	30	530	7000	no	4,5
SDSS J014245.37+131546.4	0140+130	Oct 2009	17.99	30	4	15000	yes	1
SDSS J021116.34+003128.5	0208+002	Oct 2009	18.52	30	341	9000	yes	4,1
SDSS J021148.22+211548.2	0209+210	Oct 2009	17.21	43	166	12000	no	4,5
SDSS J030407.40−002541.7	0301−006	Oct 2009	17.95	27	11	15000	yes	4,6
SDSS J031824.20+422650.9	0315+422	Oct 2009	18.32	31	10.12	10500	no	4
SDSS J034511.11+003444.3	0342+004	Oct 2009	18.52	29	1.96	8000	yes	4,6
SDSS J080359.93+122943.9	0801+124	Mar 2010	17.53	15	40.7	9000	no	4
SDSS J085106.12+120157.8	0848+121	Mar 2010	17.14	15	2.03	11000	no	4
SDSS J085830.85+412635.1	0855+416	Mar 2010	16.89	15	3.38	7000	yes	4,1
SDSS J091005.44+081512.2	0907+083	Mar 2012	17.96	38	1.01	25000	no	4
SDSS J091437.40+054453.3	0911+059	Mar 2010	17.64	15	9.2	17000	no	4,5
SDSS J100356.32+053825.6	1001+058	Mar 2010	18.48	23	672	23000	no	4,5
SDSS J100759.80+162349.6	1005+163	Mar 2012	17.80	39	19	11000	no	4
SDSS J101529.62+090703.8	1012+093	Mar 2012	18.41	31	4.09	7200	no	4,5
SDSS J103532.53+212603.5	1032+214	Mar 2012	17.23	41	2.96	7000	no	4
SDSS J105709.81+041130.3	1054+042	Mar 2012	17.58	23	2.03	8000	no	4
SDSS J111341.33+014641.7	1111+020	Mar 2012	18.47	31	?	?	yes	1
SDSS J113357.66+515204.8	1131+521	Feb 2011	17.71	21	8.64	22000	yes	4,1
SDSS J113756.50+574022.4	1135+579	Mar 2012	16.75	28	5	7800	no	4,5
SDSS J113839.51−014902.9	1136−015	Mar 2012	17.73	27	22.7	10500	yes	4,1,7
SDSS J121456.39−023402.8	1212−022	Mar 2012	17.74	33	1.92	6000	yes	8,1
SDSS J123414.11+124829.6	1231+130	Mar 2012	17.32	58	4.32	8200	yes	4,5
SDSS J124806.38+410427.2	1245+413	Mar 2012	17.71	36	7	7000	no	4,5
SDSS J125044.42+154957.4	1248+161	Mar 2010 & May 2010	18.32	99	21	10000	yes	4,5
SDSS J125715.54+341439.3	1254+345	Feb 2011	16.81	26	11	8500	yes	4
SDSS J132858.20+590851.0	1327+594	Mar 2012	18.25	29	18	25000	yes	5
SDSS J133340.34+640627.4	1332+643	Mar 2012	18.10	27	11	13500	yes	4,1
SDSS J133359.86+001654.8	1331+005	Mar 2012	18.33	23	?	?	yes	1
SDSS J134820.79+381017.2	1346+383	Mar 2012	18.04	32	13.7	35000	no	4
SDSS J141906.19+254356.5	1416+256	Mar 2012	17.46	27	2	9000	no	4
SDSS J142703.35+372110.5	1425+375	Feb 2011	17.91	29	27	19000	no	4,5
SDSS J143019.05+281100.8	1428+282	Mar 2012	17.68	39	9	9000	no	4
SDSS J150746.80+520958.0	1506+522	Jul 2011	17.27	50	65.2	18000	no	9
SDSS J150813.24+394504.9	1506+399	Mar 2012	17.75	15	13	17000	yes	4,5
SDSS J151130.17+422023.0	1509+425	Mar 2012	18.01	33	22	9750	no	4,5
SDSS J152401.59+185659.2	1521+191	Jul 2011	18.34	22	12	13500	no	5
SDSS J153843.10+084238.2	1536+085	Mar 2012	17.94	30	13	9500	no	5
SDSS J160437.36+490809.2	1603+492	Mar 2012	17.91	33	60	9000	yes	4,1
SDSS J164703.24+370910.3	1645+372	Jul 2011	17.92	38	2	16250	no	4,5
SDSS J204626.15−071037.0	2043−073	Jul 2011	17.90	46	2	8000	yes	4,1
SDSS J214930.74−072812.0	2146−077	Oct 2009	17.80	27	45	22000	yes	4,1
SDSS J215135.00+003140.5	2149+002	Oct 2009	17.84	32	∼300	9000	no	1
SDSS J215148.31+125525.5	2149+126	Oct 2009	18.32	27	21	14000	no	4,1

Table 2.2: *continued*

SDSS Target	WD	Epoch	r' (mag)	N	B_p (MG)	$T_{\rm eff}$ (K)	CSS data?	Ref
SDSS J221828.59−000012.2	2215−002	Oct 2009 & Jul 2011	18.35	72	258	15500	no	4,1
SDSS J224741.46+145638.8	2245+146	Oct 2009	17.62	35	42	18000	yes	4,1
SDSS J225726.05+075541.7	2254+076	Oct 2009 & Jul 2011	17.31	104	16.17	40000	yes	4
SDSS J231951.73+010909.3	2317+008	Jul 2011	18.44	46	9	8300	no	4,5
SDSS J232337.55−004628.2	2321−010	Oct 2009 & Jul 2011	18.31	45	4.8	15000	yes	1
SDSS J234605.44+385337.7	2343+386	Oct 2009	19.28	21	798	26000	no	4,5
SDSS J234623.69−102357.0	2343−106	Oct 2009	18.40	27	9.2	8500	no	4,5

REFERENCES.— (1) Schmidt et al. 2003; (2) Liebert et al. 2003; (3) Dufour et al. 2008b; (4) Külebi et al. 2009; (5) Vanlandingham et al. 2005; (6) Gänsicke et al. 2002; (7) Foltz et al. 1989; (8) Reid, Liebert & Schmidt 2001; (9) Dobbie et al. 2012.

2.3 Data Reduction

The data reduction was carried out using the INT Wide Field Survey pipeline (Irwin & Lewis 2001), developed by the Cambridge Astronomical Survey Unit (CASU). A detailed description of the process can be found in Irwin & Lewis (2001) and Irwin et al. (2007). The pipeline performed a standard CCD reduction of bias correction, trimming of the frames, a non-linearity correction, flat-fielding and gain correction. A master flat field frame was constructed for each waveband by combining all the flats taken during the observing run (usually from a few nights), for that given filter between 10,000 and 30,000 counts, and normalising by the median. Data taken at long wavelengths, i.e. in i' and z' filters, with exposure times longer than 100 s were defringed. Fringe patterns were caused by interference effects in the detector. A master fringe frame was constructed by stacking a selection of unique pointings taken in the same filter with exposures longer than 100 s, for which the best scale factor was determined to make the overall pattern undetectable. To remove these fringe effects, the scaled fringe frame was then subtracted from the science frames. An example of a defringed science frame and a master fringe frame is given in Figure 2.1.

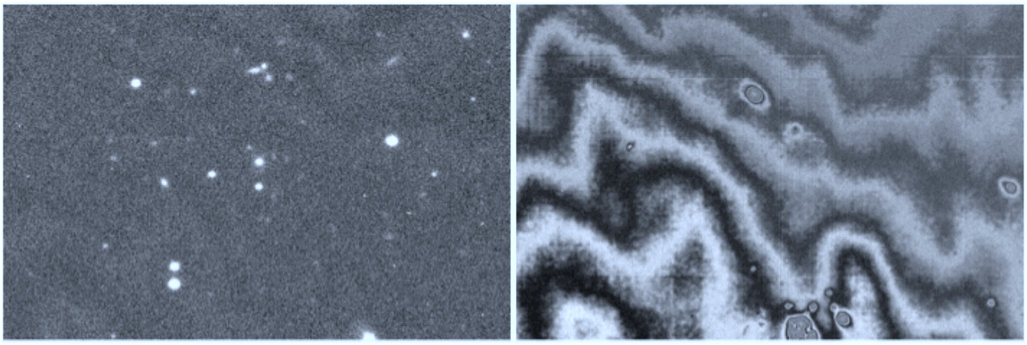

Figure 2.1: *Left:* A close-up of a frame of SDSS J1250+1549 taken in the z'-band in March 2010 corrected for fringe effects. *Right:* The master z' fringe frame for the same region of the CCD.

This was followed by an astrometric calibration of each frame, where the point source catalogue (PSC) from the Two-Micron All-Sky Survey (2MASS) was used as a reference astrometric catalogue. To get optimal positions for the stars, and thus reduce the positioning error, the aperture positions were determined by accurately finding the relative centroid positions of all stars in the frame. This was carried out by stacking ten frames for each target field (taken in the best seeing and sky conditions) to create a master frame, giving a master catalogue listing all of the sources and coordinates in the image with typical root-mean-square (rms) residuals of < 0.2 arcseconds. The master frame was then used to determine the respective positions in the individual frames in the time series.

The background level was determined by dividing the image into a coarse grid and estimating the clipped median of the counts for each bin (bad pixels were rejected using confidence maps). For a given pixel in the image, the background level was then calculated using bilinear interpolation over the background grid. This technique has been discussed in more detail in Irwin (1985).

For the aperture photometry, the flux and light curve for each star was initially calculated for a range of increasing aperture radii ($r_{\rm core}/2$, $r_{\rm core}$, $\sqrt{2}\,r_{\rm core}$, $2r_{\rm core}$ and $2\sqrt{2}\,r_{\rm core}$, where $r_{\rm core}$ was set to the typical FWHM and kept fixed for all of the data), where the rms scatter was calculated for each aperture size. The aperture that yielded the smallest rms for that star was chosen. Aperture corrections were then used to account for the different amounts of flux due to the differently-sized apertures, allowing for the same zero-point system to be used for all of the stars. The aperture corrections were calculated using non-variable stars as ratios of the flux from the differently-sized apertures. To produce light curves for each of the stars, differential photometry was performed by normalising the flux of each star with a combined flux from stable stars of comparable brightness in the field-of-view. The flux measurements were then converted to magnitudes using the zero-point estimate. Fluctuations in the photometry due to atmospheric effects, such as variations in transparency and extinction, were removed by fitting a 2D polynomial to the magnitude residuals of each non-variable star in the field to determine a zero-point correction. The photometric errors were calculated as the quadrature sum of the Poisson noise in the object's counts, Poisson noise in the sky, rms of the sky background fit and a constant value of ∼1.5 mmag to account for systematic errors. Irwin et al. (2007) discuss the photometry and light curve production in more detail.

2.4 Analysis

2.4.1 Floating-mean Periodogram

A "floating-mean" periodogram (Cumming, Marcy & Butler 1999), also known as a generalised Lomb-Scargle periodogram, is used to search for periodicity in the light curves. This technique involves fitting a sine wave plus a constant,

$$f_j = A + B \sin[\omega(t_j - t_0)], \tag{2.1}$$

to the data by minimising χ^2, for a given set of observation times t_j, magnitude measurements y_j and uncertainties σ_j^2 at trial frequencies, where $\omega = 2\pi f$. The floating-mean periodogram script is called PGRAM, part of the RVANAL package written by Tom Marsh.

The floating-mean periodogram allows the constant term A to vary with the fit and therefore treats A as an additional free parameter, rather than fixing the zero-point and fitting the sinusoid (i.e. where $A = 0$ in Eq. 2.1). As discussed by Cumming et al. (1999), this has the advantage over the Lomb-Scargle periodogram (Lomb 1976; Scargle 1982) of remaining robust when the number of observations is small, the sampling is uneven or if the period is comparable to, or longer than, the length of the observations. The resultant periodogram is an inverted plot of the χ^2 of the sinusoidal fit at each frequency, although the periodogram power can also be plotted as a function of frequency (or period).

The power of the floating-mean periodogram $z(\omega)$ is calculated using the expression (Cumming et al. 1999; Cumming 2004),

$$z(\omega) = \frac{(N-3)}{2}\frac{\chi^2_{N-1} - \chi^2(\omega)}{\chi^2(\omega_0)}, \tag{2.2}$$

where,

$$\chi^2(\omega) = \sum_{j=1}^{N} \frac{[y_j - f_j]^2}{\sigma_j^2} \tag{2.3}$$

is the χ^2 of the fit as a function of ω frequencies ($\omega = 2\pi f$) and ω_0 is the best-fitting frequency (i.e. the frequency that gives the maximum periodogram power or the minimum χ^2). Therefore, $\chi^2(\omega_0)$ is the χ^2 for the best-fitting frequency, χ^2_{N-1} is the χ^2 for the weighted constant fit (weighted sum of squares about the mean), N is the number of data points. The power $z(\omega)$ is normalised by the χ^2 of the best-fitting sinusoid $\chi^2(\omega_0)$.

The uncertainty in the period measurement σ_P is estimated using the frequency boundaries obtained when the χ^2 changes by four from the global χ^2 minimum (equivalent to 2σ errors, assuming only one useful fitted parameter, the period).

2.4.2 Significance Tests

The significance of each best-fitting period is estimated using two methods, both of which are outlined in Cumming et al. (1999): how often the maximum power of the periodogram exceeds the observed value due to noise alone, and an analytical calculation of the false alarm probability (FAP).

Monte Carlo approach for estimating the FAP

To start, the significance of the best-fitting period is tested against the hypothesis that the data is purely noise. For each star, 1000 fake data sets are generated about the mean magnitude of the observed star at the same times as the observations. Random Gaussian noise, of the same standard deviation as the observed magnitudes, is then added to the fake data. The periodogram analysis, conducted for the observed data, is then repeated for the fake data sets. The fraction of trials where the maximum power $z_{\rm max}$ exceeds the observed power $z_{\rm max}$ is defined as the FAP. A significant detection threshold is set at $FAP \leq 0.01$ (a 99% detection threshold) and is required for all of the different significance tests. A small FAP value indicates that the observed maximum power in the periodogram is less likely due to purely noise fluctuations in the data. The maximum power $z_{\rm max}$ and FAP (estimated using these Monte Carlo tests), for each target, are given in Tables 2.3–2.5.

Analytical approach for estimating the FAP

For comparison, the FAP is also determined for each target using an analytical approach, as outlined in Cumming et al. (1999). The periodogram power in Equation 2.2 is normalised by the χ^2 of the best-fitting sinusoid $\chi^2(\omega_0)$ (residual variance), and therefore the probability distribution is defined as a Fisher $F_{2,N-3}$ distribution (Cumming et al. 1999; Zechmeister & Kürster 2009) as,

$$\mathrm{Prob}(z > z_0) = \left(1 + \frac{2z_0}{N-3}\right)^{-\frac{N-3}{2}}. \tag{2.4}$$

The FAP of a best-fitting period within a frequency range is given by,

$$F = 1 - [1 - \mathrm{Prob}(z > z_0)]^M, \tag{2.5}$$

where M is the number of independent frequencies and z_0 is the observed power. For a small FAP ($F \ll 1$), it can be approximated as,

$$F \approx M\,\mathrm{Prob}(z > z_0). \tag{2.6}$$

Since the data is unevenly sampled, the number of independent frequencies M cannot be defined as $N/2$ in a frequency range from $1/T$ to the Nyquist frequency $f_{Ny} = N/2T$ (Cumming 2004). Horne & Baliunas (1986) suggest that $M \approx N$ in cases of unevenly sampled data when frequencies are searched up to the Nyquist frequency f_{Ny}. However, this approximation for the number of independent frequencies is no longer applicable if frequencies are searched beyond the Nyquist frequency. Here, the number of independent frequencies M is estimated as the number of peaks in the periodogram, $M \approx T\Delta f$, where T is the finite duration of the observations and $\Delta f = f_2 - f_1$ is the frequency range searched. However, Cumming et al. (1999) show this is a naive estimate and a much better value can be determined for M using Monte Carlo tests. These are time consuming and have not been attempted in this analysis. This analytical approach for determining the FAP for each target is also compared with the FAP estimates from the Monte Carlo test (see Tables 2.3–2.5).

2.4.3 Variability

An additional test is performed to indicate the presence of variability in the light curve (outlined in Cumming et al. 1999). For noisy data with a Gaussian distribution, the mean power of the periodogram is expected to be $\overline{z} \approx 1$. Employing the same method as for the Monte Carlo tests, the variability FAP is determined using the mean power $\overline{z}$ of the periodogram, rather than the maximum power. The FAP is calculated as the fraction of the 1000 simulated noisy light curve trials, where the mean periodogram power exceeds the mean periodogram power of the observed data. A low FAP value suggests that variability may be present in the data, or some non-Gaussian behaviour. The results of the observed mean power $\overline{\mathrm{z}}$ and respective FAP statistics are given in Tables 2.3–2.5.

2.5 Results

Periods of variability are obtained for 13 MWDs (see Table 2.3 for a summary of the results), while variability is also detected in a further 13 MWDs with poorly constrained periods (results given in Table 2.4). For the remaining 51 MWDs, no photometric variability is detected (details are given in Table 2.5). For these stars, a best-fitting period is not given, but instead a 2σ range of periods about the global χ^2 minimum in the periodogram is stated, as these values are used to calculate the FAP statistics. The following results are given for each target: the best-fitting period, the reduced χ^2 from a sine fit and constant fit, the maximum power in the periodogram $\mathrm{z}_{\mathrm{max}}$ (corresponding to the best-fitting period), the FAPs associated with $\mathrm{z}_{\mathrm{max}}$ from the Monte Carlo test and analytical method, the mean power of the periodogram $\overline{\mathrm{z}}$ and its associated FAP (from the Monte Carlo technique). Figures of the individual MWDs mentioned (i.e. light curves, periodograms and folded light curves, where appropriate) are shown in Appendix A.

Table 2.3: Analysis summary for 13 MWDs, where variability is detected with a well-defined period. The best-fitting period is listed, along with the reduced χ^2 statistics from a sine fit and constant fit. The uncertainty estimate for the period corresponds to a change in χ^2 of 4 (equivalent to 2σ). The false alarm probability (FAP) calculations are explained in Sections 2.4.2 and 2.4.3. The FAP detection limit is set at $F = 0.01$. The maximum power (at the best-fitting frequency) in the periodogram is given by z_{max} and the mean power is denoted by $\overline{z}$. Where the MWD is observed in more than one epoch, the results are given for the combined data set and for the individual epochs. The light curves, periodograms and folded light curves for the variable stars are given in Appendix A.1.

Target	WD	Best-fitting	Sine fit	Constant fit	z_{max}	False Alarm Probability		$\overline{z}$	FAP
	Number	Period	$\chi^2_{reduced}$	$\chi^2_{reduced}$		MC	Analytic		MC
SDSS J0005−1002	0003−103	2.13 ± 0.05 d	2.24	222.11	1278.35	<0.001	4.270×10^{-22} †	130.68	<0.001
G 158−45	0011−134	44.43 ± 0.12 min	4.50	8.01	41.62	<0.001	3.341×10^{-11}	2.00	<0.001
MWD 0159−032	0159−032	5.81 ± 0.01 h	2.33	7.98	52.06	<0.001	7.419×10^{-9}	6.50	<0.001
LHS 5064	0257+080	$7.72^{+0.58}_{-0.42}$ d	5.75	67.76	303.10	<0.001	5.337×10^{-28} †	36.18	<0.001
LHS 1734	0503−174	2.61 ± 1.29 d	2.81	5.65	28.33	<0.001	3.873×10^{-6}	4.11	<0.001
LB 8915 (all)	0853+163	5.694 ± 0.006 h	7.09	28.00	83.60	<0.001	2.023×10^{-12} †	10.43	<0.001
LB 8915 (Mar10)		5.69 ± 0.01 h	9.69	48.60	81.15	<0.001	8.818×10^{-11}	6.04	<0.001
LB 8915 (Feb11)		21.943 ± 0.007 min	2.83	27.67	62.49	0.001	0.000110	25.31	<0.001
G 195−19 (all)	0912+536	1.2285 ± 0.0020 d	2.99	22.15	232.95	<0.001	8.489×10^{-28} †	38.06	<0.001
G 195−19 (Mar09)		2.69 ± 0.82 d	3.38	50.47	209.80	<0.001	6.061×10^{-15} †	46.47	<0.001
G 195−19 (Mar10)		1.75 ± 0.02 d	3.54	24.71	120.25	0.001	1.361×10^{-13}	17.13	<0.001
PG 1015+014	1015+014	$98.84^{+0.14}_{-0.07}$ min	1.49	18.74	718.76	<0.001	1.987×10^{-65} †	50.15	<0.001
LHS 2273	1026+117	40.14 ± 0.60 min	2.46	4.67	27.94	<0.001	1.299×10^{-6}	3.64	0.001
SDSS J1250+1549 (May10)	1248+161	1.55 ± 0.06 h	3.70	14.48	82.64	<0.001	5.500×10^{-16} †	8.60	<0.001
SDSS J1348+3810	1346+383	$40.02^{+1.14}_{-0.02}$ min	1.96	25.12	178.04	<0.001	1.812×10^{-13}	18.41	<0.001
SDSS J2218−0000 (all)	2215−002	3.493 ± 0.004 h	2.68	14.60	157.41	<0.001	5.747×10^{-21} †	6.85	<0.001
SDSS J2218−0000 (Oct09)		3.487 ± 0.007 h	1.59	20.10	186.70	<0.001	1.413×10^{-14} †	16.51	<0.001
SDSS J2218−0000 (Jul11)		3.497 ± 0.008 h	3.03	11.01	51.02	<0.001	1.925×10^{-8}	3.78	<0.001
SDSS J2257+0755 (all)	2254+076	22.56 ± 0.42 min	2.11	3.55	35.81	<0.001	2.897×10^{-7}	3.19	<0.001
SDSS J2257+0755 (Oct09)		35.25 ± 0.02 min	1.46	4.13	32.22	<0.001	2.594×10^{-5}	5.63	0.001
SDSS J2257+0755 (Jul11)		22.34 ± 0.53 min	2.05	3.44	23.93	<0.001	9.256×10^{-6}	3.22	<0.001

† Where the approximation for the FAP (Eq. 2.6) is used instead of the full expression (Eq. 2.5).

2.5.1 Notes on variable MWDs with well-determined periods

SDSS J0005-1002: The light curve of this MWD (Fig. 2.2) shows photometric variability of 11.6% peak-to-peak, with a best-fitting period of 2.13±0.05 days. Schmidt et al. (2003) suspected that SDSS J0005-1002 may be a magnetic carbon-dominated atmosphere DQ, with possible C II multiplets. Liebert et al. (2003) reported a high effective temperature of 29,000 K, although work by Dufour et al. (2007) suggested hot DQ WDs have temperatures between 18,000 and 23,000 K. Dufour et al. (2008b) determined an effective temperature of $19,420 \pm 920$ K and magnetic field strength of 1.47 MG for SDSS J0005-1002. This star is discussed in more detail in Chapter 3. Figure 2.3 shows the CSS light curve of SDSS J0005-1002 folded on the best-fitting period. This period is not detected by the CSS period search. The uncertainties in the magnitude measurements are considerably larger than the INT data set, clearly showing the difficulty in detecting peak-to-peak variability >10% in the CSS light curves.

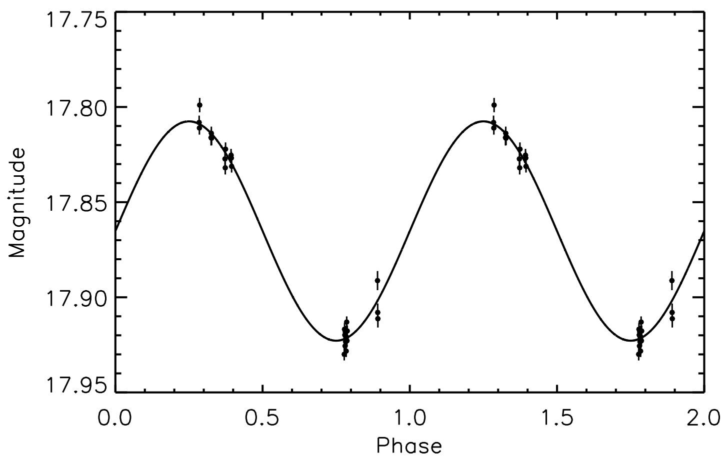

Figure 2.2: Light curve of SDSS J0005-1002 obtained from the INT is folded on the best-fitting period of 2.13 ± 0.05 days, with a reduced χ^2 of 2.24. A constant fit gives a reduced χ^2 of 222.11.

G 158-45: Putney (1997) estimated G 158-45 had a period between 11 hours and 1 day, from polarisation and flux measurements. Brinkworth et al. (2013) found tentative evidence for ~1% peak-to-peak amplitude photometric variability, with a period between

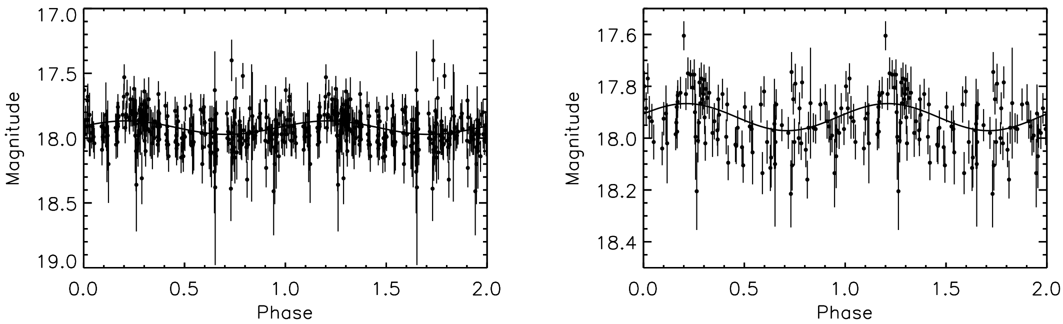

Figure 2.3: CSS light curve of SDSS J0005-1002 folded on the best-fitting period (*left*), and binned by a factor of 2.5 ($N = 100$ data points, *right*), with a model sinusoid.

30 minutes and a few days (the most likely period at 1.44 h), but a very high FAP estimate of 0.785 meant their periodicity was not reliably constrained. Here, the target is found to vary photometrically with a comparably low amplitude (~1%), but on a period of 44.43 ± 0.12 min (32.411 cycles/d) and a FAP < 0.001. This is a cool MWD ($T = 6010$ K, Bergeron et al. 2001), and therefore has a convective atmosphere, suggesting the photometric variability may be due to star spots on the surface.

MWD 0159-032: A best-fitting period of 5.82 ± 0.01 hours with peak-to-peak variability of ~3% is obtained. This DA MWD has a weak magnetic field strength ($B = 6$ MG) and is hot at $T = 26,000$ K (Achilleos et al. 1991). However, the true values may be slightly different than estimates, as Achilleos et al. (1991) report that both the continuum slope and strength of the Balmer lines are not fit satisfactorily for the low-field WDs (an observation also made by Gänsicke et al. 2002). MWD 0159-032 is too hot for star spots to form in a radiative atmosphere and the magnetic field is too weak for magnetic dichroism to have an effect. As a result, the mechanism causing the photometric variability observed for this star is unknown.

LHS 5064: Brinkworth et al. (2013) detected 4.5% photometric modulations and a probable period between 9 hour and 6 days. LHS 5064 is cool ($T = 6680$ K, Bergeron et al. 2001) and has a low magnetic field strength of <100 kG (Koester et al. 2009). This DA MWD shows ~5% peak-to-peak variability, with a period of $7.72^{+0.58}_{-0.42}$ days (see Fig. 2.4), making it the second longest rotation period measured for a MWD.

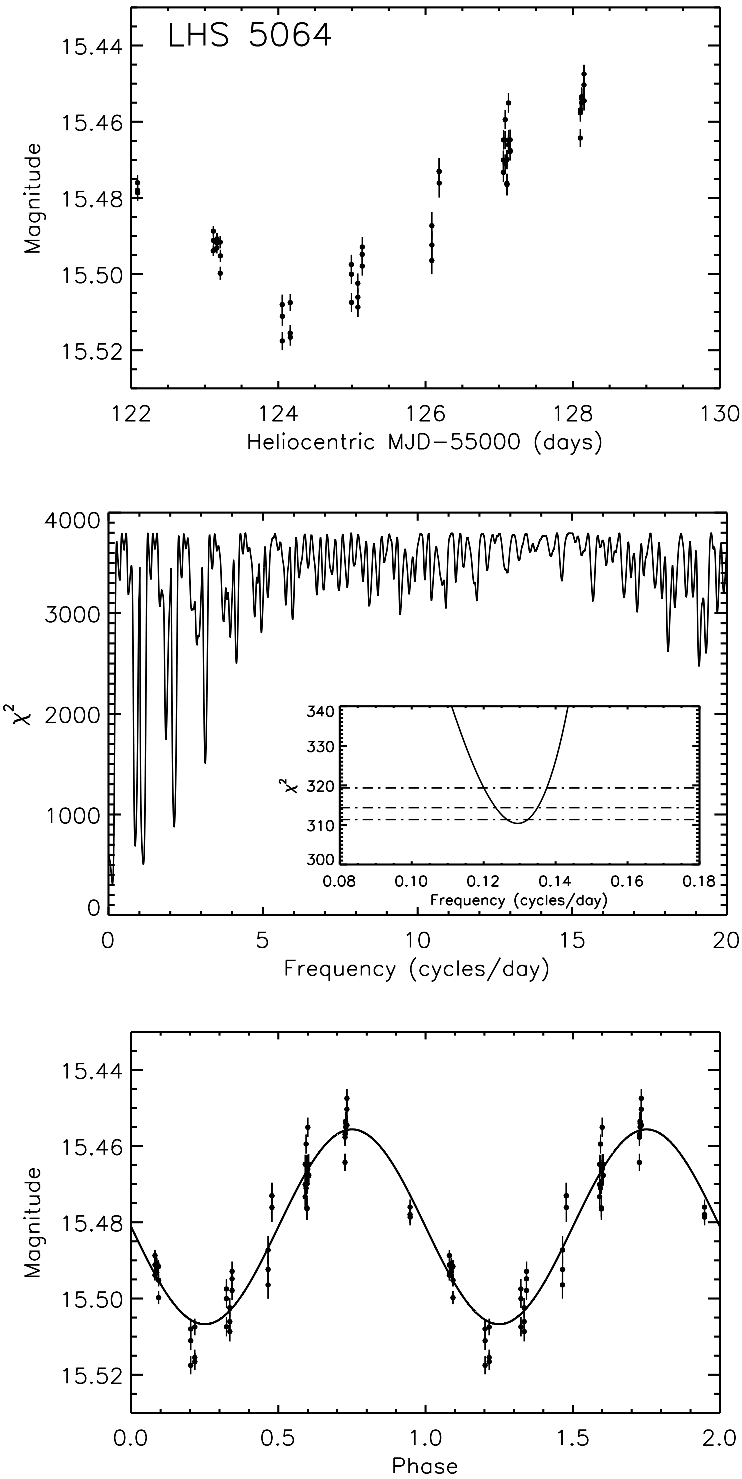

Figure 2.4: *Top:* Light curve of LHS 5064 from observations over a week in October 2009. *Middle:* Floating-mean periodogram for LHS 5064. The global minimum is detected at a frequency of 0.1295 cycles/d (period of 7.72 d). *Inset window*: Periodogram focusing at frequencies near the minimum. The dot dashed lines indicate changes in χ^2 of 1, 4 and 9 (equivalent 1σ, 2σ and 3σ uncertainties respectively). *Bottom:* Light curve is folded on the best-fitting period of $7.72^{+0.58}_{-0.42}$ days, with a reduced χ^2 of 5.75. The constant fit gives a reduced χ^2 of 67.76.

LHS 1734: A probable period of variability is found at 2.61 days (0.383 cycles/d), with a peak-to-peak amplitude of ~2%. The data do not cover much of the phase folded light curve, and therefore the period is not well constrained, with large 2σ uncertainties ranging from 0.359 up to 4.675 cycles/d (2.79 d to 5.13 h respectively). However, the FAP statistics (presented in Table 2.3) indicate this variability is unlikely to have arisen purely from noise fluctuations. The magnitude uncertainties in the CSS light curve are too large to detect a periodicity in the data. LHS 1734 is cool ($T = 5300$ K) and has a low mass for an isolated MWD ($M = 0.37 M_{\odot}$, Bergeron et al. 2001).

LB 8915: A period between 2 h and 1 day was suspected by Brinkworth et al. (2013), with probable periods at 0.47 d, 2.6 h and 5.8 h. Observations from March 2010 suggest a period of variability of 5.69 ± 0.01 hours, with an amplitude of ~4% (see light curve in Fig. 2.5, *left*). Follow-up observations from February 2011 are poor quality and give a tenuous best-fitting result of ~22 min, which is not consistent with the previous March 2010 data. An analysis of the combined data sets gives a period of 5.694 h, agreeing with the period obtained from the March 2010 data. This period is also identified in the CSS data set, with a FAP of $2{\times}10^{-12}$. The CSS folded light curve is shown in Figure 2.5 (*right*). This MWD has a H/He atmosphere with an effective temperature of $21,200 - 27,700$ K and a weak magnetic field strength of <1 MG (Wesemael et al. 2001). Brinkworth et al. (2013) suggest the helium atmosphere could be partially convective, and therefore the photometric variability may be due to a star spot on the surface of the WD.

G 195-19: Angel et al. (1972) found a period of 1.33096 ± 0.00012 d for G 195-19 at a level of ~4%, using circular polarisation measurements. A similar best-fitting photometric period is found at 1.2285 ± 0.0020 d, with 3% peak-to-peak variability, from observations taken during two epochs (March 2009 and 2010). However, this period is not obtained from the individual epochs. From the March 2009 data, a period of 2.69 d is measured, an alias of the best-fitting period, and a period of 1.75 d is determined from the March 2010 data. Complete coverage over the phase folded light curve is not achieved with our photometric observations, which may explain the difference between the period results.

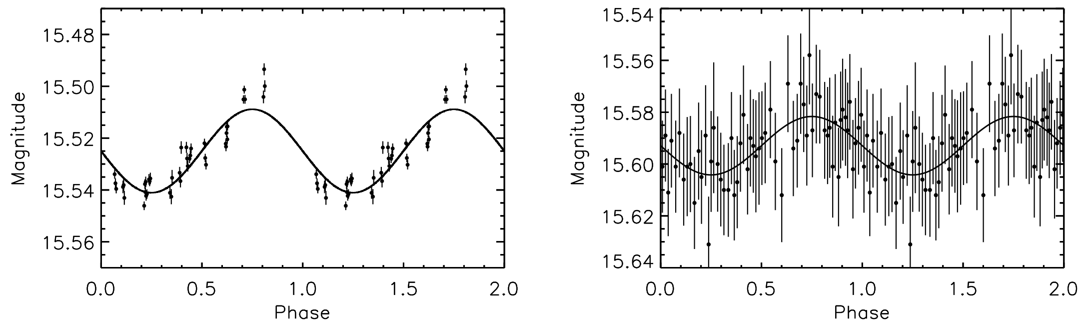

Figure 2.5: *Left:* The INT light curve of LB 8915 (taken in March 2010) is folded on the best-fitting period 5.69 ± 0.01 hours, with a reduced χ^2 of 9.69. A constant fit gives a reduced χ^2 of 48.60. *Right:* The CSS light curve of LB 8915 is folded on the same period and binned by a factor of 10 ($N = 60$). There is a slight difference in magnitudes between the two data sets, which will be due to differences in the magnitude calculation and its application.

G 195-19 is a cool MWD ($T = 7160$ K, Bergeron et al. 2001), with a high field strength ($B \sim 100$ MG, Angel et al. 1972), and therefore the photometric variability may be due to both dichroism and star spots.

PG 1015+014: Wickramasinghe & Cropper (1988) determined this DAH MWD had a magnetic polar field strength of 120 MG by time resolved spectropolarimetry, and that the circular polarisation was varying by 1.42% on a period of 98.7 min. Schmidt & Norsworthy (1991), using circular polarimetry, later determined the period to a higher accuracy at 98.74734 min. The period from photometric variations is confirmed as $98.84^{+0.14}_{-0.07}$ min, with a peak-to-peak amplitude of 4.6% (Fig. 2.6), in agreement with previous measurements (Brinkworth et al. 2013). Euchner et al. (2006) mapped the magnetic field geometry of PG 1015+014, using Zeeman tomography, and determined field strengths between 50 and 90 MG and an effective temperature of 10,000 K.

LHS 2273: Brinkworth et al. (2013) report LHS 2273 is probably varying with a period of 35 − 45 min, with a best-fitting period of 40.86 min. A comparable best-fitting period of 40.14 ± 0.60 min is found here, varying by 1.65% peak-to-peak. Bergeron et al. (1997) report LHS 2273 has a spectrum comparable to G 62-46, a known double degenerate, and therefore is suspected to be a binary composed of a magnetic DA WD and a DC WD.

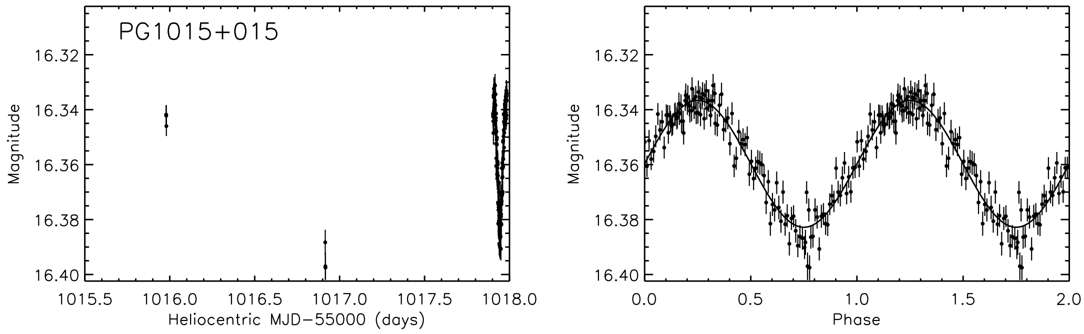

Figure 2.6: *Left:* Light curve of PG 1015+014. *Right:* The light curve is folded on the best-fitting period, $98.84^{+0.14}_{-0.07}$ min, with a reduced χ^2 of 1.49. A constant fit gives a reduced χ^2 of 18.74.

SDSS J1250+1549: This star displays a large degree of photometric variation (>10%), with a double peak clearly visible in the May 2010 light curve (Fig. 2.7). A best-fitting period of 1.55 ± 0.06 h is obtained. To within the uncertainties, the same period is determined from the sparser March 2010 data set. Steele et al. (2011) detect an infrared excess for SDSS J1250+1549 in all near-infrared bands, suggesting it has a late M companion. More recently, Breedt et al. (2012) present phase-resolved spectroscopy of this MWD and measure an orbital period of 86.3 min, using the radial velocities measured from a narrow, Hα emission line in each of their spectra. They argue that the high radial velocity amplitude and variable line strength on the orbital period suggest that the Hα emission originates from the surface of the companion star.

SDSS J1348+3810: A best-fitting period of variability of $40.02^{+1.14}_{-0.02}$ min is determined, with a peak-to-peak amplitude of 4.5% for this DAH MWD. It is one of the hottest in the sample at $T = 35,000$ K, making it too hot for star spots to form on the surface in the presence of a partially convective atmosphere. A field strength of 14 MG (Külebi et al. 2009) is too weak for magnetic dichroism to cause the photometric fluctuations, and therefore they must be the result of a different mechanism.

SDSS J2218-0000: This high field MWD (B = 225 MG, Schmidt et al. 2003) has a best-fitting period of 3.487 ± 0.007 h, with ~6% photometric peak-to-peak variability (for data taken in October 2009). Similarly, a period of 3.497 ± 0.008 h is found from observations

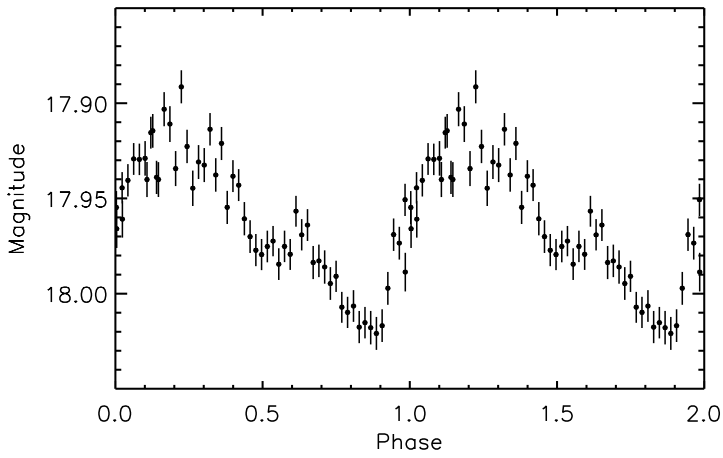

Figure 2.7: SDSS J1250+1549 light curve from May 2010 is folded on the best-fitting period of 1.55 ± 0.06 hours, with a reduced χ^2 of 3.70 from a sine fit, in comparison to the reduced χ^2 of 14.48 for the constant fit. The straightforward sinusoid does not provide an appropriate fit to the data. Steele et al. (2011) detect an infrared excess for SDSS J1250+1549 in all near-infrared bands, suggesting it has a late M companion.

taken in July 2011. Poor seeing conditions and observing at a high airmass in July 2011 means there are some spurious data points in the folded light curve. However, the FAP statistics of the individual epochs and combined data all indicate the photometric light curve is significantly variable.

SDSS J2257+0755: Observations from October 2009 show peak-to-peak variability of ~2%, with a best-fitting period of 35.25 ± 0.02 min (40.851 cycles/d). There are other minima in the periodogram within the 3σ uncertainties, with frequencies ranging from 16 to 41 cycles/d. Data from July 2011 show variations of 1.2% peak-to-peak, with a best-fitting period of 22.34 ± 0.53 min. There are no other features in the periodogram within the 3σ uncertainties, an improvement over the October 2009 data. An analysis of the combined data set gives a period of 22.56 ± 0.42 min, comparable to the July 2011 results, but the data are scattered about the best-fitting sine curve. This is the hottest MWD in the sample at $T = 40,000$ K and has a field strength of 16 MG (Külebi et al. 2009). The star will have a fully radiative atmosphere, unable to form star spots, and the field strength is too weak for magnetic dichroism to have an effect. As a result, the mechanism causing the photometric variability is unknown.

Table 2.4: Analysis summary for 13 MWDs which show signs of variability, with low false alarm probabilities (FAPs), but have poorly constrained periods. More data are required for some of the stars to determine a reliable period of variability (such as for SDSS J0017+0041 and SDSS J1035+2126). The uncertainties for the periods correspond to a 2σ change in χ^2 from the global minimum. In cases where there are many minima within the 2σ uncertainty boundaries, a range of these periods is given instead. The FAP calculations are outlined in §2.4.2 and §2.4.3. The FAP detection limit is set at $F = 0.01$. The maximum power (at the best-fitting frequency) in the periodogram is given by z_{max} and the mean power is denoted by $\bar{z}$. Where the MWD is observed in more than one epoch, the results are given for the combined data set and for the individual epochs. The light curves and periodograms for these stars are given in Appendix A.2.

Target	WD	Best-fitting	Sine fit	Constant fit	z_{max}	False Alarm Probability		$\bar{z}$	FAP
	Number	Period	$\chi^2_{reduced}$	$\chi^2_{reduced}$		MC	Analytic		MC
LHS 1038	0009+501	3.438 ± 0.004 h	3.32	6.55	36.79	<0.001	1.213×10^{-8}	3.81	<0.001
SDSS J0017+0041	0015+004	1.28 – 19.44 h	1.09	2.22	20.65	0.005	0.001441	3.90	<0.001
SDSS J0142+1315	0140+130	9.69 ± 2.68 h	1.29	5.31	44.57	<0.001	5.918×10^{-6}	5.22	<0.001
KPD 0253+5052	0253+508	1.05 ± 0.46 d	2.33	4.40	21.30	0.003	0.000435	3.37	0.012
SDSS J0318+4226	0315+422	15.04 ± 0.09 h	2.09	5.18	23.16	0.002	0.001117	2.96	0.002
SDSS J1035+2126	1032+214	1.3 - 4.1 d	0.48	1.55	45.74	<0.001	6.268×10^{-8}	5.87	<0.001
SDSS J1214−0234	1212−022	10.7 h – 4.0 d	0.80	12.66	238.09	<0.001	3.148×10^{-16} †	30.13	<0.001
SDSS J1333+0016	1331+005	3.7 h – 2.1 d	1.65	6.84	35.50	<0.001	0.000209	4.09	0.003
SDSS J1508+3945	1506+399	16.7 – 53 min	0.48	5.06	67.97	0.002	0.000228	17.09	0.002
SDSS J1604+4908	1603+492	18.2 h – 3.5 d	1.44	10.57	102.72	<0.001	3.019×10^{-11}	11.10	<0.001
SDSS J1647+3709	1645+372	84 – 190 min	0.94	1.80	17.50	0.006	0.004653	2.31	0.012
SDSS J2046−0710	2043−073	1.8 – 7.7 h	1.80	4.05	28.47	<0.001	1.275×10^{-5}	2.53	0.001
SDSS J2323−0046 (all)	2321−010	14.3 h – 3.0 d	1.41	4.89	55.49	<0.001	2.041×10^{-7}	3.56	<0.001
SDSS J2323−0046 (Oct09)		4.59 ± 0.75 h	0.75	4.76	70.24	<0.001	1.119×10^{-7}	7.00	<0.001
SDSS J2323−0046 (Jul11)		5.1 h – 1.2 d	1.86	5.44	16.68	0.150	0.154954	3.18	0.160

† Where the approximation for the FAP (Eq. 2.6) is used instead of the full expression (Eq. 2.5).

2.5.2 Notes on variable MWDs with poorly constrained periods

LHS 1038: Time-resolved spectropolarimetric measurements by Valyavin et al. (2005) yielded a rotation period of 8.02 h. Brinkworth et al. (2013) reported detecting photometric variability over a week, with a most likely period of 8.26 h, but was unable to constrain the period in a range of 2.6 – 15 cycles/d (9 – 1.6 h). No indication is found for a period of ≈ 8 h in this photometric survey. An 8 h period is difficult to detect, as the same phase of the light curve will be continually sampled during a week of observations. A probable period of 3.438 ± 0.004 h is detected for LHS 1038, with weak photometric variability at a peak-to-peak amplitude <1%. The FAPs are well below the detection threshold, indicating that the observed variability is unlikely to have arisen purely from noise fluctuations. However, a minimum is also found in the periodogram, on the edge of the 3σ boundary from the minimum χ^2 value, at $P = 3.0142$ h (7.962259 cycles/d).

SDSS J0017+0041: A tentative best-fitting period of 5.10 h with ∼1% peak-to-peak variability is found for this star. However, there are many minima in the periodogram, with periods ranging between 1.28 – 19.44 h, within the 2σ uncertainties. The FAP results are below the detection threshold, but the period cannot be constrained with the current data. SDSS J0017+0041 is a DBH WD at $T = 15,000$ K, with a field strength of 8.3 MG (Schmidt et al. 2003). Photometric variability may, perhaps, be caused by star spots on the surface of this WD in a partially convective atmosphere.

SDSS J0142+1315: This star is also a DBH WD at $T = 15,000$ K, with a weaker field strength of 4 MG (Schmidt et al. 2003). A best-fitting period is obtained at 9.69 ± 2.68 h, with peak-to-peak modulations of ∼3%. The FAP statistics indicate the variability is unlikely to have purely arisen from noise, but the best-fitting sine curve is dependent on three data points, with large uncertainties, taken on one night. More data are required of this object to constrain the period of variability.

KPD 0253+5052: A rotation period of 3.79 ± 0.05 h is reported by Friedrich et al. (1997), by measuring the broadband polarisation in the Hβ and Hγ lines. This period is not found in the photometric data, but instead a best-fitting period of 1.05 ± 0.46 d is obtained. However, the measurement for the polarised rotation period from Friedrich et al. (1997) is robust, and therefore this photometric data set is more likely to be insufficient for detecting the 3.79 h period.

SDSS J0318+4226: The light curve is folded on the best-fitting period of 15.04 ± 0.09 h, with variations of 1.8% peak-to-peak. However, the data are scattered about the sine fit and have insufficient phase coverage. Additional photometric data are required to confirm the periodicity.

SDSS J1035+2126: This is a cool and weakly magnetic WD ($T_{\rm eff} = 7000$ K, $B = 3$ MG; Külebi et al. 2009). A best-fitting period of variability is found as 3.55 d, although the 2σ uncertainties cover a range of periods from 1.34 d to 4.08 d. The photometric modulations vary by 1.5% peak-to-peak and the FAP estimations are well below the significance threshold. Külebi et al. (2009) suggest that this star may be an unresolved spectroscopic binary (e.g. with DA+DC components), as its spectrum has very shallow features, which is known to be a result of the companion suppressing the hydrogen line strengths (Bergeron et al. 1990; Liebert et al. 1993).

SDSS J1214-0234: Also known as LHS 2534, this is the first magnetic DZ WD, with Zeeman split Na I and Mg II components. Reid et al. (2001) measure a magnetic field strength of 1.92 MG and cool effective temperature of 6000 K. The light curve shows peak-to-peak fluctuations of 5.2%, but due to the data sampling, the period of variability is not constrained to one possibility. There are three aliases in the periodogram, within the 2σ uncertainties from the global χ^2 minimum, at 19.115 h, 3.819 d and 10.670 h. It also looks like the star may be variable on a longer period ($P > 5$ days). A possible period of 5.789 days is found by the Catalina Surveys (Drake et al. 2009), although it has a high FAP statistic of 0.427. Further observations are required over a longer timebase to narrow down the period.

SDSS J1333+0016: Peak-to-peak photometric variability of 3%, with a best-fitting period of 5.37 h, is detected for this MWD. However, there are many aliases in the periodogram, within the 2σ uncertainties of the best-fitting result, with periods ranging from 3.7 h to 2.1 d. Additional observations are required over a single night and over a few days to further constrain the period. Schmidt et al. (2003) report that the SDSS spectrum of SDSS J1333+0016 resembles LHS 2229, a highly magnetic (~100 MG), cool (4600 K) WD with a helium-rich atmosphere and absorption due to the presence of C_2H (Schmidt et al. 1999).

SDSS J1508+3945: Also known as CBS 229, this star is reported as a DAH+DA binary system (Gianninas et al. 2011; Dobbie et al. 2012). The magnetic component has a field strength of 13 MG and a high temperature of 17,000 K (Dobbie et al. 2012), meaning photometric variability will not be due to the presence of magnetic dichroism or star spots. A best-fitting period of 16.89 min (85.27 cycles/d) is measured, although there is an alias in the periodogram at a period of 51.07 min (28.20 cycles/d). The unfolded light curve suggests a period on a longer timescale of days may also be suitable. The FAP statistics are well within the significance limit, however the light curve only has a few data points ($N = 15$). More photometric data are required to determine whether any optical variability can be observed.

SDSS J1604+4908: Photometric modulations are clearly evident in the light curve (see Fig. 2.8), with a peak-to-peak amplitude of 4.2%. However, the target is not sampled adequately to constrain the period. The minimum χ^2 in the periodogram occurs at a frequency of 1.3052 cycles/d (a period of 18.39 h), although there are two other aliases in the periodogram, within the 2σ uncertainties, with frequencies at 0.2894 and 2.3209 cycles/d (periods of 3.46 d and 10.34 h respectively). More data are required to determine the period of variability.

SDSS J1647+3709: The best-fitting period is found between 84 and 190 min, with a most

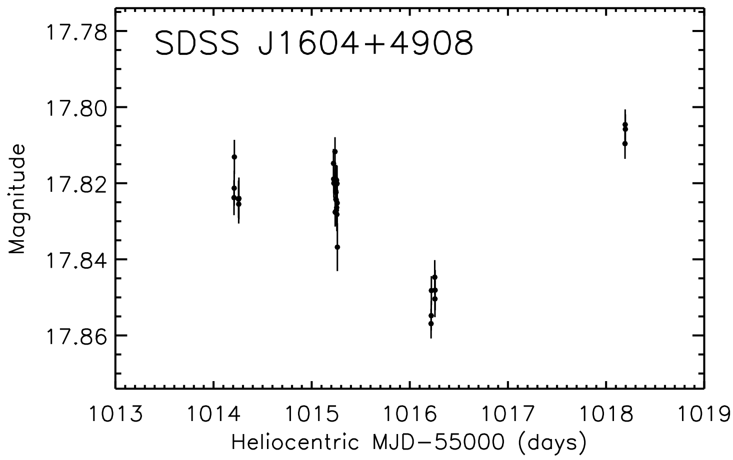

Figure 2.8: Light curve of SDSS J1604+4908 shows changes in flux over a week of observations, but a period has not been determined. More data are required to constrain the period of variability.

probable period of 89.1 min (16.15 cycles/d), at a low-level amplitude of 0.85% peak-to-peak. Variability is detected in the continual run of observations taken on the first night, which is not seen in the comparison stars. However, this same amount of variability is not seen in observations from later in the week. The FAP values are borderline at the $F = 0.01$ threshold. This DAH MWD has a weak field strength ($B = 2$ MG) and $T = 16,250$ K (Vanlandingham et al. 2005), implying the star is too hot for star spots to form in a convective atmosphere. If the photometric variability is real in SDSS J1647+3709, the mechanism causing the fluctuations is unknown.

SDSS J2046-0710: A best-fitting period is obtained at 2.13 h (127.81 min), although the 2σ uncertainties cover a large range of periods from 1.81 h to 7.68 h. The peak-to-peak amplitude is small (1.3%) and there is considerable scatter around the fitting sine curve. The FAP estimates are small, well below the $F = 0.01$ detection limit. Data taken on the first night are scattered and give no indications of photometric variability. Similarly, observations from later in the week also show no signs of modulations. As a result, the period of variability may simply be due to night-to-night fluctuations in brightness. SDSS J2046-0710 is cool with a temperature of 8000 K and has a weak magnetic field strength of 2 MG (Schmidt et al. 2003).

SDSS J2323-0046: This star varies by 2.3% peak-to-peak on a period of 4.59 ± 0.75 h, with FAP statistics well below the detection threshold ($F = 0.01$), in observations from October 2009. However, all phases are not fully covered in the folded light curve and the best-fit is dependent on just a few data points. Consequently, additional phase coverage is obtained from observations taken in July 2011. A different best-fitting period is found at 1.11 d, where the 2σ uncertainties cover timescales from 5.05 h to 1.19 d. This best-fitting period result seems unlikely, as the peak-to-peak amplitude of the best-fitting sine curve is 8%, with the data only covering a small portion of the phases. The FAP results are also above the threshold for a significant variable result. When the two epochs of data are combined, a global χ^2 minimum is found at a frequency of 1.67 cycles/d (a period of 14.38 h), with the 2σ uncertainties ranging from 14.33 h to 3.00 d. In conclusion, the rotation period of SDSS J2323-0046 could not be fully constrained.

Table 2.5: Summary of the remaining 51 MWDs, where no evidence for photometric variability is found. A best-fitting period has not been given, but rather a range of periods within 2σ of the global minimum in the periodogram. The reduced χ^2 of the sine fit is based on the best-fitting period from the minimum in the periodogram. The maximum power (at the best-fitting frequency) in the periodogram is given by z_{max} and the mean power is denoted by $\overline{z}$. The FAP estimations are based on the maximum power z_{max} obtained at the minimum in the periodogram. The FAP detection limit is set at $F = 0.01$. The FAPs clearly show that these MWDs have high FAP values, and it is unlikely that a genuine period is detected.

Target	WD Number	2σ period range around global minimum	Sine fit $\chi^2_{reduced}$	Constant fit $\chi^2_{reduced}$	z_{max}	False Alarm Probability MC	False Alarm Probability Analytic	$\overline{z}$	FAP MC
SDSS J0021+1502	0018+147	8.7 ± 1.4 min	0.78	1.16	7.58	0.690	0.9553	1.05	0.942
PG 0136+251	0136+251	22.6 ± 2.5 min	1.00	1.12	6.32	0.126	0.2689	1.70	0.085
SDSS J0211+0031	0208+002	8 min – 7.5 h	1.78	2.55	7.01	0.779	0.9948	1.44	0.688
SDSS J0211+2115	0209+210	7 – 200 min	1.47	2.02	8.86	0.251	0.4836	2.16	0.051
SDSS J0304−0025	0301−006	13.5 ± 3.1 min	1.31	2.02	8.13	0.631	0.9120	1.60	0.724
KUV 03292+0035	0329+005	62.9 ± 44.5 min	1.62	2.30	9.80	0.116	0.2793	1.60	0.190
HE 0330−0002	0330−000	61.8 ± 16.2 min	1.55	2.53	11.78	0.088	0.1369	2.28	0.050
SDSS J0345+0034	0342+004	7.2 ± 2.6 min	1.38	1.87	5.96	0.943	0.9994	1.03	0.987
G 99−37 (all)	0548−001	82.40 ± 2.62 min	3.60	4.31	18.36	<0.001	0.002656 [b]	2.21	<0.001
G 99−37 (Mar09)		7.26 ± 0.03 min	2.06	3.84	12.21	0.071	0.087390	3.32	0.032
G 99−37 (Oct09)		41.73 ± 0.05 min	3.44	4.65	16.91	<0.001	0.000162 [b]	2.69	<0.001
G 99−47 (all)	0553+053	139.34 ± 23.19 min	3.96	4.75	45.60	<0.001	2.374×10^{-14} [b,†]	3.94	<0.001
G 99−47 (Mar09)		10.00 ± 0.12 min	3.39	3.59	4.52	0.393	0.199186	1.29	0.190
G 99−47 (Oct09)		4.50 ± 0.43 h	5.52	7.93	70.35	<0.001	5.034×10^{-23} [b,†]	3.89	<0.001
GD 77 [a]	0637+478	13 min – 8 h	7.83	10.01	1.93	0.926	1.0000	0.83	0.874
G 234−4 (all)	0728+642	44.81 ± 1.41 min	1.48	2.68	22.14	0.018	0.011996	3.08	0.027
G 234−4 (Mar09)		11.00 ± 12.05 min	0.92	1.62	11.58	0.154	0.129557	3.10	0.060
G 234−4 (Mar10)		19.75 ± 13.49 min	1.86	3.06	8.00	0.642	0.985425	1.32	0.751
SDSS J0803+1229 [a]	0801+124	43.4 ± 11.5 min	1.72	5.53	16.45	0.265	0.3540	4.58	0.166
GD 90	0816+376	32.1 ± 3.7min	7.11	7.98	3.41	0.686	0.9999	1.01	0.619
SDSS J0851+1201 [a]	0848+121	8 min – 13.2 h	1.44	3.03	8.73	0.680	0.9960	2.29	0.591
SDSS J0858+4126 [a]	0855+416	12 min – 10.8 h	1.47	2.98	8.24	0.714	0.9988	2.43	0.590
SDSS J0910+0815	0907+083	14 min – 22.3 h	0.73	1.02	8.15	0.615	0.7005	1.56	0.447

Table 2.5: *continued*

Target	WD	2σ period range	Sine fit	Constant fit	z_{max}	False Alarm Probability		$\bar{z}$	FAP
	Number	around global minimum	$\chi^2_{reduced}$	$\chi^2_{reduced}$		MC	Analytic		MC
SDSS J0914+0544 [a]	0911+059	11 min – 1.2 d	0.38	1.74	25.98	0.106	0.0511	7.41	0.075
SDSS J1003+0538 [a]	1001+058	9.0 ± 0.9 min	1.15	1.65	5.75	0.963	0.9999	1.23	0.990
SDSS J1007+1623	1005+163	0.8 – 5.7 h	0.99	1.58	12.41	0.248	0.0617	1.96	0.390
LHS 2229	1008+290	34.3 min – 1.1 d	1.18	1.39	8.19	0.079	0.2976	1.69	0.053
SDSS J1015+0907	1012+093	0.9 – 10.6 h	1.69	3.61	18.17	0.028	0.006955	2.40	0.034
GD 116	1017+366	9 min – 4.6 d	0.67	0.77	6.25	0.239	0.9244	1.07	0.622
HE 1043−0502 [a]	1043−050	7 min – 20.7 h	0.70	1.91	11.35	0.606	0.9594	3.02	0.519
HE 1045−0908	1045−091	14 min – 4.9 h	1.41	2.88	8.32	0.382	0.8906	2.84	0.318
SDSS J1057+0411	1054+042	7 – 47 min	0.71	1.12	7.32	0.802	0.9659	1.54	0.718
SDSS J1113+0146	1111+020	9 – 34 min	0.91	1.28	7.07	0.757	0.9261	1.30	0.914
SDSS J1133+5152	1131+521	9 min – 1000 d	0.50	0.86	8.29	0.186	0.1086	2.22	0.154
SDSS J1137+5740	1135+579	8 min – 1.0 d	0.40	0.66	9.54	0.129	0.3629	2.10	0.139
SDSS J1138−0149	1136−015	7.2 – 63.2 min	0.69	0.99	6.82	0.593	0.8356	1.69	0.471
SDSS J1234+1248	1231+130	3.6 h – 4.2 d	0.74	0.99	10.38	0.036	0.1316	1.83	0.038
SDSS J1248+4104	1245+413	7.8 min – 3.7 h	0.50	0.73	8.62	0.256	0.6200	1.53	0.298
SDSS J1257+3414	1254+345	9 min – 1000 d	0.25	0.28	2.64	0.871	0.9885	0.83	0.789
SDSS J1328+5908	1327+594	22 min – 23.5 h	1.11	1.58	6.86	0.650	0.9595	1.36	0.638
SDSS J1333+6406	1332+643	30 min – 1000 d	0.79	1.36	10.46	0.282	0.3566	1.98	0.221
SBS 1349+5434 (all)	1349+545	49.1 ± 4.2 min	1.55	1.94	18.79	<0.001	0.011189	2.07	0.001
SBS 1349+5434 (Mar09)		42.42 ± 23.19 min	1.77	2.31	11.10	0.008	0.045583	2.35	0.003
SBS 1349+5434 (Jul11)		2.3 h – 1.2 d	1.13	1.35	8.08	0.055	0.147056	1.60	0.066
SDSS J1419+2543	1416+256	9 – 16 min	1.09	1.78	9.24	0.197	0.5715	1.92	0.254
SDSS J1427+3721	1425+375	1.7 ± 0.2 h	2.33	3.62	8.80	0.157	0.0482	1.69	0.249
SDSS J1430+2811	1428+282	10 – 31 min	0.85	1.12	6.98	0.372	0.8911	1.61	0.209
SDSS J1507+5210	1506+522	42 – 53 min	1.65	2.16	8.42	0.128	0.3009	1.82	0.044
SDSS J1511+4220	1509+425	18.9 ± 0.5 min	1.28	2.39	14.84	0.027	0.0261	1.94	0.156
SDSS J1524+1856	1521+191	9.5 min – 2.2 d	0.85	1.24	5.86	0.919	0.9997	1.85	0.480

Table 2.5: *continued*

Target	WD Number	2σ period range around global minimum	Sine fit $\chi^2_{\rm reduced}$	Constant fit $\chi^2_{\rm reduced}$	$z_{\rm max}$	False Alarm Probability MC	False Alarm Probability Analytic	$\overline{z}$	FAP MC
SDSS J1538+0842	1536+085	7.2 – 83 min	1.01	1.37	5.92	0.763	0.9992	1.00	0.922
SDSS J2149−0728	2146−077	8 min – 100 d	0.76	1.03	5.74	0.880	0.9969	1.28	0.747
SDSS J2151+0031	2149+002	7 – 56 min	0.65	0.89	6.29	0.670	0.9827	1.51	0.417
SDSS J2151+1255	2149+126	36.7 ± 30.0 min	1.77	3.23	11.76	0.277	0.1577	2.29	0.151
SDSS J2247+1456	2245+146	18 – 277 min	1.45	2.07	8.27	0.572	0.7827	1.54	0.536
SDSS J2319+0109	2317+008	28 min – 5.7 h	0.69	1.23	10.90	0.233	0.2700	2.47	0.042
PG 2329+267	2329+267	92.3 ± 26.5 min	2.50	3.34	12.30	0.048	0.0287	2.43	0.046
SDSS J2346+3853	2343+386	51 – 447 min	0.84	1.77	12.03	0.224	0.2548	2.33	0.230
SDSS J2346−1023	2343−106	31.7 ± 25.3 min	0.92	1.69	11.83	0.357	0.2724	1.88	0.462

.

[a] Few data points ($N < 15$).
[b] Despite the small FAPs, the fluctuations in the light curve are determined as not real.
[†] Where the approximation for the FAP (Eq. 2.6) is used instead of the full expression (Eq. 2.5)

Table 2.6: Summary of results for the variable comparison star in the G 99−47 field-of-view. The columns are the same as Table 2.3.

Target	Best-fitting Period	Sine fit $\chi^2_{\rm reduced}$	Constant fit $\chi^2_{\rm reduced}$	$z_{\rm max}$	False Alarm Probability MC	False Alarm Probability Analytic	$\overline{z}$	FAP MC
G 99-47 comp (all)	108.57 ± 2.22 min	3.46	5.82	151.07	<0.001	2.952×10^{-46} †	11.10	<0.001
G 99-47 comp (Mar09)	103 ± 4 min	4.29	11.43	100.80	<0.001	5.066×10^{-25} †	11.29	<0.001
G 99-47 comp (Oct09)	4.9 ± 0.6 h	5.06	8.20	99.43	<0.001	3.118×10^{-31} †	5.94	<0.001

[†] Where the approximation for the FAP (Eq. 2.6) is used instead of the full expression (Eq. 2.5).

2.5.3 Notes on some MWDs where no variability is found

SDSS J0211+2115: This MWD has a high magnetic field strength ($B = 166$ MG) and effective temperature of 12,000 K (Külebi et al. 2009; Vanlandingham et al. 2005), placing it in the hydrogen instability strip. There are many minima in the periodogram, within the 2σ uncertainties of the χ^2 minimum, at periods between $7 - 200$ min. This timescale could be indicative of pulsations and, therefore, SDSS J0211+2115 should be followed up to search for short-term pulsations. Non-radial pulsations have not been detected in a MWD.

HE 0330-0002: This helium-dominated atmosphere DBH MWD has a large field strength of 850 MG and cool effective temperature at 7000 K (Külebi et al. 2009; Schmidt et al. 2003). The light curve of HE 0330-0002 looks relatively flat. There are a few minima in the periodogram, within the 2σ uncertainties, with frequencies up to 50 cycles/d. The FAP estimates are not small enough ($F \sim 0.1$) for any modulations to be considered significant. In conclusion, no photometric variability is found in the current data for this star.

G 99-37: Bues & Pragal (1989) report that G 99-37 has a rotation period of 4.117 h, based on polarisation measurements, but there is no indication of photometric variability on this period. Data taken in March 2009 show no modulations at an amplitude of ~0.7%, which is supported by high FAP values. Poor quality data taken in October 2009 show variability that coincides with fluctuations in the seeing. Figure 2.9 shows the light curves from March and October 2009. A dip in the flux is obvious in the close-up of the October 2009 data (Fig. 2.9). Consequently, the photometry is repeated for the October 2009 data set and nearby comparison stars to determine whether the dip in flux is merely an artifact or genuine behaviour. Figure 2.10 shows the differential flux for G 99-37 and the comparison stars, where the dip is still visible in both light curves. Analysis of the seeing during these observations reveals that the poor quality data appears to coincide with the fluctuations in the seeing (Fig. 2.11). A best-fitting period of 82.40 ± 2.62 min is detected from combining both data sets, which is twice the period found from the

October 2009 data only. Therefore, I conclude that no genuine photometric variability (with amplitude >1%) is detected and that the small FAPs (from the combined data sets) are due to modulations in the October 2009 data from changing seeing conditions.

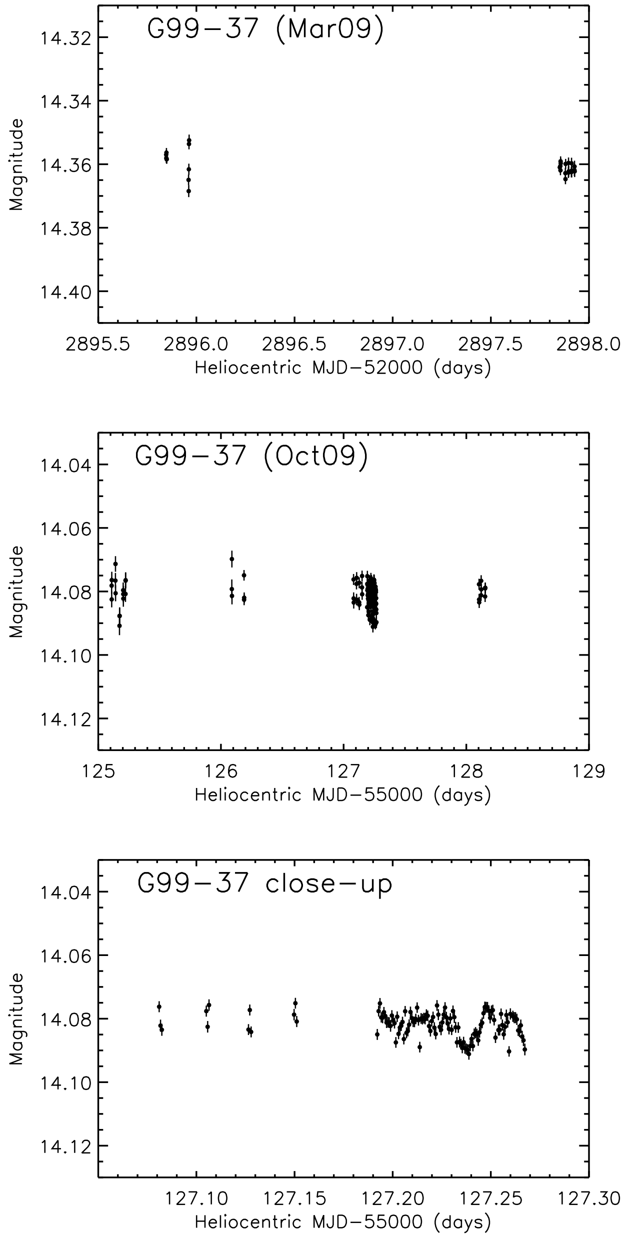

Figure 2.9: Light curves of G 99-37. *Top:* Data from March 2009. Apart from the second night, there is hardly any scatter in the magnitude. *Middle:* Light curve data from October 2009. The data are substantially more scattered than the March 2009 data set. *Bottom:* Close-up of the October 2009 light curve. A dip in the flux is evident in the October 2009 data set around 127.24 MHJD-55000. This is not seen elsewhere.

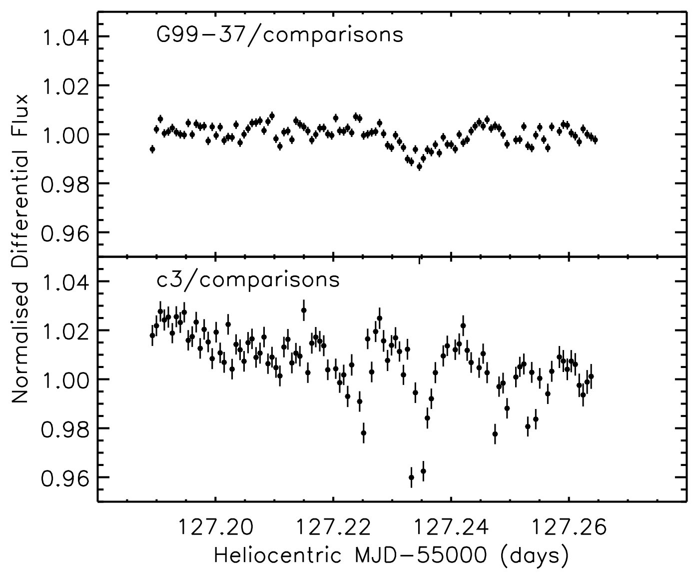

Figure 2.10: G 99-37 light curve analysis from October 2009, where the photometry is repeated using nearby comparison stars. *Top:* Differential light curve of G 99-37 with respect to the sum of the comparison stars. *Bottom:* Differential light curve of comparison star c3 with respect to the sum of the same comparison stars. The dip in flux is still visible in both light curves. However, the data points for the comparison stars become much more scattered around 127.235 MHJD-55000 (when the dip occurs). This suggests that the dip in flux is more likely a result of changing weather conditions, rather than a physical dimming in brightness.

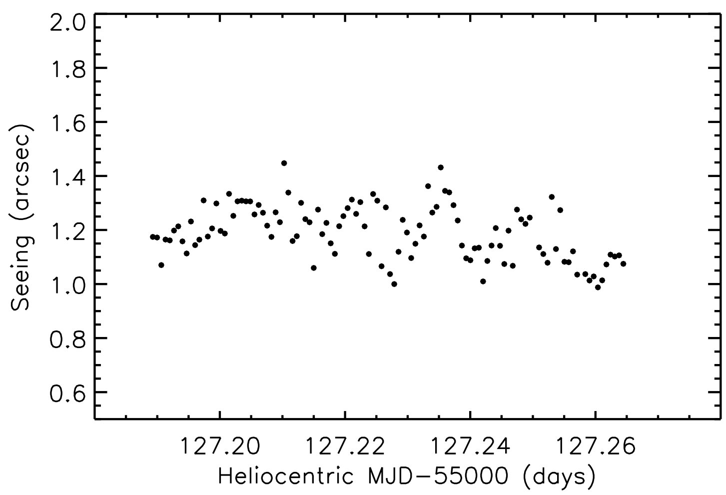

Figure 2.11: Seeing conditions for the G 99-37 observations in October 2009. The fluctuations in seeing appear to coincide with the modulations in flux in the light curve.

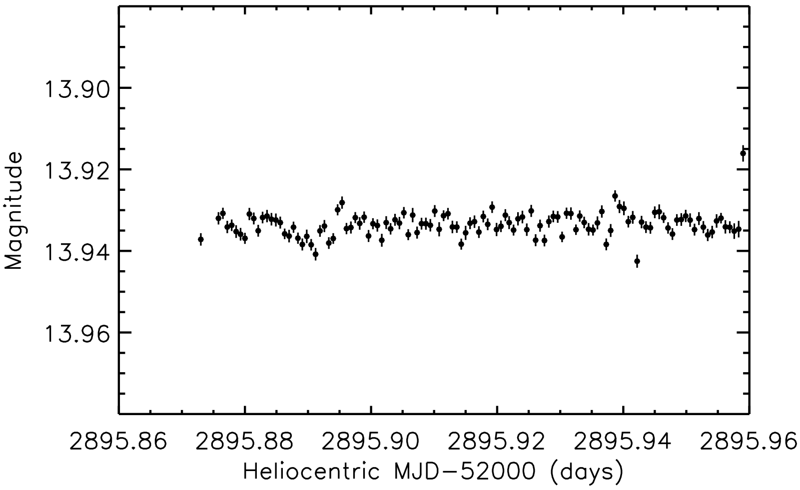

Figure 2.12: G 99-47 light curve from March 2009 over ~2 h. Photometric variability is not detected in this data at an amplitude of ~1%. Little difference is measured between the reduced χ^2 of the best-fitting sine fit compared to the constant fit.

G 99-47: Using polarisation measurements, Bues & Pragal (1989) report G 99-47 has a rotation period of 0.97 h. Low-amplitude photometric modulations (~1% peak-to-peak) are detected by Brinkworth et al. (2013), with a possible period between 26 and 27.5 min (best-fitting period at 26.8 min), noting there are many aliases within the 2σ uncertainties of the best frequency. Observations over two hours in March 2009 show no obvious signs of variability (Fig. 2.12). A best-fitting period of 4.50 ± 0.43 h is obtained from the October 2009 data, but there is substantially more scatter than in the March 2009 light curve. Analysis of the combined epochs reveals a best-fitting period of 139.34 ± 23.19 min. However, this period corresponds approximately to the length of the March 2009 data set, where no photometric modulations are detected. I, therefore, conclude that G 99-47 is not photometrically variable on short timescales (less than a week) at an amplitude of ~1%.

In searching for stable comparison stars in the G 99-47 field, a variable star is discovered with modulations of 2% peak-to-peak (referred to as G 99-47 comp, see Table 2.6 for details). The March 2009 differential light curve of G 99-47 comp is shown in Figure 2.13, in contrast with the stable comparison stars in the field. Observations from March

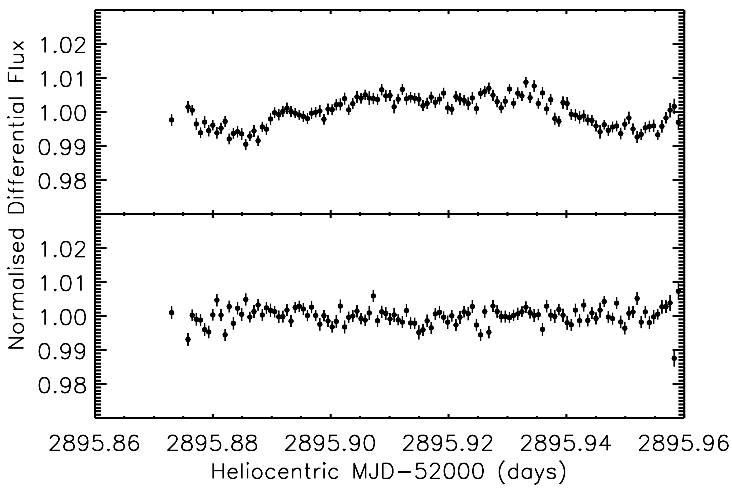

Figure 2.13: *Top:* Differential light curve of the G 99-47 variable comparison star from March 2009 (G 99-47 comp/(C1+C3+C5)). *Bottom:* Differential light curve of G 99-47 comparison stars (C1/(C3+C5)) from March 2009.

2009 reveal a best-fitting period of 103 ± 4 min (see folded light curve in Fig. 2.14). The data taken in October 2009 are poor quality and this period is not obtained, but a best-fitting period of 108.57±2.22 min is obtained from the combined data sets. The coordinates of the object are $RA = 05^{\rm h}{:}56^{\rm m}{:}16^{\rm s}.63$, $Dec = 05^{\circ}{:}22'{:}52''.6$ and it is marked in the G 99-47 finder chart (Fig. 2.15, *left*). It has not been observed by SDSS, as it lies on the edge of a plate. An SDSS image of G 99-47 comp is compared to SDSS images of post-common envelope binaries listed in Rebassa-Mansergas et al. (2010) and its colour composition suggests it may be a post-common envelope binary. In addition, the G 99-47 field was checked in The STScI Digitized Sky Survey (DSS) POSS1 and POSS2 epochs, where the MWD shows significant motion between the two epochs, but G 99-47 comp does not move comparably. Therefore, G 99-47 comp is not a common proper motion companion to the MWD.

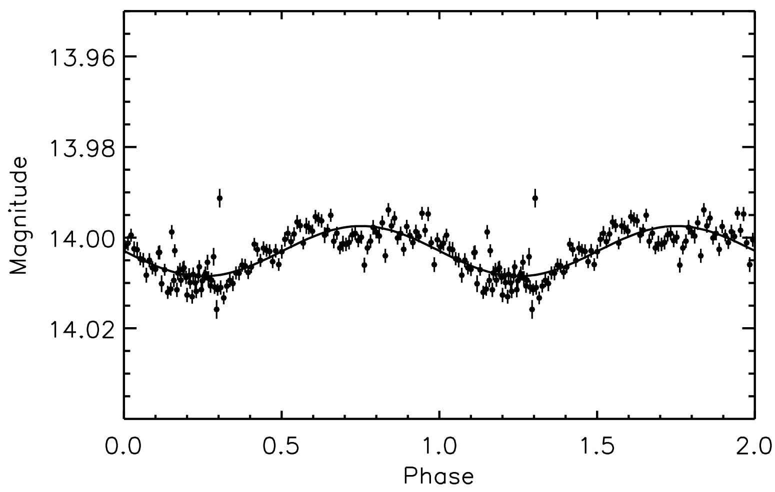

Figure 2.14: G 99-47 variable comparison star light curve from March 2009 folded on the best-fitting period of 103 ± 4 min, with a reduced χ^2 of 4.29. A constant fit gives a reduced χ^2 of 11.43. See Table 2.6 for further details of the result. G 99-47 comp is not a MWD, but shows photometric variability in the G 99-47 field-of-view. There is no information on this star in SDSS, as it lies on the edge of a plate.

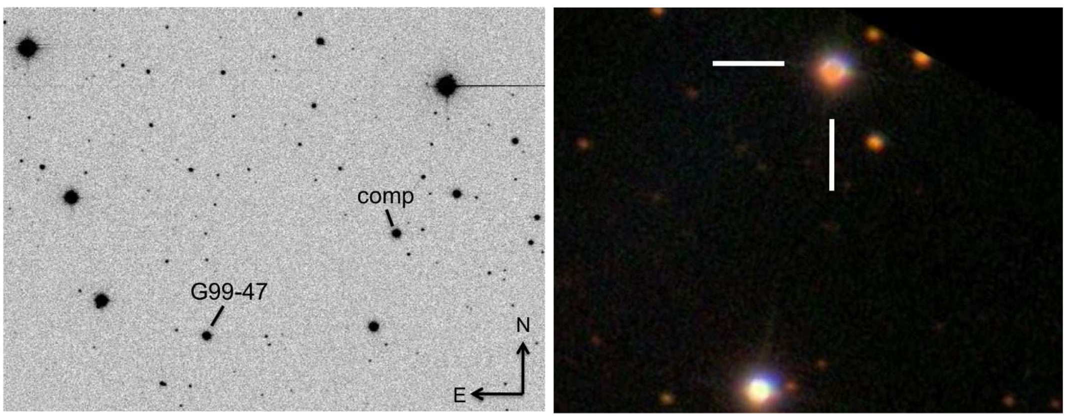

Figure 2.15: *Left:* Finder chart (6.1'×4.5') for G 99-47, where the variable comparison star is marked (RA=05^{h}:56^{m}:16^{s}.63, Dec=05°:22′:52″.6). *Right:* SDSS image (1.8'×1.4') of G 99-47 comp. It has a red and white/blue component, which could suggest it is a post-common envelope binary.

G 234-4: This MWD is reported as variable over a week of observations (Brinkworth et al. 2013), but a period for the modulations could not be derived here. From the combined data set of observations from March 2009 and 2010, a best-fitting period of 44.81 ± 1.41 min is determined. There are many aliases within the 2σ uncertainties. This period is not found in the analysis of the individual epochs (March 2009 and 2010). The FAP statistics are borderline, just above the detection threshold, meaning the periodicity may not be real. Faster periods are obtained for the individual epochs at 11 and 20 minutes for March 2009 and 2010 respectively, both with FAP values greater than the significance threshold. This MWD has a very low field strength ($B < 100\,\mathrm{kG}$) and cool effective temperature ($T = 4500\,\mathrm{K}$, Holberg, Bergeron & Gianninas 2008; Putney 1997).

HE 1045-0908: Euchner et al. (2005) report this MWD has a likely period of 2.7 h from circular polarisation spectroscopic measurements. There are many minima in the periodogram within 2σ of the best frequency between 5 and 102 cycles/d. At an amplitude of 1%, photometric variability is not detected in the data and there is no indication of the 2.7 h period. Similarly, there is no sign of the periodicity in the CSS light curve. However, the INT data set is small ($N = 15$), and therefore few conclusions can be made.

SBS 1349+5434: This MWD has a large magnetic field strength of 760 MG (Liebert et al. 1994). Brinkworth et al. (2013) found no evidence of photometric variability in the MWD's light curve. A best-fitting period of 49.1±4.2 min is determined from observations taken in March 2009 and July 2011. It has a small peak-to-peak amplitude of 0.5%. Analyses of the individual epochs of data yield different best-fitting periods and have borderline FAP statistics.

PG 2329+267: Brinkworth et al. (2013) reported a best-fitting photometric period of 2.7 h (8.675 cycles/d) for PG 2329+267. However, significant photometric variability is not detected in this data set and the scatter is small at ∼1%. The FAP statistics are just above the threshold limit ($F = 0.01$), meaning noise fluctuations may have caused the observed variations.

2.5.4 Summary

Photometric rotation periods are measured for 12 isolated MWDs in the sample (excluding the CV SDSS 1250+1549), doubling the number derived from photometric observations. Variability with poorly constrained periods is detected in an additional 13 stars. The second longest rotation period for a MWD is measured for LHS 5064 at 7.72 days. We constrain the spin period of G 158-45 from 11 h - 1 d (Putney 1997) to a much faster 44 min.

Photometric variability is measured in four DAH stars (MWD 0159-032, SDSS J1348+3810, SDSS J2257+0755 and SDSS J1647+3709), which are too hot for star spots to form in the presence of a convective atmosphere and have magnetic field strengths too weak for dichroism to be effective. Brinkworth et al. (2013) also detect photometric modulations in two MWDs with similar characteristics. The current assumption that star-like spots form on the surface (as with main sequence stars), as the WD cools to a convective atmosphere, does not apply for these stars. The variability is also not due to pulsation modes, as their temperatures are much higher than the instability strip ($T = 12 - 14,000$ K). In these cases, the mechanism causing the photometric modulations is unknown.

Photometric spin periods are not determined for G 99-37 and G 99-47, which have polarisation periods reported in the literature at 4.117 h and 0.97 h respectively. Periods in the literature for KPD 0253+5052 and HE 1045-0908 are not confirmed with the photometric data, but this is more likely due to insufficient data over the required timescales.

No significant variability is detected in 51 MWDs. Seven of these stars do not have sufficient data. The February 2011 data are dominated by highly variable seeing conditions, which has an impact on the quality of the data and the ability to detect real modulations. The February 2011 run was also only three nights, and therefore only a smaller range of frequencies could be tested with confidence.

The Catalina Sky Survey (CSS) has observed 42 MWDs in this sample (55%), however the majority of these stars are too faint for the photometry to be accurate enough to provide useful, constraining information on the period of variability. For only one MWD, LB 9815, is the same period detected in both this survey and in the CSS data set (see Fig. 2.5). In most cases, the amplitude is too small for a period to be detected in the CSS data, which have magnitude uncertainties on the order of $\sim\pm5\%$, illustrating the limitations of using data from surveys, such as CSS. The CSS light curves can really only be utilised for the MWDs with the largest photometric variations to confirm a period, as the data quality is not adequate to constrain an unknown period of variability.

Interestingly, no photometric modulations are detected in the majority of the WDs with the strongest magnetic field strengths, such as HE 0330-0002, SDSS J0021+1502, SDSS J0211+0031, SDSS J0211+2115, SDSS J1003+0538, SBS 1349+5434, SDSS J2151+0031 and SDSS J2346+3853, with field strengths ranging from 170 MG up to 800 MG. These MWDs could be similar to the slowest MWD rotators, previously noted in the literature, with suspected periods $\gtrsim$100 years. Indications of no photometric or polarimetric variability could suggest that a MWD has a long rotation period, or less likely, that the magnetic field distribution is symmetric about the spin axis of the MWD. Additionally, if no star spots exist on the surface of a convective atmosphere MWD, no photometric variability would be detected as it rotates. A homogeneous magnetic field would also mean modulations are not observed, although this is unlikely based on studies of individual MWD spectra (e.g. Külebi et al. 2009).

2.6 Discussion

2.6.1 Correlations between rotation period and other physical parameters

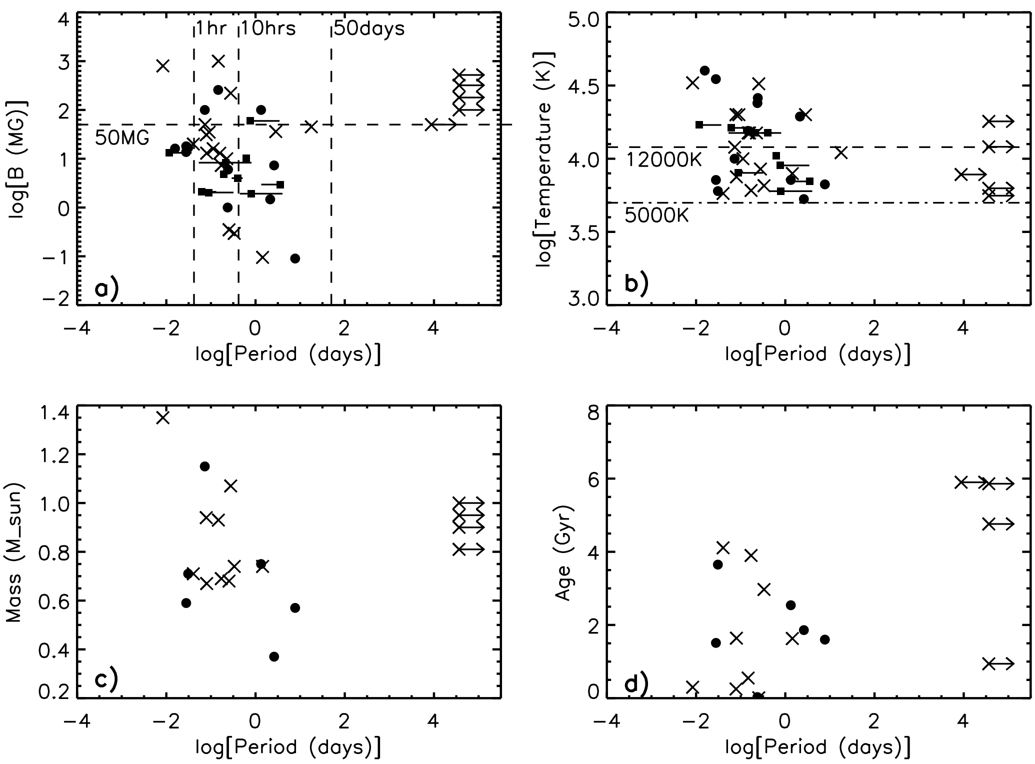

Figure 2.16: Rotation period versus intrinsic physical properties of MWDs – a) magnetic field strength, b) temperature, c) mass and d) WD cooling age. The crosses represent rotation periods from the literature (see Table A.1 for stars and parameters). The filled circles represent the MWDs with well-determined periods from this work (see Table 2.3, excluding SDSS 1250+1549). The filled squares with uncertainties are the MWDs with poorly constrained periods (see Table 2.4). Mass and cooling age estimates for MWDs are known for only a few stars.

In Figure 2.16, the periods of variability derived for the MWDs are compared with their intrinsic physical parameters, such as the magnetic field strength, temperature, mass and cooling age. The results for the 12 MWDs with well-determined periods (excluding the CV SDSS 1250+1549) are included (represented by filled circles), along with the 13 MWDs with poorly constrained periods, which are denoted by filled squares and uncertainties covering the 2σ range of possible periods. Seventeen MWDs with periods from the literature are also included and given in Table A.1. To determine whether any correlations exist between the parameters, a linear (Pearson) correlation test is used for each of the plots in Figure 2.16 to find the linear correlation coefficient and its p-value for the significance. The correlation coefficient indicates the noisiness and direction of the linear trend, but not its slope, nor any non-linear relationships. It is defined as the covariance of the two variables divided by the product of their standard deviations (using the CORRELATE function in IDL). The "slow rotators" are excluded from the correlation tests because their long periods are not measured, only suspected.

Comparison between rotation period and magnetic field strength

A negative correlation is found between the rotation period and magnetic field strength (Fig. 2.16, *top-left*), indicating that the faster MWD rotators have higher magnetic field strengths (also reported by Brinkworth et al. 2013). This suggests the MWDs may form via the merger scenario, where the star is spun-up in the common envelope (King et al. 2001) and strong magnetic fields can be generated. The MWDs then spin down slowly with age as they lose angular momentum or as their magnetic fields decay. The linear correlation test gives a weak coefficient value of -0.34 and p-value of 0.033, indicating that the null hypothesis can be rejected at a significance level of 0.05, implying the relationship is statistically significant (as the result would be highly unlikely if there is no relationship between the two parameters).

This contrasts with the previous findings of Schmidt & Norsworthy (1991) that MWDs rotate more slowly with increased magnetic field strength. They argued that angular momentum is lost during the latter stages of evolution, where a strong magnetic field in the core of an evolved star assists the transport of angular momentum to the outer envelope (also discussed in Spruit 1998, 2002). In this case, higher field strengths cause more magnetic braking, yielding slower rotators. However, Schmidt & Norsworthy (1991) noted that their correlation was weak, and that the trend was entirely influenced by the "slow rotators" that have been excluded from this analysis. If the "slow rotators" are included in the correlation analysis, a weak positive trend is, similarly, found. This same trend is seen for magnetic neutron stars, where the slowest rotators (anomalous X-ray pulsars AXPs and soft gamma repeaters SGRs) have the highest field strengths ($10^{14} - 10^{16}$ G, Ferrario & Wickramasinghe 2005).

Simulations of merging double degenerate WDs by Külebi et al. (2013a) predict the formation of surrounding discs which may significantly spin-down the MWD through magnetospheric interactions. Their model shows a non-linear relationship between the spin period and magnetic field strength, where the MWDs with higher field strengths have longer rotation periods; the opposite to the trend measured here in Figure 2.16 (*top-left*), where highly magnetic WDs have faster rotation periods. Külebi et al. (2013a) roughly estimate the correct magnetic field strengths and spin periods for the MWDs RE J0317-853, PG 1015+014 and PG 1031+234, all of which are massive ($> 0.9 M_{\odot}$), rapidly rotating (12 – 200 mins) and perhaps formed in mergers. However, their model is aimed at replicating rotation periods of massive, rapidly rotating MWDs that formed in double degenerate mergers (i.e. merger remnants), but this does not describe the characteristics of many MWDs in the sample which, for example, have spin periods longer than a few hours and have average masses of $\sim 0.6 M_{\odot}$.

However, if MWDs form through either single star evolution or from binary mergers, a relationship between the spin period and field strength could be difficult to determine, unless the stars can be separated by their likely formation mechanism (which is probably not possible in most cases). MWDs from a single star evolution may have a positive correlation between these parameters, i.e. the slowest rotators have the highest field strengths, while MWDs from mergers may show the opposite characteristics.

Alternatively, García-Berro et al. (2012) suggest that the wide variety of observed rotation periods of isolated MWDs can be explained by the alignment of the spin and magnetic axes. If the axes are mis-aligned, the WD rapidly spins down by magnetic dipole radiation, producing slow rotators, but if the two axes are aligned, the MWD will rotate rapidly (such as may be the case for RE J0317-853). Unless a particular alignment is favoured, the distribution of spin period with field strength could be random.

Nonetheless, the correlation detected here suggests that rotation period seems to increase with a decreasing magnetic field strength and therefore requires further investigation by theoreticians.

Comparison between rotation period and temperature

Similarly, a negative trend between the rotation period and effective temperature is measured (Fig. 2.16, *top-right*), implying the hotter MWDs have faster spin periods and that the cooler stars rotate more slowly. It has a correlation coefficient of -0.34 and a p-value of 0.034, suggesting it is a significant correlation. If hotter MWDs have faster spin periods then, since temperature is a proxy for cooling age, younger MWDs may also have faster spin periods. Consequently, if real, this implies that the MWDs may spin down, losing angular momentum with time. Therefore, a relationship could also exist between the rotation period and cooling age of the WD, where older MWDs have longer spin periods. In contrast, but from a smaller sample of MWDs, Schmidt (1987) and Schmidt & Norsworthy (1991) claimed no correlation existed between these two parameters, although they probably included the "slow rotators" in their sample.

Comparison between rotation period and cooling age

No correlation is found between the rotation period and cooling age for the MWDs in this sample (Fig. 2.16, *bottom-right*). The correlation coefficient is -0.087, with a p-value of 0.679, indicating that no linear trend is present. However, there are only a small number of rotating MWDs that also have estimated cooling ages. MWDs can have unsatisfactory cooling age estimates because their masses and radii are poorly constrained and magnetic models usually assume a gravity value (e.g. $\log g = 8$). If MWDs spin down over their lifetime, then a positive relationship between age and period might be expected, as the older (cooler) MWDs have longer rotation periods and younger (hotter) ones rotate more quickly. The MWDs in this sample have a variety of compositions and masses, possibly making it difficult to detect the relationship between the spin period and cooling age. On the other hand, a larger sample size may confirm the trend.

Comparison between rotation period and mass

From the plot of rotation period and mass (Fig. 2.16, *bottom-left*), it seems like there may be a negative relationship between these parameters, suggesting higher mass MWDs have faster rotation periods. The linear correlation coefficient gives a value of -0.33, but with a p-value of 0.102, suggesting the null hypothesis cannot be rejected and that the trend is not statistically significant. A negative correlation might be expected if high-field MWDs form in mergers, where they are thought to have higher masses and rapidly rotate.

2.6.2 Comparing physical parameters for rotators and non-rotators

Comparison between magnetic field strength and temperature

The magnetic field strength is also compared with the MWD temperature (see Fig. 2.17) for rotators with known periods and for "non-rotating" MWDs (this includes MWDs that have been investigated for photometric variability, where no modulations are detected, and MWDs that have not been studied for variability). No correlation is found between field strength and temperature for the non-rotators, however there is a significant positive trend for the rotators (Fig. 2.17, *top*), with a p-value of 0.02. Theoretically, in contrast, no correlation is expected between field strength and temperature, since the timescale for field decay by ohmic diffusion is longer than the WD cooling age, assuming the magnetic field is frozen into the WD (Schmidt 1987; Külebi et al. 2009).

Furthermore, Figure 2.17 shows few hot ($T > 30,000\,\mathrm{K}$) or low-field ($B < 1\,\mathrm{MG}$) MWDs are known. Although the SDSS has tripled the number of known MWDs, SDSS spectra are only able to identify Zeeman split features due to fields >1 MG. Lower field strengths in WDs are usually measured from spectropolarimetry or from fitting broadened hydrogen line cores in high resolution, high signal-to-noise (S/N) data.

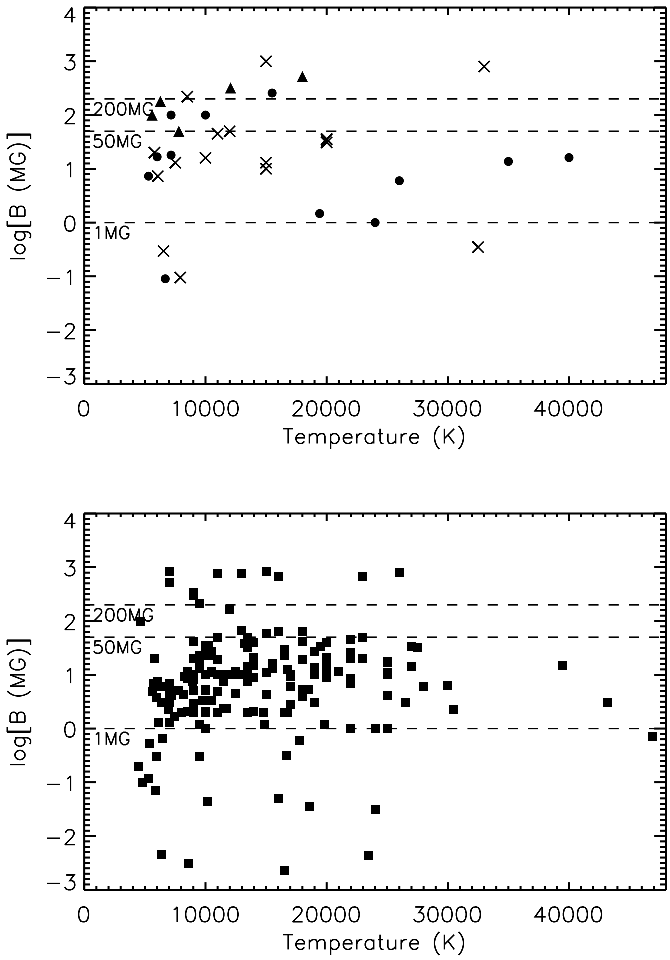

Figure 2.17: *Top:* Comparison of magnetic field strength and temperature for the MWD rotators, where the symbols are previously defined in Figure 2.16 and the filled triangles are the slow rotators. *Bottom:* The same comparison between these parameters for the non-rotating MWDs.

Photometric variability has until recently not been observed in low-field ($B < 1$ MG), hot ($T > 14{,}000$ K for DAs and $T > 29{,}000$ K for DBs, Winget & Kepler 2008) MWDs, possibly because they have fully radiative atmospheres and therefore are unable to form surface star spots. The field strengths are also too small for magnetic dichroism to have an effect on the observed brightness of the MWD (Külebi 2012, priv. comm.). However, photometric variability is found in four such stars in this work. In addition, the hot, low-field MWD BOKS 53856, discovered in the *Kepler* field (Holberg & Howell 2011), is also an exception showing periodic variability on 6.1375 hours. However, Holberg & Howell (2011) were unable to find a satisfactory explanation behind the photometric modulations that was also consistent with the star's other characteristics. For example, while an M or K dwarf companion in a close CV system would account for the photometric variability, no emission lines were observed in its spectra due to the presence of a secondary star. Furthermore, BOKS 53856 has a fully radiative photosphere and as a result is unlikely to form surface star spots like the localised high-field spot proposed for WD 1953-011 as the cause of its photometric variations (Maxted et al. 2000; Brinkworth et al. 2005).

Comparison between magnetic field strength and mass

Figure 2.18 (*top*) for the rotating MWDs suggests that there might be two populations present: the low-field MWDs ($B < 1$ MG) clustered near the bottom of the plot at masses of $0.5 - 0.7 M_{\odot}$ and the higher field ($B > 1$ MG) MWDs, covering a wide range of masses from $0.4\,M_{\odot}$ up to $1.35\,M_{\odot}$. This could indicate different evolutionary paths between the low-field (<1 MG), low mass ($0.5 - 0.7 M_{\odot}$) and high-field (>1 MG), high mass (>0.8 $M_{\odot}$) MWDs. For example, the low-field, low mass stars may be from single star evolution, e.g. magnetic A and F stars, and the high-field, high mass stars from mergers. A positive trend is detected between the magnetic field strength and mass for the high-field MWDs, which has a correlation coefficient of 0.65 and p-value of 0.0003, implying the relationship is statistically significant. However, the distribution appears much more random for the non-rotators (Fig. 2.18, *bottom*), although there is no obvious reason why the two plots should differ significantly. Furthermore, there are not as many high-field MWDs in the non-rotators plot as for the rotating MWDs. This could simply be a selection effect, as the mass is harder to determine for higher mass, highly magnetic WDs.

Comparison between magnetic field strength and cooling age

The comparison between field strength and cooling age is shown in Figure 2.19 for the MWD rotators and non-rotators. No significant correlations are found between the two parameters. If MWDs form in mergers one might expect to see a negative trend between the cooling age and field strength, where the younger MWDs have higher field strengths (and rotate more quickly). Furthermore, this same trend might be anticipated if the magnetic field decays with age and therefore the older MWDs have weaker field strengths.

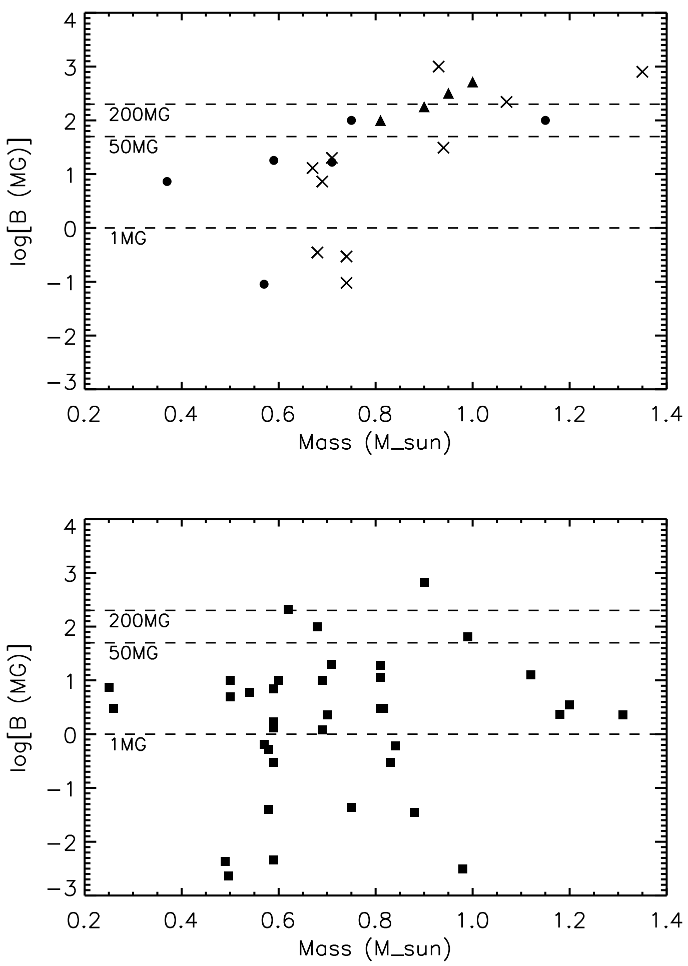

Figure 2.18: *Top:* Comparison between field strength and mass for the MWD rotators. Symbols are previously defined in Figure 2.16. The filled triangles are the slow rotators. *Bottom:* The same comparison between these parameters for the non-rotating MWDs.

However, currently the data in Figure 2.19 are scattered and there are not enough data points to meaningfully test for any correlations.

2.6.3 Comparison of rotation periods for MWDs and non-magnetic WDs

In Figure 2.20, the distribution of rotation periods for MWDs is compared with estimated rotation periods of non-magnetic WDs. The spin periods for the non-magnetic WDs are calculated using an estimate for their radii and from their rotation velocities ($v \sin i$, given in Karl et al. 2005; Berger et al. 2005), which are often upper limits, meaning

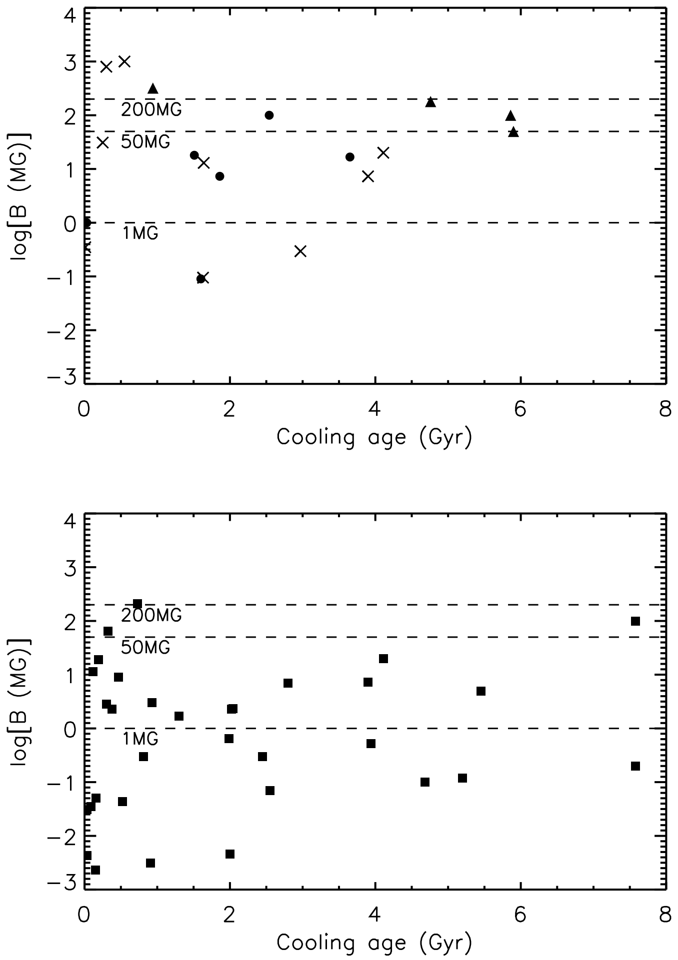

Figure 2.19: *Top:* Comparison between field strength and cooling age for the MWD rotators. Symbols are previously defined in Figure 2.16. The filled triangles are the slow rotators. *Bottom:* The same comparison between these parameters for the non-rotating MWDs.

the estimated spin periods are lower limits as the inclinations are unknown. Figure 2.20 appears to show that the majority of non-magnetic WDs have rotation periods less than two hours, although there are exceptions, with a few having estimated rotation periods up to 18 hours. The limitations of using the line cores to measure rotation of slowly rotating non-magnetic WDs means estimates cannot be made for much longer than a few hours, and none are measured longer than one day. By contrast, the photometric variability of MWDs allows longer spin periods to be probed; seven MWDs have well-defined periods longer than a day. Of course, this observation does not necessarily mean that MWDs have longer rotation periods. To compare the two populations, a Kolmogorov-Smirnov (K-S)

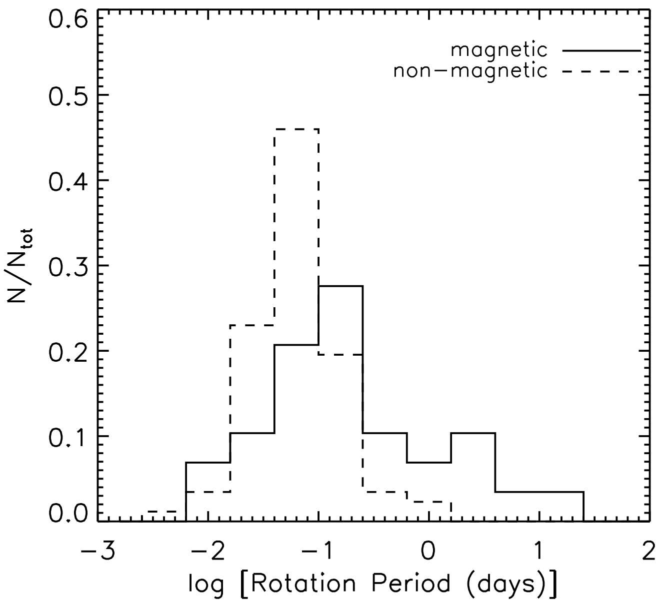

Figure 2.20: Histogram of rotation periods for magnetic (solid line) and non-magnetic WDs (dashed line). The non-magnetic distribution peaks around 2 hours. The very slow MWD rotators, with estimated rotation periods of $\gtrsim$100 years, are not included. The magnetic population appears to extend to longer rotation periods than the non-magnetic stars. This is probably an observational bias, as slow non-magnetic rotators are unlikely to be detected with the current methods of measuring rotation velocities.

test is used (the KSTWO function in IDL), where the K-S test statistic is determined as the maximum deviation between the cumulative distribution functions of the two samples. The K-S test of the MWDs in comparison with the non-magnetic population gives a p-value of 4×10^{-5}, suggesting that there is a very small probability the two populations are drawn from the same distribution. However, it is most likely that the difference between these distributions is an observational selection effect and not real, due to the disparate methods for measuring the spin period in magnetic and non-magnetic WDs.

2.7 Conclusions

In summary, results have been presented from this photometric variability survey of 77 MWDs to determine rotation periods. Well-defined spin periods are measured for 12 isolated MWDs, while variability is detected in a further 13 MWDs, with poorly constrained rotation periods. Well-constrained periods are determined for six MWDs for which variability on poorly constrained timescales had previously been noted by Brinkworth et al. (2013). Photometric variability is, unexpectedly, observed in four hot, low-field MWDs, which have an unknown mechanism causing the modulations. They are too hot for star spots to form in a partially convective atmosphere and their magnetic field strengths are too weak for magnetic dichroism to have an effect. Hot, high-field MWDs appear to rotate faster than cooler, weaker field strength stars (Fig. 2.16), which may indicate MWDs form via a binary merger. If they form from a merger, then they may be expected to be born with shorter rotational periods and then slow down with age, and to generate higher field strengths. A comparison between the magnetic field strength and mass (for the MWDs with known rotation periods, Fig. 2.18) may indicate the presence of two populations: low-field (<1 MG), low mass ($0.5-0.7 M_{\odot}$) MWDs and high-field (>1 MG), high mass (>0.8 $M_{\odot}$) MWDs, which in turn could provide insight into the progenitors of these stars. In addition, Figure 2.17 compares the magnetic field strength and temperature for the rotators and non-rotators, revealing there are very few hot or low-field MWDs, highlighting the observational limitations in identifying MWDs. MWDs that show no signs of variability over a week of observations should still be re-observed photometrically or polarimetrically in the following years for signs of long term modulations.

3

A Long Period Variable Hot DQ Magnetic White Dwarf

The carbon-dominated hot DQ magnetic white dwarf, SDSS J000555.90−100213.5, was observed as part of the survey using the Isaac Newton Telescope, as detailed in the previous chapter. This class of star is particularly interesting since a surprisingly large fraction of hot DQ white dwarfs have magnetic fields (~70%) and/or are photometrically variable on short timescales of <1000 s. By contrast, for the first time, a photometric period on the order of days at 2.110 ± 0.045 days is measured for SDSS J000555.90−100213.5, with a peak-to-peak amplitude of 11%. Variability on short timescales (less than three hours) is also ruled out at an amplitude of $\lesssim \pm 0.5\%$. Short period hot DQ white dwarfs have been interpreted as non-radial pulsators, but in the case of SDSS J000555.90−100213.5, it is more likely that the variability is due to rotation.

3.1 Background

Hot DQ WDs have atmospheres dominated by carbon, containing little or no hydrogen or helium (Dufour et al. 2007, 2008b). Only 14 hot DQs have been discovered so far, making them a rare class of WD (Dufour et al. 2010a; Liebert et al. 2003). In addition, their effective temperatures appear to cover a very specific range of $18,000 - 24,000$ K (Dufour et al. 2008b). Zeeman split lines, indicative of the presence of magnetic fields, have been detected or at least suspected, in 10 of the 14 catalogued DQs (70%, Dufour et al. 2010a, 2013). In contrast, the fraction of MWDs in the general WD population is thought to be in the range of $3 - 15$% (Kleinman et al. 2013; Jordan et al. 2007; Liebert, Bergeron & Holberg 2003), suggesting that perhaps all hot DQs are magnetic.

Dufour et al. (2008b) postulated that hot DQs descend from pre-WD stars, like H1504+65, which are thought to have undergone a violent late thermal pulse (a born-again AGB phase) burning its remaining hydrogen and helium layers, leaving behind an atmosphere composition mixture of carbon and oxygen. As the star cools, the carbon and oxygen separate by gravitational diffusion and the atmosphere appears carbon dominated. However, since no WDs hotter than ~ 23,000 K are found with carbon-dominated atmospheres, Dufour et al. (2008b) and Althaus et al. (2009) suggested that a small amount of residual helium could eventually diffuse upward and form a thin layer, ultimately forming a full atmosphere and thus appearing as helium atmosphere WDs. These stars then cool normally as DO/DB stars until developing a convection zone. Once the carbon convection zone becomes active enough, the thin radiative helium layer gets diluted, transforming it into a carbon-dominated atmosphere WD. This could possibly take place around 24,000 K (Dufour et al. 2008b). The hottest DQ known, SDSS J010647.92+151327.8, is also the only one with helium in its spectrum, and therefore is perhaps in the process of converting from a DB to a hot DQ. There is also now strong evidence that the hot DQs are linked with the massive, cooler DQs (Dufour et al. 2013). Until recently, the likelihood of their proposed evolutionary sequence remained tentative, as only one object was known to have a temperature in the ~13,000 – 18,000 K range. However, with the latest WD catalogue (SDSS DR7, Kleinman et al. 2013), many new carbon-dominated atmosphere WDs have been discovered with temperatures in the gap between the coolest, hot DQ ($T_{\rm eff} \sim 18{,}000$ K) and the hottest, cool DQ ($T_{\rm eff} \sim 12{,}000$ K). A colour – colour diagram of all the carbon-dominated atmosphere WDs shows a noticeable sequence of the hot DQs to the cool DQs (Dufour et al. 2013). The carbon abundances also appear to decrease along the sequence as they cool. Given the high incidence of magnetism in the hot DQs, the same would be expected for the cooler DQs in the sequence, but only a few of the new "warm" DQs currently appear to be magnetic, although this may change with higher signal-to-noise/resolution spectra.

Montgomery et al. (2008) observed six stars from the hot DQ WD sample for pulsations and discovered the first photometrically variable hot DQ, SDSS J142625.71-575218.3 (hereafter SDSS J1426-5752), with modes at 417.7 s and 208.8 s (first harmonic). Their theoretical calculations predicted that SDSS J1426-5752 should be the only star in their sample to pulsate, as it was the nearest to the high-temperature boundary (the "blue edge") of the DQ WD instability strip. Since then, however, variability has been detected for a further four hot DQ WDs (SDSS J2200-0741 and SDSS J2348-0942, Barlow et al. 2008; SDSS J1337-0026, Dunlap et al. 2010 and SDSS J1153+0056, Dufour et al. 2011), where the latter is detected in the FUV using the Hubble Space Telescope (HST) and Cosmic Origins Spectrograph (COS) and the amplitudes of the modes are 2–4 times larger than those observed in the optical.

Here, the sixth variable hot DQ, SDSS J000555.90−100213.5 (hereafter SDSS J0005-1002) is introduced. It was first discovered as a possible magnetic DQ WD in the SDSS DR1 (Schmidt et al. 2003). It has the largest mean field strength for a hot DQ at 1.47 MG, measured from the line splitting in its spectrum (Dufour et al. 2008b), and has an effective surface temperature of 19,420 K. As part of the photometric variability survey of MWDs (Chapter 2), modulations were detected for SDSS J0005-1002 on the timescale of days. This periodicity is much longer than has been observed for the other hot DQ variables, which have thus far been interpreted as pulsations (Barlow et al. 2008; Dunlap et al. 2010; Dufour et al. 2011). The cause of variability in SDSS J0005-1002 is discussed, along with the photometric variability of hot DQ stars in general, the unusual pulsations some of them display, and the role of magnetism and its possible influence.

3.2 Observations & Data Reduction

Two different telescopes were used to observe SDSS J0005-1002: the INT in La Palma and the 1.0 m telescope at the South African Astronomical Observatory (SAAO). A detailed log of the observations is given in Table 3.1.

Table 3.1: Observations log of SDSS J0005−1002.

Telescope	UT Date	Start Time (UTC)	T_{exp} (s)	N	Filter *
INT WFC	2009-10-17	23:03:42	60	3	r′
INT WFC	2009-10-18	21:15:48	120	9	r′
INT WFC	2009-10-21	23:28:50	120	12	r′
INT WFC	2009-10-23	01:23:23	120	3	r′
SAAO 1.0m STE3	2012-09-08	21:09:28	180	75	none **
SAAO 1.0m STE3	2012-09-10	22:08:12	180	54	none **
SAAO 1.0m STE3	2012-09-11	22:04:26	180	55	none **
SAAO 1.0m STE3	2012-10-18	20:24:41	180	13	none **
SAAO 1.0m STE3	2012-10-22	18:57:44	90	29	none **
SAAO 1.0m STE3	2012-10-23	18:46:04	120	60	none **

* The SAAO STE3 CCD is sensitive to the red of the spectrum, so observations peak at a wavelength of 600 − 700 nm.
** Data either collected by myself or as part of a program where I was the principal investigator.

3.2.1 INT Optical Photometry

Using the INT WFC in La Palma, SDSS J0005-1002 was observed during an observing run from 17-23 October 2009 as part of a survey of MWDs (see Chapter 2). The details of the observations are listed in Table 3.1. The data were reduced using the INT Wide

Field Survey CASU pipeline, as described previously in §2.3.

3.2.2 SAAO 1.0m Optical Photometry

SDSS J0005-1002 was also observed using the 1.0 m telescope located at the South African Astronomical Observatory (SAAO) from 29 August – 11 September 2012 (by myself) and 17 – 23 October 2012 (by Matt Burleigh). The SAAO CCD (STE3) instrument was used for both runs, and has a field-of-view of 512×512 pixels and a pixel scale of 0.31 arcsec/pixel. The target was observed in clear light (i.e. with no filter) in 2×2 binning. Observation details are given in Table 3.1.

The data were reduced using the SAAO CCD pipeline which subtracted the bias and normalised by the master flat field frame. Photometry of the target and comparison stars was performed using the STARLINK package AUTOPHOTOM. Figure 3.1 shows the SAAO STE3 field-of-view with the stars marked accordingly. The aperture width was fixed for a given night and was defined as 1.5 times the mean seeing (FWHM, Naylor 1998). Selecting a slightly smaller aperture size limited the contamination of background noise in the aperture, which was high due to a significant amount of moonlight during the September run. The sky background level was determined using the clipped mean of the pixel values in an annulus around the stars and the measurement errors were estimated from the sky variance. To remove atmospheric fluctuations, the target light curve was divided by the light curve of the sum of the comparison stars.

3.3 Analysis & Results

All time stamps are converted to a barycentric Julian date (BJD) using an IDL implementation by Eastman, Siverd & Gaudi (2010). To assess the periodicity of the light curves, two different methods are used: a Fourier analysis using *Period04* (Lenz & Breger 2005)

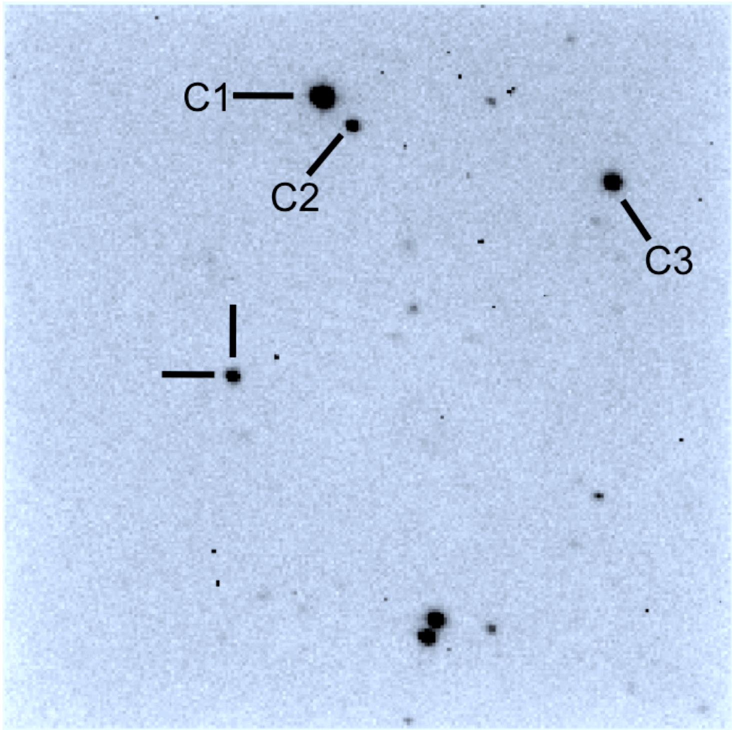

Figure 3.1: Finder chart for SDSS J0005-1002, showing the SAAO STE3 CCD field-of-view (2.6’×2.6’), where the target and comparison stars are marked. North is towards the top of the frame and east is to the left.

and a least-squares fit of a sinusoid using MPFIT in IDL (Markwardt 2009).

3.3.1 Fourier analysis

Figure 3.2 shows the light curve obtained from the INT data and resulting Fourier Transform (FT) for SDSS J0005-1002 and its comparison stars. A maximum amplitude is measured at a frequency of 0.490103 cycles/d (P = 2.04 d). There are also aliasing peaks at low frequencies with comparable amplitude to the main peak (see inset Fig. 3.2, *lower panel*) due to the window function (shown in Fig. 3.4). Fluctuations are not detected in the relative flux of the comparison stars, which is reflected in the small amplitude in the FT.

The light curve of the SAAO data and FT for the target and comparison stars are shown in Figure 3.3. As found from the INT light curve, the relative flux of the comparison stars is stable from night-to-night. The FT (Fig. 3.3, *top of lower panel*) has a maximum peak at 0.501235 cycles/d (P = 1.99 d), which approximately agrees with the Fourier analysis of the INT data. The window function of the SAAO data is shown in Figure 3.5. The structure of the peaks in the window function are comparable to those found in the real FT.

3.3.2 Least-squares sine wave fit

The light curves are also fit with a sinusoid plus a constant (defined in Eq. 2.1) using MPFIT in IDL (Markwardt 2009) and folded on the best-fitting period. Again, slightly different best-fitting periods are determined for the two data sets, but they agree within error estimates. For the INT data, a best-fitting period of 2.104 ± 0.030 days is found, with a reduced χ^2 of 3.77 (χ^2 of 86.7 over 23 degrees of freedom dof). For the SAAO data, a best-fitting of 2.110 ± 0.001 days is found, with a reduced χ^2 of 3.26 (χ^2 of 918.6 over 282 dof). These periods are slightly different from the values determined from the Fourier analysis.

3.3.3 Uncertainty in the period

The period uncertainties are independently estimated by bootstrapping the data. Both data sets are fit with a sine wave using MPFIT, then the light curves are resampled by randomly selecting the same number of points and re-fit with a sine wave ("resampling with replacement", Brinkworth et al. 2005; Diaconis & Efron 1983). This is repeated 20,000 times. The resultant distribution of possible periods is given in Figure 3.6. The distribution of periods for the INT data peaks at 2.110 days with a 2σ error of 0.045 days, while the SAAO data distribution of periods peaks at the same period with a 2σ error of 0.003 days.

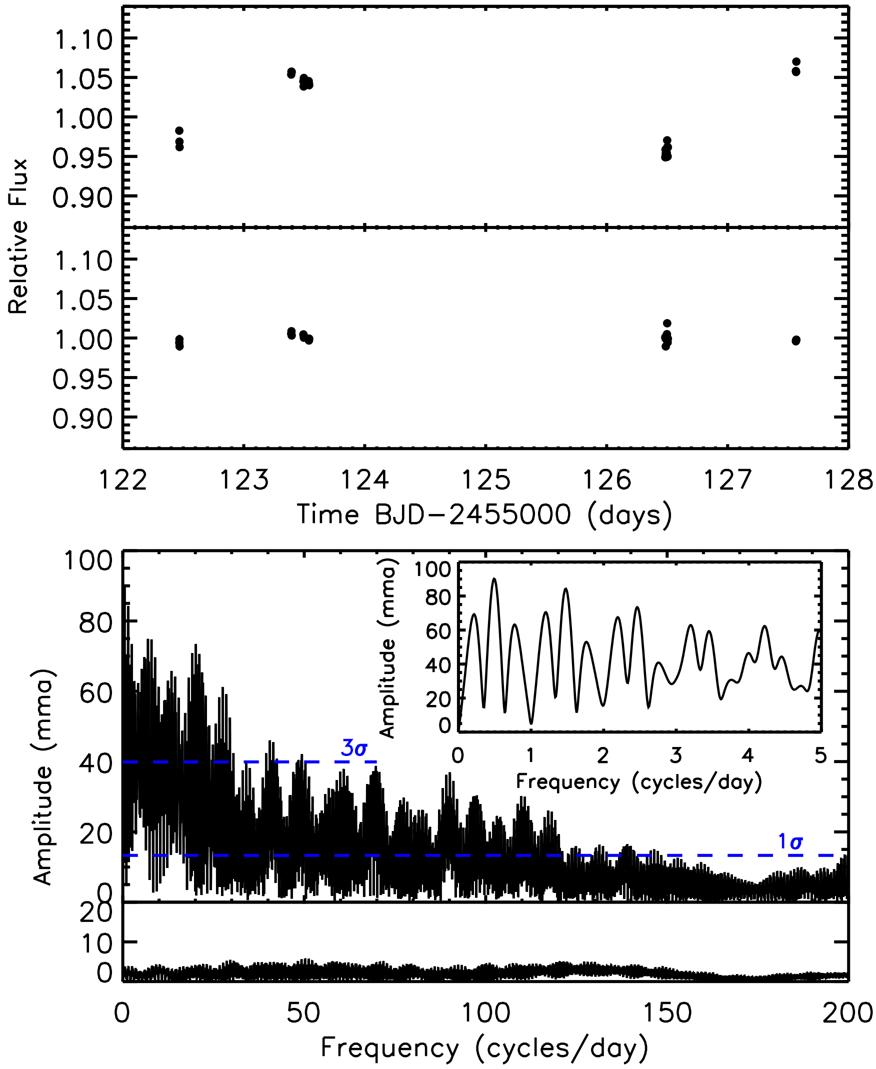

Figure 3.2: *Top of upper panel:* Differential light curve of SDSS J0005-1002 (target/(C1+C3)) taken using the INT WFC in r′-band over five nights in October 2009. *Bottom of upper panel:* Differential light curve of the comparison stars (C2/(C1+C3)). The change in observed flux for the target is not seen in the light curve of the comparison stars. *Top of lower panel:* FT of SDSS J0005-1002 light curve, where frequencies have been searched up to approximately the Nyquist frequency. The inset figure shows the low frequencies in more detail. The maximum amplitude is measured at a frequency of 0.490103 cycles/d (P = 2.04 d). The other peaks at low frequencies are aliases due to the window function (Fig. 3.4). The dashed lines indicate the σ and 3σ noise levels. *Bottom of lower panel:* FT of the light curve of the comparison stars. The amplitude for the comparison stars is much smaller than the amplitude in the FT for the target. The amplitude is given in units of milli-modulation amplitude (mma), meaning 10 mma corresponds to 1%.

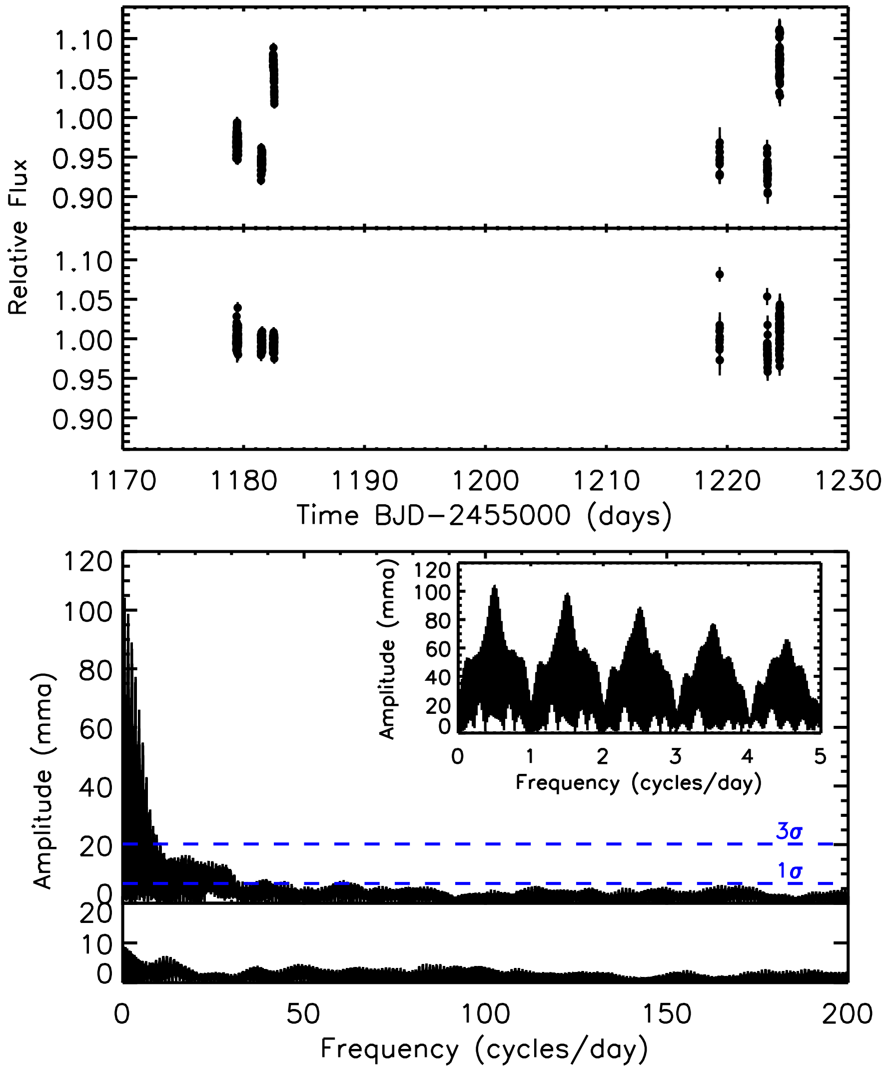

Figure 3.3: *Top of upper panel:* Differential light curve of SDSS J0005-1002 (target/C3) taken using the STE3 instrument on the SAAO 1.0 m with no filter over four nights in September 2012 and six nights in October 2012. *Bottom of upper panel:* Differential light curve of the comparison stars (C2/C3). The scatter on short timescales (i.e. over one night) is comparable between nights. Variations in flux are observed from night-to-night in the light curve of SDSS J0005-1002, while the light curve of the comparison stars is stable. The scatter in the SAAO data is understandably larger than in the INT data, as SDSS J0005-1002 is V=18.3 and was observed with a smaller 1.0 m telescope. It also has a smaller field-of-view, thus limiting the number of appropriate comparison stars available for differential photometry. *Top of lower panel:* The corresponding FT of the target light curve, searching up to approximately the Nyquist frequency. The inset figure shows the low frequencies in more detail. The maximum peak is measured at 0.501235 cycles/d (P = 1.99 d). The other peaks at low frequencies are aliases due to the window function (Fig. 3.5). The dashed lines indicate the σ and 3σ noise levels. *Bottom of lower panel:* FT of the light curve of the comparison stars.

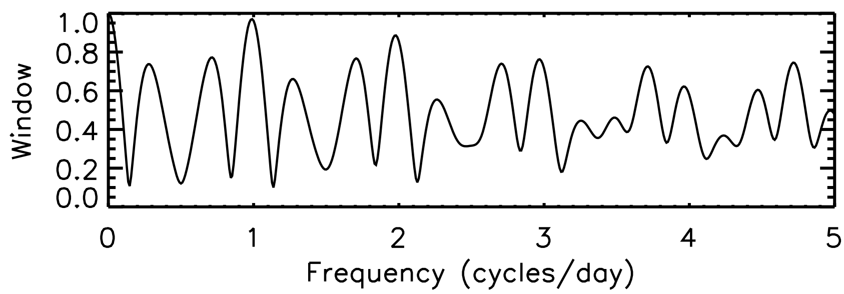

Figure 3.4: Window function of the INT data in Figure 3.2. The structure of the peaks is the same as those seen in the FT of the real light curve.

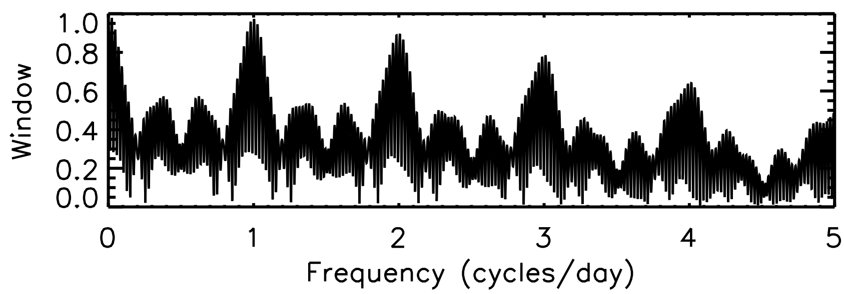

Figure 3.5: Window function of the SAAO data in Figure 3.3. The structure of the peaks is the same as those seen in the FT of the real light curve.

3.3.4 Folding the light curve

In Figure 3.7, both sets of light curves are folded on the 2.110 day period. The SAAO light curve is folded on the ephemeris for the time at minimum flux,

$$BJD = 2456179.1036(48) + 2.110(45)E.$$

However, this is not used to fold the INT data set, as the period estimate is not accurate enough to link the two data sets, which are separated by nearly three years. Unfortunately, complete coverage over all phases is not achieved, due to the 2 day timescale of variability. As a result, it cannot be definitively determined whether the photometric variations are sinusoidal or not.

The amplitude of the INT folded light curve is 10.9 ± 0.3%, which is not the same as

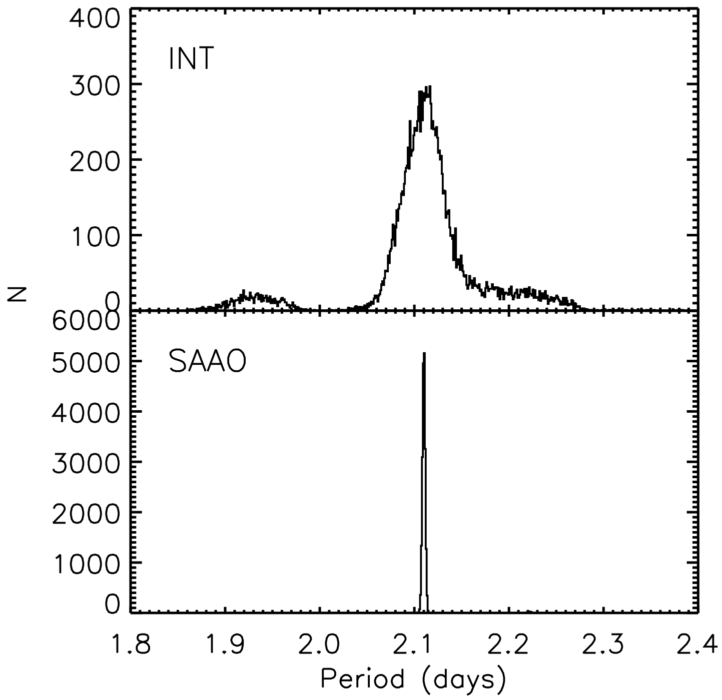

Figure 3.6: Distribution of possible periods for the INT and SAAO data sets after bootstrapping 20,000 times. *Top:* The INT data peaks at a period of 2.110 days with a corresponding 2σ error of 0.045 days, estimated from fitting a Gaussian curve to the peak. *Bottom:* The distribution from bootstrapping the SAAO data peaks at the same period of 2.110 days with a 2σ error of 0.003 days.

the amplitude of the SAAO folded light curve at 14.7 ± 0.2%. This is not surprising as the SAAO data was taken without a filter and the INT data was taken in the r′-band. Photometric variability in MWDs is known to exhibit a wavelength dependence due to spectroscopic variations in the presence of a changing magnetic field configuration (e.g. RE J0317-853, Vennes et al. 2003).

Using the method outlined in Dawson & Fabrycky (2010) for determining whether the periodic signal is appropriately identified, fake noiseless sinusoids are generated with the same period, phase and amplitude as found for the real INT and SAAO data sets. The FT of the noise-free light curve is then compared with the real FT (see Figs. 3.8 and 3.9). In both cases, the FT of the noiseless sinusoid replicates the FT of the observed light curve very well, where the maximum peaks at the same frequency with the same amplitude.

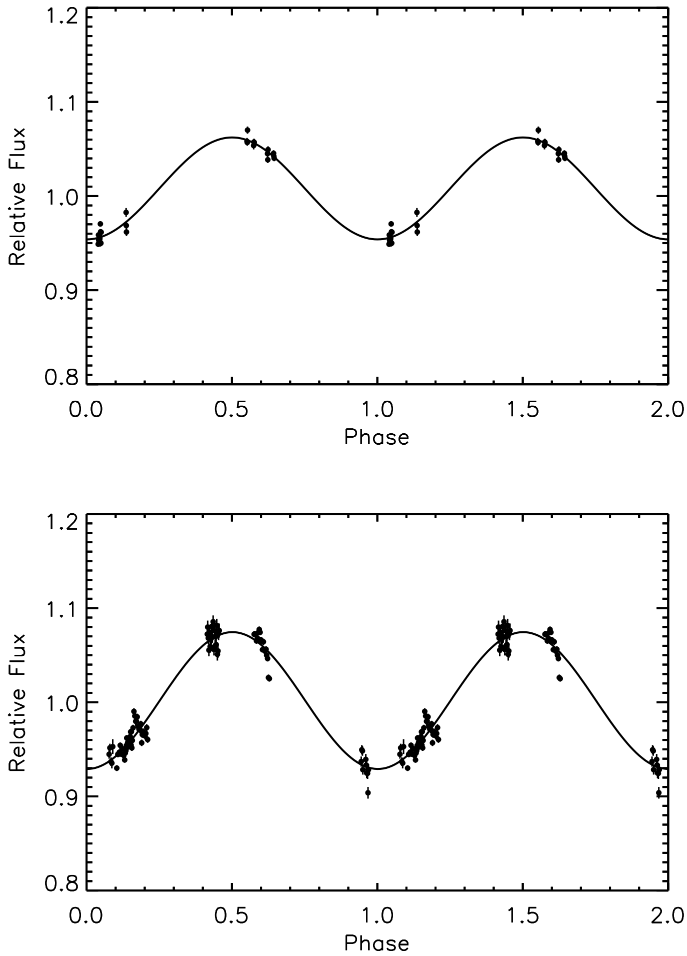

Figure 3.7: *Top:* INT light curve folded on 2.110 days with a starting time of 2455122.1804753 BJD at minimum flux. The best-fitting sine curve has a reduced χ^2 of 3.61 and a peak-to-peak amplitude of 10.9%. *Bottom:* The SAAO light curve is folded on the same period using the ephemeris and binned by a factor 2. It has a reduced χ^2 of 3.26 and a peak-to-peak amplitude of 14.7%. The ≈2 day period has made it difficult to observe all phases of the variability with rotation.

Since the fake light curve is created with a single sinusoid and reproduces the observed FT so accurately, it suggests that the photometric variability of SDSS J0005-1002 can be described well with a simple sinusoid. This is particularly interesting since observations over all phases could not be acquired due to the 2 day period.

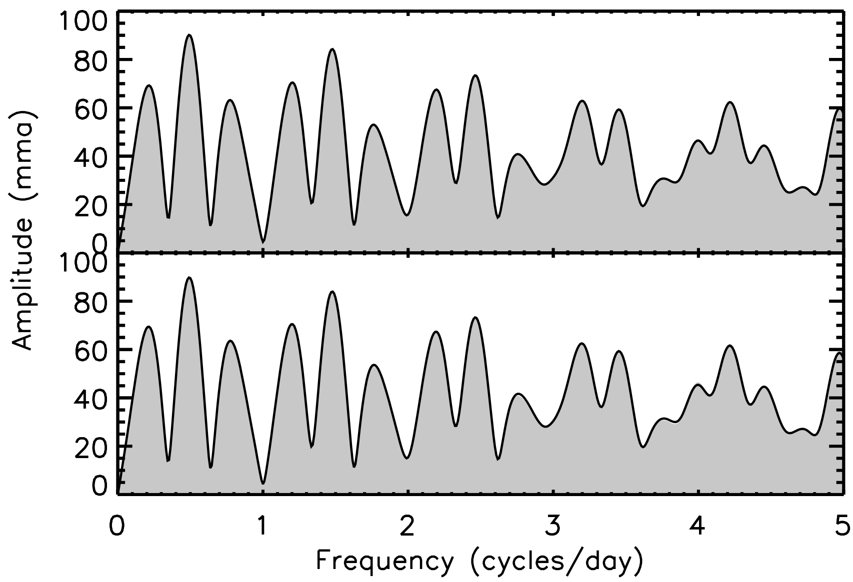

Figure 3.8: *Top:* FT of the SDSS J0005-1002 INT data (same as shown in Fig. 3.2). *Bottom:* FT of a noiseless 2.110 day sinusoid sampled at the same times as the INT data (solid line), with the FT of the real INT data for reference (in grey). The FT of the noiseless sinusoid reproduces the observed FT very well; the peaks have the same frequencies and the same amplitudes.

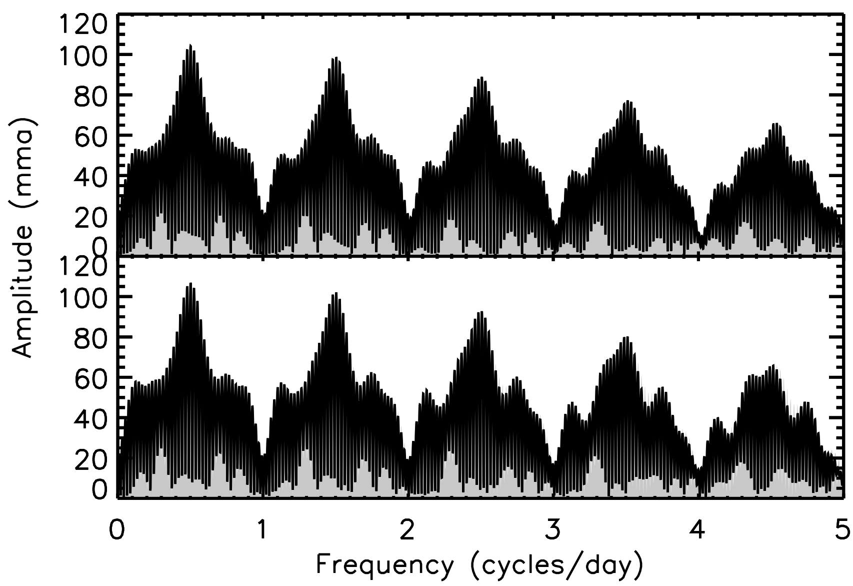

Figure 3.9: *Top:* FT of the SDSS J0005-1002 SAAO data (same as shown in Fig. 3.3). *Bottom:* FT of a noiseless 2.110 day sinusoid sampled at the same times as the SAAO data (solid line), with the FT of the real SAAO data for reference (in grey, but it is mostly hidden by the main fake FT in the panel). The FT of the noiseless sinusoid reproduces the observed FT very well; the peaks have the same frequencies with the same amplitudes.

3.3.5 Variability on short timescales

Since other magnetic hot DQ WDs show short term fluctuations on timescales of 210–1050 s (Barlow et al. 2008; Dunlap et al. 2010; Dufour et al. 2011), the nightly SAAO light curves, each of which are up to 3 hours long (see Table 3.1), are analysed for short period modulations. The nightly light curves of the target and comparison stars, and corresponding FTs are shown in Figure 3.10. The nightly SAAO light curves are not corrected for differential refraction effects due to changes in the airmass during observing because I did not want to unintentionally remove any real long term changes in the flux. The flux in the nightly light curves are consistently stable and do not show the secular change in flux with time, indicative of residual atmospheric effects. The red data points in Figure 3.10 are fake data points from a noise-free 2.110 day sinusoid sampled at the same times as the SAAO light curve (used for the FT analysis in Fig. 3.9). They show good agreement with the real data points, illustrating that real variability could have been removed by correcting for any differential refraction. There is some scatter on short timescales in the relative flux, but these features are also evident in the analysis of the comparison stars. The peaks in the FTs at low frequencies correspond approximately to the length of the nightly light curves.

To confirm whether any peaks in the individual FTs are real, false alarm probabilities (FAPs) are determined for each of the SAAO data sets using the method in Alcock et al. (2000) and Kovács, Zucker & Mazeh (2002). The significance Sg of the highest peak in the FT is calculated using,

$$Sg = \frac{A_{max} - < A >}{\sigma_A}, \quad (3.1)$$

where A_{max} is the amplitude A at the highest peak in the FT, $< A >$ is the average amplitude and σ_A is the standard deviation of A for the given frequency range. This procedure is carried out for 1000 fake light curves, which are generated by randomly shuffling the target light curve and repeating the analysis. A probability distribution function (PDF) is then calculated from the simulated light curves. Figure 3.11 shows the resulting PDF

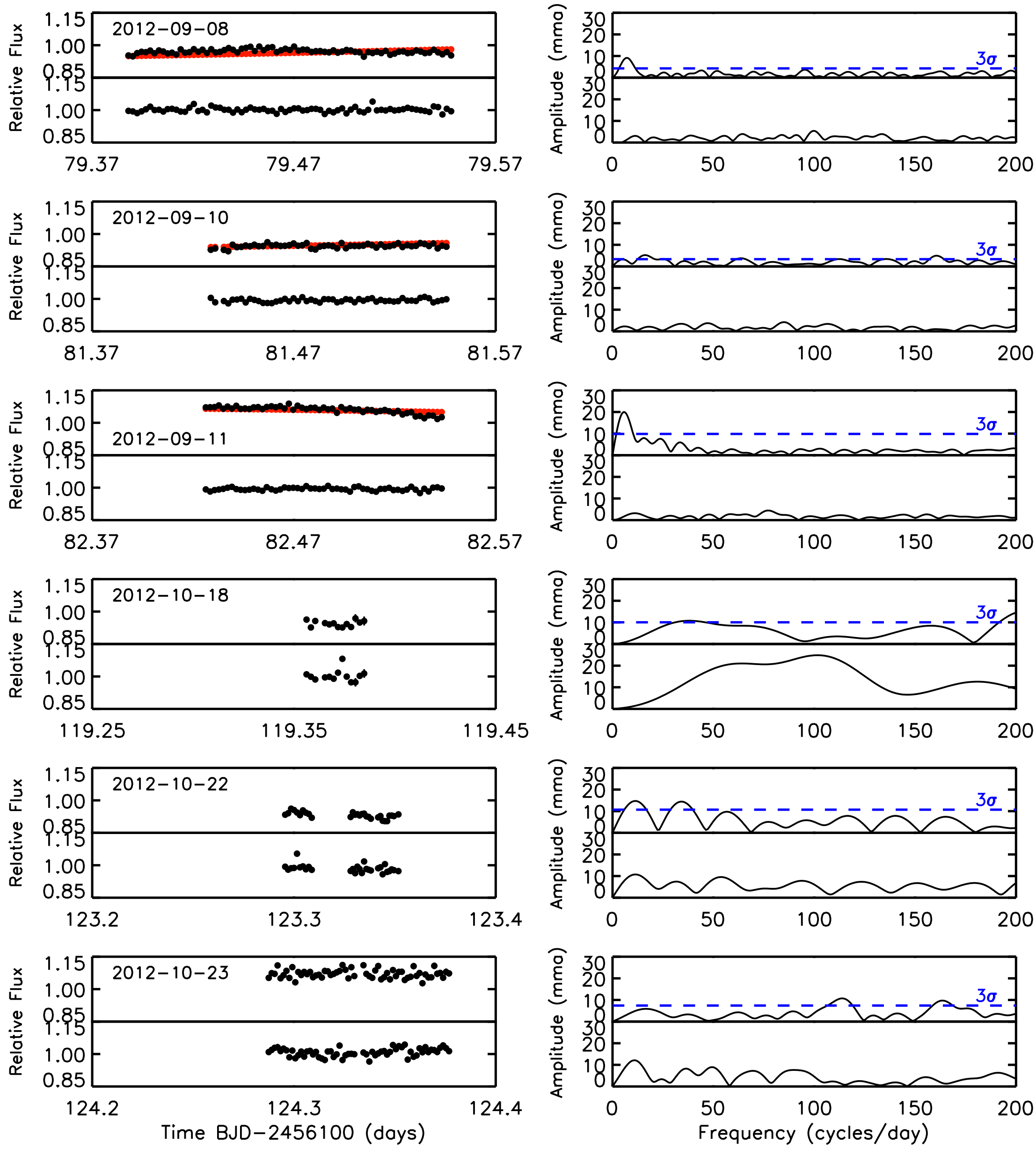

Figure 3.10: Light curves of the individual SAAO nights (*left*) and the corresponding FTs (*right*). Each panel shows the results for the target (*top*) and for the comparison stars (*bottom*). The relative flux for the target is calculated as the target flux divided by the C3 flux, while the comparison star relative flux is determined as C2 flux/C3 flux. There is no evidence for short period fluctuations at a 3σ detection limit (three times the noise level, dashed line) of $\lesssim \pm 0.5\%$ in amplitude for the two best light curves taken on 2012-09-08 and 2012-09-10. Some scatter is seen in the light curves. However, these features on short timescales are also evident for the comparison stars. The peaks at small frequencies in the FTs correspond to the length of the observations. The red data points are a noise-free 2.110 day sinusoid sampled at the same times as the SAAO light curve.

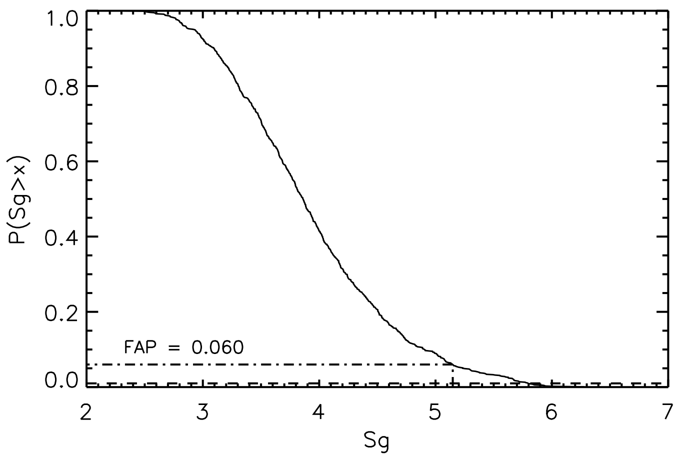

Figure 3.11: Probability distribution function (PDF) derived for 1000 simulated light curves of the SAAO data taken on September 8, 2012. The significance of the highest peak in the FT for the real light curve is $Sg = 5.15$, corresponding to a FAP of 0.060 (dot-dashed line). This is above the dashed line that represents a FAP of 0.01 (the 99% detection threshold). Therefore, this shows there is no evidence for significant photometric variability (on short timescales) in the light curve taken on September 8, 2012 of SDSS J0005-1002.

for the SAAO light curve obtained on September 8, 2012. The FAPs are determined for each of the nightly SAAO light curves as 0.060, 0.424, 0.030, 0.434, 0.295 and 0.347 respectively. These are all above a FAP threshold of 0.01. Furthermore, no significant peaks are detected in the FTs in Figure 3.10 above a 3σ detection limit (three times the noise level σ, dashed line in Fig. 3.10). Consequently, there is no evidence for photometric variability in SDSS J0005-1002 on a timescales less than 3 hours (this agrees with findings from K. Williams & B. Dunlap 2012, priv. comm.) at an amplitude of $\lesssim\pm0.5\%$ (3σ) for the two best light curves taken on 2013-09-08 and 2012-09-10.

At this detection limit, the small-amplitude pulsations exhibited by the other variable hot DQs may be undetectable in some of the current SAAO data sets. The variable hot DQ pulsations have semi-amplitudes typically of 7 mma (0.7%) in the optical, with SDSS J1426-5752's main pulsation period having the highest amplitude at 17.5 mma (1.75%, Montgomery et al. 2008). However, the typical pulsation semi-amplitudes would have, at least, just been detectable in the two best SAAO data sets with detection limits of $\lesssim\pm0.5\%$.

3.4 Discussion

For the first time, long period photometric variations are discovered for the hot DQ WD, SDSS J0005-1002, at a period of 2.110±0.045 days and peak-to-peak amplitude of ~ 11%. There is also no evidence for fluctuations on timescales of less than a few hours at an amplitude of $\lesssim\pm0.5\%$. In contrast, the other variable hot DQs show short term fluctuations up to ~1000 s. The vast majority of pulsating WDs have modes shorter than 2000 s (e.g. Winget & Kepler 2008). The longest pulsation mode ever measured is 4444 s (Hermes et al. 2012), but this is for a rare extremely low mass WD ($M \sim 0.17 M_{\odot}$). The variability seen in SDSS J0005-1002 is therefore believed to be due to rotation, and not pulsations, as no WD has ever been observed to pulsate with modes of days.

The spin period for SDSS J0005-1002 is consistent with rotation period measurements for pulsating WDs, which are typically around a day and determined from the splitting of their pulsation modes (Kawaler 2004; Winget & Kepler 2008). Approximately 40% of MWDs show photometric variations with rotation, and the majority have spin periods of hours to a few days (Brinkworth et al. 2013; Chapter 2).

Up to 70% of hot DQ WDs are magnetic (Dufour et al. 2010a, 2013), which is a much higher incidence of magnetism than is observed for the general WD population (3 – 15%, Kleinman et al. 2013; Jordan et al. 2007; Liebert, Bergeron & Holberg 2003). Interestingly, no magnetic field has ever been detected for a pulsating hydrogen-dominated atmosphere DA WD, despite several hundred DA MWDs now known, whereas magnetic fields are measured in some pulsating carbon-dominated hot DQ WDs.

Although Montgomery et al. (2008) predicted that the prototype variable hot DQ SDSS J1426-5752 should indeed pulsate, they found that the observed pulse shape was different to that seen for normal DA WD pulsators, having a flat maximum and sharp minimum. Large amplitude pulsating DA WDs are typically characterised by the opposite behaviour, a flat minimum and sharp maximum. This unusual pulse shape is also seen for SDSS J2200-

0741 (Barlow et al. 2008; Dufour et al. 2009) and SDSS J1337-0026 (Dunlap et al. 2010, although Dufour et al. 2011 did not find this in their FUV light curves). Since these stars also have magnetic fields[1], Green et al. (2009) and Dufour et al. (2009) suggested that the different pulse shape could be due to the presence of the magnetic field. Furthermore, another hot DQ SDSS J2348-0942 has no known magnetic field and a sinusoidal pulse shape, suggesting the presence of magnetism may influence the observed pulse shape in magnetic DQs.

Green et al. (2009) and Dufour et al. (2009) suggested that these magnetic hot DQs could be the WD analogs of the main-sequence rapidly oscillating Ap (roAp) stars, which have sufficiently strong magnetic fields (on the order of a few kG) capable of affecting the pulsations and exhibit a similar pulse shape to SDSS J1426-5752. Rotation periods of roAp stars are on the order of several days and have single or multi-periodic pulsation modes of 4 – 21 minutes (e.g. Ryabchikova et al. 2005; Kurtz 1982, 1990; Elkin et al. 2005).

The pulsations interpretation for the short term variable hot DQs is probably real in most cases. However, not all of them exhibit multi-periodic modes in their FTs, a characteristic indicative of pulsators, and therefore the single mode pulsators may actually be photometrically variable due to rotation. Rapid rotation periods as short as tens of minutes have been measured for RE J0317-853 at 725 s (Barstow et al. 1995; Ferrario et al. 1997a) and SDSS J2257+0755 at 1354 s (Chapter 2), comparable to the length of pulsation modes. However, both of these DA WDs have effective temperatures $T_{\rm eff} > 30,000$ K well beyond the hydrogen instability strip, and therefore their photometric variations are not pulsation modes. All hot DQs should be observed for both long and short period photometric variability. This can also be used as a method for indicating whether some of the other hot DQs may be magnetic. For example, a hot, variable WD was detected in the *Kepler* field by Holberg & Howell (2011) with photometric modulations of ≈5% peak-to-peak on a period of 6.1375 h. Subsequent high S/N spectra confirmed that the

[1]Dufour et al. (2013) recently detected a magnetic field for SDSS J1337-0026.

star was in fact magnetic.

Magnetism in WDs, in general, is thought to originate from either a magnetic main-sequence progenitor star or generate in a binary merger (§1.2.2), and therefore, magnetism is expected to be found at all points along the WD cooling tracks. If the hot DQs are linked with the previously known cooler DQs in an evolutionary sequence (as suggested by Dufour et al. 2008b, 2013), one would expect to find the same high incidence of magnetism in the cooler, helium-dominated atmosphere WDs as observed for the hot DQs, which does not appear to be the case (Dufour et al. 2013). Perhaps the magnetic field detected in hot DQs is generated in the developing carbon-oxygen convection zone, as the star converts from a DB to a hot DQ, rather than being a fossil field from the progenitor main-sequence star or created during the common envelope phase (Dufour 2013, priv. comm.). Subsequently, as the star cools further and the convection reduces, the magnetic field dies, explaining the absence of magnetism in the cooler DQs.

3.5 Conclusions

In summary, hot DQ WDs remain enigmatic objects. Most, if not all, are magnetic, in contrast to the WD population in general, and many appear to pulsate. For the first time, long period photometric variations have been discovered for a hot DQ WD, SDSS J0005-1002, with a period of 2.110 ± 0.045 days and a peak-to-peak amplitude of $\sim 11\%$. The modulations were first observed as part of the MWD variability survey using the INT (detailed in Chapter 2) in 2009 and was followed-up more recently using the 1.0 m telescope at the SAAO. The nightly SAAO light curves show no evidence for short term fluctuations on timescales less than a few hours at an amplitude level of $\lesssim\pm0.5\%$ for the two best light curves.

All hot DQs should be monitored for long period modulations, indicative of rotation, while some hot DQ "pulsators", especially those with a single oscillation mode, should be observed to ascertain whether some of the short term variables are rotators after all. The photometric variation may be due to star spots in a convective atmosphere, or changes in the Zeeman splitting and line strengths due to a varying field strength and configuration across the surface of the star. Therefore, these stars, and SDSS J0005-1002 in particular, should be targeted for high-resolution, time-resolved spectroscopic observations to investigate how the spectral features change with rotational phase; and although more difficult to obtain, time-resolved spectropolarimetry over the rotation period would provide a unique insight into a possibly changing magnetic field and the cause of the fluctuating brightness. Magnetism may play a key role, or provide clues, to the origin and evolution of hot DQ WDs.

4

Searching for Long Term Variability in Magnetic White Dwarfs

Here, I present the results from a search for long term photometric variability in ten bright, isolated magnetic white dwarfs. These stars were previously investigated by Brinkworth et al. (2013) and were found to be photometrically stable on short timescales (hours – one week), but showed possible long term modulations over many months between observing seasons. Observations were carried out over a two year period using the robotic Liverpool Telescope in La Palma, Spain. None of the stars in the sample show significant photometric variability, although the magnetic white dwarf G 240-72 appears to show photometric modulations over months. However, a number of factors have restricted the usefulness of the data, and therefore the conclusions that can be made. I recommend this investigation should be repeated in the future, where the CCD has a larger field-of-view, the targets are observed at a higher sampling rate to probe periods around a month and the observations are kept as consistent as possible.

4.1 Background

As part of Carolyn Brinkworth's thesis (Brinkworth 2005; Brinkworth et al. 2013), a survey was conducted using the 1.0 m Jacobus Kapteyn Telescope (JKT) in La Palma, searching for photometric variability on short timescales (hours – one week) in a sample of bright MWDs selected from Wickramasinghe & Ferrario (2000). Some of these targets indicated possible photometric fluctuations on much longer timescales (months) between observing seasons. Consequently, these bright, isolated MWDs were followed up as part of a long term observing campaign with the Liverpool Telescope (LT), also located in La Palma, between March 2005 and January 2007. The sample of stars is summarised in Table 4.1. Since these stars had previously been investigated for variability on short timescales over a week, they were not observed further in the survey using the INT (Chapter 2), apart from the weakly magnetic WD PG 0136+251 which was monitored on both short (Chapter 2) and long timescales.

To date, the longest period measured for an isolated MWD is 17.856 days for KUV 813-14, obtained from polarisation measurements (Schmidt & Norsworthy 1991). Longer periods have been inferred from changes in spectral features in individual spectra. In the case of G 77-50 (Farihi et al. 2011b), a possible rotation period of 28 – 33 days is measured. As previously mentioned, there are also MWDs that may be very "slow rotators", with rotational periods $\gtrsim$100 years, as no changes have been detected in polarisation measurements over decades of observations (West 1989). However, it is worth noting that these long spin periods are only suspected and have not actually been measured. The absence of variability could also be due to a symmetric magnetic field distribution about the spin axis along the line of sight, although it is unlikely they would all have the same alignment. Spruit (1998) predicted that efficient transport of angular momentum from the core to the outer envelope could produce slowly rotating cores with periods >10 years, however MWDs with spin periods on this time scale have not been detected. Four MWDs suspected to be these "slow rotators" are observed in this variability survey using the LT.

Table 4.1: List of 10 isolated bright MWDs observed with the LT.

Target	WD	No. of epochs used	V (mag)	B_p (MG)	T_{eff} (K)	Mass ($M_\odot$)	WD Age (Gyr)	P_{lit}	Refs
PG 0136+251 *	0136+251	4	15.8	$\lesssim$0.1	39640	1.20	0.75		1,2,3
EUVE J1439+75.0	1440+753	6	15.3	14.8	39500	0.9 – 1.2	0.005 – 0.3		4
PG 1658+441	1658+441	6	14.6	2.3	30510	1.31	0.38		1,5,3
G 240-72	1748+708	14	14.2	$\gtrsim$100	5590	0.81	5.86	$\gtrsim$100 yr	6,7,8,9
G 183-35	1814+248	6	16.9	~14	6500			~50 mins to few years	10,11
G 141-2	1818+126	8	15.9	~3	6340	0.26	0.93		8,12
G 227-28	1820+609	11	15.7	$\lesssim$0.1	4780	0.48	4.68		8,11
G 227-35	1829+547	4	15.6	170 – 180	6280	0.90	4.76	$\gtrsim$100 yr	13,8
Grw+70°8247	1900+705	17	13.2	320	16000	0.95	0.94	$\gtrsim$100 yr	14,15,8,6,7
GD 229	2010+310	9	14.9	520	18000	$\geq$1.0		$\gtrsim$100 yr	16,6,9,17

* PG 0136+251 was also observed on short timescales for photometric variability in Chapter 2. See Table 2.5 for the results from data taken with the INT.

REFERENCES.— (1) Schmidt et al. 1992, (2) Vennes 1999, (3) Liebert, Bergeron & Holberg 2005, (4) Vennes et al. 1999, (5) Liebert et al. 1983, (6) Angel 1978, (7) Angel et al. 1981, (8) Bergeron et al. 2001, (9) Berdyugin & Piirola 1999, (10) Putney 1995, (11) Putney 1997, (12) Greenstein 1986, (13) Putney & Jordan 1995, (14) Wickramasinghe & Ferrario 1988, (15) Jordan 1992, (16) Wickramasinghe et al. 2002, (17) Schmidt et al. 1996.

4.2 Observations

Observations of 10 bright ($V < 16$), isolated MWDs were conducted using the robotic 2.0 m Liverpool Telescope (LT) on La Palma, over four observing seasons, between March 2005 and January 2007. The targets were selected from a previous survey by Brinkworth et al. (2013), where the stars were found to be photometrically stable on short timescales (hours – one week), but showed possible long term modulations between observing seasons. A summary of the 10 MWDs observed is given in Table 4.1.

Observations were taken in the SDSS r' filter to minimise the differential extinction between the blue targets and the generally redder comparison stars. Exposures times ranged from 10 to 25 seconds. Sets of five exposures were taken consecutively (N in Table 4.2) in 2×2 binning, which were later co-added to achieve a signal-to-noise ratio (S/N) of approximately 500 for each target. This procedure meant low-amplitude variability could be detected in the target due to the high S/N ratio, without saturating brighter stars in the field-of-view. A detailed list of the observations can be found in Table 4.2.

For observations of each target to be carried out, the following criteria were specified as part of the observing strategy: the distance between the target and the moon had to be more than 30° apart, the target was within 60 minutes of the meridian (i.e. hour angles HA ranging from -1 to +1 hour), and observations were not taken during twilight. Targets could have been observed in bright time, with seeing conditions >1.3 arcseconds. Each target would be observed once a month, while visible, for four semesters, with the aim of collecting a sufficient number of data points per target (~15 epochs). However, as evident from Table 4.2, this number of epochs was not achieved for most of the targets, and some were observed substantially less. Furthermore, the minimum criteria for observing conditions was not adhered to in all cases, where some observations were taken during twilight or when the moon was less than 30° away from the target. In contrast, the minimum monthly interval between epochs was strictly followed, which meant variations on a timescale of less than two months could not be reliably tested.

Liverpool Telescope (LT)

The LT is a 2.0 m fully robotic, autonomous telescope located at the Observatorio del Roque de los Muchachos in La Palma, Spain (Steele et al. 2004). The optical CCD camera, RATCam, was used for the observations. It has a 4.6’ × 4.6’ field-of-view at 0.278 arcsec/pixel (for 2×2 binning). The LT focuses on rapid-response observations of unpredictable transient phenomena, small scale surveys and variability studies on timescales from seconds to years. The robotic nature of the telescope allowed spin periods of slowly rotating MWDs to be investigated, to build a more complete understanding of their period distribution.

Table 4.2: Detailed list of observations taken with the LT of the 10 isolated MWDs. *N* is the number of frames taken for that epoch. The date and Julian day are given for each epoch, along with the altitude of the observation and the weather conditions (including the seeing).

Target	Date	MJD-52000	*N*	Alt(°)	Conditions* (seeing)	Notes
PG 0136+251	2006 Jun 21	1908	5	26	Moon 17° away (1.2”)	not used (1)
	2006 Jul 22	1939	5	31	Good (1.0”)	
	2006 Aug 20	1968	5	72	(1.5”)	not used (2)
	2006 Sep 14	1993	5	66	Clear (1.0”)	
	2006 Oct 20	2028	5	66	Good (0.9”)	not used (2)
	2006 Nov 13	2053	5	69	(0.8”)	
	2007 Jan 14	2114	5	34	Cloud (2.0”)	
EUVE J1439+75.0	2005 Jun 15	1536	5	~68	(1.4”)	
	2005 Aug 16	1598	5	~30	(1.3”)	
	2006 Mar 18	1813	5	44	(1.2”)	
	2006 Apr 19	1845	5	44	(1.6”)	
	2006 May 17	1872	5	41	Twilight (1.3”)	not used (2)
	2006 Aug 15	1962	5	39	Twilight (1.6”)	
	2006 Sep 10	1988	5	30	(1.0”)	
	2006 Nov 10	2050	5	26	Twilight (1.7”)	not used (2)
PG 1658+441	2005 Apr 30	1490	5	~65	Good (1.1”)	
	2005 Jun 15	1536	5	~66	Good (1.0”)	not used (2)
	2005 Jul 15	1566	5	~74	Good (0.9”)	not used (2)
	2005 Aug 14	1596	5	~60	Good (0.9”)	not used (2)
	2006 Mar 18	1813	5	44	(1.2”)	not used (2)
	2006 Apr 27	1853	5	59	Some cirrus (1.1”)	
	2006 May 17	1873	5	60	(0.9”)	
	2006 Jul 15	1932	5	32	(1.0”)	
	2006 Aug 15	1962	5	69	Twilight (0.9”)	not used (2)
	2006 Sep 09	1988	5	29	(0.8”)	used (3)
	2006 Oct 21	2029	5	31	(0.9”)	
G 240-72	2005 May 07	1498	5	~42	(1.9”)	
	2005 Jun 05	1527	5	~40	Twilight (1.9”)	
	2005 Jul 05	1557	5	~48	Good (1.0”)	
	2005 Aug 04	1587	5	~41	Some cirrus (1.5”)	
	2005 Sep 03	1617	5	~30	(1.3”)	
	2005 Oct 10	1653	5	40	(1.5”)	used (4)
	2006 Mar 25	1820	5	39	(2.4”)	not used (1)
	2006 Apr 22	1847	5	27	(1.9”)	not used (2)

Table 4.2: *continued*

Target	Date	MJD-52000	N	Alt(°)	Conditions* (seeing)	Notes
	2006 May 23	1878	5	39	(1.9”)	
	2006 Jun 21	1907	5	42	Twilight (1.3”)	
	2006 Jul 21	1937	5	47	Twilight (1.0”)	
	2006 Aug 15	1963	5	39	Good (1.4”)	
	2006 Sep 18	1996	5	43	Good (1.2”)	
	2006 Oct 21	2029	5	40	Good (0.9”)	
	2006 Dec 01	2070	5	29	Twilight (1.5”)	not used (1)
	2006 Dec 31	2101	5	27	Twilight (3.1”)	
	2007 Jan 13	2114	5	29	(2.0”)	
G 183-35	2005 May 03	1493	5	~75	Twilight (1.0”)	not used (1)
	2005 Jun 21	1542	5	~82	Good (0.8”)	not used (2)
	2005 Jul 17	1568	5	~60	Twilight (0.7”)	not used (2)
	2005 Aug 16	1598	5	~83	Good (0.8”)	not used (5)
	2005 Aug 28	1610	5	~72	Clear	used (4)
	2006 Mar 20	1815	5	61	Good (1.1”)	
	2006 Jun 17	1904	5	60	Good (0.9”)	
	2006 Aug 14	1962	5	55	Good (0.8”)	not used (5)
	2006 Sep 10	1989	5	30	Good (1.1”)	
	2006 Oct 11	2019	5	28	Good (1.1”)	
	2007 Jan 19	2120	5	26	Twilight(1.3”)	
G 141-2	2005 Jun 01	1522	5	~73	(1.5”)	used (4)
	2005 Jun 21	1542	5	~72	(1.2”)	not used (2)
	2005 Jul 17	1568	5	~68	Twilight (0.8”)	
	2005 Aug 16	1598	5	~68	Good (0.9”)	used (4)
	2006 Mar 20	1815	5	56	Twilight (1.0”)	
	2006 Apr 27	1853	5	49	Some cirrus (1.4”)	
	2006 Jun 17	1904	5	59	Good (0.8”)	
	2006 Aug 14	1962	5	52	Good (0.9”)	not used (1)
	2006 Sep 10	1989	5	27	(1.2”)	
	2006 Oct 11	2019	5	40	Clear (1.2”)	
G 227-28	2005 Aug 30	1612	5	~55	(1.2”)	
	2006 Apr 23	1849	5	57	(1.3”)	
	2006 May 23	1879	5	50	(1.0”)	
	2006 Jun 21	1907	5	53	Good (1.0”)	
	2006 Jul 21	1937	5	54	Twilight (0.8”)	
	2006 Aug 15	1963	5	45	Good (0.9”)	
	2006 Sep 14	1993	5	26	Clear (1.2”)	
	2006 Oct 21	2029	5	46	Good (0.8”)	
	2006 Dec 03	2072	5	27	(1.1”)	used (3)
	2007 Jan 13	2114	5	29	Twilight (1.8”)	
	2007 Jan 13	2114	5	30	Twilight (1.8”)	
G 227-35	2006 Aug 15	1963	5	53	Good (1.0”)	
	2006 Sep 15	1993	5	42	Good (1.0”)	
	2006 Oct 21	2029	5	49	Good (0.8”)	
	2007 Jan 13	2114	5	26	Twilight (1.6”)	
Grw+70° 8247	2005 Mar 17	1446	5	~32	1.4”	
	2005 May 08	1498	4		(1.7”)	not used (6)
	2005 Jun 06	1527	5	~45	Twilight (1.5”)	
	2005 Jul 05	1557	5	~47	Good (1.0”)	
	2005 Aug 04	1587	5	~48	Some cirrus (1.5”)	
	2005 Sep 03	1616	5	~45	Cirrus (1.3”)	
	2005 Oct 10	1653	5	45	(1.3”)	
	2005 Nov 05	1679	5	32	Some cirrus (1.9”)	
	2006 Mar 25	1820	5	34	(1.6”)	
	2006 Apr 22	1847	5	26	Some cirrus (2.1”)	
	2006 May 23	1878	5	33	Poor seeing (2.4”)	used (4)

Table 4.2: *continued*

Target	Date	MJD-52000	N	Alt(°)	Conditions* (seeing)	Notes
	2006 Jun 21	1907	5	37	(1.6”)	
	2006 Jul 21	1937	5	45	Twilight (0.9”)	
	2006 Aug 15	1963	5	44	Good (1.2”)	
	2006 Sep 14	1993	5	31	Good (1.3”)	
	2006 Oct 21	2029	5	43	Good (0.9”)	
	2006 Nov 16	2055	5	26	Cirrus (1.9”)	
	2007 Jan 13	2114	5	26	Twilight (1.7”)	
GD 229	2005 May 02	1493	5	~79	Twilight (0.8”)	not used (1)
	2005 May 31	1521	5	~87	Twilight (1.7”)	
	2005 Jun 29	1551	5	~66	Some cirrus (1.1”)	not used (2)
	2005 Jul 23	1575	5	~85	(1.4”)	not used (2)
	2005 Aug 30	1612	5	~80	Some cirrus (1.0”)	
	2005 Oct 23	1666	5	77	Good (1.0”)	
	2006 Apr 06	1832	5	38	Good (1.0”)	
	2006 Apr 28	1854	5	57	(1.3”)	
	2006 Jun 21	1908	5	48	Good (1.1”)	
	2006 Jul 21	1937	5	47	Good (0.8”)	
	2006 Aug 20	1967	5	68	Twilight (1.2”)	not used (2)
	2006 Sep 14	1993	5	37	Good (1.1”)	
	2006 Oct 21	2029	5	70	Some cirrus (0.9”)	

Notes –
* Observing conditions were summarised from information in the FITS header and from the CONCAM archive, where CONCAM was a night time all-sky camera to monitor cloud coverage.
(1) This epoch of data was not used due to the poor quality of the images. Here, the data was perhaps taken in twilight, at low altitude/high airmass or when the moon was <30° away.
(2) This epoch of data was not used, because field rotation meant some of the comparison stars were no longer in the field-of-view.
(3) This epoch of data was used even though it was poor quality.
(4) This epoch of data was used despite stars showing slight trailing.
(5) This epoch of data was not used because the photometry was highly variable.
(6) This epoch of data was not used due to a telescope error.

4.3 Data Reduction and Analysis

The data were reduced with the LT pipeline which performed a bias subtraction, trimmed the overscan regions and flat-fielded the frames. However, this meant a more thorough and careful data reduction could not be carried out, as only the reduced frames were provided.

Photometry

Aperture photometry was performed on each of the targets and their respective comparison stars in the field using the STARLINK package, AUTOPHOTOM. The sky background level was estimated from the clipped mean of the pixel values in the annulus around each star. The uncertainty in the count measurements was calculated from the sky variance. To select the optimal size aperture for the photometry, the signal-to-noise (S/N) ratio was determined for a range of aperture sizes, as shown in Figure 4.1. As the aperture size increased, the S/N ratio increased, until it reached an optimal aperture width, where the S/N then levelled off and started to decrease due to the additional noise in the enlarged aperture. The aperture size was approximately twice the average seeing (FWHM) for each of the epochs (Naylor 1998). The aperture size was kept constant for frames within the same epoch, but was allowed to vary for different epochs. This meant sizeable differences in the seeing/weather conditions were accommodated. The aperture sizes ranged from 5 to 22 pixels, where an aperture of 7 pixels was the most common. Differential photometry was performed for each MWD, where the target flux count was divided by the sum of fluxes from the comparison stars. To combine the five frames of data taken at each epoch, the mean flux of each star was calculated and used to determine the differential flux for the epoch.

Selecting Comparison Stars

The comparison stars for each target were also investigated for any photometric fluctuations. If comparison stars were found to exhibit variable behaviour, they were removed from the analysis. A comparison star was also eliminated if it was saturated, too faint, or if it displayed considerable scatter on the order of a few percent greater than the target. A

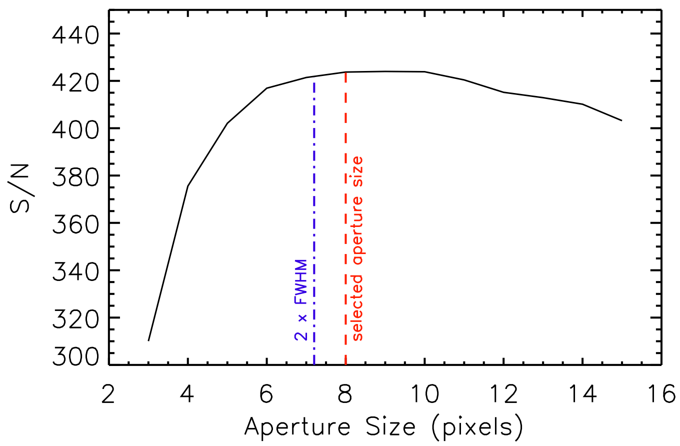

Figure 4.1: An example of the signal-to-noise (S/N) ratio with increasing aperture size for the MWD G 240-72 observed in July 5, 2005. The red dashed line indicates the aperture size used for the analysis and the blue dot-dashed line represents the aperture width at 2×FWHM, where the FWHM is a measure of the seeing.

star was defined as "too faint" when the S/N ratio was less than 100 (approximately equal to 1% uncertainties), as these faint stars usually added the most scatter to the differential flux. Even if some targets had a S/N $<$ 100, similarly faint comparison stars were still avoided to reduce additional noise in the differential flux. Unfortunately, in most cases, it was not possible to select comparison stars that showed scatter of $<\pm 1\%$ and still have any stars remaining.

An example illustrating how the comparison stars were selected for G 240-72 is shown in Figures 4.2 and 4.3. In the first instance, the target flux was divided by the flux of each comparison star separately (Fig. 4.2). If the light curves looked similar using different comparison stars, then they were assumed to be photometrically stable and that the observed variations were perhaps associated with the target MWD. On the other hand, if light curves appeared drastically different, the comparison star was possibly varying. Light curves including faint comparison stars (of a small S/N ratio) contributed more scatter and larger uncertainties to the differential light curves (e.g. bottom panel in Fig. 4.2). When the comparison stars C1 and C3 were used to calculate the differential flux for G 240-72 in Figure 4.2, the light curves looked similar, and therefore these stars were considered further as the comparison stars for the differential photometry. Figure 4.3 shows

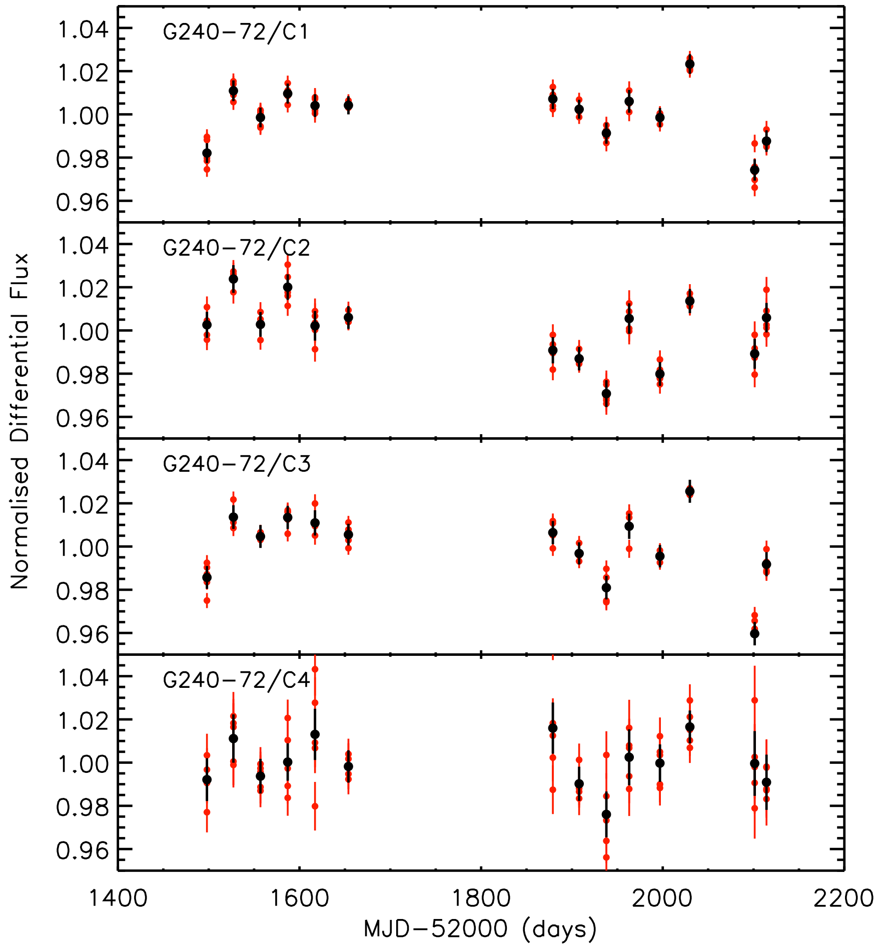

Figure 4.2: Differential light curves of G 240-72, where the differential flux was calculated as the target flux divided by the flux of one of the comparison stars. The two light curves using the flux from C1 and C3 were very similar, suggesting the two comparison stars were probably photometrically stable and that the variations in the light curve were most likely associated with G 240-72.

light curves of G 240-72 with respect to the sum of the fluxes of C1 and C3, along with the two other comparison stars. This clearly demonstrated that C2 was not appropriate as a comparison star, since it displayed a long term photometric variation, while C4 showed considerably more scatter in the light curve. Finally, in the case of G 240-72, C1 and C3 were selected as the comparison stars. This procedure was carried out for all of the MWDs in the sample to find appropriate comparison stars for the differential photometry.

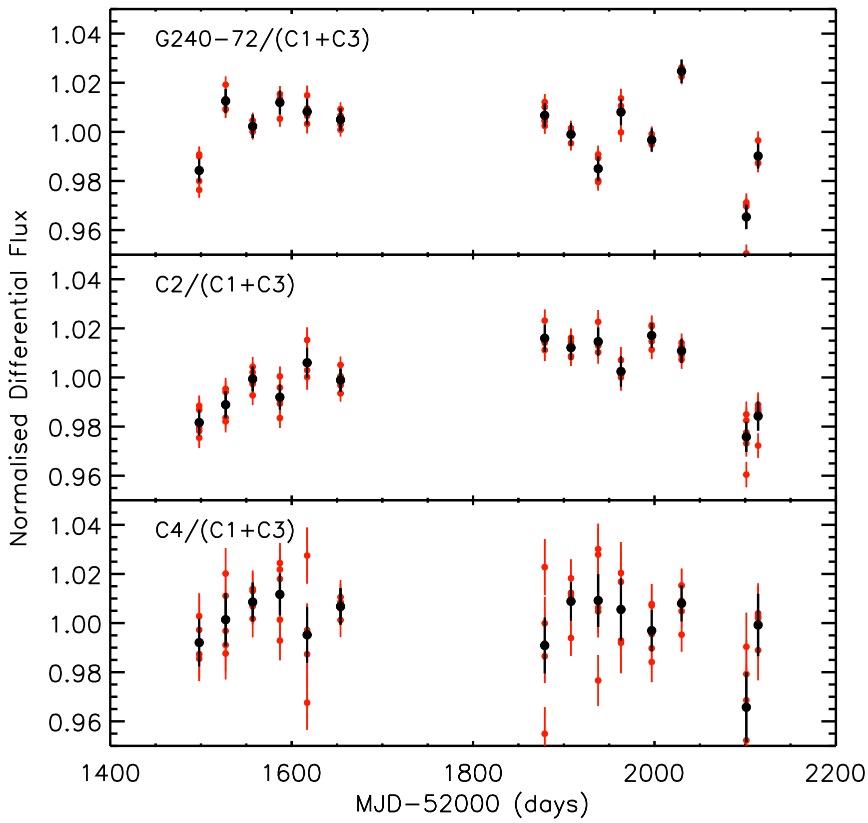

Figure 4.3: Differential light curves of stars in the G 240-72 field-of-view with respect to the same comparisons to determine the most stable stars for the analysis. The red points represent all the data taken at each epoch, while the black data points are the mean fluxes for the epochs. *Top panel:* Light curve for G 240-72, where the differential flux is calculated as target/(C1+C3). *Middle panel:* Differential light curve of C2/(C1+C3). C2 shows a long term photometric variation, and so is not used as a comparison star to G 240-72. *Lower panel:* Differential light curve of C4/(C1+C3). C4 is also not used as a comparison star, because the differential flux exhibits more scatter than the other light curves since it is the faintest star. The comparison stars C1 and C3 are selected for the differential analysis for G 240-72.

Periodicity Analysis

The light curves were analysed using the same technique as outlined in Chapter 2 (§2.4.1), where a floating-mean periodogram (Eq. 2.1) was used to determine whether any periodicity was present within the frequency ranged searched[1]. The frequency range changed for the different targets, depending on the sampling rate for the particular target. The maximum frequency in the range was based on the Nyquist frequency, $f_{Ny} = 1/2T$. However, as discussed in §2.4, the Nyquist frequency was no longer applicable if the data were

[1]In the case of G 240-72, a Fourier Transform was also used as an additional test for variability. The same method was used as outlined in Chapter 3, utilising *Period04* (Lenz & Breger 2005).

unevenly sampled, but given that the data were sampled so sparsely, I felt a conservative frequency range was the best option.

The significances of the "best-fit" periodicities were assessed using the Monte Carlo tests and analytical approach, described previously in §2.4.2 and §2.4.3. The detection threshold was set to a $FAP \leq 0.01$, where a small FAP statistic implied there was a very small probability that noise fluctuations alone would cause a signal greater than that obtained from the real data.

4.4 Results

Significant long term photometric variability is not detected in any of the ten MWDs studied in this sample. Too few data points in the light curves have been a considerable limitation for determining any period of variability. A summary of the results for each target is given in Table 4.3 and each MWD is discussed in more detail in the following subsections.

Table 4.3: Summary of results for the 10 isolated MWDs in the long term variability study using the LT. The best-fitting period corresponds to the frequency at the minimum χ^2 value in the periodogram, while the uncertainty estimate for the period is given by a change in χ^2 of 4 (equivalent to 2σ) from the minimum. Alternatively, where this is not appropriate, the 2σ range of periods from the χ^2 minimum is given instead. The reduced χ^2 is given for the best-fitting period sine curve fit and for a constant fit. The calculation of the FAPs is detailed in Chapter 2 (§2.4.2 and §2.4.3). The significance is set at $FAP \leq 0.01$ (a 99% detection threshold). z_{max} is the maximum power in the periodogram (at the best-fitting frequency) and $\overline{z}$ is the mean power.

Target	Best-fitting Period	Sine fit reduced χ^2	Constant fit reduced χ^2	z_{max}	False Alarm Probability		$\overline{z}$	FAP
					MC	Analytic		
PG 0136+251	100 – 10000 d	0.00	0.80	0.00	1.000	1.000000	0.00	1.000
EUVE J1439+75.0	56 – 10000 d	0.14	1.46	16.73	0.577	0.538073	6.90	0.596
PG 1658+441	33 – 10000 d	0.17	1.00	9.14	0.935	0.913852	4.71	0.896
G 240-72	31 – 51 d	6.05	9.11	3.89	0.946	0.815939	1.42	0.883
G 183-35	50 – 10000 d	0.01	0.37	155.00	0.035	0.001779	46.71	0.053
G 141-2	51 – 457 d	0.21	1.62	19.14	0.242	0.124656	7.55	0.169
G 227-28	74^{+22}_{-13} d	1.22	3.65	9.00	0.343	0.134273	3.32	0.331
G 227-35	50 – 10000 d	0.00	1.25	0.00	1.000	1.000000	0.00	1.000
Grw+70°8247	79 – 388 d	1.85	2.37	3.20	0.972	0.627690	1.17	0.982
GD 229	$84.0^{+2.9}_{-3.3}$ d	2.50	4.28	4.36	0.855	0.649483	1.53	0.816

4.4.1 PG 0136+251

PG 0136+251 was removed from the list of MWDs by Kawka et al. (2007). This decision was based on findings from Schmidt et al. (1992), where there was only negligible evidence for a magnetic field ($B \leq 0.1$ MG), but noted a low-field strength on the order of kilo-Gauss could still be present. Otherwise, it is a hot ($T_{\rm eff} \sim 39,000$ K) and ultra-massive ($M \sim 1.2$ $M_{\odot}$) DA WD. There has been some discrepancy in the literature regarding the temperature and mass estimates for the star (Schmidt et al. 1992; Vennes et al. 1997).

The finder chart in Figure 4.4 highlights the target and comparison stars. C1 and C2 are used as the comparison stars for the differential photometry. Comparison star C3 is eliminated because it is too faint (S/N ~ 40) and introduces additional scatter into the light curve. Suitable data of PG 0136+251 are only obtained on four epochs between July 2006 and January 2007. As a result, no conclusions can be made from the sparse data set. The differential light curve in Figure 4.5 (*left*) appears flat and a constant fit to the data (with a reduced χ^2 of 0.80) gives a much more appropriate fit than the best-fitting sine curve (with a reduced χ^2 of 0.00). There are no significant features in the periodogram (Fig. 4.5, *right*) and nearly all of the χ^2 values lie within the 1σ uncertainties from the minimum χ^2. Unsurprisingly, the FAP statistics are very high at 1.00. To conclude, there is no evidence of photometric variability in this sparse data set of PG 0136+251, although it should be observed more thoroughly at a higher sampling rate. There is still some uncertainty as to whether it is even a MWD. PG 0136+251 is also observed over a week with the INT (in Chapter 2), where no significant photometric variability is detected (FAP > 0.01) at an amplitude of ~1%.

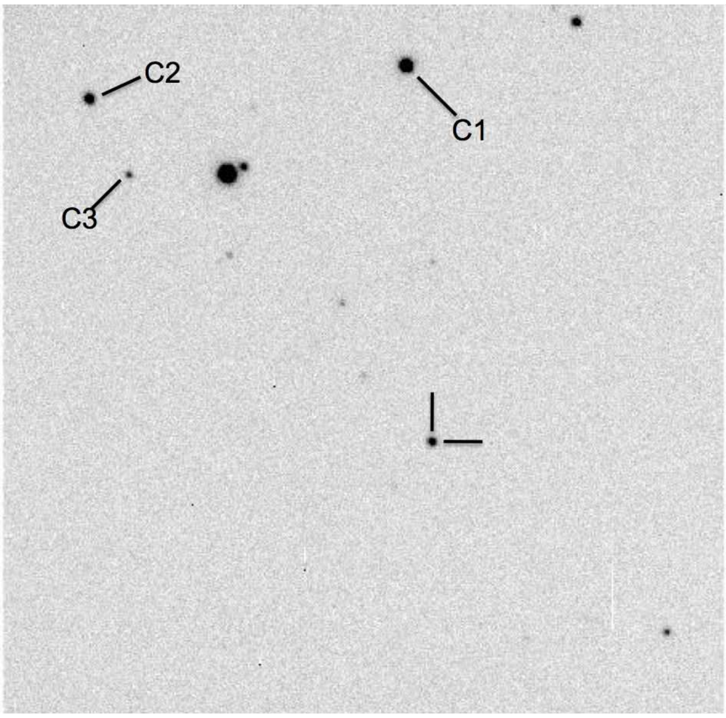

Figure 4.4: Finding chart for PG 0136+251 indicating three comparison stars. Comparison star C3 is too faint (S/N ~ 40) and is excluded from the photometry.

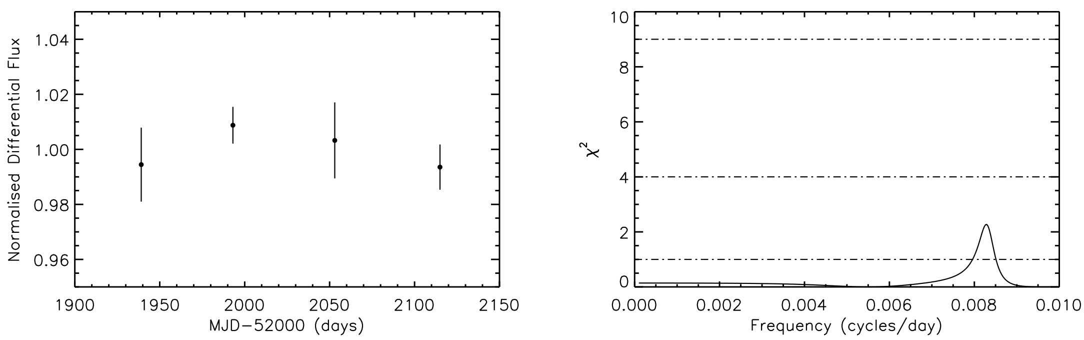

Figure 4.5: *Left:* Normalised differential light curve of PG 0136+251, where the differential flux is calculated as target/(C1+C2). *Right:* Corresponding periodogram, where there is no obvious minimum in the χ^2. The dot-dashed lines indicate a change in χ^2 of 1, 4 and 9 (representing 1σ, 2σ and 3σ uncertainties respectively).

4.4.2 EUVE J1439+75.0

The star field of EUVE J1439+75.0 is shown in Figure 4.6, where the MWD and comparison stars are marked. Comparisons C1, C3 and C4 are used for the differential analysis, while the two faintest stars C2 and C5 are excluded to reduce the amount of additional scatter in the light curve. However, all of the comparison stars show large amounts of scatter in the flux (±2%). In this case, any photometric variability that is detected, may belong to a comparison star rather than the target. In Figure 4.7 (*right*), the entire periodogram lies within the 3σ uncertainty boundary from the χ^2 minimum at a frequency of 0.002092 cycles/d ($P = 478$ d), equivalent to the duration of the observations. There are many minima in the periodogram with similar χ^2 values across the frequency range. A constant fit to the data set gives a reduced χ^2 of 1.46. The FAP estimates are high (FAP ~ 0.58), well above the threshold for a significant detection. However, this is not surprising considering the small number of data points ($N = 6$) collected over a period of 17 months.

This MWD is a known, unresolved double degenerate (Vennes, Ferrario & Wickramasinghe 1999). Their analysis, using optical spectroscopy, reveals the system to consist of a hot, non-magnetic DA WD and a magnetic DA WD. The MWD is massive at $M = 0.88-1.19\ M_{\odot}$, hot ($T_{\rm eff} = 20,000-50,000$ K) and has a field strength of 14−16 MG. Assuming a maximum separation of 1.95 arcsec (7 pixels) based on the MWD and WD being unresolved, an orbital separation between the two WDs is determined as 244 AU at a distance of 125 pc (Vennes, Ferrario & Wickramasinghe 1999), or 197 AU at 101 pc (Farihi, Becklin & Zuckerman 2008). Therefore using Kepler's third law, an upper limit to any likely orbital period is 2550 – 2920 years using a total mass for the WDs as 2.24 – 1.7 $M_{\odot}$ (Vennes, Ferrario & Wickramasinghe 1999) at 125 pc (or 1850 – 2120 years at 101 pc). Such a long orbital period would not be detectable on any reasonable timescale.

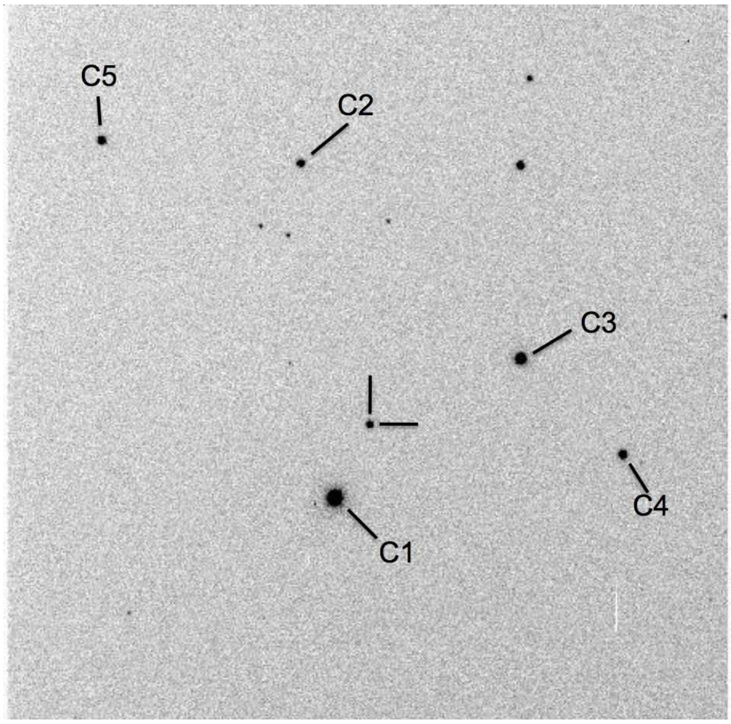

Figure 4.6: EUVE J1439+75.0 finding chart with five comparison stars. C1, C3 and C4 are used for the differential analysis, and C2 and C5 are eliminated.

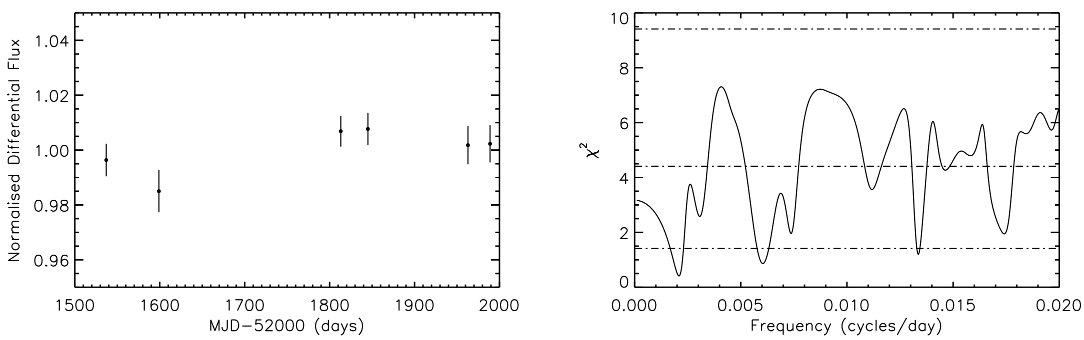

Figure 4.7: *Left:* EUVE J1439+75.0 normalised differential light curve, where the differential flux is calculated using target/(C1+C3+C4). *Right:* Periodogram with the global minimum occurring at a frequency of 0.002092 cycles/d (P = 478 d), equivalent to the length of the observations. The dot-dashed lines indicate a change in χ^2 of 1, 4 and 9 (i.e 1σ, 2σ and 3σ uncertainties respectively).

4.4.3 PG 1658+441

This MWD was first discovered as part of the Palomar – Green Survey (Green et al. 1986). A magnetic field was measured from the Zeeman splitting of the Balmer lines as 2.3 MG (Liebert et al. 1983), with a pure hydrogen atmosphere at $T_{\rm eff} = 30,000$ K. It is one of the most massive MWDs known at $1.31 M_{\odot}$ (Schmidt et al. 1992). Brinkworth et al. (2013) observed PG 1658+441 for photometric variability, although they could not draw any conclusions, as there was only one stable comparison star and therefore any modulations were possibly from the comparison star instead of the target. A mechanism to cause photometric variability in PG 1658+441 would be unknown, as it is too hot for star spots to form in the presence of a partially convective atmosphere and its magnetic field strength is too weak for magnetic dichroism to be a factor.

Figure 4.8 shows the PG 1658+441 star field with the comparison stars for the analysis. Only comparison stars C2 and C4 are used for the differential photometry, as C1 shows variations between observing seasons of ∼3% and C3 is faint (S/N ∼ 50), exhibiting considerable scatter in the differential flux. There are only a few data points ($N = 6$) in the differential light curve (Fig. 4.9, *left*). No significant periodicity is detected in the periodogram analysis (Fig. 4.9, *right*), where the entire floating-mean periodogram lies within the 3σ uncertainty limits from the χ^2 minimum. In addition, there are a few aliases of comparable χ^2 across the frequency range searched. A constant fit to the data points provides an equally suitable fit (with a reduced χ^2 of 1.00) as the best-fitting sine curve. The FAP estimates are very high at ∼ 0.9, indicating that any fluctuations are most likely due to random noise.

Similar to RE J0317-853, PG 1658+441 may also be a product of a double-degenerate merger (Schmidt et al. 1992). In this scenario, the MWD is perhaps expected to rotate rapidly and exhibit photometric or magnetic field fluctuations, but there is no evidence so far of this behaviour. However, García-Berro et al. (2012) propose the variety of spin periods can be explained by the alignment of the spin and magnetic axes, and where slow rotation is due to the two axes being nearly perpendicular, efficiently braking the remnant by magnetic dipole radiation.

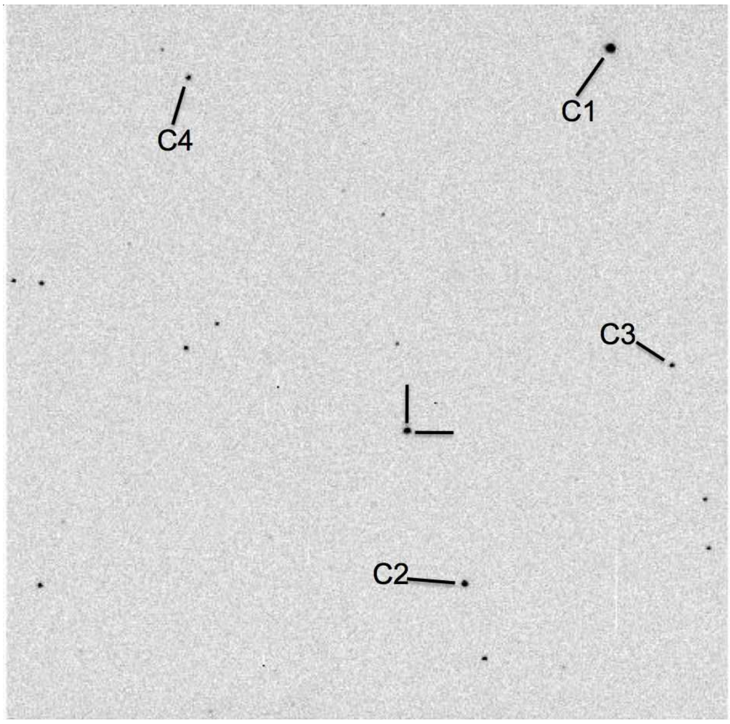

Figure 4.8: Finding chart for PG 1658+441 with four comparison stars. Only comparison stars C2 and C4 are used for the differential photometry, as C1 shows photometric modulations of ~3% between observing seasons and C3 is too faint (S/N ~ 50), contributing considerable scatter.

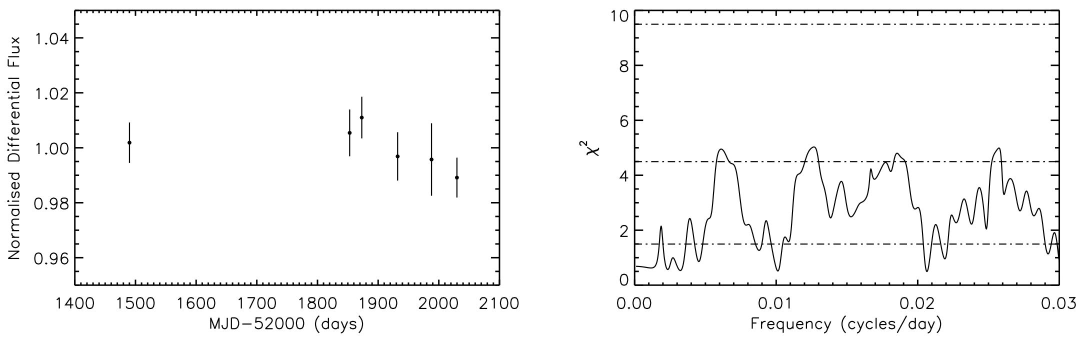

Figure 4.9: *Left:* PG 1658+441 normalised differential light curve with data taken between April 2005 and October 2006. *Right:* The corresponding periodogram for PG 1658+441. The minimum χ^2 occurs at a frequency of 0.020657 cycles/d (P = 48.41 d), although there are many aliases present. The dot-dashed lines indicate a change in χ^2 of 1, 4 and 9 (equivalent to 1σ, 2σ and 3σ errors respectively).

4.4.4 G 240-72

G 240-72 has long been suspected to be a very slow rotator. Berdyugin & Piirola (1999) reported the detection of long term variations in its polarisation in observations obtained in November 1996 and 1997, in comparison with measurements by Angel et al. (1974) and West (1989). They measured modulations on a timescale of more than 20 years, which implied a possible rotational period of ~200 years. This MWD has a helium-dominated atmosphere, cool effective temperature ($T_{\rm eff}$ = 5590 K, Bergeron et al. 2001) and high magnetic field strength ($B \gtrsim 100$ MG, Angel 1978).

No evidence for short term variability was found by Brinkworth et al. (2013), however they did report an increase in flux of ~2.5% over 10 months. Consequently, to investigate periods around a year, G 240-72 was observed from May 2005 until January 2007 for signs of photometric variability. The light curve shows significant modulations ($4-5$% peak-to-peak, see Fig. 4.11), although a period of variability is not constrained with the current data. There are many aliases in the periodogram (Fig. 4.12, *left*), with the minimum χ^2 occurring at a frequency of 0.019769 cycles/d (a period of 50.58 d). Similarly, the FT of G 240-72 in Figure 4.12 (*right*) has a frequency of 0.018176 cycles/d (P = 55.02 d) at the maximum amplitude. This peak is above the 3σ noise level threshold, indicating G 240-72 may be variable above the noise. Furthermore, the peak amplitude in the FT of the comparison stars light curve (Fig. 4.13, *right*) is below the 3σ noise level from the FT for the target light curve. The light curve of the comparison stars is stable at an amplitude of ~±1%. The features in the periodogram analysis of the comparison stars (Fig. 4.13) are not replicated in the periodogram analysis of G 240-72 (Fig. 4.12), illustrating the peaks at higher frequencies for the comparison stars are not influencing the possible periodicity in the target light curve. Despite the target light curve displaying clear signs of photometric variability, the FAP results suggest the period detected is not significant with a FAP $\approx$ 0.9 (see Table 4.3). In conclusion, G 240-72 may be photometrically variable over months, but a period has not been determined.

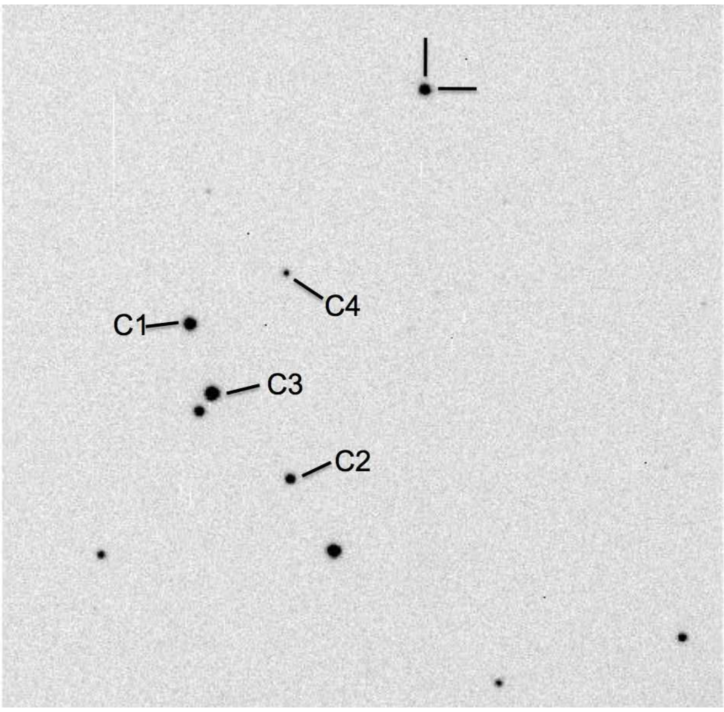

Figure 4.10: Finding chart for G 240-72 with four comparison stars. C2 is eliminated from the analysis because it displays long term variations (Fig. 4.3), and C4 is too faint to use (since its S/N ratio is a factor of four less than the S/N of the target).

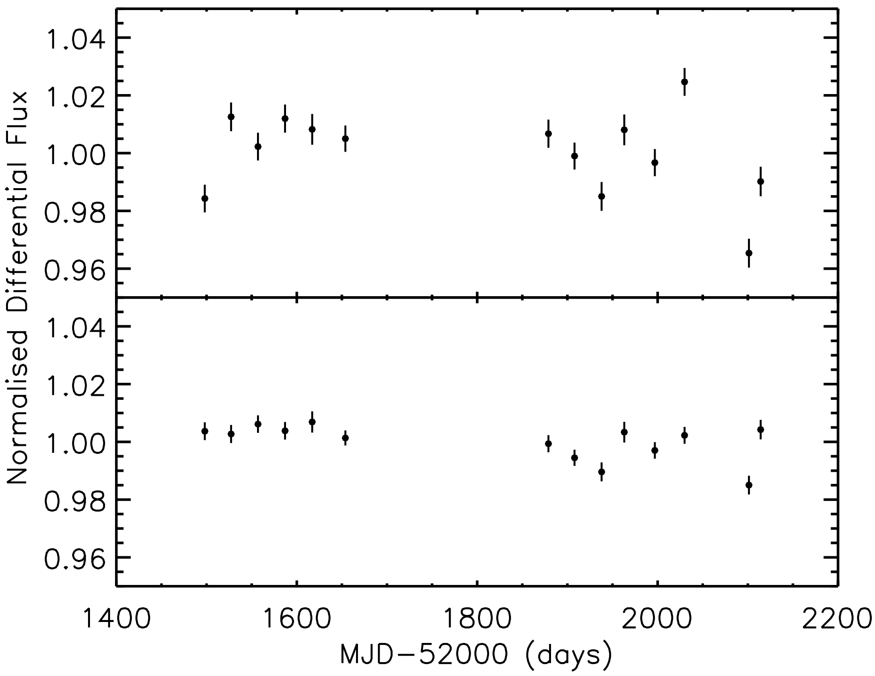

Figure 4.11: *Top panel:* Normalised differential light curve of G 240-72, where the differential flux is calculated using target/(C1+C3). *Lower panel:* Normalised differential light curve of the comparison stars, where the differential flux is determined from C1/C3.

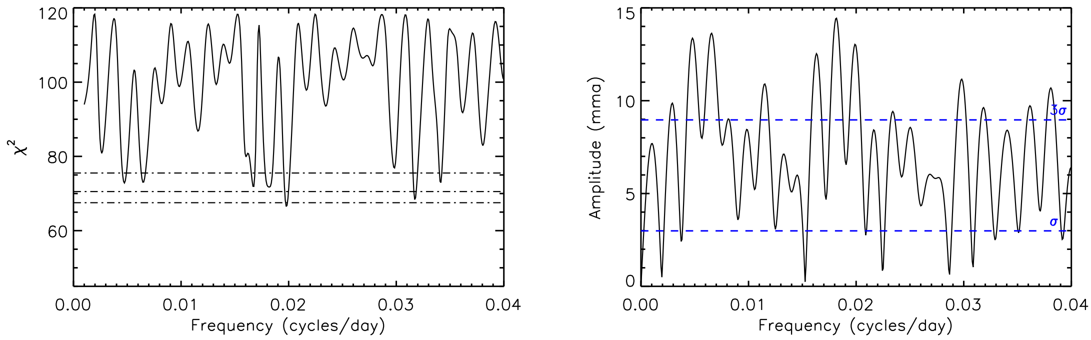

Figure 4.12: *Left:* Floating-mean periodogram for the G 240-72 light curve. The frequency at the minimum χ^2 is 0.019769 cycles/d (P = 50.58 d). The dot-dashed lines indicate a change in χ^2 of 1, 4 and 9 (1σ, 2σ and 3σ uncertainties respectively). *Right:* FT of the G 240-72 light curve. The maximum peak has a frequency at 0.018176 cycles/d (P = 55.02 d) and is above the 3σ noise level. The dashed lines indicate the σ and 3σ noise level. The amplitude is given in units of milli-modulation amplitude (mma), meaning 10 mma corresponds to 1%.

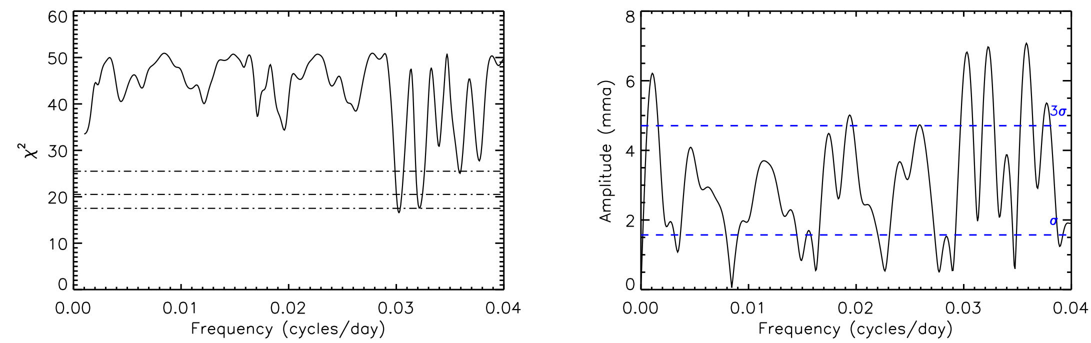

Figure 4.13: Same analysis as above but for the light curve of the G 240-72 comparison stars C1/C3. *Left:* Floating-mean periodogram for the G 240-72 comparison stars light curve. The frequency at the minimum χ^2 is 0.03025 cycles/d (P = 33.06 d), corresponding to the sampling rate of the observations. The dot-dashed lines indicate a change in χ^2 of 1, 4 and 9 (representing 1σ, 2σ and 3σ uncertainties respectively). *Right:* FT of the G 240-72 comparison stars light curve. The maximum peak has a frequency at 0.035823 cycles/d (P = 27.92 d). The light curve of the comparison stars is stable at an amplitude of ~±1%. The dashed lines indicate the σ and 3σ noise level. The amplitude is given in units of milli-modulation amplitude (mma), meaning 10 mma corresponds to 1%.

4.4.5 G 183-35

The magnetic field strength of G 183-35 was first measured by circular spectropolarimetry by Putney (1995), where the dipole field strength was estimated as 14 MG. Putney (1997) later postulated that G 183-35 was probably rotating with a period between 50 minutes and a few years, based on changes in the shape of the σ-components in the polarisation between observing seasons. By contrast, Brinkworth et al. (2013) found no evidence of photometric variability on timescales less than a year.

Four comparison stars (C2, C4, C5 and C6 as marked in Fig. 4.14) are used for the differential photometry, while comparisons C1 and C3 are eliminated. C1 exhibits a high degree of scatter (>4%) in comparison to the other stars, which dominates the differential flux because it is the brightest star in the field. C3 adds further uncertainty to the differential flux because it is the faintest comparison star (S/N ~ 70), comparable to the MWD. However, since the target is so faint in contrast to the comparison stars, the light curve of G 183-35 shows scatter of ±2-3%. The data points in the differential light curve (Fig. 4.15, *left*) have large uncertainties (±2%) and it is clear that a constant fit to the data is more suitable than a sine fit (Table 4.3). The entire periodogram is within the 2σ uncertainty boundary from the global χ^2 minimum (Fig. 4.15, *right*). The FAPs are above the significance threshold. In conclusion, no photometric variability is found in this data set for G 183-35.

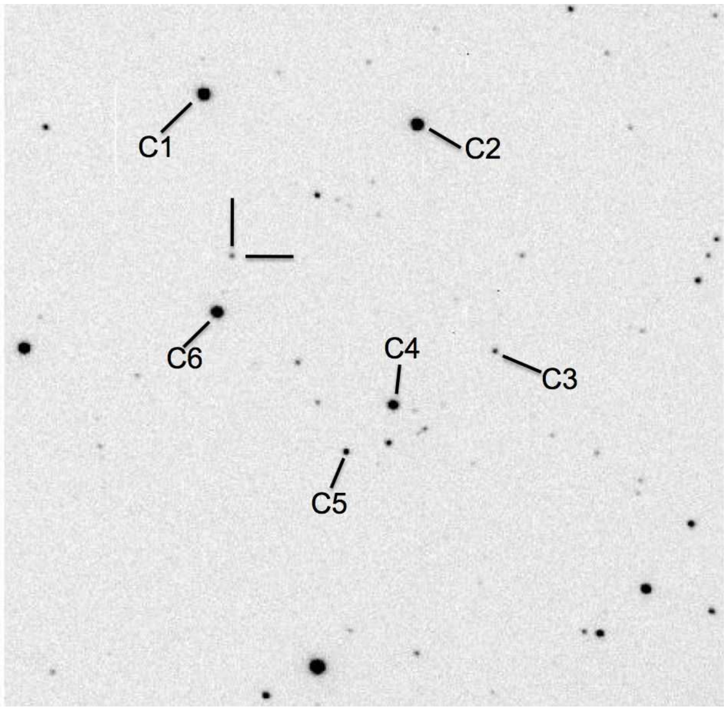

Figure 4.14: Finding chart for G 183-35 with six comparison stars. All of the comparison stars are used in the analysis, apart from C1 and C3, which both contribute a large degree of scatter to the light curve.

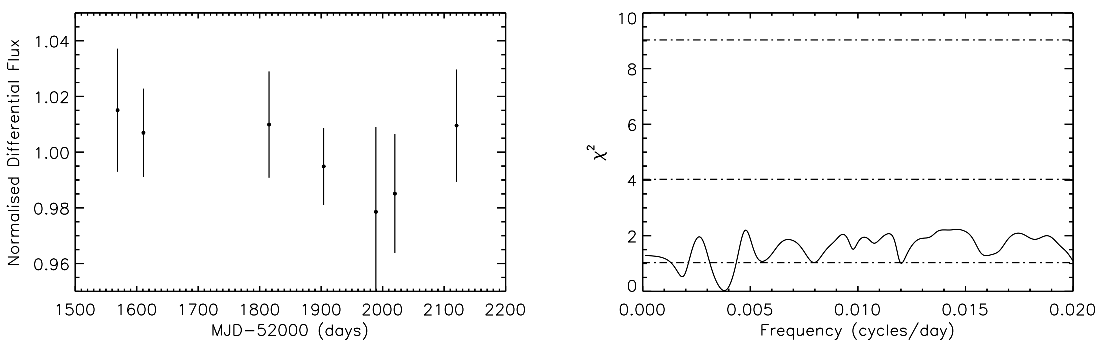

Figure 4.15: *Left:* G 183-35 normalised differential light curve, observed between July 2005 and January 2007. *Right:* The floating-mean periodogram of the G 183-35 light curve, where the dot-dashed lines indicate a change in χ^2 of 1, 4 and 9 (1σ, 2σ and 3σ errors respectively).

4.4.6 G 141-2

A magnetic field ($B \sim 3$ MG) was first measured for G 141-2 by Greenstein (1986) from line broadening in its spectra. It is a cool MWD ($T_{\rm eff}$ = 6340 K), has a very small mass at 0.26 $M_\odot$ and is suspected to be an unresolved double-degenerate. Bergeron et al. (1997) suggested G 141-2 was an unresolved binary consisting of a hot DA and a cool DC, where subsequent observations revealed a split, asymmetric Hα line. Meanwhile, Putney (1997) found no evidence of splitting in their spectra, nor any polarised Zeeman σ-components. Consequently, as the star rotates it is possible that its field strength and structure changes, so at particular phases the Hα line splitting is more noticeable than at other times. This is a reasonable assumption, since Külebi et al. (2009) illustrate that MWDs can have complex field structure distributions.

Previous studies of G 141-2 to search for photometric variability were not able to conclude whether the MWD was variable or not, due to the amount of fluctuations exhibited by the comparison stars (Brinkworth et al. 2013). However, their observations indicated that variability on timescales less than 10 months was unlikely and that it was probably varying over years.

As a result, G 141-2 has been observed on eight occasions between June 2005 and October 2006 to search for long term fluctuations in the flux. Figure 4.16 shows the MWD and the comparison stars in the field-of-view. The comparison stars C2, C3, C5 and C6 are used to calculate the differential flux. C1 and C4 are excluded from the analysis because they both show large amounts scatter in the differential flux of > 4%. The light curve is shown in Figure 4.17 (*left*). The majority of the periodogram lies within the 3σ uncertainties of the χ^2 minimum (Fig. 4.17, *right*). There are many aliases in the periodogram, but none of the signals are significant. Finally, the FAPs are above the threshold, indicating there is no significant periodicity present in the light curve and that any variability is probably due to noise fluctuations.

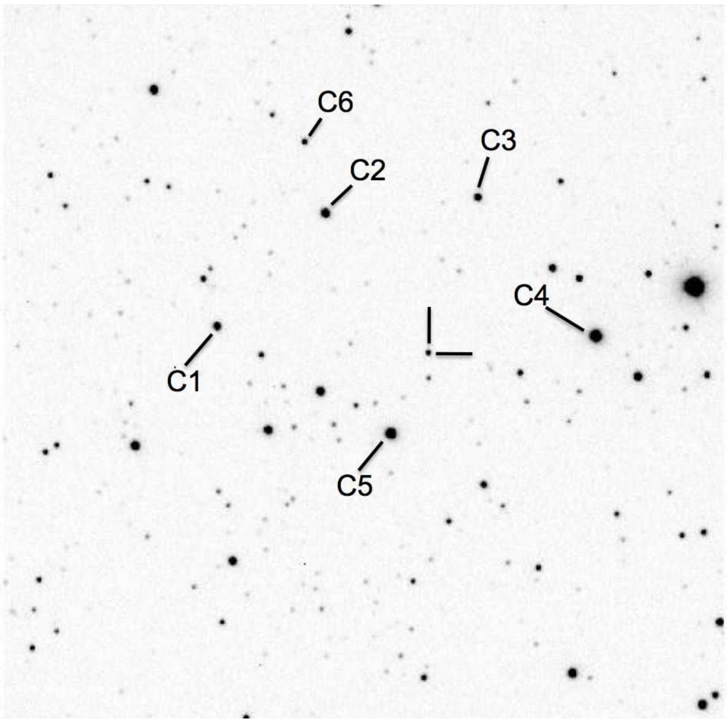

Figure 4.16: Finding chart for G 141-2 with six comparison stars marked. Only C2, C3, C5 and C6 are used for the analysis, as both C1 and C4 show large amounts of scatter in the flux (> 4%).

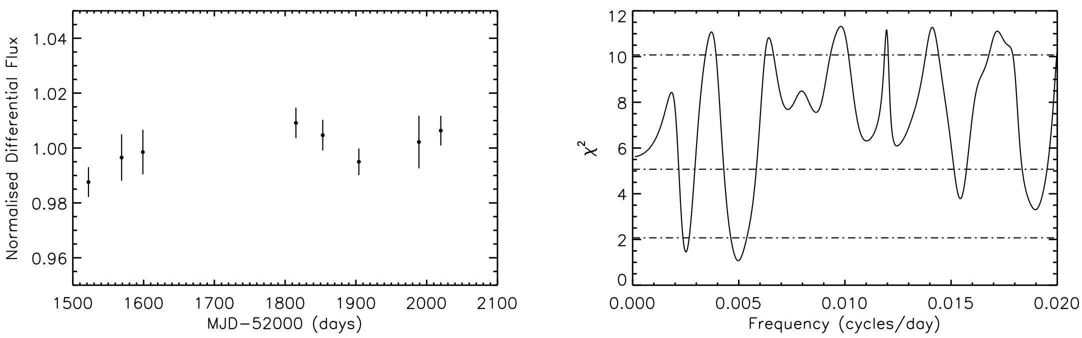

Figure 4.17: *Left:* G 141-2 normalised differential light curve (target/(C2+C3+C5+C6)) with data taken between June 2005 and October 2006. *Right:* Periodogram of the G 141-2 light curve, with the χ^2 minimum occurring at a frequency of 0.004964 cycles/d (P = 201.43 d). The dot-dashed lines indicate a change in χ^2 of 1, 4 and 9 (representing 1σ, 2σ and 3σ uncertainties respectively).

4.4.7 G 227-28

G 227-28 has a cool effective temperature ($T_{\rm eff}$ = 4780 K), helium atmosphere and has a low mass for a MWD at 0.48 $M_\odot$ (Bergeron et al. 2001). Putney (1997) found no detectable circular polarisation for G 227-28, while Wickramasinghe & Ferrario (2000) later considered it to be a possible MWD. Bergeron et al. (2001) reported that it has a weak field strength of ≤ 0.1 MG. G 227-28 was observed on short timescales for photometric variability (Brinkworth et al. 2013), but a period was not obtained, although they reported detecting a change in differential flux of 3% over a year. Consequently, the MWD was observed a total of nine times for long term fluctuations as part of this survey between August 2005 and January 2007.

The MWD and comparison stars are highlighted on the finder chart given in Figure 4.18. C2 and C5 are excluded from the analysis, as C2 is saturated and C5 is too faint (the S/N is a factor of two less than the target's S/N), introducing additional scatter into the light curve. However, the remaining comparison stars still show a considerable amount of scatter, which could be the cause of the modulations in the differential light curve (Fig. 4.19, *left*). There appears to be a general increase in the differential flux over the observed time. However, the data sampling is not sufficient to determine whether this variation is real or not. The minimum in the periodogram (Fig. 4.19, *right*) has a frequency of 0.01345 cycles/d (a period of 74±17 d). A sine fit, using the best-fit frequency, gives a more reasonable fit (with a reduced χ^2 of 1.22) than a constant fit to the data (with a reduced χ^2 of 3.65). Nevertheless, the FAP estimates are large at FAP $\sim$ 0.3, which is above the threshold for a significant detection.

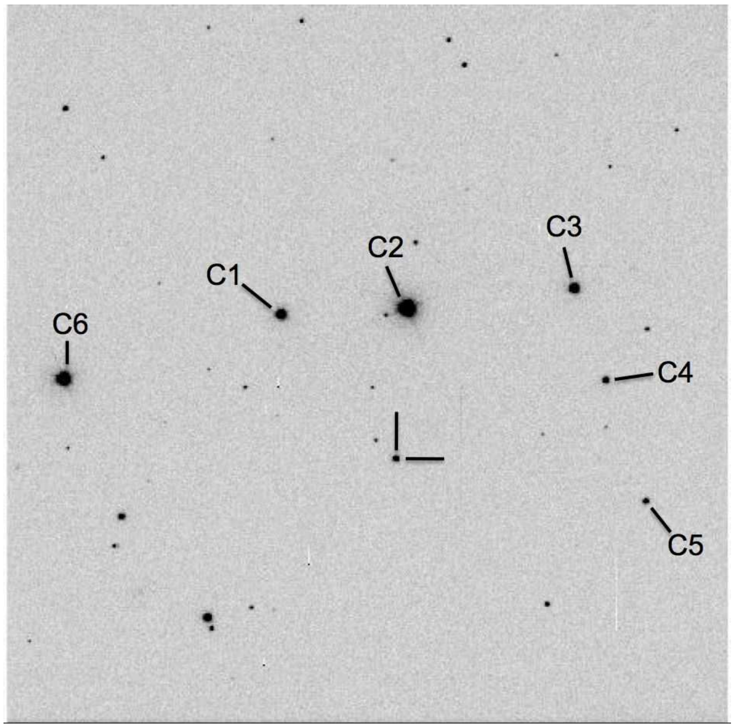

Figure 4.18: Finding chart for G 227-28 with six comparison stars marked. Comparison stars C1, C3, C4 and C6 are used for the differential photometry analysis, while C2 and C5 are eliminated from the analysis because C2 is saturated and the S/N ratio of C5 is approximately a factor of two less than the target's S/N.

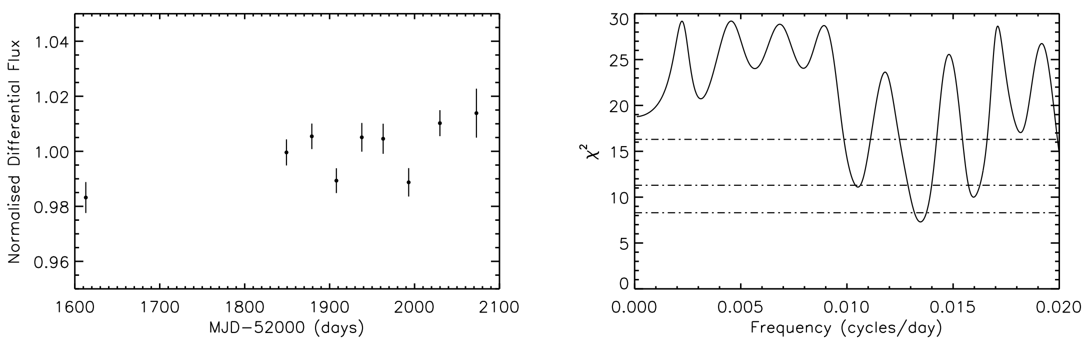

Figure 4.19: *Left:* G 227-28 normalised differential light curve (target/(C1+C3+C4+C6)). *Right:* Floating-mean periodogram, with the minimum χ^2 at a frequency of 0.01345 cycles/d ($P = 74 \pm 17$ d). The dot-dashed lines indicate a change in χ^2 of 1, 4 and 9 (1σ, 2σ and 3σ errors respectively).

4.4.8 G 227-35

A high magnetic field strength of 170 – 180 MG was determined by Putney & Jordan (1995) using linear and circular spectropolarimetry observations to obtain a suitable model for the field strength and structure. The precise atmospheric composition of G 227-35 is uncertain. Putney & Jordan (1995) used a hydrogen-rich magnetic model to estimate the field strength, while Bergeron et al. (2001) used a helium atmospheric model to fit the spectra and estimated the temperature and mass as $T_{\rm eff} = 6280\,{\rm K}$ and $M = 0.90\,M_{\odot}$ respectively. This MWD is also thought to belong to the class of "slow rotators", with a possible period of $\gtrsim$100 years, as no changes have been observed in its polarisation over 12 years (West 1989).

The comparison stars C2 and C3 are eliminated from the analysis because they are considerably brighter than the target and dominate the target differential flux results. As a result, only C1 and C4 are used as comparison stars for the analysis (marked in Fig. 4.20). G 227-35 is observed only four times between August 2006 and January 2007 (Fig. 4.21, *left*), and with such a sparse data set, little information can be taken. All of the χ^2 values in the periodogram lie within 2σ of the minimum χ^2 (a $\Delta\chi^2$ of 4), indicating there are no significant frequencies in the periodogram. A very high FAP statistic is estimated at 1.00. To conclude, no evidence of periodic variability is detected in this small data set.

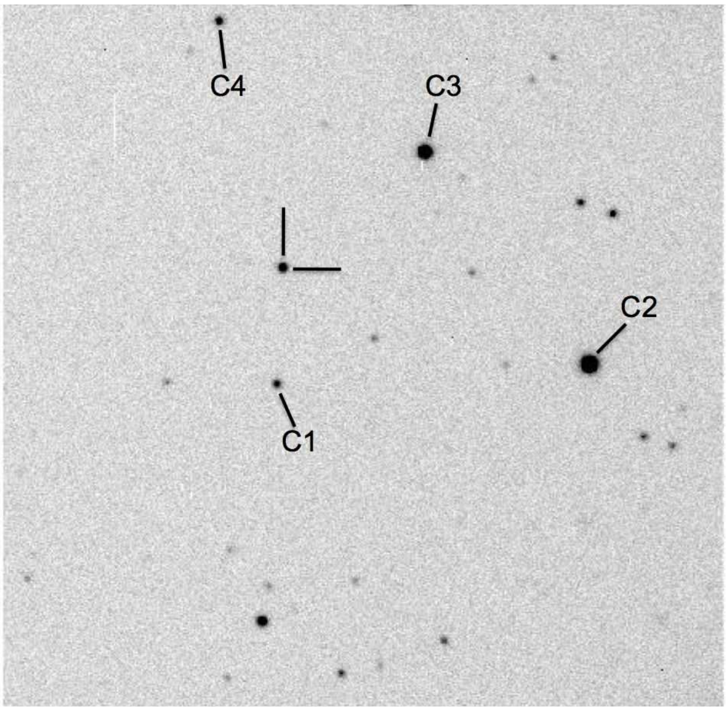

Figure 4.20: Finding chart for G 227-35 with four comparison stars indicated. Only C1 and C4 are used for the final differential photometry.

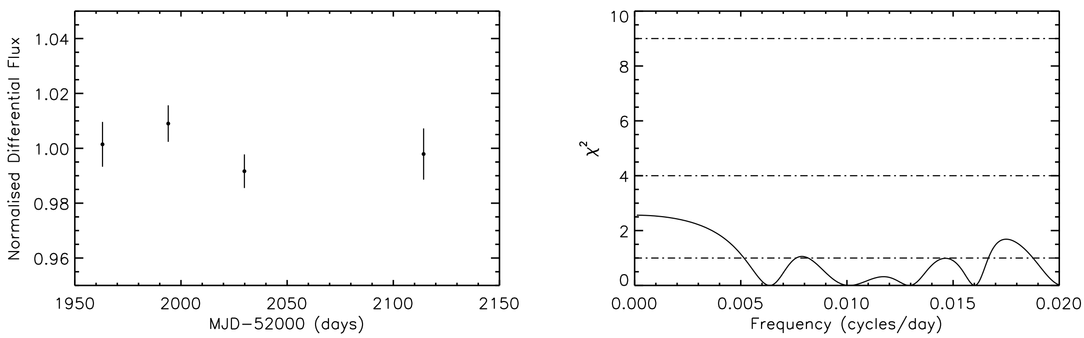

Figure 4.21: *Left:* G 227-35 normalised differential light curve, where the differential flux is calculated using target/(C1+C4). *Right:* Floating-mean periodogram. The dot-dashed lines indicate a change in χ^2 of 1, 4 and 9 (1σ, 2σ and 3σ uncertainties respectively).

4.4.9 Grw+70°8247

This MWD is believed to be a "slow rotator" with a period $\gtrsim$100 years, as its polarisation curves have remained unchanged over 25 years of observations (Angel et al. 1981; West 1989). It has a high magnetic field of 320 MG and temperature of 16,000 K (Wickramasinghe & Ferrario 1988; Jordan 1992). Grw+70°8247 was previously observed for photometric variability on short timescales by Brinkworth et al. (2013), who found no evidence of modulations, but noted that the scatter in the comparison stars' flux was greater than the scatter seen in the target flux, meaning any detection of variability was unreliable.

Figure 4.22 shows the field-of-view with the MWD and comparison stars marked. C1 is the only comparison star that is used for the differential analysis and consequently any variable behaviour associated with either the MWD or C1 cannot be separated. C2, C3 and C4 are excluded from the differential analysis because they are too faint (with S/N ratios a factor of 2 – 4 less than the S/N of the target) and contribute a large amount of scatter to the light curve, while C5 is not used due to field rotation and so is not consistently in the field-of-view. No significant variability is detected in the Grw+70°8247 light curve over the 22 month period of observations (Fig. 4.23, *left*). The majority of the periodogram is within the 3σ uncertainties from the χ^2 minimum (Fig. 4.23, *right*) at a frequency of 0.007384 cycles/d (P = 135.43 d). There are also a few minima in the periodogram of similar χ^2 values, implying sinusoids of different periods can produce equally suitable fits to the light curve. The FAP estimates for Grw+70°8247 are high, meaning it is highly probable that noise fluctuations are responsible for any variability present in the light curve. This result agrees with the hypothesis that it is possibly a "slow rotator".

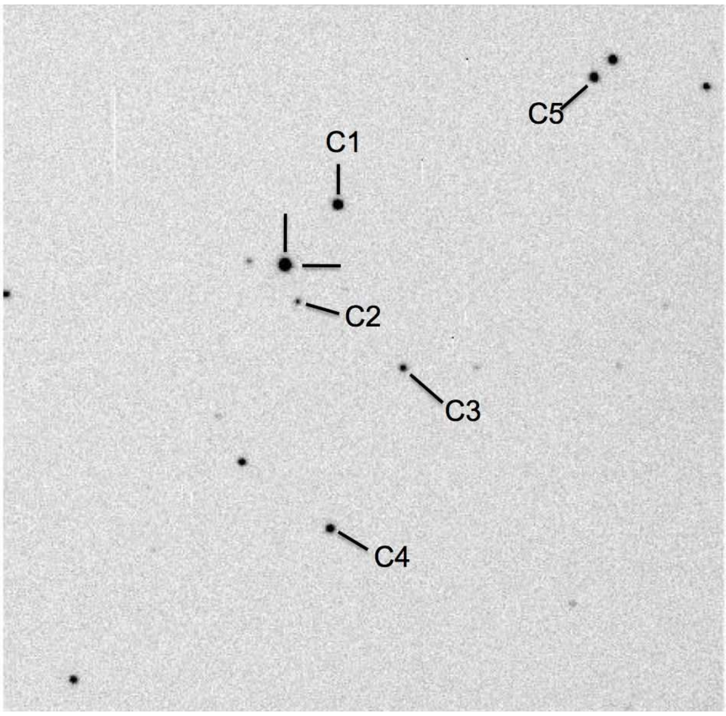

Figure 4.22: Finding chart for Grw+70°8247 with the comparison stars. C1 is the only comparison star used for the analysis. C2, C3 and C4 are eliminated because they are too faint (their S/N ratios are a factor of 2 – 4 less than S/N of the target), contributing a large degree of scatter to the light curve, and field rotation means C5 is not consistently in the field throughout the epochs.

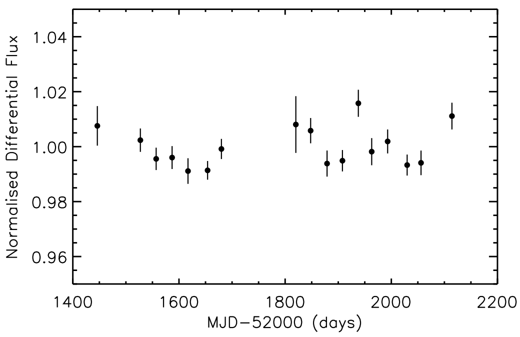

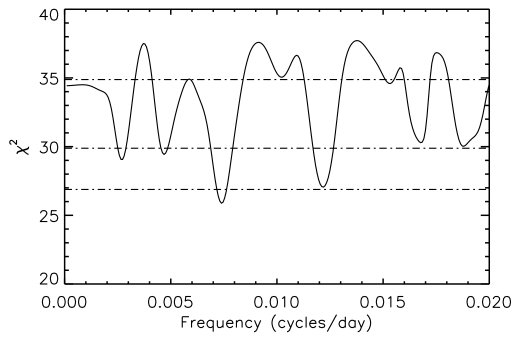

Figure 4.23: *Left:* Grw+70°8247 normalised differential light curve with data taken between March 2005 and January 2007. The differential flux is calculated as target/C1. *Right:* The corresponding floating-mean periodogram. The global minimum has a frequency at 0.007384 cycles/d (P = 135.43 d), where the dot-dashed lines indicate a change in χ^2 of 1, 4 and 9 (1σ, 2σ and 3σ uncertainties respectively).

4.4.10 GD 229

This DBH MWD is strongly polarised with a field strength of 520 MG (Wickramasinghe et al. 2002). Monitoring suggested that it was rotating very slowly as its polarisation appeared stable over many years (West 1989). However, later observations by Berdyugin & Piirola (1999) reported that the polarisation was definitely varying on a timescale of approximately ten years and if the changes were due to slow rotation, perhaps caused by magnetic braking, then the rotational period would be roughly 80 – 100 years.

GD 229 and its comparison stars are highlighted on the finder chart in Figure 4.24. For the differential photometry, the comparisons stars C1, C3 and C4 are used, while C2 and C5 are excluded from the analysis because C2 displays a large amount of scatter and C5 is not in the field-of-view frequently enough to be included due to field rotation. The scatter of the three comparison stars is ±1% and comparable to the scatter in the light curve of the target (Fig. 4.25, *left*). Consequently, any photometric fluctuations may be either due to the comparison stars or the target, thus making it difficult to differentiate between them. The minimum χ^2 in the periodogram (Fig. 4.25, *right*) is at a frequency of 0.011903 cycles/d ($P = 84.02$ d), with a poor reduced χ^2 of 2.5. I conclude that random noise fluctuations are most likely responsible for the variations in the light curve, which is reflected by the high FAP estimates of ~ 0.8.

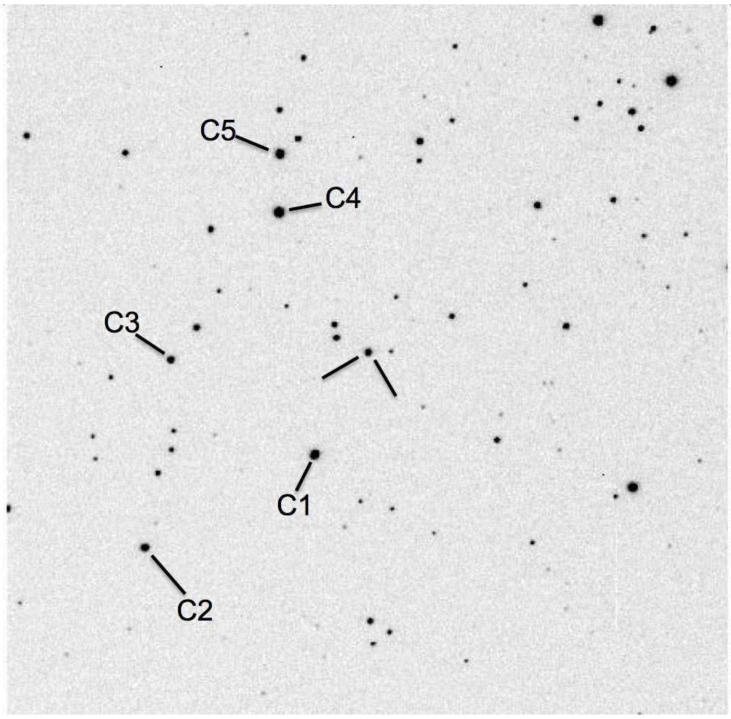

Figure 4.24: Finding chart for GD 229 with five comparison stars. The comparison stars C1, C3 and C4 are used for the differential photometry. C2 and C5 have not been used because C2 shows a large amount of photometric scatter and C5 is not present in enough epochs due to field rotation.

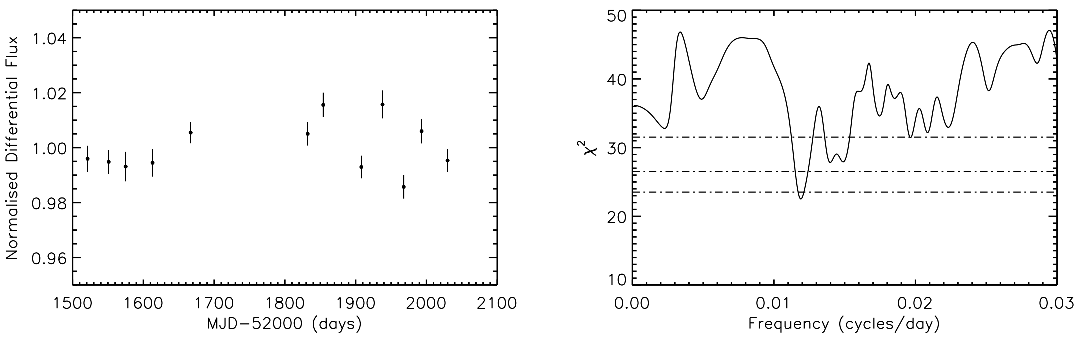

Figure 4.25: *Left:* GD 229 normalised differential light curve from May 2005 to October 2006, where the differential flux is calculated using target flux/(C1+C3+C4). *Right:* Floating-mean periodogram, where the minimum χ^2 is at a frequency of 0.011903 cycles/d (a period of 84.02 d). The dot-dashed lines indicate a change in χ^2 of 1, 4 and 9 (1σ, 2σ and 3σ uncertainties respectively). The 2σ uncertainties cover a frequency range of 0.011509 – 0.012394 cycles/d (a corresponding period range of 80.7 – 86.9 d).

4.5 Discussion

This investigation searches for long term photometric variability in ten bright, isolated MWDs on a timescale of months to years. No evidence has been found for significant photometric variations in any of the targets in the sample. G 240-72 appears to display modulations over months at an amplitude of 4 – 5% peak-to-peak, consistent with results from Brinkworth et al. (2013), but a definitive period is not determined. Variations on this timescale are much shorter than its suspected rotation period of $\gtrsim$ 100 years. However, no variability is measured over the observed timescale in the other "slow rotators", Grw+70°8247, G 227-35 and GD 229, confirming the possible likelihood of long rotation periods in these MWDs.

Considerable difficulties have been encountered in searching for long term photometric variability over two years of observations. For example, it seems that the de-rotator on the LT was not operational for some of the observations and as a result the star fields around the target could differ vastly between epochs. This made it challenging to select consistent comparison stars for all of the epochs. Furthermore, the target and comparison stars frequently fell on different parts of the CCD, introducing possible systematic uncertainties that have not been accounted for in the photometry. The comparison stars often exhibit more scatter than the target and consequently obtaining a reliable differential flux is problematic or not possible, making it difficult to search for low-level amplitude photometric variability. Many of the observations for each target are taken on an approximate monthly basis, rather than being randomly scheduled, therefore imposing a strong selection effect and limiting the range of frequencies that could be definitively searched. Spin periods of less than two months could not be reliably probed.

Crucially the minimum observing conditions are not adhered to in some cases, where some targets have been observed during twilight, at a distance of less than 30° from the moon and at high airmass. In combination with observing during a bright moon and in seeing of >1.3", the data quality are poor on occasions. Most of the data sets are too sparse ($N = 4$ for two MWDs) for significant photometric modulations and periods to be detected, and therefore the abilities of the survey are limited.

Given the data quality, it is clear the data are insufficient to test for long term photometric variability in MWDs. These stars should be re-observed over years for any subtle photometric changes. If this investigation is re-considered for future tests with a different telescope, greater control is required. For example, data reduction for this data was performed by the LT pipeline. Ideally, more control over the photometric data reduction would be preferred to ensure calibration frames, such as biases, darks and flat frames, are taken and appropriately applied for an optimal reduction. The colour of the comparison stars has not been checked in this analysis, and therefore differences in colour between MWDs and their comparison stars could have had an influence on the observed photometric variability. Obviously, for a thorough analysis of long term variations, this should be a consideration. In addition, a larger field-of-view would be ideal, to ensure a sufficient number of suitable comparison stars are available for differential photometry. The absence of stable comparison stars is a dominant limitation on the analysis.

4.6 Conclusions

In summary, a search is conducted into the long term photometric variability (months – years) for a sample of 10 bright, isolated MWDs. They were previously studied by Brinkworth et al. (2013) for short term modulations and were found to be photometrically stable on a timescale of minutes to one week. No significant evidence for photometric variability is detected here. However, G 240-72 may fluctuate on a timescale of months, as previously indicated by Brinkworth et al. (2013). The abilities of this survey to detect long term variations in MWDs are severely hampered by the quality of the data, where targets are not imaged frequently enough to probe periods around a month with any statistical confidence, while no de-rotator on the Liverpool Telescope at the time of the observations means the same comparison stars are not consistently in the field-of-view. Furthermore, target scheduling means some targets have been observed in less than appropriate conditions, such as during twilight. As a result, all of these stars, and in particular G 240-72, should be targeted for a more thorough and comprehensive long term photometric variability study.

5

Long Term Monitoring of RE J0317−853

The rapidly rotating ($P = 725$ s), highly magnetic (300 MG $< B <$ 800 MG), massive ($M \sim 1.3 M_{\odot}$) white dwarf, RE J0317−853, has been photometrically monitored since 1994, to determine whether any changes have occurred in the arrival time of the maximum flux. For the first time this method has been applied to a variable magnetic white dwarf, where a rate of period change $\dot{P}$ is measured to be $\dot{P} = (9.6 \pm 1.4) \times 10^{-14}$ s/s from an "Observed minus Calculated" (O – C) time of maximum flux analysis. The measured $\dot{P}$ appears to be consistent with the influence expected from the orbital motion between the wide binary pair of RE J0317−853 and LB 9802. Interestingly, the indications of a possible periodicity in the residuals from the best-fit tentatively suggest the presence of a nearby low-mass companion to RE J0317−853. The survival of a low-mass companion in a close orbit to a white dwarf through the post main-sequence evolution is discussed and I suggest that if confirmed, the companion may have formed in a disc around the magnetic white dwarf following a merger.

5.1 Background

5.1.1 RE J0317−853

RE J0317−853 (hereafter RE J0317) is one of the most interesting isolated MWDs known. It was first discovered by Barstow et al. (1995) as an extreme-ultraviolet (EUV) source by the ROSAT[1] Wide Field Camera. An optical spectrum of RE J0317 and a far-ultraviolet (FUV) spectrum, taken with the IUE[2] satellite, were compared with synthetic spectra generated using a simple dipole model for a range of temperatures and field strengths (and a fixed value for log g of 8.0) by Barstow et al. (1995) to determine a best-fit dipolar magnetic field strength of 340 MG with an offset from the centre along the dipole axis of 0.2 stellar radii toward the southern magnetic pole. In this dipole model, the field strength ranges from 664 MG at the south pole to 197 MG at the north pole. A similar result was obtained by Ferrario et al. (1997a) of $B = 450$ MG with an offset of $z = -0.35R_{\rm WD}$ at a line of sight inclination to the magnetic axis of $i = 30 - 60°$, determined by comparing circular polarisation data to different model configurations of dipolar field strengths and offset parameters. Spectropolarimetry observations revealed fluctuations in the circular polarisation of ~8% over the spin period (Ferrario et al. 1997a). A slightly larger field strength range of 180 − 800 MG was determined by Burleigh et al. (1999), who modelled phase-resolved FUV spectra taken with the *Hubble Space Telescope* (HST) Faint Object Spectrograph (FOS) using an expansion into spherical harmonics, making it one of the most magnetic isolated WDs. The offset dipole model and the multipolar expansion model were compared by Vennes et al. (2003), who found that the models failed to simultaneously explain the magnetic field dependence of the FUV spectrum and the phase-resolved properties of the optical polarisation spectrum. Consequently, Vennes et al. (2003) proposed that RE J0317 might have a spot similar to WD 1953-011 (Maxted

[1]Röntgensatellit (ROSAT) was an X-ray telescope launched in 1990 and operated for over eight years.

[2]The International Ultraviolet Explorer (IUE) satellite was launched in early 1978 and operated for almost 18 years. It observed in the ultraviolet part of the spectrum (10–350 nm) and was controlled in real time by astronomers.

et al. 2000; Brinkworth et al. 2005) with a high-field magnetic spot and an overall lower magnetic field, and whether this could explain some of the observed characteristics, such as the rapid transition from a low B-field to a high B-field in the line spectra.

In addition, RE J0317 is one of the hottest MWDs. Using the IUE UV spectrum, Barstow et al. (1995) suggested the MWD had a very high effective temperature of $30,000 - 50,000$ K, with a best-fit at 49,000 K. Analysis of the EUVE[3] spectrum by Vennes et al. (2003) accounted for the interstellar EUV absorption using the interstellar medium Lyman lines, which revealed a cooler temperature estimate of 33,800 K.

Barstow et al. (1995) obtained high-speed photometry of RE J0317, revealing periodic variations in the optical wavebands every 725.4 ± 0.9 s, with a semi-amplitude of 0.084 mag. These results were later confirmed by Vennes et al. (2003), who detected fluctuations in the circular polarisation data with a period of 725.727 ± 0.001 s. The optical light curve is not perfectly sinusoidal, but instead has a slightly flattened minimum (Barstow et al. 1995). Furthermore, when observed in the EUV, the photometric variation is double-peaked on the same period (Ferrario et al. 1997a). Over the years, the modulations have proven to be very stable in amplitude and shape. The fluctuations in the optical with rotation have been attributed to changes in the continuum opacity (otherwise referred to as magnetic dichroism, Ferrario et al. 1997a), due to a varying magnetic field strength across the surface. However, the double-peaked light curve observed in the EUV is not explained by magnetic dichroism. In the case of Feige 7, which has a field strength of $B = 35$ MG (Achilleos et al. 1992), the photometric modulations were also attributed to magnetic dichroism and changes in the field strength with rotational phase, but the effect was heightened by inhomogeneities in the chemical composition across the stellar surface. As a result, Ferrario et al. (1997a) suggested that the additional periodicity, at half the rotation period observed in the EUV light curve, could be caused by heavy-element abundance inhomogeneities at the magnetic poles. The variability is unlikely to be caused by pulsations, as the star is hot and well outside the hydrogen instability strip.

[3]The Extreme Ultraviolet Explorer (EUVE) satellite.

RE J0317 was assumed to be in a double-degenerate wide-binary system with LB 9802, a non-magnetic DA WD, due to the visual proximity of the stars on the projected sky. Using the $T_{\rm eff}$ and log g parameters for LB 9802 and the evolutionary models of Wood (1992), a distance to the star was derived in the range of 33 – 37 pc (Barstow et al. 1995). Assuming a distance of 36 pc to the nearby non-magnetic WD, Barstow et al. (1995) determined that RE J0317 has a radius of ≈$0.0035R_{\odot}$ and a corresponding mass of $1.35M_{\odot}$ (log g=9.5). A mass of 1.32 ± $0.03M_{\odot}$ was estimated by Vennes & Kawka (2008) using $T_{\rm eff}$=33,800 K and log g=9.4 at a distance of 27 pc (Kawka et al. 2007). These mass values indicate RE J0317 is one of the most massive isolated WDs discovered. Only 10 WDs have masses larger than $1.1M_{\odot}$ (Kawka et al. 2007). The binary relationship between RE J0317 and LB 9802 was confirmed from the common proper motion of the system using SuperCOSMOS observations at the UK Schmidt Telescope (UKST) taken ~25 years apart (Farihi, Becklin & Zuckerman 2008). Recent work by Külebi et al. (2010) aimed to constrain the mass and radius estimates, and thus the cooling age, for RE J0317 using parallax measurements acquired from HST's Fine Guidance Sensor. A distance of 30.05 pc was calculated from the parallax of LB 9802, indicating a separation of 7" (Vennes et al. 2003; Külebi et al. 2010) on the sky, equivalent to 210 AU between the two WDs. Külebi et al. (2010) estimated the mass and radius of RE J0317 for a range of effective temperatures 30, 000 – 50, 000 K (Barstow et al. 1995) using a variety of WD cooling models, where the mass value of RE J0317 ranged between 1.3 $M_{\odot}$ for an effective temperature of 30,000 K and >1.38 $M_{\odot}$ for an effective temperature of 50,000 K. These estimates implied cooling ages of 280 – 320 Myr for RE J0317, while the cooling age of the DA companion LB 9802 is 280 Myr. Therefore, when the progenitor masses of the WDs and main-sequence lifetimes were considered, there was a difference in the total age estimate for RE J0317 and LB 9802 of 100 Myr. Similarly, previous total age estimates suggested that RE J0317 was younger than LB 9802, leading to an "age discrepancy" (Ferrario et al. 1997a). However, Külebi et al. (2010) noted that if the effect of magnetism on the structure of the WD was considered, where the WD radius increased for a given mass and thus the cooling age also increased, the difference in the total age was eliminated.

Külebi et al. (2010) discussed RE J0317's possible evolutionary scenarios: either by single star evolution from a progenitor star with an initial mass of $7{-}8M_{\odot}$, or from the merger of two WDs. Tout et al. (2008) postulated that high-field MWDs are the result of a binary star merger, where the magnetic field is generated in a common envelope. The high mass, high temperature and rapid rotation of RE J0317 support the merger hypothesis. These factors, along with the age discrepancy between RE J0317 and LB 9802, led Ferrario et al. (1997a) to suggest that RE J0317 was the result of a double-degenerate merger. If the cooling age of RE J0317 is significantly younger than the less massive LB 9802, it would suggest that RE J0317 probably did not evolve from a single star (otherwise it would be older, since high mass stars evolve faster than lower mass ones). Külebi et al. (2010) claimed the single star route was the favourable option at $T_{\mathrm{eff}} = 30,000$ K, as the total ages of RE J0317 and LB 9802 were comparable if the effect of magnetism on the structure (radius) of RE J0317 was included. However, the binary merger scenario could not be ruled out due to the large amount of uncertainty in common envelope theory and merger timescales.

Despite all of the observations, modelling and work that has been performed over the years to understand RE J0317, there is still considerable uncertainty in its physical parameters and thus it still remains an enigma.

5.1.2 Investigating the change in arrival time of a signal

A wealth of knowledge can be obtained from studying the changes in the arrival time of an expected signal. RE J0317 has shown its photometric modulations are stable since its discovery. Therefore, I have searched for possible changes in the timing of the variability using many years of data, potentially looking for signs of a substellar companion orbiting the star.

Planets beyond our Solar System were first discovered around the millisecond pulsar

PSR B1257+12 by Wolszczan & Frail (1992) from the small variations in the pulse arrival time. A pulsar is a rapidly spinning, highly magnetic neutron star that forms during the collapse of a massive star. These millisecond pulsars have spin periods of $1.4\,\mathrm{ms} < P < 30\,\mathrm{ms}$ and magnetic fields of >1000 MG (Lorimer 2008). As the star rotates, radio emission from the star is directed along the magnetic axis of the star in a beam; analogous to the periodic beam of light observed from a lighthouse. The periodic pulses of light with rotation can act as an extremely accurate clock, with period changes of only $\dot{P} \sim 10^{-20}$ s/s (e.g. PSR J1713+0747, Splaver et al. 2005 and PSR J0437-4715, Verbiest et al. 2008). This stability allowed Wolszczan (1994) and Konacki & Wolszczan (2003) to detect changes in the pulse timing due to the presence of three planetary companions of 0.020, 4.3 and 3.9 $M_{\oplus}$ (Earth masses) at 0.19, 0.36 and 0.46 AU respectively, which caused the pulsar to move around the system's centre of mass, resulting in small variations in the arrival time of the radio pulse. In theory, it is even possible to detect objects as small as asteroids using this technique (Wolszczan 1997). However, planets orbiting pulsars have proven to be extremely rare, with only a couple of systems known (PSR B1257+12, Wolszczan & Frail 1992 and PSR B1620-26, Sigurdsson et al. 2003).

This technique has also been extended to search for planetary companions to pulsating WDs by searching for changes in the arrival time of their pulsation modes (Mullally et al. 2008). Ideal pulsating WDs exhibit a few isolated, relatively low amplitude modes, whereas multiplets or closely spaced modes are difficult to resolve and can make it difficult to accurately determine the phase. From a sample of 15 DAV WDs observed over four years, Mullally et al. (2008) reported that the WD GD 66 showed variations in the "Observed minus Calculated" (O – C) time of maxima, consistent with a planet minimum mass of 2.36 M_{Jup} at an orbital separation of 2.75 AU with a best-fit period of 5.69 years, assuming a circular orbit (Mullally et al. 2009). If confirmed, this would have been the first planet discovered orbiting a WD. However, they have since performed the O – C analysis for other frequency modes in the FT and do not find the same outcome as the main mode (Mullally 2012, priv. comm.). This is worrying, as it suggests that the timing variations are due to internal fluctuations occurring within the pulsating WD and not the presence of a genuine planet orbiting GD 66 (which would show the same variations in the O – C diagram regardless of the frequency mode analysed). For the remaining stars in the sample, Mullally et al. (2008) were able to place constraints on the presence of planetary companions to the stars, given the data sampling. In contrast to other planet searching techniques, such as the transit or radial velocity methods, timing analysis can be sensitive to objects in wider orbits (like those observed in our Solar System), provided that the observations cover a sufficiently long baseline.

The change in arrival time of pulsation modes has also been utilised in asteroseismology to gain further insight into the internal properties of a WD, such as its core composition and its rate of evolution (Althaus et al. 2010). The fundamental limit on the stability of the rate of period change $\dot{P}$ of a WD is its cooling timescale. Along with a number of millisecond pulsars, some pulsating DAV WDs are the most stable clocks at optical wavelengths (Kepler et al. 2005) on timescales of 10^9 years. Kepler et al. (2005) used the $\dot{P}$ of the main pulsation mode of the ZZ Ceti star G 117-B15A to measure its evolutionary rate of change, finding that it was consistent with the cooling rate of WD models for C or C/O cores (typically of $\dot{P} \sim 2-5\times10^{-15}$ s/s, Brassard et al. 1992; Benvenuto et al. 2004).

The method is also used for eclipsing binary systems where changes in the eclipse times can be used to search for companions, such as the possible planetary companions to the post-common envelope binaries HW Vir (Lee et al. 2009) and NN Ser (Beuermann et al. 2010). For example, NN Ser is a short-period eclipsing binary consisting of a DA WD and an M dwarf in a detached system. The O – C eclipse timings show large amplitude variations, suggesting there are two planets orbiting the binary (Beuermann et al. 2010). Such systems open up questions on how the planetary companions formed and evolved. Beuermann et al. (2010) discussed two possible formation scenarios for the planets orbiting NN Ser: old, first generation planets that formed in a circumbinary protoplanetary disc, or young, second generation planets that formed in a disc from the common envelope (Perets 2010).

A similar technique known as "transit timing variations" has proved to be very fruitful for detecting multiple planetary systems transiting or orbiting main-sequence stars using observations from the *Kepler* satellite, due to the unprecedented quality of the data (e.g. Mazeh et al. 2013; Lissauer et al. 2011; Fabrycky et al. 2012; Holman et al. 2010; Steffen et al. 2010 and references therein). The planets orbiting the host star cause the mid-point of the transit (from one of the planets) to shift, allowing the multiple planetary system characteristics to be accurately modelled and constrained.

This technique of searching for subtle timing variations is observationally intensive, as a great deal of time is required over long baselines to even start searching for signals. The method also requires good and appropriate models to describe the data to determine the best transit/eclipse times or times of maximum/minimum flux. Nevertheless, it can be applied to a variety of systems and situations and has been used extensively with much success.

Following the prescription outlined in Kepler et al. (1991), if the period of variability is changing slowly with time then the time of maximum flux, $T_{\rm max}$, can be expanded as a Taylor series as,

$$T_{\rm max} = T^0_{\rm max} + \frac{dT_{\rm max}}{dE}(E - E_0) + \frac{1}{2}\frac{d^2T_{\rm max}}{dE^2}(E - E_0)^2 + ..., \tag{5.1}$$

where E is the epoch cycle number. The change in arrival time of maximum flux with epoch, $\frac{dT_{\rm max}}{dE}$, is the period of the photometric variability, P. Therefore, the double differential can be simplified to,

$$\frac{d^2T_{\rm max}}{dE^2} = \frac{dP}{dE} = \frac{dP}{dt}\frac{dt}{dE} = \dot{P}P. \tag{5.2}$$

Setting $E_0 = 0$, defining the observed time of arrival O as the time of maximum flux $T_{\rm max}$ ($O \equiv T_{\rm max}$) and dropping the terms higher than second order, the following is obtained,

$$O = T^0_{\rm max} + PE + \frac{1}{2}P\dot{P}E^2. \tag{5.3}$$

The expected time of maximum flux, C, can then be determined assuming a constant period, such as,

$$C = T_0' + P'E, \tag{5.4}$$

where T_0' and P' are the reference time of maximum and period respectively, and are estimated parameters. Finally, the difference between the observed and calculated time can be defined as,

$$O - C = \Delta T_0 + \Delta PE + \frac{1}{2}P\dot{P}E^2, \tag{5.5}$$

where $\Delta T_0 = T^0_{\rm max} - T_0'$ and $\Delta P = P - P'$.

If a planet is orbiting a star, the distance between the star and an observer will change periodically as the system orbits its centre of mass. If the star has stable periodic pulsations or variations, the presence of a planet will cause a change in the observed arrival time of an otherwise stable and predictable signal compared to the assumption of a constant period. The orbital separation, a_p, can be determined from Kepler's laws as,

$$a_p^3 = \frac{G(M_\star + m_p)P^2}{4\pi^2}, \tag{5.6}$$

where a_p is in AU, P is the orbital period in years, $M_\star$ is the mass of the WD in solar masses, m_p is the companion mass in solar masses and where $G/4\pi^2 = 1$. The semi-major axis, $a_\star$, of the WD's orbit about the centre of mass of the system is given by (as shown in Fig. 5.1),

$$a_\star M_\star = m_p(a_p - a_\star) \tag{5.7}$$

$$a_\star = \frac{m_p a_p}{M_\star + m_p}. \tag{5.8}$$

The approximation that $M_\star \gg m_p$ cannot be assumed, as the companion mass could be comparable to the mass of a WD. The projected semi-major axis of the WD's orbit around the centre of mass becomes $a_\star \sin i$, if the planet's orbit has an inclination angle i to the line of sight. As the companion orbits the WD, the distance to the observer will fluctuate,

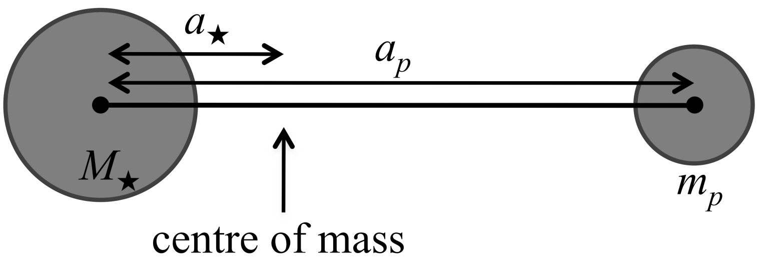

Figure 5.1: Diagram of a star and companion orbiting about the centre of mass, where $M_\star$ is the mass of the star (or WD in this case), m_p is the mass of a companion, a_p is the orbital separation and $a_\star$ is the distance from the star to the centre of mass.

giving a change in the arrival time of maximum flux as,

$$\tau = \frac{a_\star \sin i}{c} \tag{5.9}$$

$$\tau = \frac{m_p a_p \sin i}{(M_\star + m_p)c} \tag{5.10}$$

where c is the speed of light. As a result, the semi-amplitude of the signal τ increases with the orbital separation of the planet and therefore, given a long enough time base, planets at wider orbits are easier to detect.

Furthermore, the curvature of the O – C plot, $\dot{P}$, can also be determined as a function of the mass of the companion and their orbital separation (see Kepler et al. 1991 for the derivation),

$$\dot{P} = \frac{P}{c}\frac{Gm_p}{a_p^2}\cos\theta \sin i, \tag{5.11}$$

where $\dot{P}$ is measured from the O – C diagram as given by Equation 5.5, P is the period of the photometric variability (as also in Eq. 5.5), θ is the position angle in the orbit and i is the inclination angle of the orbit (the angle between the plane of the sky and the plane of the orbit). Assuming the maximum radial velocity occurs for an edge-on system (i = 90°) and for $\theta = 0$ (tangential velocity = 0), the expression is simplified to

$$\dot{P} \approx 1.97 \times 10^{-11} P \frac{m_p/M_\odot}{(a_p/AU)^2} s/s. \tag{5.12}$$

This approach, however, breaks down if there is a planet present and the data set spans a significant fraction of the orbit. In this event, the assumption that $\dot{P}$ is constant is no longer valid, and therefore Equation 5.11 can only be used to constrain the presence of planets, but not to measure the parameters once it is found.

5.2 Photometric Data

Three different telescopes have been used over the past 19 years to observe RE J0317: the 1.0 m at the South African Astronomical Observatory (SAAO), the PROMPT telescopes at the Cerro Tololo Inter-American Observatory (CTIO) and ULTRACAM at the New Technology Telescope (NTT). A detailed log of the photometric observations is given in Table 5.1.

5.2.1 SAAO 1.0 m

RE J0317 was first observed using the 1.0 m telescope at the SAAO in 1994 by Darragh O'Donoghue to measure the periodic photometric variability. Since then, the telescope has remained a consistent facility in this project with a total of 148 hours of time-series photometry, although three different instruments have been used on the 1.0 m telescope: the UCT CCD, the STE4 CCD and the STE3 CCD. The UCT CCD was used for the majority of the early epochs, with the STE4 CCD being used only once in 2008 and the STE3 CCD for the 2012/13 observing season.

The UCT CCD has a cooled camera with a 576×420 pixels thinned, back-illuminated CCD and is primarily designed for high-speed photometry. To obtain no deadtime during readout, the UCT CCD operates in frame transfer mode. This means that half of the chip is covered by a mask and at the end of an exposure, the image on the unmasked half is transferred to the masked half, which is then read out during the next exposure on the unmasked section. This operating mode allows exposure times as short as 10 s with no time lost for readout. Therefore, 10 s exposures were taken using the UCT CCD without a filter (i.e. in white light).

Care was required when observing with the UCT CCD because the field-of-view ($109'' \times 74''$) was very small. This meant that the telescope had to be positioned appropriately so comparison stars also fell on the CCD and the target avoided bad pixels/regions. In addition, poor seeing conditions meant photometry could be problematic, as the target and its WD companion (RE J0317 and LB 9802) would blend together as their projected separation is only $\sim 7''$ (Külebi et al. 2010).

Two other instruments were also used on the 1.0 m telescope: the STE4 and STE3 CCDs. The primary difference between these two instruments is the field-of-view. They are back-illuminated detectors of 1024×1024 pixels and 512×512 pixels for STE4 and STE3 respectively, with 0.31 arcsec/pixel. For both detectors, 2×2 binning was used with an exposure time of 10 s. STE3/4 are not high-speed photometers and thus do not have a frame transfer mode. This meant there was a readout time between exposures of ~6 s, which was kept to a minimum by using STE3 (in 2012/13) and 2×2 binning. Ideally, I would have used the UCT CCD for the 2012/13 observing campaign for consistency with previous data. Sadly, however, the UCT CCD was no longer operational and there was no high-speed photometer replacement available for the observing season.

5.2.2 PROMPT

RE J0317 was monitored intensively over the late 2010/early 2011 semester with the Panchromatic Robotic Optical Monitoring and Polarimetry Telescopes (PROMPT), located at the Cerro Tololo Inter-American Observatory (CTIO) in Chile. Built by the University of North Carolina at Chapel Hill (UNC-CH), PROMPT consists of six 0.41 m telescopes. PROMPT was primarily designed to take rapid, simultaneous multi-wavelength observations of gamma-ray burst afterglows. It is operated by a prioritised, queue-scheduling system called SKYNET and is 100% automated. The telescopes are mounted with rapid-readout (<1 s) cameras, with a field-of-view of 10 arcminutes and 0.6 arcsec/pixel (Reichart et al. 2005).

The campaign with PROMPT in 2010/11 meant that sufficient data could be acquired over a single season to obtain a reliable ephemeris. The PROMPT observations were carried out by Brad Barlow, part of the SKYNET consortium at UNC-CH. The exposures were taken without a filter for 30 s for approximately 4 h observing runs, although they varied between 3 and 7.5 hours. In total, PROMPT observed RE J0317 on 17 nights for a total of 78 hours.

5.2.3 ULTRACAM

Photometric data of RE J0317 was also acquired with ULTRACAM mounted on the 3.58 m New Technology Telescope (NTT) at La Silla, Chile, in May/June 2011, courtesy of Tom Marsh. The ULTRACAM instrument is a collaboration between Tom Marsh, Vik Dhillon and the Astronomy Technology Centre (Edinburgh). It is a high-speed, 3-channel, frame transfer CCD camera. RE J0317 was observed in u', g' and r' simultaneously on six separate occasions (for <1 h each) over three nights.

Table 5.1: Observations log of RE J0317 − 853.

Date	Start Time (UTC)	$T_{\rm exp}$ (s)	Length (hr)	Filter *	Telescope/ Instrument
1994-11-08	00:17:03	10	2.22	white	SAAO 1.0 m UCT
1994-11-12	21:57:06	10	3.99	white	SAAO 1.0 m UCT
1998-08-21	01:56:03	10	2.26	white	SAAO 1.0 m UCT
1998-08-24	03:36:10	10	0.69	white	SAAO 1.0 m UCT
1998-08-25	00:58:52	10	2.81	white	SAAO 1.0 m UCT
1998-11-10	21:10:52	10	3.45	white	SAAO 1.0 m UCT
1998-11-11	19:57:56	10	4.26	white	SAAO 1.0 m UCT
1998-11-12	19:40:22	10	4.65	white	SAAO 1.0 m UCT
1998-11-14	18:20:14	10	6.00	white	SAAO 1.0 m UCT

Table 5.1: *continued*

Date	Start Time (UTC)	T_{exp} (s)	Length (hr)	Filter *	Telescope/ Instrument
1999-09-02	18:22:46	10	7.04	white	SAAO 1.0 m UCT
1999-09-04	19:00:22	10	3.17	white	SAAO 1.0 m UCT
2000-01-11	19:31:24	10	0.71	white	SAAO 1.0 m UCT
2000-01-13	18:56:34	10	1.51	white	SAAO 1.0 m UCT
2000-01-14	19:12:48	10	1.19	white	SAAO 1.0 m UCT
2000-01-17	18:37:46	10	1.58	white	SAAO 1.0 m UCT
2006-10-26	23:21:59	10	3.46	white	SAAO 1.9 m UCT
2006-10-28	00:58:51	10	0.80	white	SAAO 1.9 m UCT
2006-10-31	01:18:42	10	3.17	white	SAAO 1.9 m UCT
2007-12-07	18:51:55	10	2.99	white	SAAO 1.0 m UCT
2007-12-08	20:11:21	10	2.89	white	SAAO 1.0 m UCT
2007-12-09	23:07:42	10	1.40	white	SAAO 1.0 m UCT
2008-11-06	00:09:34	10	2.34	white	SAAO 1.0 m STE4
2008-11-09	23:19:43	10	1.68	white	SAAO 1.0 m STE4
2009-10-31	23:53:00	10	3.18	white	SAAO 1.0 m UCT
2009-11-04	00:23:08	10	2.40	white	SAAO 1.0 m UCT
2010-09-05	03:01:55.9	30	3.94	Open	PROMPT-4
2010-09-30	00:56:41	10	2.41	white	SAAO 1.0 m UCT **
2010-10-17	00:15:35	10	2.81	white	SAAO 1.0 m UCT **
2010-10-26	23:23:07	10	3.42	white	SAAO 1.0 m UCT **
2010-12-08	00:37:15.3	30	5.18	Open	PROMPT-3
2010-12-11	00:38:40.4	30	7.27	Open	PROMPT-3
2010-12-14	00:41:54.3	30	6.20	Open	PROMPT-3
2010-12-18	00:45:03.9	30	6.22	Open	PROMPT-3
2010-12-19	00:44:36.8	30	7.46	Open	PROMPT-3
2010-12-22	03:54:41.6	30	3.90	Open	PROMPT-3
2010-12-23	00:46:30.3	30	0.56	Open	PROMPT-3
2010-12-24	03:49:29.6	30	3.93	Open	PROMPT-3
2010-12-26	02:40:33.3	30	3.97	Open	PROMPT-3
2010-12-28	01:40:14.9	30	5.26	Open	PROMPT-3
2010-12-29	02:42:17.7	30	3.89	Open	PROMPT-3
2010-12-30	01:51:25.1	30	4.93	Open	PROMPT-3
2011-01-06	00:49:37.1	30	4.10	Open	PROMPT-3
2011-01-11	00:49:33.8	30	3.92	Open	PROMPT-3
2011-01-12	00:41:49.6	30	2.97	Open	PROMPT-3
2011-01-15	00:37:43.5	30	3.88	Open	PROMPT-3
2011-01-19	20:22:05	10	3.78	white	SAAO 1.0 m UCT
2011-01-25	01:05:19	10	1.88	white	SAAO 1.0 m UCT
2011-05-29	09:34:59.3	2.89	1.10	u′g′r′	NTT ULTRACAM
2011-05-31	08:27:05.1	2.89	0.67	u′g′r′	NTT ULTRACAM
2011-05-31	09:07:19.5	2.89	0.92	u′g′r′	NTT ULTRACAM
2011-06-01	06:28:58.3	2.25	0.62	u′g′r′	NTT ULTRACAM
2011-06-01	07:56:41.5	2.82	0.65	u′g′r′	NTT ULTRACAM
2011-06-01	09:25:15.5	3.82	1.02	u′g′r′	NTT ULTRACAM
2012-08-10	03:03:26	10	1.30	white	SAAO 1.0 m STE3

Table 5.1: *continued*

Date	Start Time (UTC)	T_{exp} (s)	Length (hr)	Filter *	Telescope/ Instrument
2012-08-30	01:14:17	10	2.96	white	SAAO 1.0 m STE3 **
2012-08-31	01:20:24	10	1.36	white	SAAO 1.0 m STE3 **
2012-09-02	01:21:23	10	2.81	white	SAAO 1.0 m STE3 **
2012-09-03	01:12:46	10	1.81	white	SAAO 1.0 m STE3 **
2012-09-05	01:15:22	10	0.76	white	SAAO 1.0 m STE3 **
2012-09-08	01:23:24	10	2.62	white	SAAO 1.0 m STE3 **
2012-09-09	01:14:08	10	0.90	white	SAAO 1.0 m STE3 **
2012-09-11	01:09:21	10	2.73	white	SAAO 1.0 m STE3 **
2012-09-12	01:05:51	10	1.37	white	SAAO 1.0 m STE3 **
2012-10-04	23:33:57	10	3.58	white	SAAO 1.0 m STE3 **
2012-10-07	00:02:52	10	1.28	white	SAAO 1.0 m STE3 **
2012-10-23	21:25:24	10	1.41	white	SAAO 1.0 m STE3
2012-11-07	21:42:25	10	3.47	white	SAAO 1.0 m STE3
2012-11-08	21:46:14	10	3.16	white	SAAO 1.0 m STE3
2012-11-09	19:58:52	10	2.87	white	SAAO 1.0 m STE3
2012-11-10	20:01:09	10	2.81	white	SAAO 1.0 m STE3
2012-11-13	21:03:15	10	2.36	white	SAAO 1.0 m STE3
2012-12-06	21:19:11	10	1.69	white	SAAO 1.0 m STE3 **
2012-12-11	21:20:45	10	1.23	white	SAAO 1.0 m STE3 **
2013-01-02	19:46:12	10	3.07	white	SAAO 1.0 m STE3 **
2013-01-03	19:14:15	10	3.57	white	SAAO 1.0 m STE3 **
2013-01-04	19:18:44	10	3.42	white	SAAO 1.0 m STE3 **
2013-01-05	19:11:12	10	3.52	white	SAAO 1.0 m STE3 **
2013-01-06	19:13:34	10	3.56	white	SAAO 1.0 m STE3 **
2013-01-07	20:49:48	10	1.81	white	SAAO 1.0 m STE3 **
2013-01-08	20:49:07	10	1.92	white	SAAO 1.0 m STE3 **

* The SAAO 1.0 m UCT CCD is sensitive to the blue end of the visible spectrum, so the white light observations peak at 400 − 500 nm. While, the SAAO 1.0 m STE3/4 CCD is red sensitive and white light observations are at 600 − 700 nm.
** Data either collected by myself or as part of a program where I was the principal investigator.

5.3 Data Reduction and Analysis

5.3.1 SAAO 1.0 m

The photometric data taken at SAAO was reduced using their pipeline which performed: a bias subtraction, flat-fielding and extraction of the brightness of the stars on the frame using DuPHOT. To start, the bias was measured from the overscan strip region and was subtracted from the image. The overscan strip and other unwanted edges of the CCD were then trimmed off. The science images were then corrected using the normalised master flat field. The script then performed variable aperture photometry and PSF-fitting photometry for each star in the field-of-view brighter than a given threshold. Differential photometry was conducted using the flux measurements of the target and best comparison stars in the field. An example of a SAAO 1.0 m STE3 light curve is given in Figure 5.4, along with its corresponding FT.

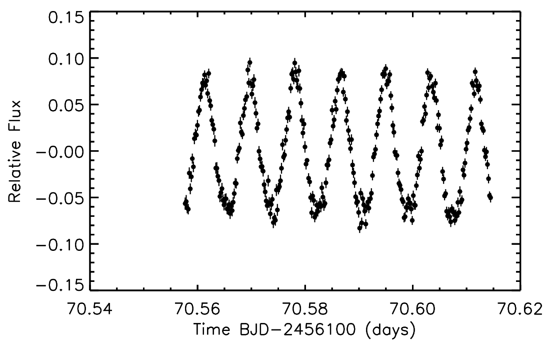

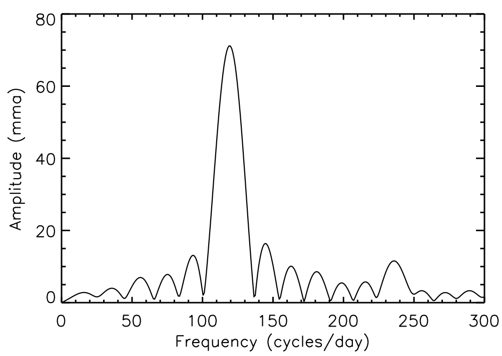

Figure 5.2: An example of a SAAO 1.0 m STE3 light curve of RE J0317−853 taken on August 30, 2012 (*left*) and its corresponding Fourier transform (*right*). The FT peaks at a frequency of 119.11825 cycles/day (a period of 725.330 s). The amplitude is given in units of milli-modulation amplitude (mma), meaning 10 mma is equivalent to 1%.

5.3.2 PROMPT

A standard photometric data reduction was carried out for the PROMPT data. Using STARLINK packages, such as FIGARO, KAPPA and CONVERT, all of the frames were initially converted from FITS format to sdf (starlink data format) and then the edges of the images were trimmed. A master bias frame and master dark frame were constructed by taking the median of a number of appropriate images. The master bias frame was then subtracted from the flat fields before they were combined and normalised to make the master flat frame. Individual flat frames with counts higher than 40,000 counts were excluded. Since the dark frames were not taken with the same exposure time as the science frames, the darks had to be scaled appropriately. First, the master bias image was subtracted from the master dark, which was then scaled to the same exposure time as the science images. The master bias was then added back onto the "scaled" master dark. The master dark frame (scaled to the appropriate exposure time) was subtracted from the science frames which were then finally flat fielded (i.e. divided by the de-biased normalised master flat frame). Where possible, the three sets of calibration frames were taken on the same night as the science observations; however, this could not always be achieved, in which case the calibration frames were taken from the nearest night to the observations.

Once the photometric data reduction was carried out, aperture photometry was performed on the science frames using AUTOPHOTOM (the same method as outlined in §3.2.2 for the SAAO photometry of the hot DQ). The aperture size was set to ∼1.7 times the mean seeing (FWHM) which was kept constant within an epoch but was allowed to change with the average seeing conditions from night-to-night. The typical aperture size was 6 – 7 pixels. It is worth noting that PROMPT drifts due to a tracking error in the mount of 0.4 arcmin/hour (Barlow et al. 2011). In addition, the telescope occasionally underwent a "pier flip", as the target moved through the meridian, part way through observing runs; as a result, the star flux did not always fall on the same pixels on the CCD. An example of the PROMPT field-of-view is given in Figure 5.3 with the target and comparison stars marked.

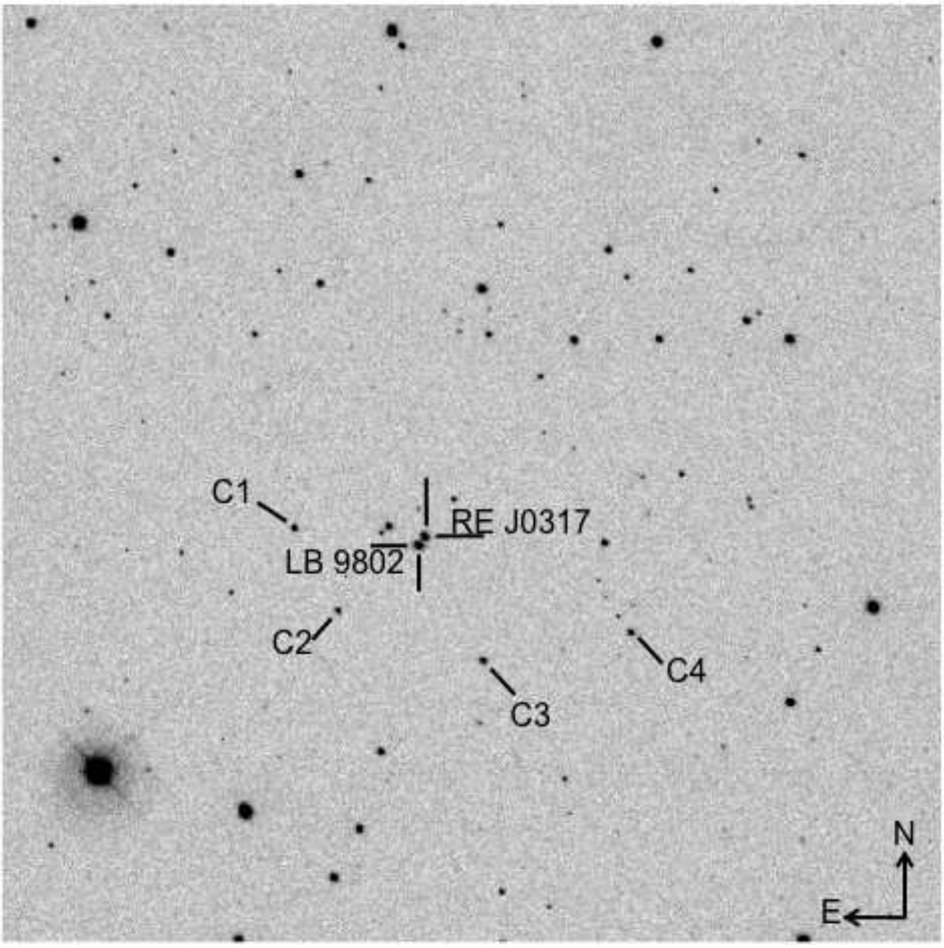

Figure 5.3: Finder chart for RE J0317−853 in the PROMPT field-of-view (10'×10'). RE J0317 and its DA WD companion, LB 9802, have been marked along with four comparison stars.

Comparison stars C1, C2, C3 and C4 were selected for the differential photometry. Stars were avoided that may drift out of the field-of-view during an observing run and that were not stable with high star flux standard deviations. An example of one of the PROMPT light curves is shown in Figure 5.4, along with its corresponding FT.

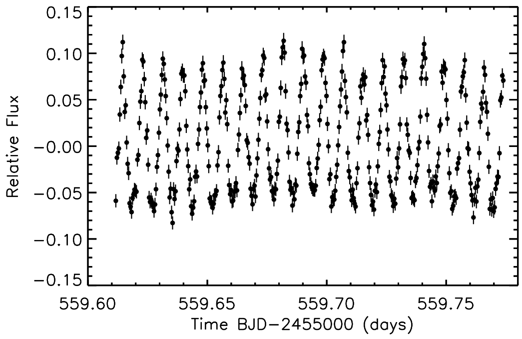

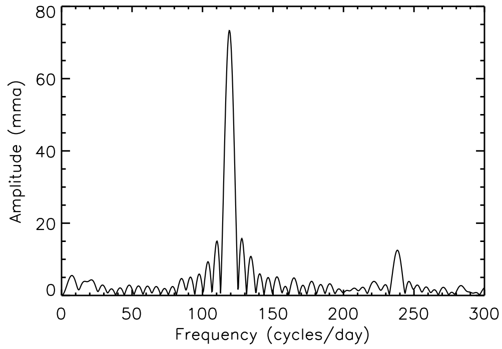

Figure 5.4: An example PROMPT light curve of RE J0317−853 taken on December 29, 2010 (*left*) and its corresponding FT (*right*). The FT peaks at a frequency of 119.01396 cycles/day (a period of 725.965 s).

5.3.3 ULTRACAM

The ULTRACAM data were reduced using the ULTRACAM pipeline software[4] (Dhillon et al. 2007). This followed the usual photometric data reduction procedure. The bias frames were combined to create a master bias frame. Care was required to ensure the bias frames were taken in the same operating mode, readout speed and binning as the science images. The flat frames were bias subtracted and then combined and normalised to make a master flat by taking the median. Individual flats with less than 5000 counts and more than 47,000, 27,000 and 27,000 counts for frames taken in r', g' and u' respectively were excluded. The bias subtraction and flat fielding of the science frames were performed under the same routine as the aperture photometry, called REDUCE. To start, the position of the stars for the photometry were defined for each of the three wavebands. Three stars were specified: the target, a comparison star and a reference star for the seeing. The reference star could change between epochs, depending on how the stars were aligned on the CCDs, but the specified comparison star was kept consistent. In addition, a mask was used in the photometry to limit the amount of unwanted flux from the comparison star to the target. This was especially important as the observations were taken in poor seeing conditions, varying from 1.5” up to 4” for the poorest data set. The seeing was typically ~2” for the ULTRACAM data. A variable aperture was set to 1.7×FWHM for

[4]The ULTRACAM software is available at: `http://deneb.astro.warwick.ac.uk/phsaap/software/ultracam/html/index.html`

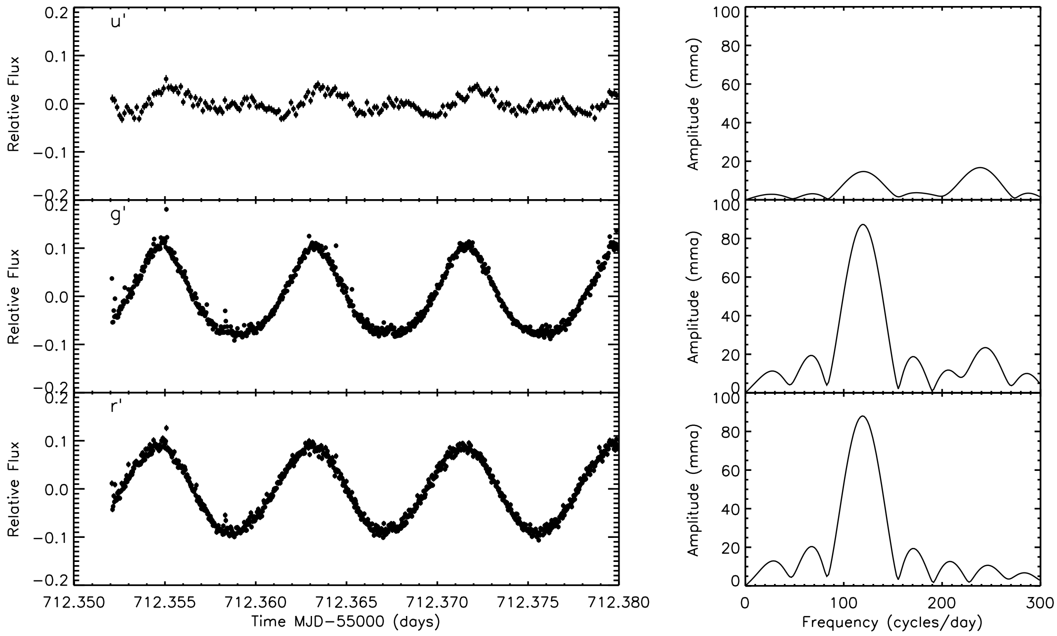

Figure 5.5: *Left:* An example of the ULTRACAM data taken on the NTT of RE J0317−853 in filters u', g' and r' simultaneously. The optical variability dependence on wavelength is clearly evident in these light curves. In g' and r' the light curve looks nearly sinusoidal, while in u' the light curve is double-peaked. *Right:* The corresponding FTs for each of the wavebands.

the photometry and the star signal was extracted using Moffat profile fitting. The sky background level was estimated using the clipped mean. Once the light curves were obtained for each of the three stars, the differential flux was calculated as the target's flux divided by the sum of the comparison star flux and the reference star flux. Examples of the u', g' and r' differential light curves and FTs obtained with ULTRACAM on the NTT are shown in Figure 5.5. The wavelength dependence of the optical variability is clearly evident. The r' light curve looks nearly sinusoidal and the g' light curve has a flatter minimum, while the u' light curve is double-peaked on the spin period and the amplitude is much less.

5.3.4 Combined data sets

Once differential light curves were obtained for each of the runs, they were normalised using a second-order parabola to remove any remaining atmospheric extinction effects. The observation times were then corrected to a consistent format. The Julian Dates (JD) obtained from the PROMPT data were modified from the time at the start of the exposure to the mid-exposure time. This was not required for the data from SAAO or ULTRACAM, as the mid-exposure JDs were given in the reduction processes. All time stamps were then converted to Barycentric Julian Date (BJD) using an IDL script developed by Eastman et al. (2010). Each of the individual light curves (listed in Table 5.1) were analysed using a floating-mean periodogram. The frequency measured at the minimum χ^2 in the periodogram was used to fit the light curves with a sine wave using MPFIT in IDL (Markwardt 2009). The sine wave model is defined as,

$$y = A\sin\left(2\pi\frac{t}{P} + 2\pi\frac{\phi}{P}\right), \tag{5.13}$$

where A is the semi-amplitude, P is the period in seconds, ϕ is the phase in seconds (between zero and P with every cycle) and t is the time in seconds from the mid-point of the run. Light curves taken at the same epoch (i.e. week/month) with the same instrument were combined into one. As a result, light curves would consist of ~9 hours of data spread over a much longer baseline of a few days. This reduced the uncertainty in the time of maximum by the square root of the total observing time, since a better sine fit was obtained over a longer period of time, compared with a single night of data. Figure 5.6 shows the semi-amplitude of the sine fits of the 22 combined light curves. As seen in the Figure 5.6, the amplitude measurements are quite variable for the SAAO 1.0 m STE3 instrument, although the PROMPT and SAAO 1.0 m UCT amplitudes are consistent over time. There are differences between the telescopes/instruments used (i.e. the data taken with the SAAO UCT consistently has a semi-amplitude of ~90 mma, whereas the semi-amplitude of the PROMPT light curves is less at ~72 mma). The differences in the semi-

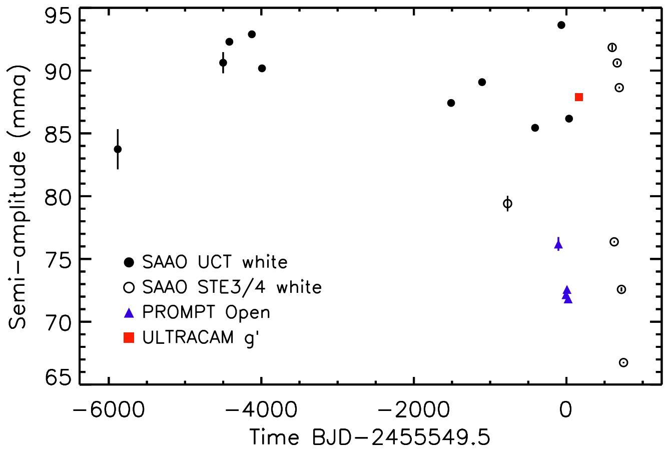

Figure 5.6: Semi-amplitudes of the best-fitting sinusoids to the light curves for each epoch. The black filled circles indicate data taken at SAAO with the UCT CCD in white light, the black unfilled circles are data taken at SAAO with the STE4/STE3 CCD in white light, the blue triangles represent data from the PROMPT telescopes with no filter and the red square is ULTRACAM data on the NTT taken in the g' filter. The semi-amplitude is given in units of milli-modulation amplitude mma (10 mma corresponds to 1%). Differences in semi-amplitude are evident between different instrument/telescope combinations, although the semi-amplitude appears to be generally consistent for the same configuration (although not the case for STE3/4 light curves).

amplitude may be due to the wavelength of the observed light curves, but also the time-sampling of the light curves. SAAO UCT and ULTRACAM are high-speed photometers and therefore collect more data across the phase than PROMPT and SAAO STE3/4. The best-fitting period for each of epochs is shown in Figure 5.7 which are found to be very consistent and to agree within ~0.01 s. The two exceptions are both single night light curves, and not combined with other data sets taken over many nights.

5.4 The O – C Diagram

Following the O – C method described earlier in §5.1.2 (and detailed in Barlow et al. 2011; Sterken 2005; Kepler et al. 1991), an initial estimate for the best-fitting period is determined as $P' = 725.72776 \pm 0.00015$ s using a least-squares sine curve fit (using MPFIT) to all of the 2010/2011 light curves taken with PROMPT.

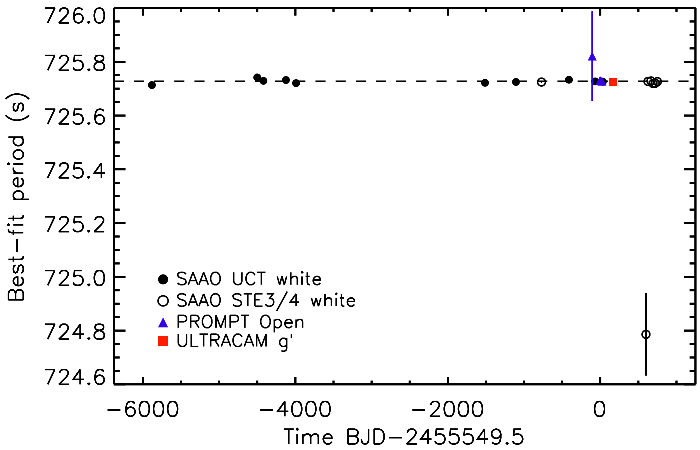

Figure 5.7: Periods of the best-fitting sinusoids to the light curves for each epoch. The symbols were previously defined in Figure 5.6. The best-fitting period is consistent across all of the epochs, although there is a miscellaneous point at a time of approximately 2456050 BJD with a period of 724.8 s. The dashed line represents the ephemeris best-fitting period at $P = 725.727684 \pm 0.000002$ s (see Table 5.3).

To determine the "Observed" times of maximum (O), the light curves for each epoch are shifted to their respective mid-point (mean) time. A least-squares sine curve is then fit to the data sets using Equation 5.13, where the period (in seconds), phase (in seconds) and amplitude are free floating parameters. Formal 1σ errors are output from MPFIT for each of these parameters. The time of maximum light is then calculated using, $O = T_{\rm ref} - \phi + P/4$, where the error in "O" is the sum in quadrature of the error in the phase and period.

Using the estimate for the period, the corresponding cycle numbers E are calculated using the linear ephemeris expression ($T_0' + P'E$, Eq. 5.4), assuming a constant period P. The "Observed" time of maximum light for the December 24, 2010 epoch (PROMPT light curves) is used as the reference time of maximum T_0' for the ephemeris. Exceptional care has been required to ensure the cycle number E is correct over such long periods of time. (When the appropriate cycle number of the epoch is lost, it is illustrated by a sudden change in the O – C points of half the rotation period.) The "Calculated" times of maximum are determined using the same ephemeris (Eq. 5.4) and cycle numbers E of the observed epochs.

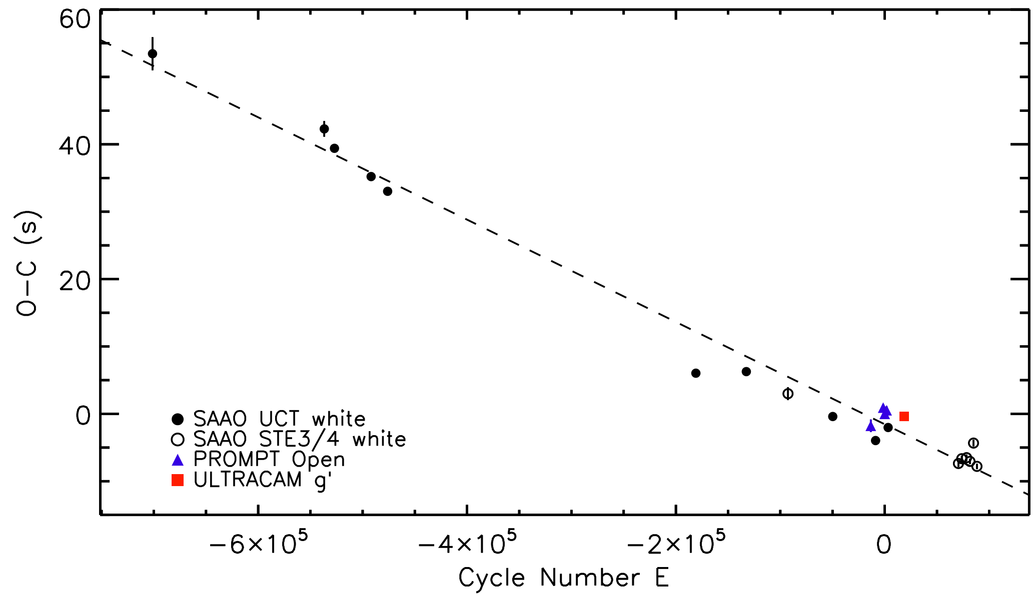

Figure 5.8: The O – C diagram of RE J0317−853 constructed using the initial period estimate. The negative slope indicates that the O – C diagram is calculated with a period slightly longer then the true period. The dashed line is the best-fitting linear fit (Eq. 5.14), which is used to determine the real period.

The resulting O – C diagram (using the initial period estimate) is shown in Figure 5.8, where the data points are determined by subtracting the "Calculated" times of maximum from the "Observed" times of maximum. The plot shows a change in the O – C of ≈80 s over the last 19 years. The negative slope indicates that the O – C diagram is constructed with a period slightly longer then the true period. An uncertainty in the period of ΔP = 0.0001s over 19 years (∼789,000 cycles) equates to ≈80 s, corresponding to the $\Delta(O - C)$ observed in Figure 5.8.

To determine the real period, a straight line of the form $O - C = a + bE$ is fit to the O – C diagram (Fig. 5.8), equivalent to,

$$O - C = (T^0_{\rm max} - T'_0) + (P - P')E, \qquad (5.14)$$

where $T^0_{\rm max}$ is the actual time of maximum, T'_0 is the time of maximum that is used to construct the O – C diagram, P is the real period and P' is the initial estimate for the period that is used to calculate the O – C diagram. Therefore, the actual period and time of maximum flux are determined from the following expressions, using the results from the linear fit,

$$P = b + P' \tag{5.15}$$

$$T^0_{\max} = a + T'_0. \tag{5.16}$$

The O – C diagram is then re-calculated using the new period and time of maximum estimates and is repeated until the fit could no longer be improved. The final O – C diagram using the true period is shown in Figure 5.9 and the O – C values are given in Table 5.2. The linear ephemeris for the time of maximum flux is,

$$2455556.7250473(67)\mathrm{BJD} + 0.00839962597(2)E. \tag{5.17}$$

For completeness, a parabola (the dashed line in Fig. 5.10) as described by Equation 5.5 is fit to the O – C data points using the MPFIT non-linear least squares routine, where the points are weighted by their estimated errors. Fitting the O – C expression (Eq. 5.5) yields an estimate for the rate of period change ($\dot{P}$). The residuals obtained from subtracting the parabola from the O – C points are shown in the lower panel of Figure 5.10. The observed rate of period change ($\dot{P}$) from the parabolic fit is found to be $(9.6 \pm 1.4) \times 10^{-14}$ s/s. A determination for the $\dot{P}$ term in the O – C expression, however, does not necessarily mean it is significant. Following Pringle (1975), the test statistic is calculated as $\lambda = 30.18$ where,

$$\lambda = \frac{\sigma_1^2 - \sigma_2^2}{\sigma_2^2}(n-3), \tag{5.18}$$

and σ_1 and σ_2 are the biased variances of the linear fit and the parabolic fit respectively, and n is the total number of data points. The null hypothesis (or linear fit) can be rejected at the 99.9% confidence level, since $F(1, 19)$ at 99.9% = 15.08, and therefore the parabolic fit is significant. The best-fitting ephemeris parameters for the times of light maximum are given in Table 5.3.

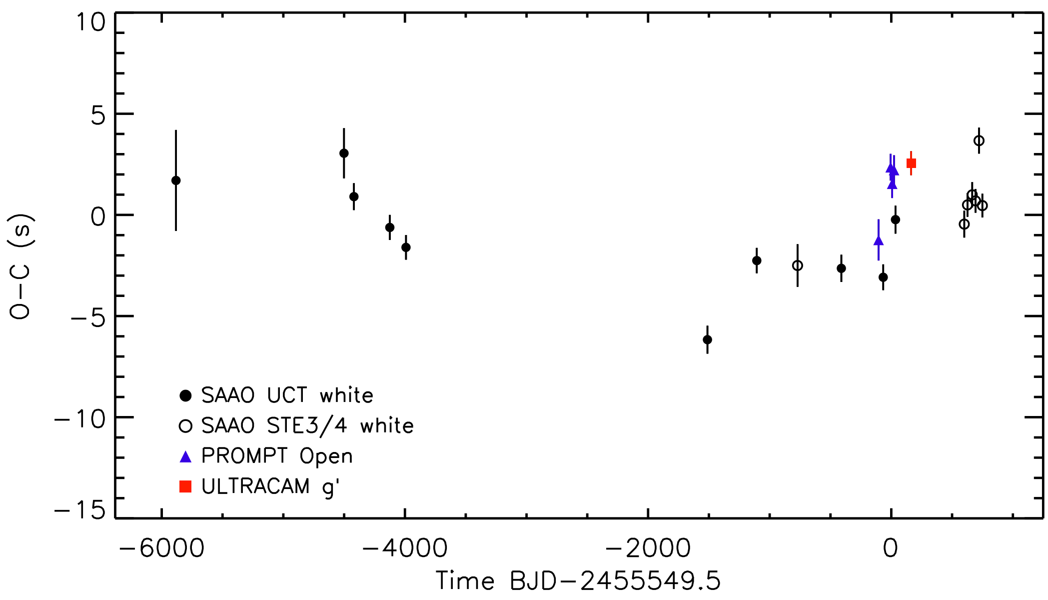

Figure 5.9: The O – C diagram of RE J0317−853. The symbols have been previously defined in Figure 5.6. The best-fitting linear ephemeris gives a reduced χ^2 of 5.92 (χ^2 of 118.37 over 20 dof). There is some scatter in the O – C points.

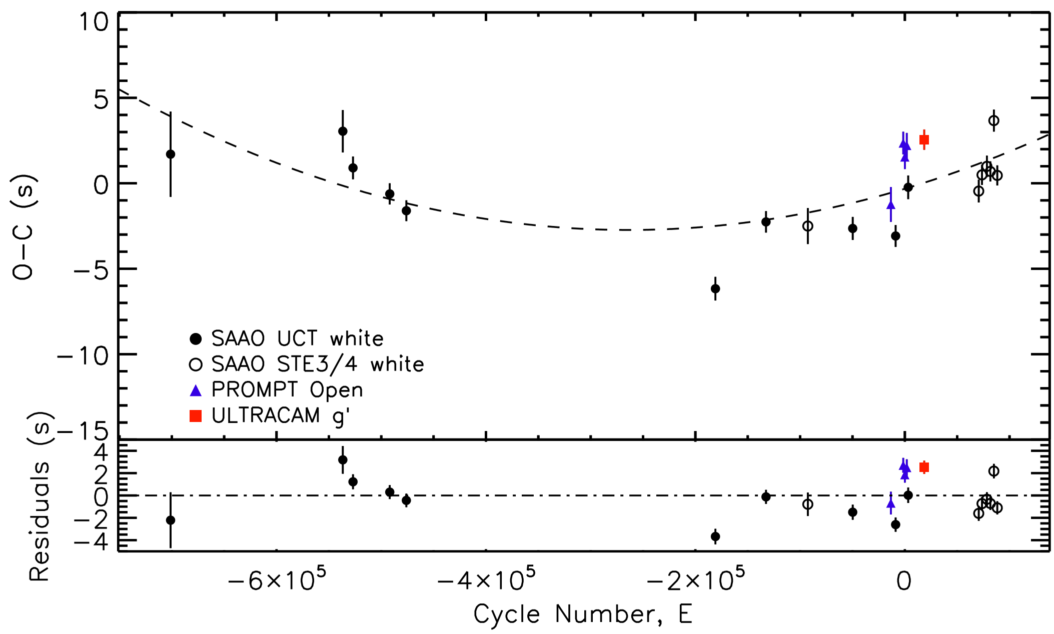

Figure 5.10: *Top panel*: The O – C diagram of RE J0317−853 with the best-fitting parabola (dashed line), which has a reduced χ^2 of 3.87 (χ^2 of 73.57 over 19 dof). The symbols have been previously defined. *Lower panel*: The residual O – C points after subtracting the parabola (dashed line).

Table 5.2: Times of observed light maximum and corresponding O – C values. Observations taken at the same epoch have been combined into a single epoch to reduce errors, hence there are fewer epochs listed here in comparison to the complete observations log in Table 5.1.

Time of maximum (BJD)	O – C (s)	O – C Error (s)
2449667.0417293	1.7	2.5
2451048.6206244	3.0	1.2
2451130.4497558	0.9	0.7
2451425.3438068	-0.6	0.6
2451558.3266738	-1.6	0.6
2454037.5434237	-6.2	0.7
2454443.4049963	-2.3	0.6
2454778.5248709	-2.5	1.1
2455138.5496377	-2.6	0.7
2455444.6992214	-1.2	1.0
2455483.0770911	-3.1	0.6
2455544.1844330	2.4	0.7
2455556.7166655	1.5	0.7
2455572.1047881	2.2	0.7
2455583.9902305	-0.2	0.7
2455712.4205439	2.6	0.6
2456149.6546394	-0.5	0.7
2456176.0798737	0.5	0.6
2456214.9617481	1.0	0.6
2456242.4369212	0.7	0.6
2456270.9116877	3.7	0.6
2456298.3868271	0.5	0.6

Table 5.3: Ephemeris parameters for the times of light maximum from Equation 5.5.

Parameter	Value	Error	Units	Comments
T_0	2455556.7250473	±0.0000067	days	time of maximum light
P	725.727684	±0.000002	s	period of photometric variability
$\dot{P}$	9.6×10^{-14}	$\pm 1.4 \times 10^{-14}$	s/s	change in period

5.5 Discussion

Here, possible mechanisms that could influence the arrival times of the maximum flux are discussed; this includes the possible spin-down of an isolated MWD due to magnetic dipole radiation, the reflex motion of a wide binary degenerate pair and the presence of planetary companions.

5.5.1 Spin-down by magnetic dipole radiation

In the first instance, the rate of period change ($\dot{P}$) was assumed to be the result of RE J0317 spinning down, possibly due to magnetic dipole radiation. Isolated neutron stars are known to spin down by magnetic dipole radiation (Ostriker & Gunn 1969; Gunn & Ostriker 1970). Magnetic dipole radiation occurs when the spin axis and the magnetic field axis of the pulsar are misaligned, causing a magnetic dipole moment and the emission of electromagnetic dipole radiation. The energy of the radiation is equivalent to the rotational kinetic energy of the neutron star. Consequently, the loss of rotational energy from magnetic dipole radiation causes the pulsar to spin down. This effect has not yet been observed for a MWD, but since RE J0317 has one of the highest magnetic field strengths for a WD, it is one of the best candidates to attempt to detect spin-down via this mechanism.

Assuming magnetic dipole radiation is occurring in RE J0317, the minimum magnetic field strength can be estimated for the period P and period derivative $\dot{P}$ using,

$$B_{min} = \left(\frac{3c^3 I}{8\pi^2 R^6}\right)^{1/2} (P\dot{P})^{1/2}, \tag{5.19}$$

where I is the moment of inertia given by $I = 2/5MR^2$ in gcm^2, and M and R are the mass and radius of the WD respectively in units of grams and centimetres. This expression is in cgs units, with the B-field given in units of Gauss. Using a mass and radius of $1.35M_\odot$ and $0.003R_\odot$ respectively for RE J0317 (Barstow et al. 1995), the expression can be simplified to,

$$B_{min} = 7.53 \times 10^{14}(P\dot{P})^{1/2}. \tag{5.20}$$

The estimates for P and $\dot{P}$, as determined from the parabolic fit to the O – C points, are then used to calculate the minimum B-field required for magnetic dipole radiation to cause the amount of measured spin-down for the parameters of the star. A minimum B-field of ~6200 MG is calculated. This estimate is very high and well above the range of field strengths measured for RE J0317 with a maximum at 800 MG (Burleigh et al. 1999). No magnetic field strength has ever been measured for a MWD larger than 1000 MG. There is considerable uncertainty in the mass and radius estimates: Külebi et al. (2010) report possible masses for RE J0317 of $1.28M_\odot$ to $>1.46M_\odot$ and radii of $0.00293 - 0.00416R_\odot$ depending on the core composition model and temperature used. Even taking this uncertainty into consideration, it does not account for the large estimated B_{min}.

The characteristic age τ can be determined as a function of the period P and the rate of period change $\dot{P}$ by,

$$\tau \equiv \frac{P}{2\dot{P}}. \tag{5.21}$$

The P and $\dot{P}$ values that are determined from the O – C fitting process give a characteristic timescale of 120 Myr. This is roughly comparable to the cooling age of RE J0317 (~300 Myr, Külebi et al. 2010), although it is on the young side.

By contrast, since all of the parameters in Equation 5.19 are known, the expression can be rearranged to calculate the expected value of $\dot{P}$ given the measured magnetic field strength. Using the measured range of magnetic field strengths 180 – 800 MG (Burleigh et al. 1999), the corresponding $\dot{P}$ is found to span 7.9×10^{-17} s/s up to 1.6×10^{-15} s/s for the respective B-field boundaries. This is 1 – 3 orders of magnitude smaller than the value determined from the O – C diagram with Equation 5.5. The $\dot{P}$ value derived for 800 MG is comparable to the $\dot{P}$ values expected from the WD core cooling ($\dot{P} \sim 10^{-15}$ s/s, Winget & Kepler 2008), which is essentially a measurement of the evolutionary timescale of the WD. The $\dot{P}$ calculated for 180 MG would be undetectable as other mechanisms, such as

WD cooling, would be more dominant. This illustrates that spin-down due to magnetic dipole radiation will only ever be measurable for the highest field, isolated MWDs. Furthermore, this B-field range yields characteristic timescales in the range of 7 – 146 Gyears. The timescale derived for the lower field strength stars (at 180 MG) is longer than the age of the Universe, further demonstrating that this effect would not be observable for the majority of MWDs. For the higher field strength WDs (at 800 MG), the timescale is comparable to the cooling age of old WDs, although it is not compatible with the age of this MWD. Consequently, from these discrepancies, magnetic dipole radiation has been ruled out as the cause of the $\dot{P}$ in the O – C diagram.

5.5.2 Reflex Motion

In the previous section, I discussed the possibility that the $\dot{P}$ obtained from the O – C diagram was from the MWD spinning down as a result of magnetic dipole radiation, but concluded that it was an unlikely scenario. Since RE J0317 is in a wide binary with the non-magnetic DA WD LB 9802, the $\dot{P}$ could be caused by the degenerate companion to the MWD.

Due to the close proximity between RE J0317 and the nearby WD LB 9802 on the projected sky, Barstow et al. (1995) assumed that the two stars were probably linked. The common proper motion of the double-degenerate pair was later confirmed using SuperCOSMOS observations from the UK Schmidt Telescope (UKST) separated by a baseline of ~25 years (Farihi, Becklin & Zuckerman 2008). Külebi et al. (2010) measured a separation of 7” (equivalent to 210 AU at a distance of 30.05 pc) using HST observations. Assuming a total mass of $2.02 - 2.31 M_{\odot}$ and a circular orbit, Külebi et al. (2010) calculate that the orbital period is approximately 2004 – 2143 years.

Using Equation 5.12, the expected upper limit on the $\dot{P}$ due to reflex motion is calculated as $(2.42 - 2.78) \times 10^{-13}$ s/s using the mass of the MWD companion LB 9802

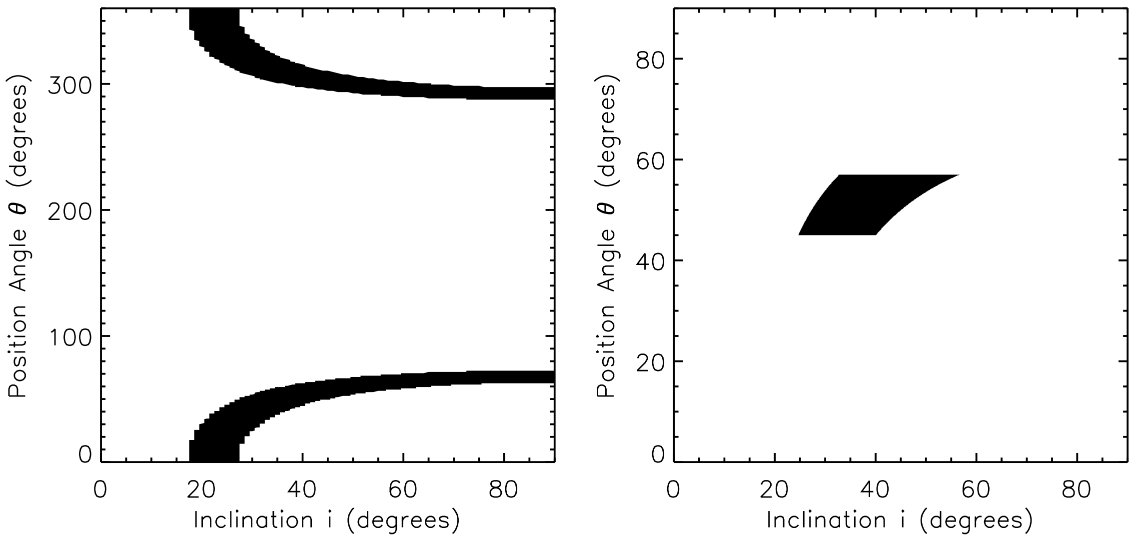

Figure 5.11: The orbital inclination angle with the position angle in the orbit ($i-\theta$). The dark regions indicate angles where the theoretical $\dot{P}$ matches the measured $\dot{P}$ value within uncertainties. *Left:* All possible angles are explored across the inclination and position angle. *Right:* The parameter space is constrained further using measurements for the orbital velocity and tangential space velocity from Külebi et al. (2010).

($0.76-0.84M_{\odot}$), the separation between the two stars ($a_p = 210 \pm 2$ AU) and the period of RE J0317's photometric variability. Assuming the measured $\dot{P}$ is correct, the difference between the upper limit and the measured $\dot{P}$ can place constraints on the position angle θ and inclination angle i of the binary system. From Equation 5.11, the $\cos\theta \sin i$ term required for the theoretical $\dot{P}$ and measured $\dot{P}$ to match within uncertainties is determined. Figure 5.11 (*left*) shows the $i-\theta$ parameter space for an inclination angle between $0-90°$ and a position angle between $0-360°$, where the black regions indicate the combinations of i and θ that are required for the theoretical $\dot{P}$ to be consistent with the measured $\dot{P}$. The $i-\theta$ parameter space is constrained further in Figure 5.11 (*right*), where the orbital velocity ($2.92-3.12$ km/s) and tangential space velocity (2.33 ± 0.12 km/s) from Külebi et al. (2010) are used to calculate a range of position angles and therefore inclination angles. For the theoretical $\dot{P}$ to be consistent with the measured $\dot{P}$, the possible position angles and inclination angles are $\theta = 45-57°$ and $i = 24.7-56.8°$ respectively.

Additionally, to establish whether the orbital motion of the pair would be detected in the O – C analysis, simulations are conducted for a range of companion masses and orbital separations to the MWD, RE J0317. The same method is used here as outlined in Mullally et al. (2008) to place constraints on the parameter space of companions to which the current data sampling is sensitive.

Figure 5.12 is a relief map of the companion mass – orbital separation parameter space given the time sampling, where the dark shaded regions represent the highest sensitivity. Assuming a circular orbit, the motion of RE J0317 and a companion about the centre of mass can be described by a sinusoid in an O – C diagram, where the period P of the light curve is calculated using Equation 5.6 and the semi-amplitude τ is determined by Equation 5.10. These parameters are calculated for a given companion mass and orbital separation. An O – C sinusoid is generated for a given companion mass m_p and orbital separation a_p and sampled at the same times as in the O – C diagram, with the same O – C uncertainties. Random Gaussian noise is added to the synthetic O – C points distributed by the standard deviation of the actual O – C data. The light curve is then analysed using a floating-mean periodogram and the power of the maximum peak is determined. Using this information, the false alarm probability is then calculated using the same method detailed in §2.4.2 on significance tests. In brief, the false alarm probability is determined as the number of times noise fluctuations alone from 1000 fake O – C plots cause a larger signal in the periodogram than the signal from the original. This process is repeated across the entire companion mass – orbital separation parameter space. The dark shaded regions in Figure 5.12 indicate a false alarm probability of 1% or less. The non-magnetic WD companion LB 9802 lies within the parameter space that would be detected with the current data sampling (represented by a white ring in Fig. 5.12). Consequently, it is possible that the $\dot{P}$ measured from the O – C diagram (Fig. 5.9) is due to the reflex motion of RE J0317 with its non-magnetic WD companion.

As a result, this hypothesis is additionally tested by fitting the O – C data points with a sinusoid representing the reflex motion expected in the O – C diagram between RE J0317 and LB 9802 orbiting about the centre of mass of the system. For a circular orbit ($e = 0$), this effect can be modelled with a sine curve plus a constant. Figure 5.13 (*top*) shows

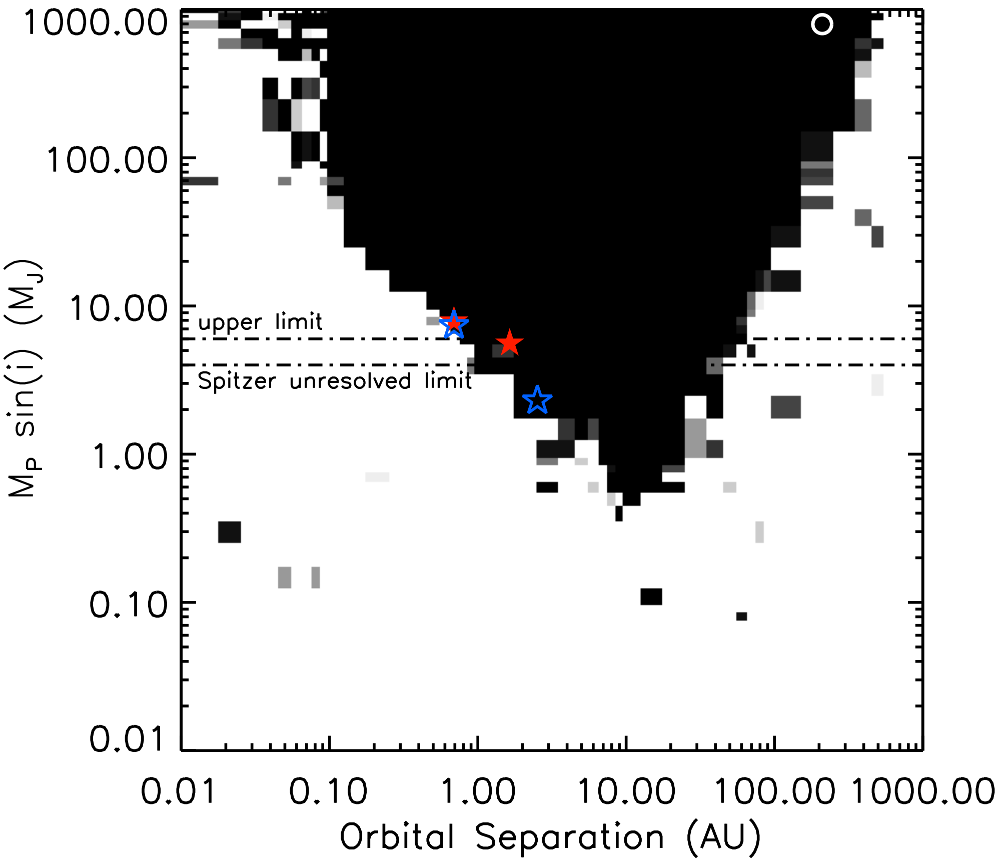

Figure 5.12: Relief map of the companion mass – orbital separation parameter space showing the regions where companions orbiting RE J0317−853 could be detected given the O – C time sampling. The dark shaded regions represent the highest sensitivity and indicate a false alarm probability of 1% or less. The white ring (*top-right*) is the location of the non-magnetic WD companion LB 9802 of $0.76 M_\odot$ at a separation of 210 AU. The dot-dashed lines indicate upper limits on an unresolved companion of $4 - 6 M_{\rm Jup}$ from *Spitzer* observations (Farihi, Becklin & Zuckerman 2008). The filled red stars represent a possible companion from the O – C data points of $M \approx 5.6 M_{\rm Jup}$ at 1.64 AU and from the O – C residuals from the parabolic fit of $M \approx 7.9 M_{\rm Jup}$ at 0.69 AU (as explained further in §5.5.3). The unfilled blue stars represent the possible companions of $M \approx 2.3 M_{\rm Jup}$ at 2.52 AU and $M \approx 7.4 M_{\rm Jup}$ at 0.69 AU obtained from the residuals from fitting a circular orbit and an eccentric orbit ($e = 0.3$) respectively for the orbital motion of the degenerate WD pair.

the best-fit orbital motion (for $e = 0$) to the data points from the O – C analysis. The inset focuses on the data points. The residuals of the best-fit are shown in the lower panel. Considering the length of the orbital period and the limited phase coverage of the data points, the fit is unsurprisingly poor with a reduced χ^2 of 10.92. The period P and semi-amplitude τ of the orbital motion are calculated using Equation 5.6 and Equation 5.10 respectively using the orbital separation as $a_p = 210$ AU, RE J0317's mass as $M_\star = 1.35M_\odot$ and the companion WD mass as $m_p = 0.76M_\odot$ (parameter values taken from Barstow et al. 1995 and Külebi et al. 2010). For the final fit in Figure 5.13 (*top*), the eccentricity, period and semi-amplitude are kept as fixed parameters, and only the y-offset γ in the O – C and the phase ϕ are allowed to float. When the period and semi-amplitude are left as free floating parameters, they remain unchanged at their starting values and the minimisation is not appropriately optimised. This is not surprising due to the large number of free parameters in comparison to the total number of data points and the small amount of coverage over the orbital period. With future observations of RE J0317, the parameters in the model could be improved; possibly providing an useful independent estimate for the total mass of the system and thus an accurate mass of the MWD, which has been difficult to determine due to the magnetic nature of the star and because it is so massive, at the limit of many models.

The orbital motion fit is also considered for a range of eccentricities. It is unlikely that the orbit is circular, especially since the favoured hypothesis for the formation of RE J0317 is a merger. For an eccentric orbit, the O – C data is modelled with the following expression,

$$O - C = \gamma + \tau \frac{1 - e^2}{1 + e\cos(2\pi t/P)} \sin\left(\frac{2\pi t}{P} + \phi\right) \tag{5.22}$$

where γ is the y-offset in the O – C in seconds, τ is the semi-amplitude in seconds (defined in Eq. 5.10 in terms of a_p, m_p and $M_\star$), e is the eccentricity of the orbit, P is the orbital period in years, t are the times of maximum flux for the O – C data points in years and ϕ is the phase in years. If the eccentricity is set to zero, Equation 5.22 simplifies to the expression for a circular orbit: a simple sine curve plus a constant. The best-fitting eccentric orbit occurs for $e = 0.3$ with a reduced χ^2 of 6.74, as shown in Figure 5.13 (*bottom*). As with the circular orbit case, the period and semi-amplitude are kept fixed at the approximations determined. The eccentric $e = 0.3$ case yields a more suitable fit to the O – C points than the circular case and visually is more comparable to the parabolic fit in Figure 5.10. The scatter in the residuals in both sets are pretty similar at approximately a few seconds. However, it is also worth remembering that ~20 years of observations over a potentially 2000 year orbit is a small fraction and the orbital motion fit parameters, such as the orbital period and amplitude, are not well constrained. Nevertheless, the theoretical $\dot{P}$ calculation due to a nearby companion (Eq. 5.11) and the companion mass – orbital separation parameter space simulations (Fig. 5.12) demonstrate that the observed $\dot{P}$ from the O – C diagram (Fig. 5.10) is most likely due to the orbital motion between RE J0317 and its WD companion LB 9802.

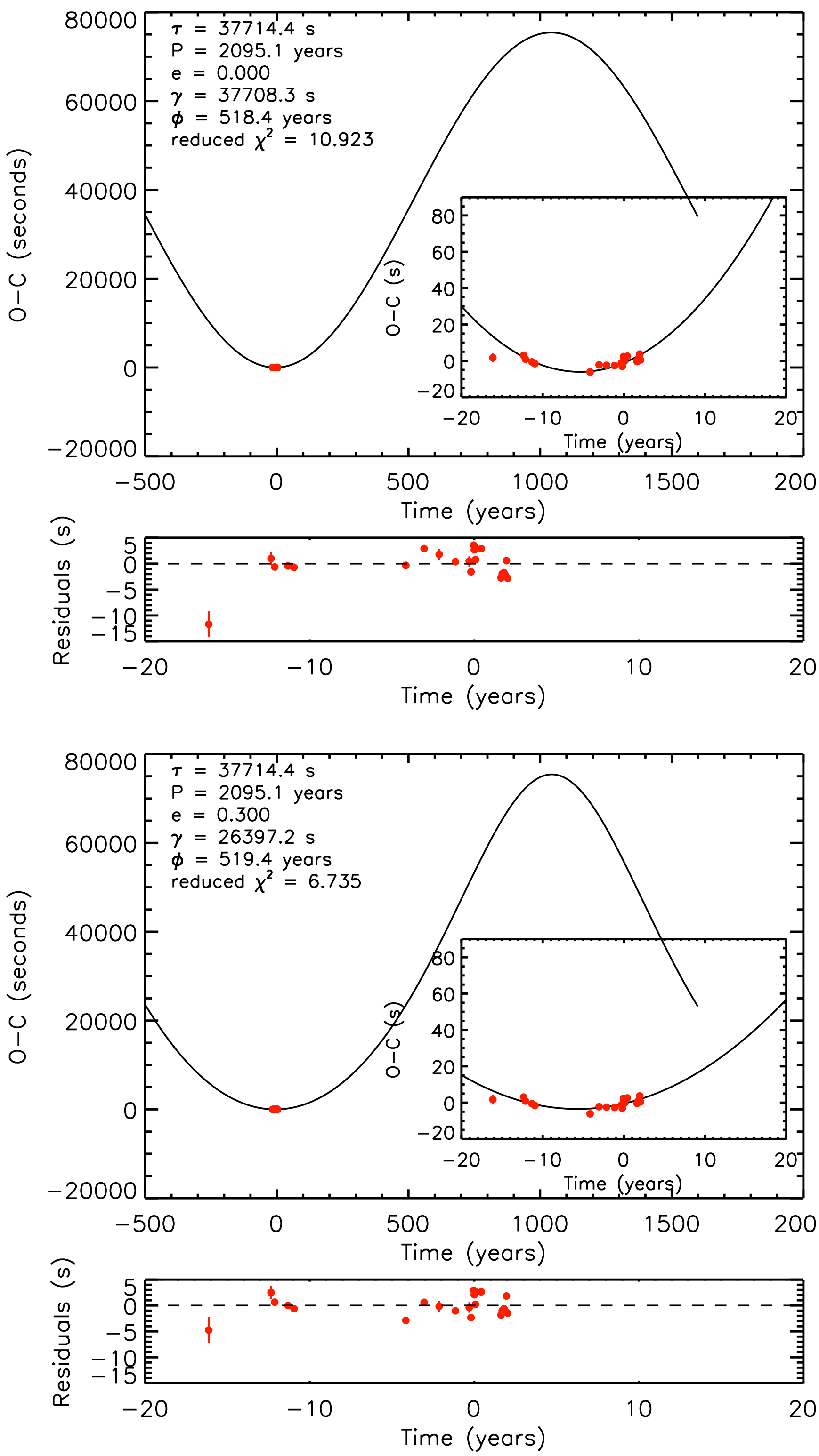

Figure 5.13: Orbital motion fit of the double-degenerate wide binary on the O – C diagram assuming a circular orbit ($e = 0$, *top*) and an eccentric orbit ($e = 0.3$, *bottom*). The red circles are the O – C data points and in both plots the inset focuses on the data points with the model. The lower panel for each figure is the residuals to the fit. The fit details are printed on each figure and the parameters are explained in the text.

5.5.3 Planetary companion?

The data in the O – C diagram (Fig. 5.9) appear to exhibit some non-random scatter. This has been investigated further to determine whether a period of variability exists in the O – C data and if it is significant. The following subsections examine and discuss the variations in: the O – C data points (Fig. 5.9), the O – C residuals from the best-fitting parabolic fit (Fig. 5.10), the O – C residuals from a circular orbital motion fit of the two WDs (Fig. 5.13, *top*) and the O – C residuals from an eccentric orbital motion fit of the two WDs (Fig. 5.13, *bottom*).

Analysis of the O – C data points

The O – C data points are analysed for any periodicity using a Fourier transform and floating-mean periodogram. Figure 5.14 shows the FT, floating-mean periodogram and the corresponding sine curve model (i.e. assuming a circular orbit), using the frequency at the χ^2 minimum, with the O – C data (Fig. 5.14, *bottom*). The minimum χ^2 in the periodogram is taken at a frequency of 0.553729 cycles/year (a period of 1.806 years), which is used to fit a sine curve to the O – C points, giving a semi-amplitude of 3.2 ± 0.3 s for the best-fit. Consequently, using Equations 5.6 and 5.10, a planetary companion causing these fluctuations may have a minimum mass of $m_p \sin i = 5.6 M_{\mathrm{Jup}}$ at an orbital separation of $a_p = 1.64$ AU. This sine fit to the O – C data points gives a reduced χ^2 of 5.88. An estimate for the false alarm probability (FAP, method detailed in §2.4.2) yields a value of 0.164; above the significance threshold at $FAP \leq 0.01$. Further data over the coming years could improve the FAP estimate to give a significant result. However, if the periodicity is not real and is just a product of the window function, the FAP will not improve. An F-test indicates there is a significant difference between a constant fit and the sine fit at a 90% confidence level.

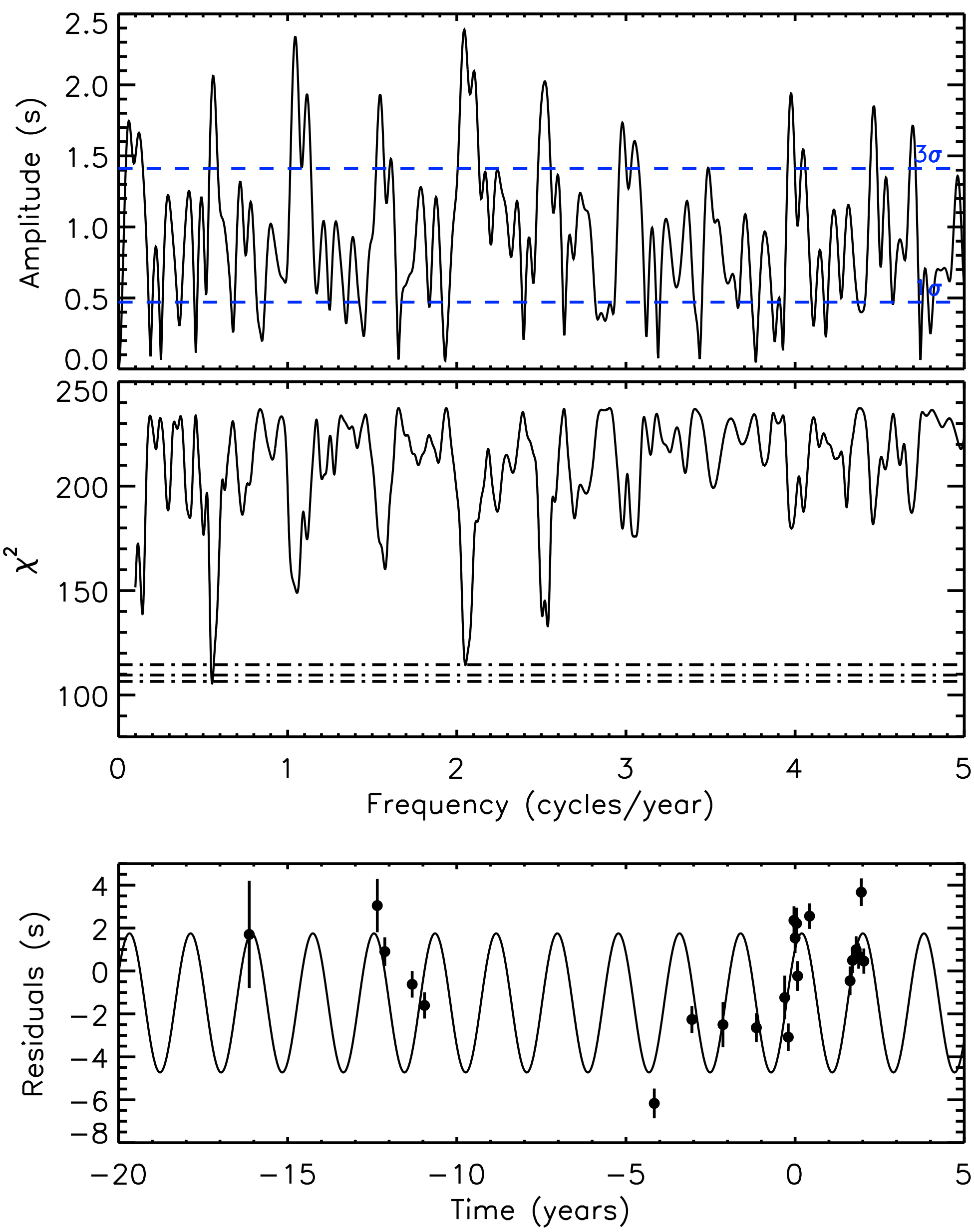

Figure 5.14: *Top panel:* FT of the O – C data points shown in Figure 5.9. The dashed lines indicate the σ and 3σ noise levels. *Middle panel:* Floating-mean periodogram. The χ^2 minimum has a frequency at 0.553729 cycles/year (a period of 1.806 years). Aliases in the periodogram are also seen at 1 and 2 cycles/year. The dot-dashed lines on the periodogram indicate a change in χ^2 of 1, 4 and 9 from the global minimum (equivalent to 1σ, 2σ and 3σ uncertainties respectively). *Lower panel:* The best-fitting sinusoid has a period of 1.806 years and a semi-amplitude of 3.2 ± 0.3 s, with a reduced χ^2 of 5.88. Such fluctuations could be caused by a possible companion of $m_p \sin i = 5.6 M_{\rm Jup}$ at a separation of $a_p = 1.64$ AU.

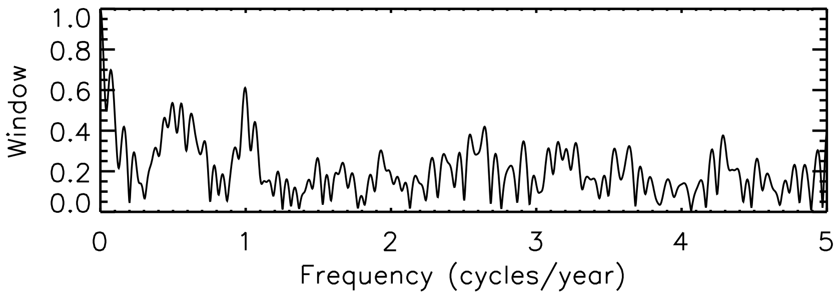

Figure 5.15: Window function of the O – C data points. Aliases in the real periodogram are expected at $|f \pm f_S|$ where f is the sinusoid frequency and f_S is the frequency of the window function feature.

The window function of the O – C diagram is shown in Figure 5.15. There is a peak in the window function at 1 cycle/year, but there is also a lot of complicated structure at frequencies around 0.5 cycles/year. Following the prescription in Dawson & Fabrycky (2010) for identifying aliases in periodograms of radial velocity data, fake O – C data points are generated with the same frequency, phase and amplitude as the peaks in the real FT. The corresponding FTs for the noise-free O – C data are then compared with the real FT, as shown in Figure 5.16, in particular focusing on similarities between the amplitude and location of the peaks. Lomb (1976) simply remarked, "If there is a satisfactory match between an observed spectrum and a noise-free spectrum of period P, then P is the true period.". Furthermore, the data are not sufficient to determine the true period if several candidate sinusoids cannot suitably reproduce the periodogram.

The FT of the noise-free $P = 1.806$ years sinusoid (Fig. 5.16, *fourth row*) best reproduces the peaks of the observed FT, as the amplitude of the sinusoid frequency is comparable to the real FT. However, not all of the peaks are as consistent with the real data, which could simply be an effect of noise in the real O – C data on the FT. The real FT (Fig. 5.16, *first row*) has aliases at frequencies ~1 cycle/year and ~2 cycles/year, where the latter alias is particularly strong as it is also the length of the observing season (~6 months). The features at ~1.5 and ~2.5 cycles/year appear to be aliases of the possibly real frequency at P =1.806 years. FTs of the noise-free sinusoids based on these periods do not reproduce all of the dominant peaks found in the real FT or with the same amplitude. However, I am reluctant to definitively claim whether the 1.806 year period is real or not as the noise-free

FT does not quite reproduce the observed one.

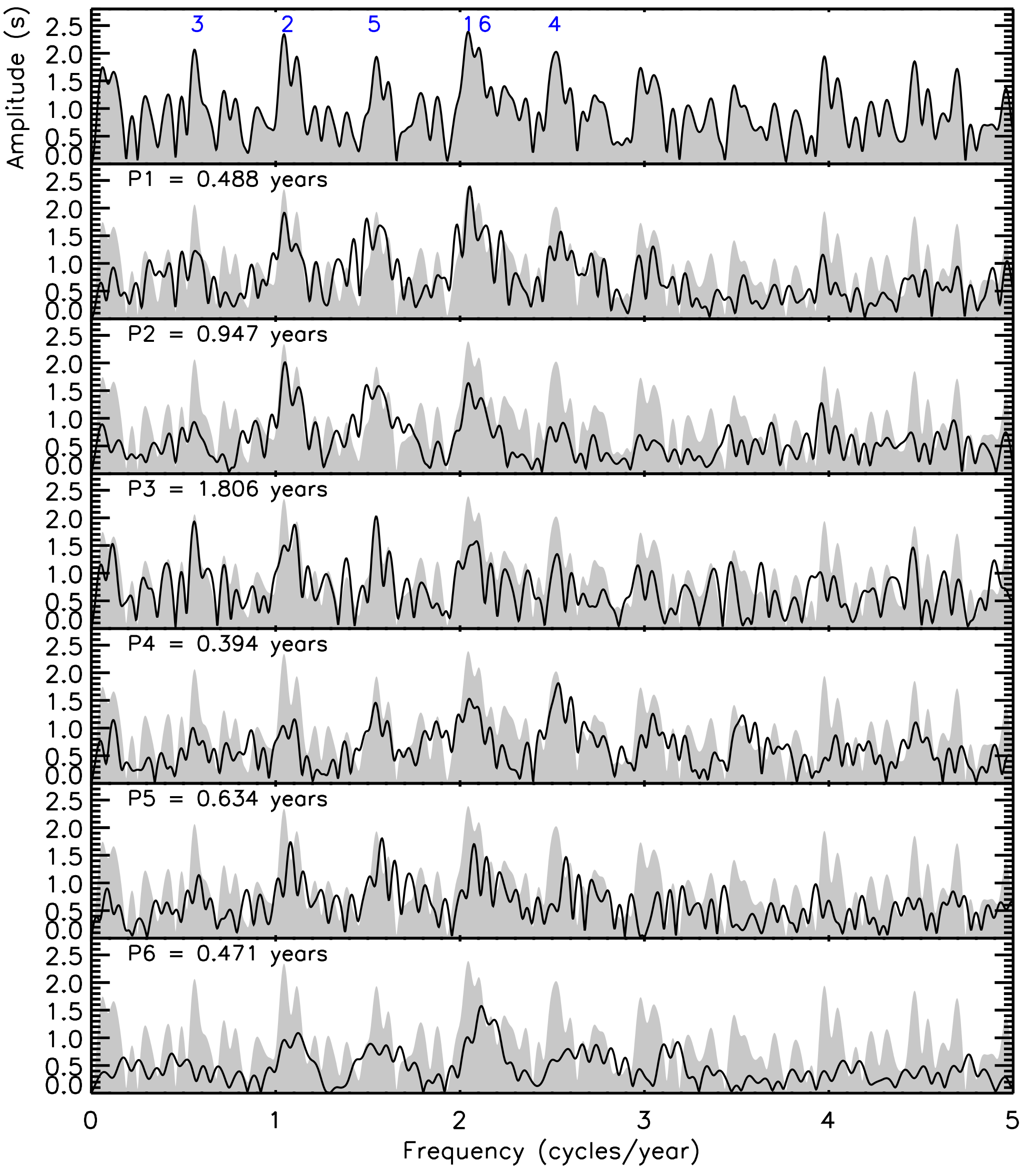

Figure 5.16: The top row shows the FT of the O – C data points (also shown in Fig. 5.14). The other rows show FTs of fake, noiseless sinusoids sampled at the same times as the real data set (solid line), with the FT of the real data in grey for reference. The numbers in the top row indicate the frequencies used to create the fake sinusoids. The FT of the sinusoid with a period of 1.806 years (P3) reproduces many of the real peaks in the FT, apart from the aliasing peaks at frequencies around 1 and 2 cycles/year. However, none of the FTs of the fake sinusoids resemble the FT of the real data, and therefore the data are probably not sufficient to determine a true period.

Analysis of the O – C residuals from the parabolic fit

The O – C residuals from the best-fitting parabolic fit shown in Figure 5.10 have also been examined for variations. The corresponding FT and floating-mean periodogram are given in Figure 5.17, where both periodograms show features at a frequency of 2.046900 cycles/year (a period of 0.489 years). The best-fitting sinusoid to the O – C residuals using this period (Fig. 5.17, *bottom*) has a semi-amplitude of 1.9 ± 0.2 s and gives a reduced χ^2 of 3.23. Using Equations 5.6 and 5.10, a planetary companion would have a minimum mass of $m_p \sin i = 7.8 M_{\rm Jup}$ and orbital separation of $a_p = 0.69$ AU to cause the periodicity in the fluctuations in the O – C residuals. There are no other minima in the floating-mean periodogram within the 3σ uncertainties of the global χ^2 minimum, although there are a number of peaks in the FT across the frequency range above the 3σ noise level. Therefore, the 0.489 year period is probably an alias due to the window function. An estimate for the false alarm probability is 0.528, which is well above the significance threshold at a FAP $\leq$ 0.01. An F-test between a constant fit to the data and the sine fit reveals the null hypothesis (constant fit) can be rejected at a 90% confidence level, indicating the O – C residuals from the parabolic fit may be variable. However, more observations are required to determine the periodic nature of the modulations. An analysis of the aliasing peaks in the FT of the O – C residuals is shown in Figure 5.18, where FTs are calculated for noise-free sinusoids sampled at the same times as the O – C data with periods corresponding to peaks in the real FT (denoted by numbers in the top row of Fig. 5.18). None of the selected periods reproduce the peaks in the real FT, suggesting the data are insufficient to determine a true periodicity, and that the data are not variable on a period of 0.489 years.

Analysis of the residuals from the O – C orbital motion fit of the two WDs

In addition, this investigation has been extended to search for periodicities in the residuals from the best-fitting orbital motion models between the two white dwarfs, RE J0317 and LB 9802, shown in Figure 5.13. As before, the residuals are analysed using a FT and floating-mean periodogram. Figures 5.19 and 5.20 show the FTs and floating-mean periodograms of the residuals for both cases of eccentricities ($e = 0$ and $e = 0.3$) and the

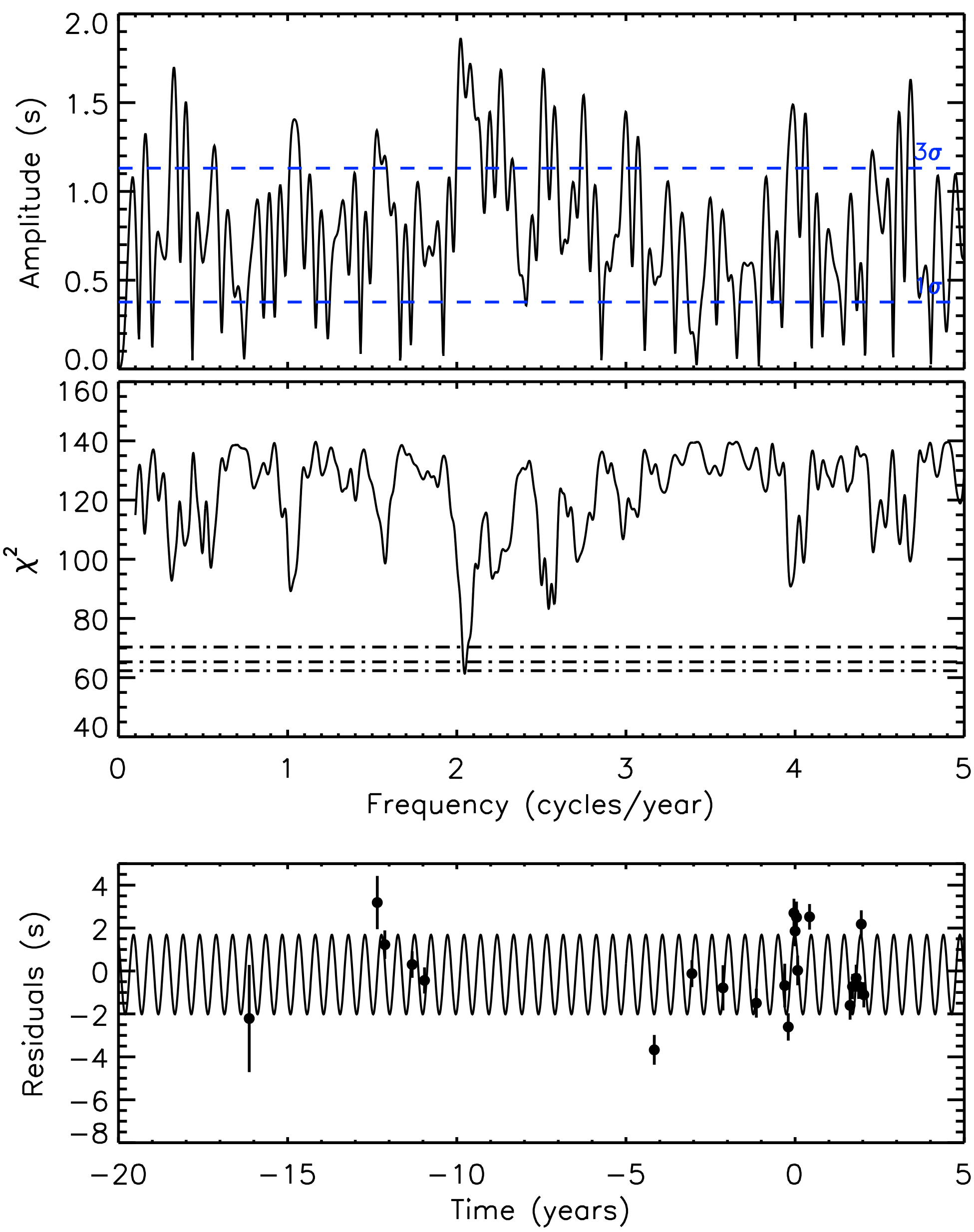

Figure 5.17: *Top panel:* FT of the O – C residuals from the parabolic fit in Figure 5.10. The dashed lines indicate the σ and 3σ noise levels. *Middle panel:* Floating-mean periodogram. The χ^2 minimum has a frequency at 2.046900 cycles/year (a period of 0.489 years). Aliases in the periodogram are also seen at 1 and 2 cycles/year. The dot-dashed lines indicate a change in χ^2 of 1, 4 and 9 from the global minimum (equivalent to 1σ, 2σ and 3σ uncertainties respectively). *Lower panel:* The best-fitting sinusoid has a period of 0.489 years and a semi-amplitude of 1.9 ± 0.2 s, with a reduced χ^2 of 3.23. Such fluctuations could be caused by a possible companion of $m_p \sin i = 7.9 M_{\rm Jup}$ at a separation of $a_p = 0.69$ AU.

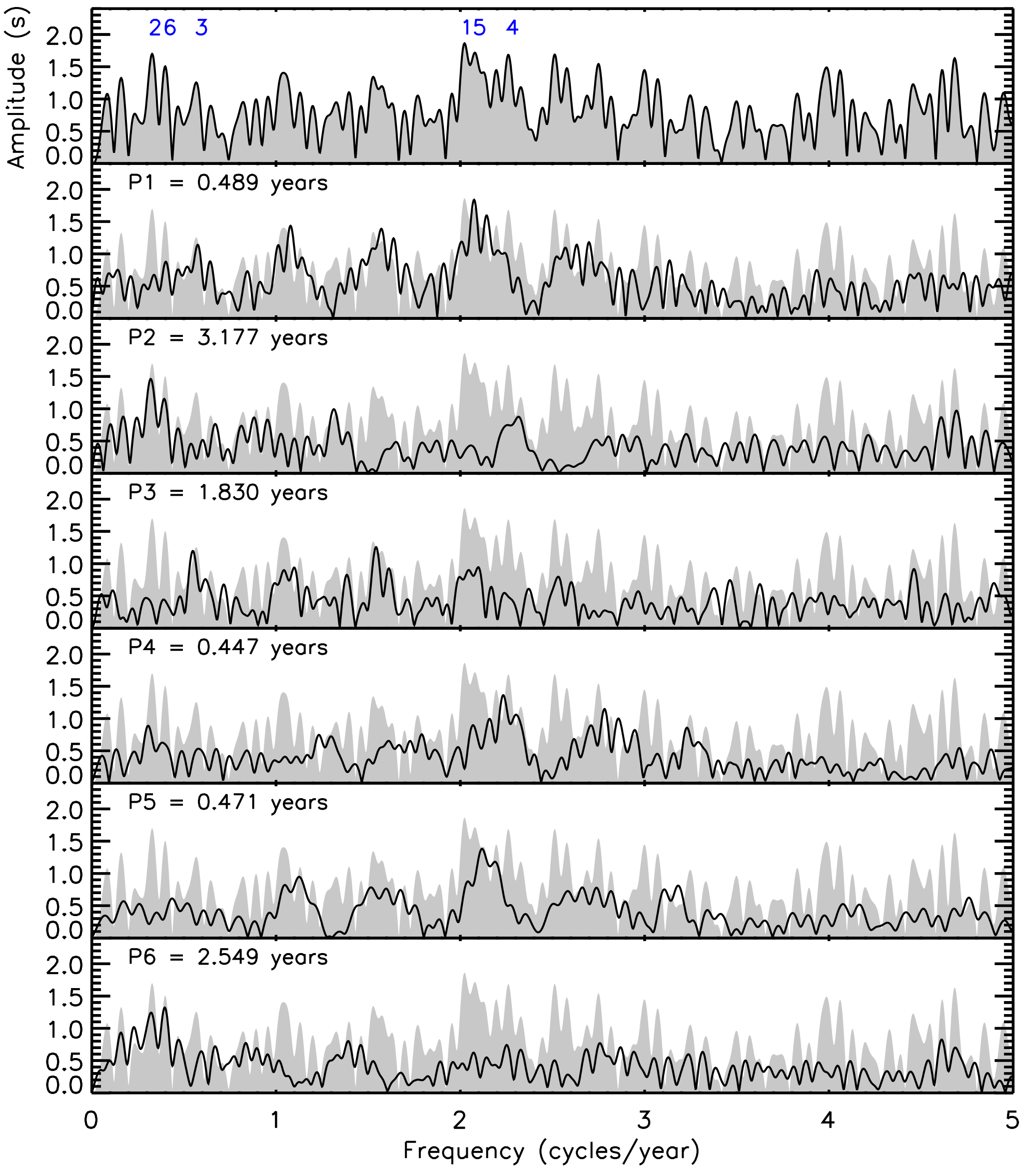

Figure 5.18: The top row shows the FT of the O – C residuals from the parabolic fit (also shown in Fig. 5.17). The other rows show FTs of fake, noiseless sinusoids sampled at the same times as the real data set (solid line), with the FT of the real data in grey for reference. The numbers in the top row indicate the frequencies used to create the fake sinusoids. None of the FTs of the noiseless sinusoids reproduce the FT of the real data, implying a true period has not been detected.

corresponding best-fitting sinusoids are plotted with the residuals, using the frequency at the minimum χ^2 in the periodogram. The eccentricity of the best-fitting planetary orbit is kept fixed at $e = 0$.

The residuals from the circular orbit case (Fig. 5.19) have a minimum χ^2 in the periodogram at a frequency of 0.290630 cycles/year (a period of 3.44 years). A best-fitting sine curve to the residuals with this period has a semi-amplitude of 2.0 ± 0.2 s. This yields a possible planetary companion with a minimum mass of $m_p \sin i = 2.3 M_{\rm Jup}$ at a separation of $a_p = 2.52$ AU to cause the fluctuations in the O – C residuals, giving a reduced χ^2 of 5.45. For the eccentric orbital motion $e = 0.3$ case (Fig. 5.20), the periodogram of the residuals has the minimum χ^2 at a frequency at 2.046461 cycles/year. Therefore, the best-fitting sinusoid has a period of 0.489 years and a semi-amplitude of 1.8 ± 0.2 s, giving a reduced χ^2 of 3.42. These photometric modulations correspond to a possible companion at $a_p = 0.69$ AU with a minimum mass of $m_p \sin i = 7.4 M_{\rm Jup}$. Both periodograms in Figures 5.19 and 5.20 have features at approximately the same frequencies, illustrating the effect of the window function (Fig. 5.15). Statistically, neither of these fits are significant results with false alarm probabilities of 0.309 and 0.340 for $e = 0$ and $e = 0.3$ respectively. Similarly, an F-test shows the sine fit in both cases is not a significantly better fit than a constant fit at a level of 90%. An additional concern is the comparable size of the residuals' uncertainties and the semi-amplitude of the best-fitting sine curve. If the uncertainties are underestimated, which is entirely possible as they are only formal 1σ uncertainties, then the periodic modulations may disappear (or at least be substantially harder to detect). The eccentricity of the planetary orbit was also investigated, where it was allowed to float free during the fitting process, however in all cases the fitting favoured a circular orbit. Studies of planets orbiting main-sequence stars have shown there is a vast range in orbital eccentricities (Kane et al. 2012), and therefore it is plausible planetary systems orbiting WDs would also have eccentric orbits.

Farihi, Becklin & Zuckerman (2008) used observations from the Spitzer Infrared Array Camera (IRAC) to search for infrared excesses at $4.5\,\mu$m to put constraints on planetary

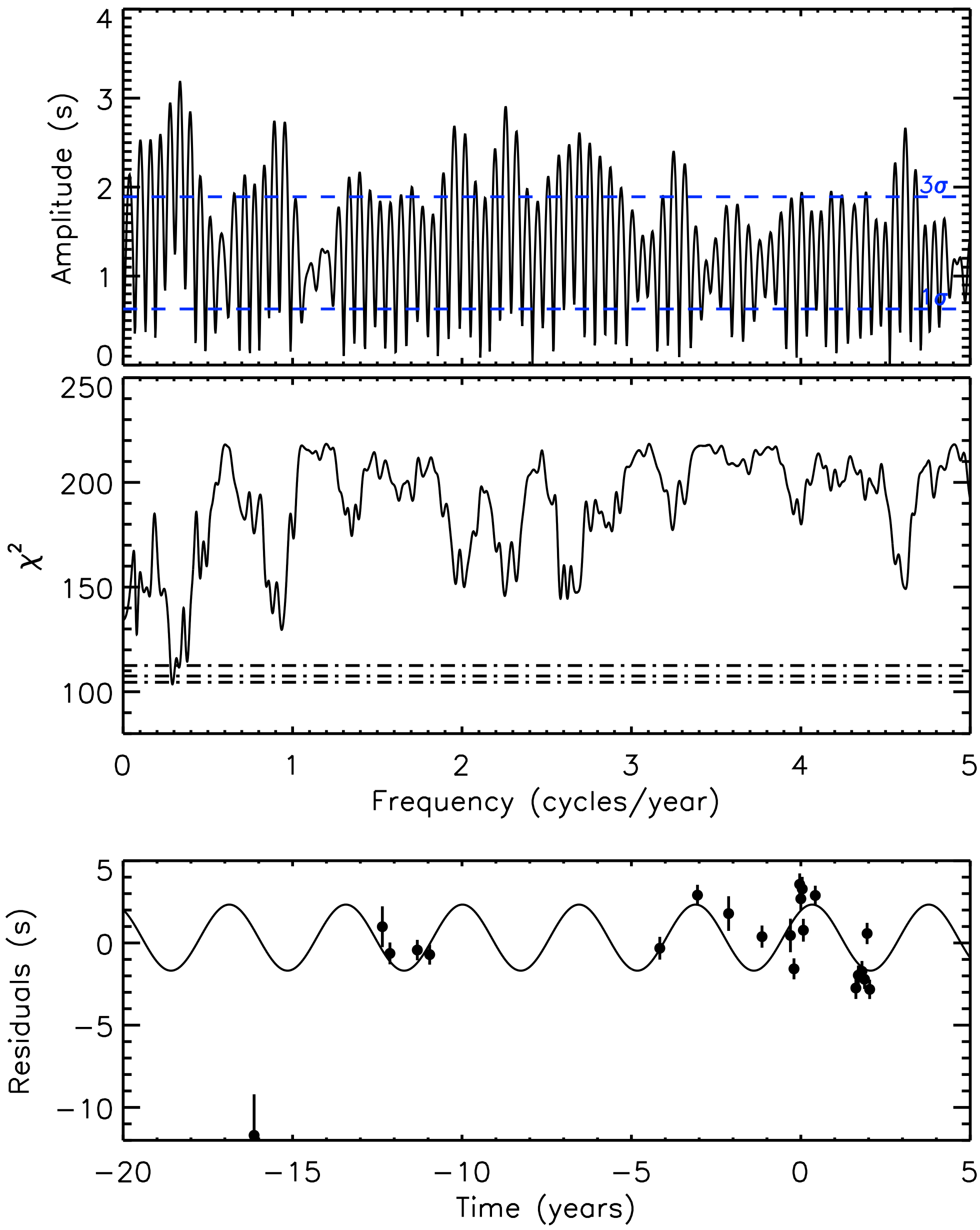

Figure 5.19: *Top panel:* FT of the residuals from the O – C circular orbital motion fit of the two WDs in Figure 5.13 (*top*). The dashed lines indicate the σ and 3σ noise levels. *Middle panel:* Floating-mean periodogram of the residuals from the circular fit. The minimum χ^2 occurs at a frequency of 0.290630 cycles/year (a period of 3.44 years). Aliases in the periodogram are also seen at 1 and 2 cycles/year. The dot-dashed lines indicate a change in χ^2 of 1, 4 and 9 from the global minimum (equivalent to 1σ, 2σ and 3σ uncertainties respectively). *Lower panel:* The best-fitting sinusoid to the residuals has a period of 3.44 years and a semi-amplitude of 2.0 ± 0.2 s, with a reduced χ^2 of 5.45. Such fluctuations may be caused by a companion of $m_p \sin i = 2.3 M_{\rm Jup}$ at a separation of $a_p = 2.52$ AU.

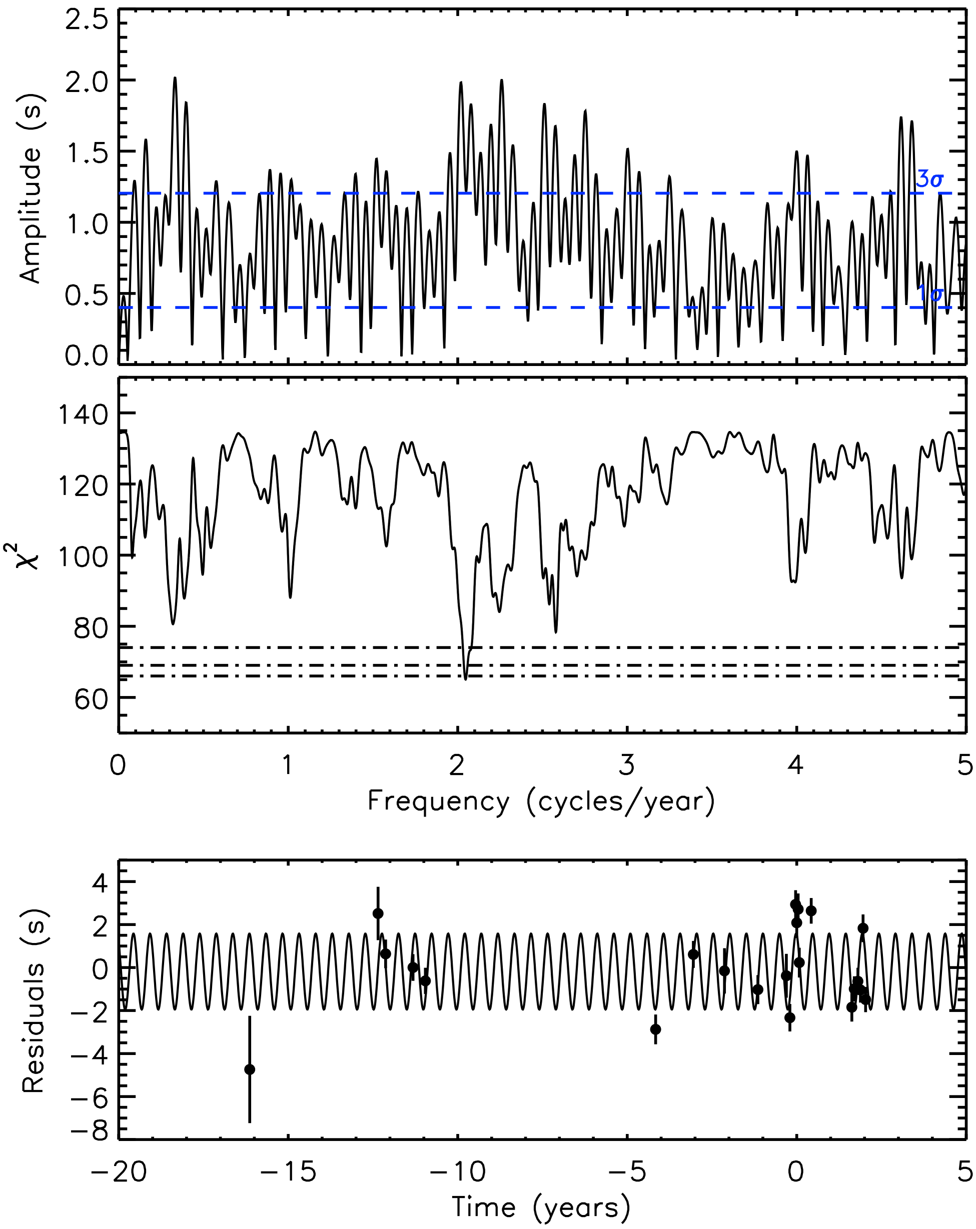

Figure 5.20: *Top panel:* FT of the residuals from the O – C eccentric ($e = 0.3$) orbital motion fit of the two WDs in Figure 5.13 (*bottom*). The dashed lines indicate the σ and 3σ noise levels. *Middle panel:* Floating-mean periodogram of the residuals from an eccentric $e = 0.3$ fit, where the minimum χ^2 has a frequency of 2.046461 cycles/year ($P = 0.489$ years). The dot-dashed lines indicate a change in χ^2 of 1, 4 and 9 from the global minimum (equivalent to 1σ, 2σ and 3σ uncertainties respectively). *Lower panel:* The best-fitting sinusoid has a period of 0.489 years with a semi-amplitude of 1.8 ± 0.2 s and reduced χ^2 of 3.42. This may correspond to a planetary companion of $m_p \sin i = 7.4 M_{\rm Jup}$ at $a_p = 0.69$ AU.

companions to WDs. They found no infrared excess in the spectral energy distribution of RE J0317. Using evolutionary model predictions for the luminosity of substellar objects at various ages, an unresolved upper limit is estimated as $\sim 6 M_{\rm Jup}$ for a companion to RE J0317, assuming an age of 450 Myr (the total evolutionary age of LB 9802). However, uncertainties in the total age of RE J0317 suggest this mass limit could be smaller at $\sim 4 M_{\rm Jup}$ using an age estimate of 300 Myr (possible age of RE J0317 if it formed in a merger, Külebi et al. 2010). This possible companion mass range has been marked on Figure 5.12 with dot-dashed lines, which is also comparable to the companion masses obtained from the O – C modulations. It is evident from Figure 5.12 that a companion of $4 - 6 M_{\rm Jup}$ at a distance of $\gtrsim 1$ AU could be significantly detected in the O – C analysis with the current data sampling, as it lies right within the detectable region. A concerted effort was made during the 2012/13 observing season to obtain extensive, regular observations over a six month period to determine whether the fluctuations in the O – C points were real with a significant detection. However, even with this additional data, the picture remains unclear. With all this in mind, I believe a planetary-size companion to RE J0317 remains uncertain and that the scatter in the O – C points may be due to underestimated uncertainties in the O – C data points.

Discussion

The fluctuations in the O – C diagram (shown in Fig. 5.14) may correspond to a planetary companion with a minimum mass of $m_p \sin i = 5.6 M_{\rm Jup}$ at an orbital separation of $a_p = 1.64$ AU, while the O – C residuals to the parabolic fit (Fig. 5.17) indicate a possible companion of mass $m_p \sin i = 7.9 M_{\rm Jup}$ at $a_p = 0.69$ AU. The periodicity analysis of the O – C residuals of the orbital motion model between the two WDs (Fig. 5.19 & 5.20) are not too dissimilar with $m_p \sin i = 2.3 M_{\rm Jup}$ at $a_p = 2.52$ AU for the WDs in a circular orbit and $m_p \sin i = 7.4 M_{\rm Jup}$ at $a_p = 0.69$ AU for the WDs in an eccentric $e = 0.3$ orbit. However, would a planetary system orbiting RE J0317 survive the post main-sequence evolution or possibly form as a second generation planet following a binary merger?

Several theoretical studies have discussed the survival of planetary systems during the post main-sequence evolution of their host star and have found that it is indeed possible (Burleigh et al. 2002; Debes & Sigurdsson 2002; Villaver & Livio 2007). If planets avoid contact with the expanding envelope of the RGB and AGB stars, they are expected to survive the post main-sequence evolution to the WD stage. Villaver & Livio (2007) suggest the AGB phase will have the most impact on the orbit of the planet. They indicate that gas giants of $<15\,M_{\rm Jup}$, with initial orbits within the stellar envelope of a $1M_{\odot}$ main-sequence star during the AGB evolution, will probably spiral-in, totally evaporate and not survive. Furthermore, they predict this planetary mass limit for engulfment inside the AGB envelope extends dramatically up to $\sim 120M_{\rm Jup}$ for a $5M_{\odot}$ star. In contrast, Casewell et al. (2012) detect a $25-30M_{\rm Jup}$ brown dwarf companion to the Praesepe white dwarf WD 0837+185 in a 4.2 hour orbit (orbital separation ~ 0.006 AU). The mass of the white dwarf's progenitor star has been constrained to $\sim 3.5M_{\odot}$, indicating the substellar companion must have been engulfed by the star's envelope at the end of the AGB phase and survived. Therefore, this discovery demonstrates the uncertainties in the theoretical model predictions. Those orbiting beyond the stellar envelope will expand to larger radii due to the substantial mass-loss during the AGB evolution, where the planets are expected to be found at $r \geq 30$ AU around the most massive WDs. Several radial velocity surveys of red giant stars have revealed planetary companions, indicating that planets can at least survive to the RGB stage of the stellar evolution (e.g. Frink et al. 2002; Sato et al. 2003; Hatzes et al. 2005; Lee et al. 2013). Furthermore, brown dwarf companions ($30-60M_{\rm Jup}$) have been discovered in close orbits to the WDs GD 1400, WD 0837+185, WD 0137-349 and NLTT 5306 with orbital periods of 10 h, 4.2 h, 2 h and 1.7 h respectively (Farihi & Christopher 2004; Burleigh et al. 2011; Casewell et al. 2012; Maxted et al. 2006; Burleigh et al. 2006; Steele et al. 2013), illustrating that companions of this mass can survive the RGB/AGB evolution. Since RE J0317's tentative planet is low mass $\leq 8\,M_{\rm Jup}$ and in a close orbit $\lesssim 2$ AU, it is still uncertain that it would have survived the post main-sequence evolution of a single star to the WD stage.

Burleigh et al. (2002) proposed that nearby young and massive WDs could be directly imaged in the infrared with 8-m class telescopes for planetary systems (companions $\gtrsim 3M_{\rm Jup}$) in wide orbits ($\gtrsim 5$ AU). However, sadly, their direct imaging search yielded no planetary companions to WDs (Hogan et al. 2009). Similarly, Faedi et al. (2011) found no planetary transits to WDs in the WASP [5] survey. In fact, no planet has yet been discovered around an isolated WD. Silvotti et al. (2007) reported finding a $\sim 3M_{\rm Jup}$ planet around an extreme horizontal branch star and Mullally et al. (2009) provided exciting evidence for a $2.4M_{\rm Jup}$ planet in a 5.7 year orbit around the pulsating WD GD 66, but have since found that the other pulsation modes are not consistent, suggesting there are other physical processes likely occurring in the star, causing the variability in the timing.

The discovery of debris discs around WDs has provided strong circumstantial evidence for the existence of planetary systems at these stars (e.g. Reach et al. 2005; Gänsicke et al. 2006; Zuckerman et al. 2010). Elements heavier than hydrogen and helium in the atmosphere of a WD should rapidly sink below the photosphere, due to high surface gravities and limited radiative forces. This takes place on the diffusion timescale (days – months for H-rich DAZ WDs) and therefore metal-rich WDs must be polluted from an external source. Surveys have revealed a growing number of metal-lined WDs with infrared excesses and debris discs, showing similar compositions to Solar System asteroids (Gänsicke et al. 2008; Farihi et al. 2009; Dufour et al. 2010b; Farihi et al. 2011a; Klein et al. 2011; Zuckerman et al. 2011 and references therein). It is thought that the heavy elements in most of the heavily polluted WDs originate from asteroids or minor rocky planets, which become tidally disrupted into a disc orbiting the WD and ultimately accrete onto the WD (Jura et al. 2009; Farihi et al. 2010; Melis et al. 2011; Debes et al. 2012). For example, the polluted white dwarf GD 362 has a large infrared excess emission due to a close orbiting debris disc dominated by silicates. Its optical spectrum includes 15 heavy elements with comparable abundances to the Earth-Moon system (Zuckerman et al. 2007). In turn, this suggests that these WDs could have complex orbiting planetary systems. Debes & Sigurdsson (2002) investigated the stability of planetary systems around

[5] The UK Wide-Angle Search for Planets (WASP, Pollacco et al. 2006).

WDs and found that systems comprising of two or more planets could become unstable due to the mass-loss from the star. Instabilities may cause close encounters: where planets could collide, a planet could be ejected, or planets could acquire highly eccentric orbits, and therefore such interactions and perturbations are believed to be the origin of debris discs around WDs.

Livio et al. (2005) suggested that dusty discs could form around massive WDs created from the merger of two WDs which could explain the presence of any gas giant planets at close-in orbits around massive WDs. Their hypothesis suggests that when two WDs merge, the less massive WD totally dissipates and forms a disc around the more massive WD. The disc then expands, cools and accretes onto the remaining WD. The disc could be composed of CO-rich or He-rich material (Wickramasinghe et al. 2010) and the disc dynamics are thought to be similar to protostellar discs (Livio et al. 2005). Dust and rocks form and clump to create a rocky core when the temperature is cool enough in the outer regions of the disc; similar to the formation of planets around millisecond pulsars (Hansen et al. 2009; Currie & Hansen 2007). Fischer & Valenti (2005) found that the probability of a star hosting a planet dramatically increases with the metallicity of the star, therefore the formation of planets could be highly efficient in dust discs around WDs. Wickramasinghe et al. (2010) highlight that not only should the WD be massive but also have a high magnetic field, created during the common envelope of the merger. As mentioned previously, the merger hypothesis is a possible evolutionary scenario for the formation of RE J0317, therefore a planet could have formed as a second generation planet following a binary merger. Wickramasinghe et al. (2010) speculate that the MWD GD 356 may have a rocky planet with a metallic core that formed in a circumstellar disc as the result of a merger of two WDs.

However, this scenario does present some difficulties. RE J0317 is hot $T_{\rm eff} > 30,000\,$K, and so any metals present should be detectable in its spectrum due to radiative levitation (Chayer et al. 1995). No metal lines are found in its optical spectra, although the presence of a strong magnetic field does add an additional complication. *Spitzer* observations confirm that RE J0317 does not have a dust disc or an infrared excess (Farihi, Becklin & Zuckerman 2008), which does not support the argument that a second generation planet could have formed in a disc around the star. On the other hand, a planet could form and the disc could dissipate on timescales up to $\sim 10^7$ years, all within the cooling age of RE J0317 (~300 Myr), leaving behind a possible planetary companion with no disc surrounding the WD. Livio et al. (2005) estimate the radius of a dust disc resulting from a WD merger extends out to ~ 1 AU with a mass of $\sim 0.007\,M_\odot$ ($\sim 7.3 M_{\rm Jup}$). Therefore, low-mass planets ($\lesssim 8 M_{\rm Jup}$), like those tentatively suggested in this work, may be capable of forming in a disc following a double-degenerate merger. However, if the disc only extends to a radius of ~ 1 AU, then it may be difficult to form planets at larger radii, potentially limiting the possibility of a second generation planet in orbit around RE J0317. If RE J0317 did form in a merger, the progenitor would have undergone possibly two common envelope phases. Given the uncertainties in the merger physics involved at these stages, such as the size of the envelopes and the tidal forces involved, it is unknown how the surrounding planets would be impacted. Consequently, the expectation that planets in $1-5$ AU orbits will be destroyed cannot be concluded, and furthermore, a planet could perhaps migrate inwards to a close-in orbit. In conclusion, there is strong evidence for the possibility that a planet in orbit around RE J0317 could have formed as a second generation planet in a disc following the merger of two WDs. It is also plausible, however, that a planet from the main-sequence may survive to the WD stage, given the uncertainties in the common envelope phases of the evolution.

5.6 Modelling the light curve

While analysing the light curves as part of the O – C investigation, I noticed that the photometric light curves for RE J0317 are not sinusoidal, but have a “pointy” maximum and a “flattened” minimum (see the ULTRACAM light curves in Fig. 5.5). In an attempt to improve upon the light curve fitting using a sinusoid, the light curve was modelled using a surface spot model as described in Wynn & King (1992). The script was developed by Graham Wynn and produces a synthetic light curve based on the inclination angle, magnetic axis angle and spot size on the surface of a star.

5.6.1 Setting up the model

Using the basic disc-less model developed by King & Shaviv (1984) and Wynn & King (1992) for X-ray light curves of accreting magnetic cataclysmic variables (CVs), known as polars (B~$10 - 80\,$MG) and intermediate polars (B~$1 - 10\,$MG, Chanmugam 1992), it was adapted (and re-written in IDL) to simulate the light curve of a rotating isolated MWD with a spot on the stellar surface. The shape of the light curve depends on the fraction of the spot (or spots) visible to the observer as the star rotates. The geometry of the MWD is shown in Figure 5.21. The light curve of the rotating star can be produced solely as a function of the inclination angle i to the observer’s line of sight, the angle to the magnetic axis m from the spin axis and the angle of half of the spot β.

The spot covers a portion of the sphere and therefore as the star rotates, different regions are observed at different angles by the observer. Consequently, the fraction of the spot visible to the observer is determined by dividing the spot into smaller sections of equal size (as shown in Fig. 5.22), where each section could be treated as a spot at a single angle to the line of sight. The total flux from the spot, at any given rotational phase, is then simply calculated as the sum of all of the visible sections to the observer.

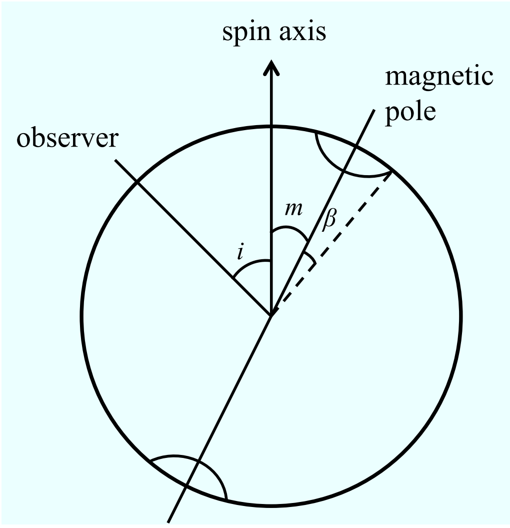

Figure 5.21: The geometry of the magnetic white dwarf with two opposite circular spots (or pole caps) at the magnetic axis angle m (upper pole) and $\pi - m$ (lower pole), as given by Wynn & King (1992), from the spin axis to the magnetic pole. The inclination angle i from the observer's line of sight to the spin axis and the angle of half of the spot β are also marked.

Assuming the spot is flat and circular, it is divided into n rings, each of which are divided further into sectors of equal area. The area of each ring is calculated as,

$$A_{\rm ring} = \pi(d + \Delta d)^2 - \pi d^2 = 2\pi d\Delta d + \pi(\Delta d)^2, \tag{5.23}$$

where d is the radius to the inner edge of the ring and Δd is the width of the rings, as shown in Figure 5.22. The radius to the jth ring is given as $d = (j - 1)\Delta d$ with an area of

$$A_j = 2\pi(j - 1)(\Delta d)^2 + \pi(\Delta d)^2. \tag{5.24}$$

The area of each sector is required to be equal (i.e. the area of the first ring $\pi(\Delta d)^2$) and therefore the total number of sectors within the outer radius of the j ring $d = (j-1)\Delta d+\Delta d$ is defined as,

$$N_j = \frac{\pi((j - 1)\Delta d + \Delta d)^2}{\pi(\Delta d)^2} = j^2. \tag{5.25}$$

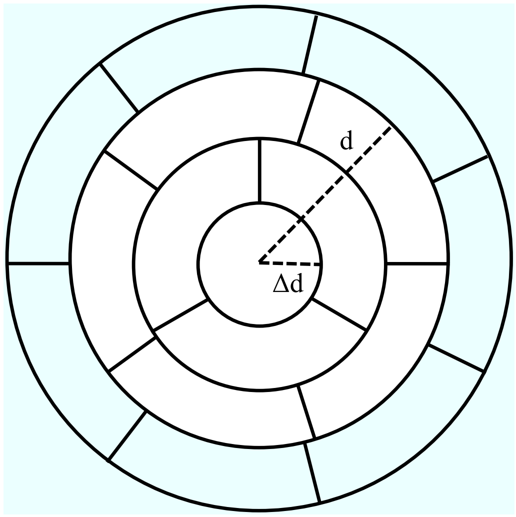

Figure 5.22: The spot is divided into sectors of equal area, each equivalent to the area of the first ring $\pi(\Delta d)^2$, where Δd is the width of the rings and d is the radius to the inner edge of the ring.

Hence, if a spot is divided into n rings, each of equal width Δd, there will be a total of n^2 sectors, all with an area of $\pi(\Delta d)^2$. The sectors of the spot visible at each spin phase are determined by transforming the coordinates of the spot to a coordinate system aligned with the observer's line of sight (shown in Fig. 5.23), where r is the angular distance from the magnetic pole, θ is the azimuthal position angle of the spot and the radius of the WD is defined as unity. This is achieved using four coordinate transformations.

To start, the spherical coordinates describing the position of the spot on the surface are converted to cartesian coordinates aligned with the magnetic axis ($x_{\rm m}$, $y_{\rm m}$, $z_{\rm m}$),

$$\begin{aligned} z_{\rm m} &= \cos r \\ x_{\rm m} &= \sin r \cos\theta \\ y_{\rm m} &= \sin r \sin\theta. \end{aligned} \tag{5.26}$$

The magnetic axis coordinates are then transformed to the rotational axis coordinates ($x_{\rm r}$,

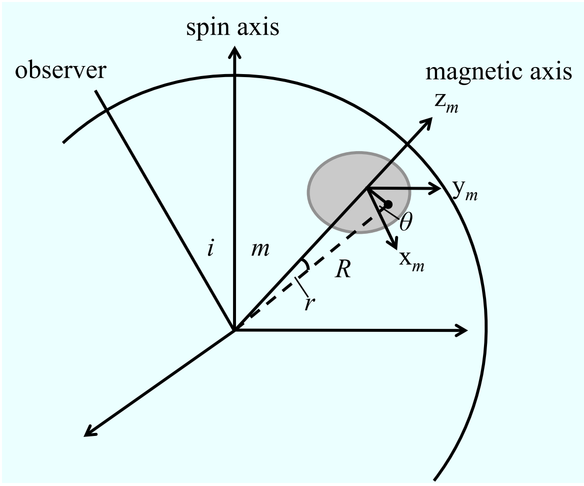

Figure 5.23: The orientation of the spot on the surface of the white dwarf. The sector spherical coordinates (R, r, θ) are transformed to cartesian coordinates aligned with the magnetic axis ($x_{\rm m}$, $y_{\rm m}$, $z_{\rm m}$).

$y_{\rm r}$, $z_{\rm r}$) by rotating it by the magnetic angle m about the y axis.

$$
\begin{aligned}
z_{\rm r} &= z_{\rm m}\cos m - x_{\rm m}\sin m \\
x_{\rm r} &= x_{\rm m}\cos m + z_{\rm m}\sin m \\
y_{\rm r} &= y_{\rm m}
\end{aligned}
\tag{5.27}
$$

To then change the coordinate system to the line of sight phase, the spin axis is rotated by the phase difference between the magnetic axis and the line of sight about the z axis.

$$
\begin{aligned}
z_{\phi} &= z_{\rm r} \\
x_{\phi} &= y_{\rm r}\sin\Delta\phi - x_{\rm r}\cos\Delta\phi \\
y_{\phi} &= -y_{\rm r}\cos\Delta\phi - x_{\rm r}\sin\Delta\phi
\end{aligned}
\tag{5.28}
$$

The final transformation step involves rotating the coordinates to the observer's line of sight, where the system is rotated by the inclination angle i about the y axis. The resulting

z_o axis is then aligned along the observer's line of sight.

$$\begin{aligned} z_o &= z_\phi \cos i + x_\phi \sin i \\ x_o &= x_\phi \cos i - z_\phi \sin i \\ y_o &= y_\phi \end{aligned} \tag{5.29}$$

This procedure is carried out for each sector within the spot, which is divided into 100 rings, where the width Δd is calculated as the half-angle of the spot β divided by the 100 rings. The visibility of each sector in the spot is determined by whether the coordinate z_o is positive or negative. The sector is visible at a given phase if $z_o > 0$, as $z_o = \cos\eta$ where $\eta < 90°$ and is the angle from the sector to the line of sight. Conversely, if $\eta > 90°$, the z_o coordinate would be negative, implying it is not visible at that rotational phase. As a result, this is used to calculate the fraction of the spot visible at a given phase.

In the model, the spot is defined as a "dark" spot. As the spot comes into view with rotation, the overall brightness of the star reduces, similar to spots observed on the surface of the Sun. Star spots in a convective atmosphere are caused by the inhibition of convection by the magnetic field, and are cooler (and therefore darker) than the surrounding atmosphere. This effect is observed in WD 1953-011, which photometrically varies sinusoidally by ≈2% on a period of 1.44 days (Brinkworth et al. 2005). Using the same model, they predicted the variation was due to a spot covering ∼10% of the surface (Maxted et al. 2000; Brinkworth et al. 2005).

To start, the initial model assumes the spot is a constant effective temperature, where each of the sectors in the spot (of equal area) are defined as having the same luminosity. Alternative models are also investigated where the brightness of the spot is allowed to vary linearly or exponentially from the centre of the spot to the outer edge. The faintest (and coolest) sector of the spot is specified at the centre of the spot and with increasing n rings to the edge of the spot, the luminosity increases. The linear and exponential variation in brightness with n rings is defined as j/n and $1 - e^{-2j/n}$ respectively (for the jth ring).

5.6.2 Finding the best system parameters

To find the best spot model to describe the observed light curve of RE J0317, the appropriate parameters for angles i, m and β are determined. The parameter space is investigated by generating model light curves with inclination angles i ranging between 0° and 90°, for magnetic axis angles m between 0° and 90° and half-spot angles β between 0° and 90°. Estimates for values i and m were reported in Burleigh et al. (1999) as $i = 56°$ and $m = 29°$, where the phase-resolved spectra of RE J0317 was modelled using an offset dipole model and a more general method involving the expansion into spherical harmonics.

For a given magnetic axis, half-spot angle and inclination, the corresponding model light curve is calculated and the χ^2 value of the model light curve in comparison to a real optical RE J0317 light curve is determined. The χ^2 values are then plotted as a contour plot as a function of the physical parameters. Figure 5.24 shows the contour plots of $\log(\chi^2)$ with magnetic axis angle m and the half-spot angle β for a range of inclination angles i for the one spot model of constant luminosity. The dark regions on the greyscale indicate a small χ^2 value and therefore a better fit, while the lighter regions represent poor fits. The white crosses indicate the location in the parameter space of the minimum χ^2 for that inclination. In addition to determining the χ^2, a K-S test (as explained in §2.6.3) of the fit is calculated to compare the model light curve and the observed light curve. For the same one spot model of constant luminosity, the K-S test statistic contour plot is given in Figure 5.25 and similarly the location of the minimum K-S test statistics in the parameter space are marked on the contour plots. The K-S test statistic is calculated using the IDL routine KSTWO, which finds the maximum deviation between the cumulative distribution of the data and the light curve model, where a smaller value indicates less of a difference between the data and the model. I find the "best" parameter regions are fairly consistent between the minimum χ^2 contour plots and the minimum K-S test statistic contour plots. This is repeated for three other scenarios: two spots of constant luminosity, two spots with linearly changing luminosity and two spots with exponentially changing luminosity.

These contour plots can be found in Appendix B.1. Obviously, there are endless combinations that could be explored. For example, the position of the spot could be offset asymmetrically from the magnetic pole axis. This is not explored as there would have been many possibilities. The minimum χ^2 and K-S test statistic (as marked in the contour plots Fig. 5.24 and 5.25) are then plotted as a function of inclination, magnetic axis and half-spot angle in Figures 5.26, 5.27 and 5.28 respectively for the four cases investigated (one spot of constant luminosity, and two spots of constant luminosity, linearly changing luminosity and exponentially changing luminosity). Figures 5.26 and 5.27 of the best fit values with the inclination and magnetic axis angle appear the same since the location of the spot is defined at an angle of $i + m$ and therefore the model light curves are the same.

Investigating the i, m and β parameter space for the best solution reveals that the minima in the statistical tests differed between the four models depending on the number of spots and how the luminosity of the spot is defined. Unfortunately, and perhaps unsurprisingly, there is a considerable amount of degeneracy and in no case is there an obvious minimum in the parameter space. As a result, this made it difficult to constrain the system parameters to find the best solution. For example, in Figure 5.28, the minimum χ^2 values decrease up to a spot half angle of $20 - 30^{\circ}$, but then the minimum χ^2 stays fairly constant with $\beta = 30 - 90^{\circ}$. Similarly, the minimum χ^2 and K-S test statistic values for the inclination angle and magnetic axis angle are also inconclusive, and optimal parameters have not been determined unambiguously.

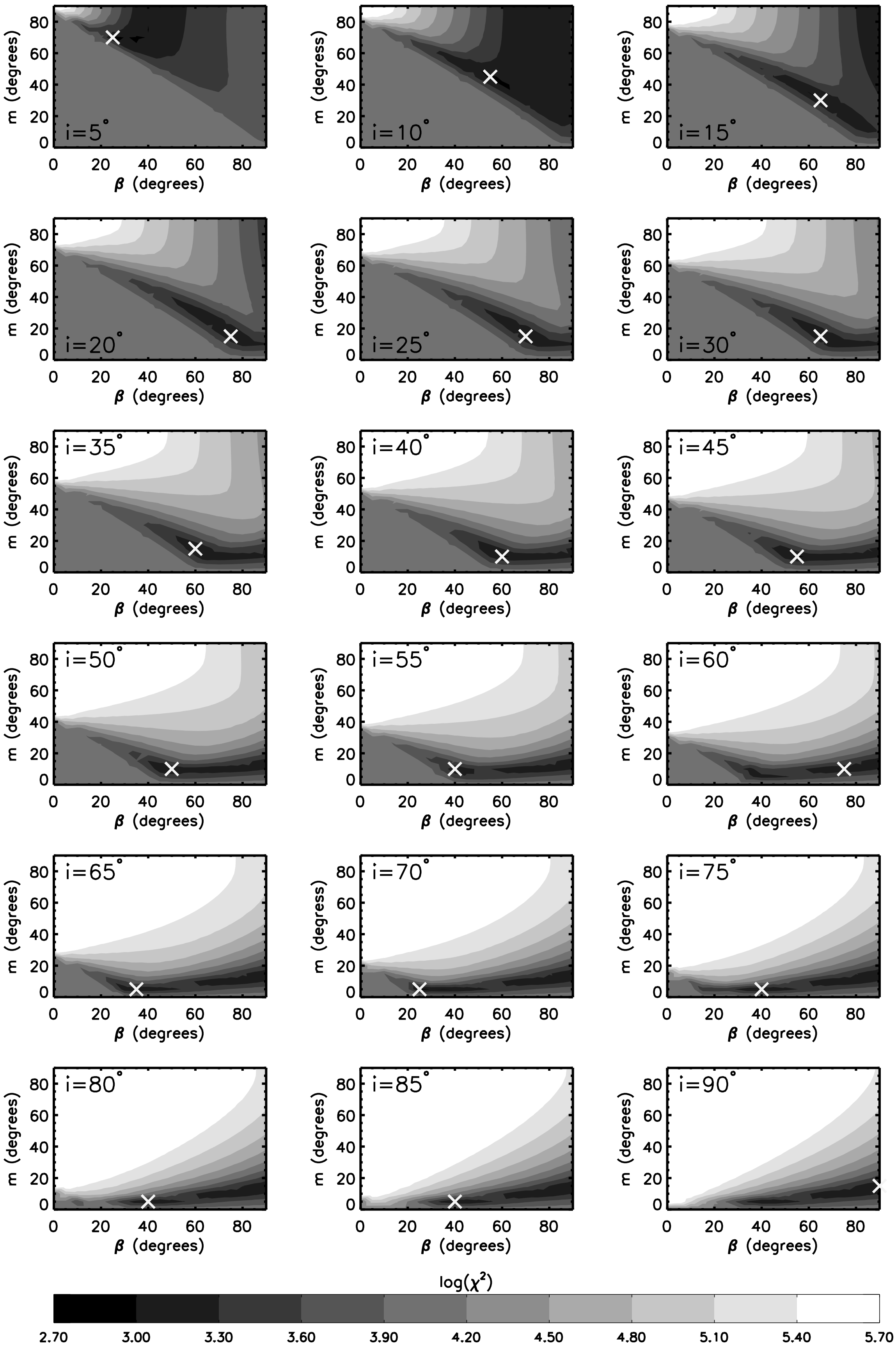

Figure 5.24: Contour plots of $\log(\chi^2)$ with magnetic axis angle m and half spot angle β for a range of inclination angles i. Here, the model consists of one spot of constant luminosity. The white crosses indicate the location of the minimum χ^2 value for that inclination.

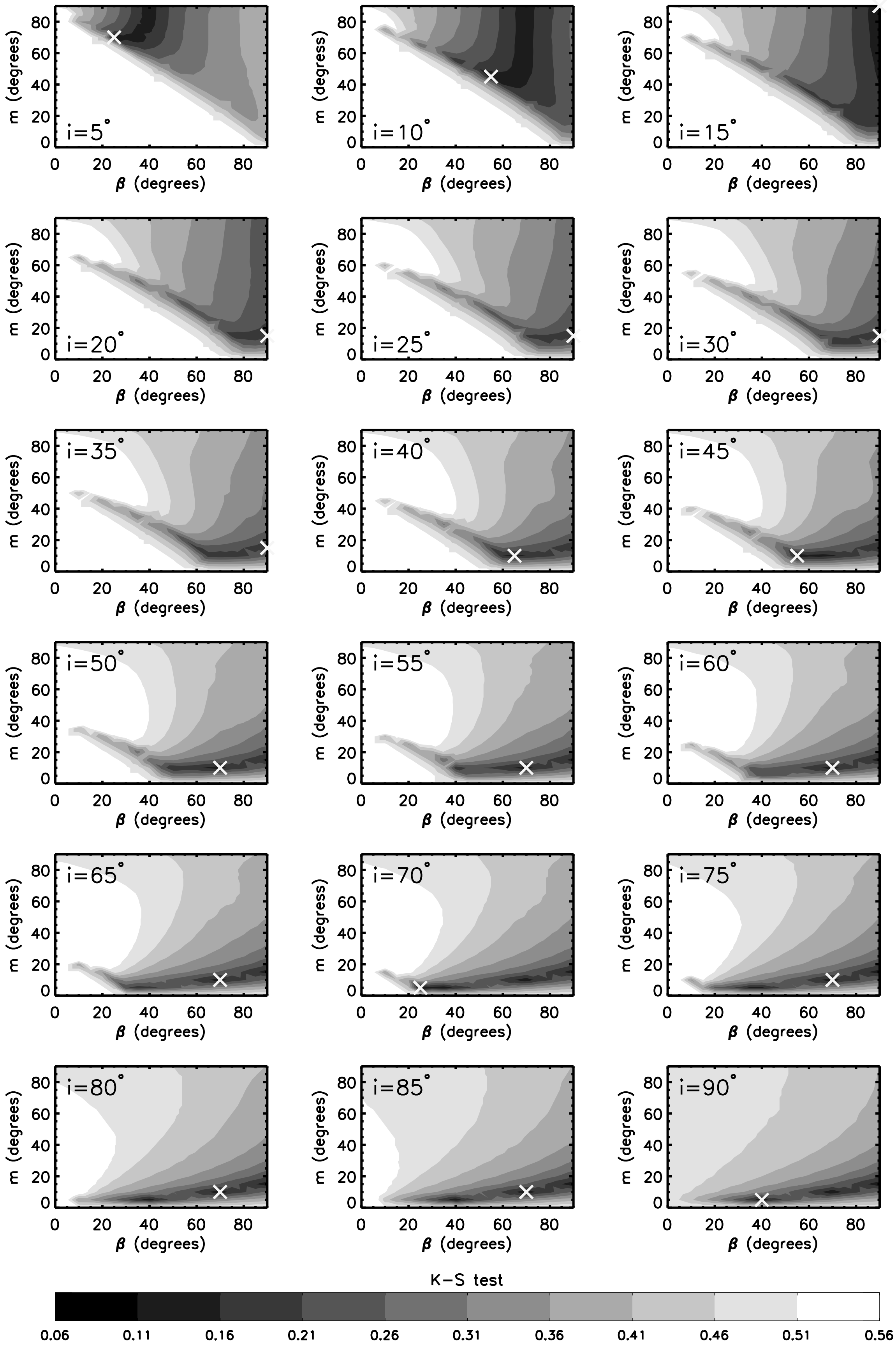

Figure 5.25: Contour plots of the K-S test statistic for the one spot model of constant luminosity. The white crosses indicate the location of the minimum K-S test statistic for that inclination.

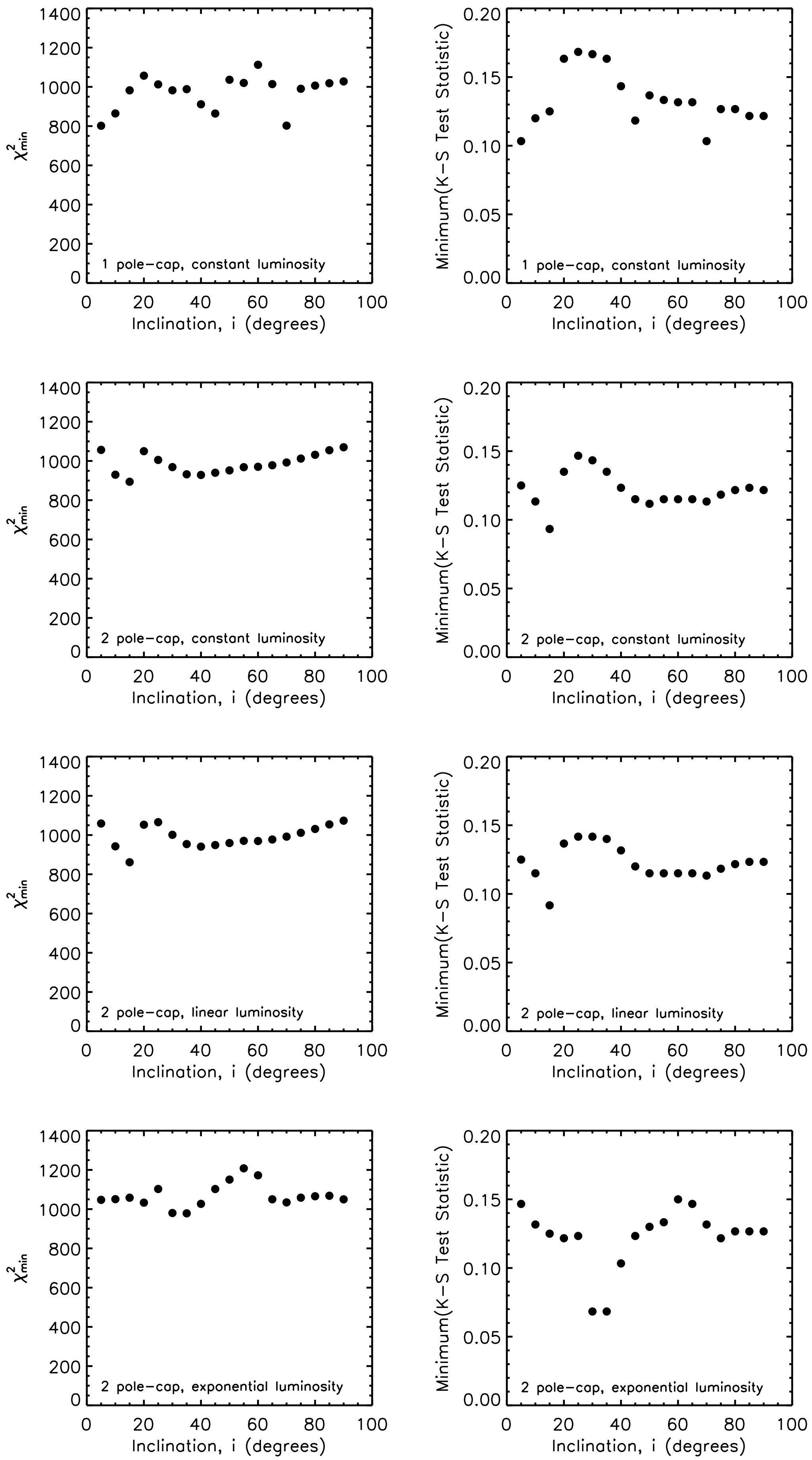

Figure 5.26: Minimum χ^2 and K-S test statistic as a function of m and β with inclination i.

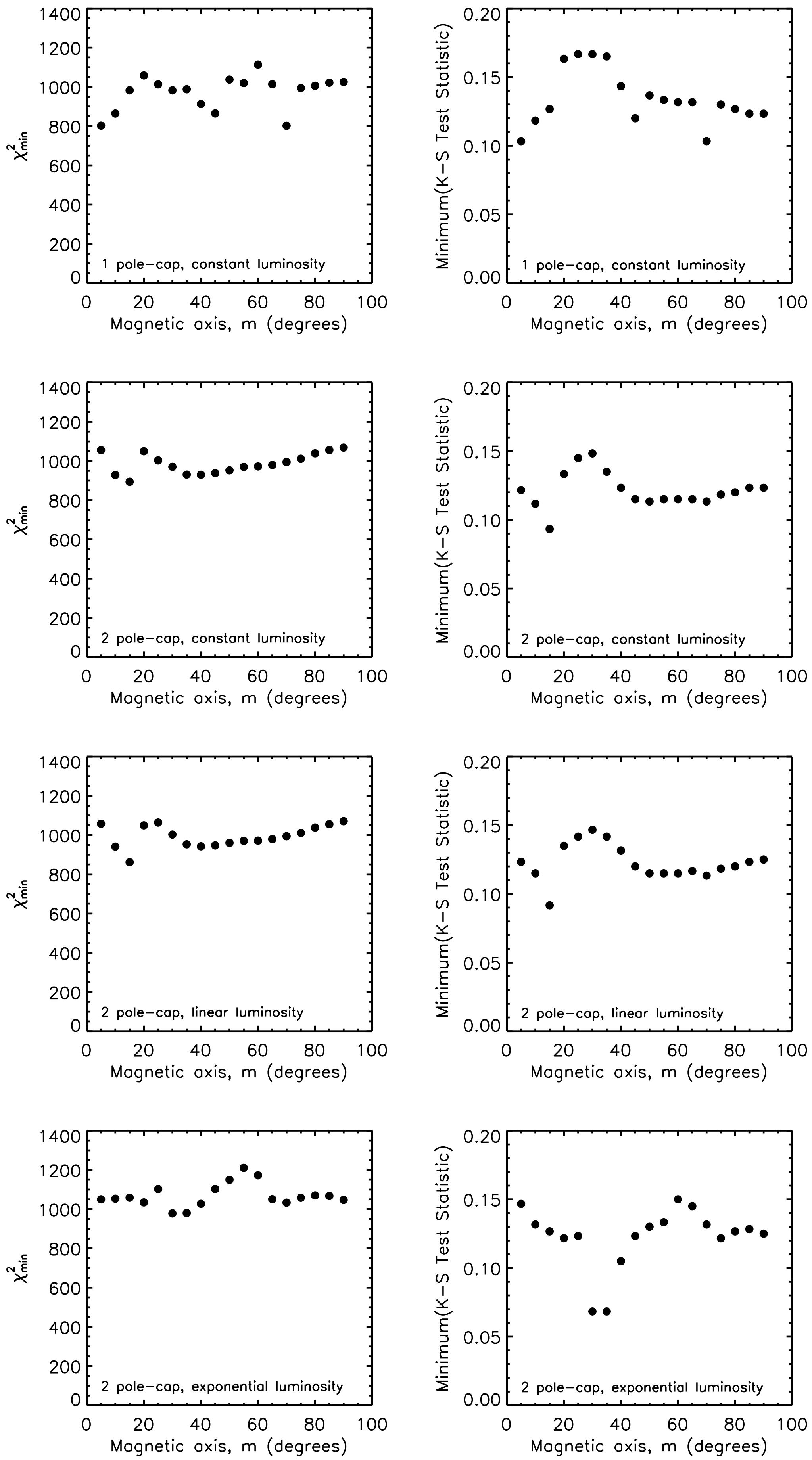

Figure 5.27: Minimum χ^2 and K-S test statistic as a function of i and β with magnetic axis m.

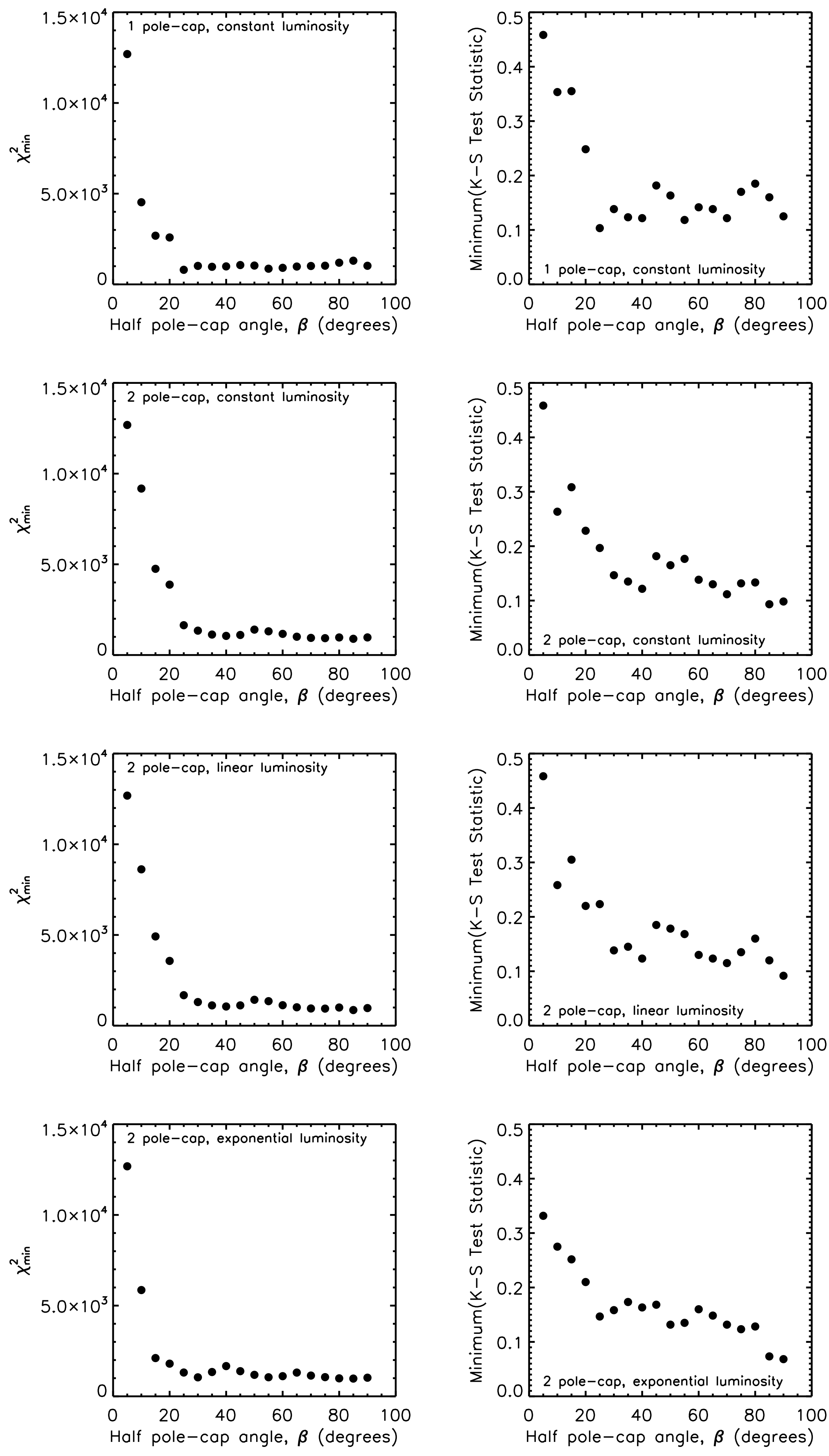

Figure 5.28: Minimum χ^2 and K-S test statistic as a function of i and m with spot half angle β.

Since the more complicated models for describing the spot (i.e. where the luminosity of the spot changes from the centre of the spot to the outer edge) do not yield better fits to the photometric variability, the simplest model is chosen for the light curves of one spot on the star of constant luminosity. For the one spot model of constant luminosity, the combination of parameters that statistically appears to give the "best" fits (the lowest χ^2 values) have been selected. Four examples are shown in Figure 5.29, where the model generated for a given set of parameters is shown with the data in a phase folded light curve and in a light curve as a function of the period cycles. These models clearly show that despite the difference in the input angles, the model light curves look very similar in all cases, demonstrating the degeneracies in accurately trying to determine the parameters of the system. However, the scatter in the photometry in the light curve will not help efforts to find the precise parameters. For the first two models in Figure 5.29, the spot is positioned at the same location ($i+m$) and since β is set to the same value in both of these examples, they result in the same model light curve. The bottom two models in Figure 5.29 have very similar i, m and β values, but not precisely the same. However, there is no observable difference between the model light curves. The final parameters chosen for the model light curve are: $i = 5°$, $m = 70°$ and $\beta = 25°$.

As mentioned previously, Burleigh et al. (1999) determined i and m as 56° and 29° respectively ($|i + m| = 85°$). These quantities for i and m differ from those used in Figure 5.29 (*top*), although the position of the spot ($|i + m|$) is not too dissimilar. In any case, the light curve model is overly simplified: physically it is not a dark spot on the surface of the MWD causing the photometric variations, nor would a spot-like feature have a constant luminosity. It is strictly a geometric representation of the photometric variability observed for RE J0317 and therefore has its limitations. RE J0317's photometric modulations are likely caused by magnetic dichroism (the effect of a strong changing magnetic field on the opacity of the star as it rotates, Ferrario et al. 1997a). Modelling in Burleigh et al. (1999) suggests the magnetic field varies between 180 MG and 800 MG across the surface with rotation. Finally, the amplitude of the variability is known to change with wavelength, which is not accounted for in this geometric model. Of course, physically, the inclination and magnetic axis angles would remain the same regardless of the wavelength of the observations of the MWD, although the corresponding model light curve may no longer appropriately fit the observed light curves at different wavelengths.

5.7 Conclusions

An O – C analysis is conducted for RE J0317 using time-series optical observations taken over a nearly 20 year period. The best-fitting period of RE J0317's photometric variability is determined as 725.727684 ± 0.000002 s, along with a significant measurement for the rate of period change $\dot{P}$ at $(9.6 \pm 1.4) \times 10^{-14}$ s/s. This $\dot{P}$ value is most likely due to the orbital motion between RE J0317 and its wide binary WD companion. The reflex motion of RE J0317 around the centre of mass with its white dwarf companion dominates the $\dot{P}$ and if the magnetic white dwarf is spinning down due to magnetic dipole radiation it will only cause a very small effect, undetectable within the uncertainties. In addition, the seemingly non-random scatter in the O – C data points is studied for any periodicity. A periodogram analysis does not reveal a significant periodic signal and thus a determination for a mass and orbital separation of a possible planetary companion to RE J0317, although there may be tentative evidence for a companion with a minimum mass of $5.6M_{\rm Jup}$ at a separation of 1.64 AU in a 1.81 year circular orbit. Further observations in the coming years may help to determine whether this is a real periodicity or an alias associated with the complex window function. I have discussed whether such a planet could even exist around a white dwarf and have concluded that it is unlikely that the planet survived the post main-sequence evolution of a single star and settled in a close ∼2 AU orbit, suggesting that it may have formed as a second generation planet in a dust disc around RE J0317 following the merger of two white dwarfs. Finally, a model of a spot on the surface of a star is used to investigate the geometry of the system and the resulting photometric variability that would be viewed from an observer based on three angles describing the system (the inclination, magnetic axis angle and the half-spot angle). Since the model is purely geometric, the possible angles that may cause the observed photometric variability are not constrained unambiguously.

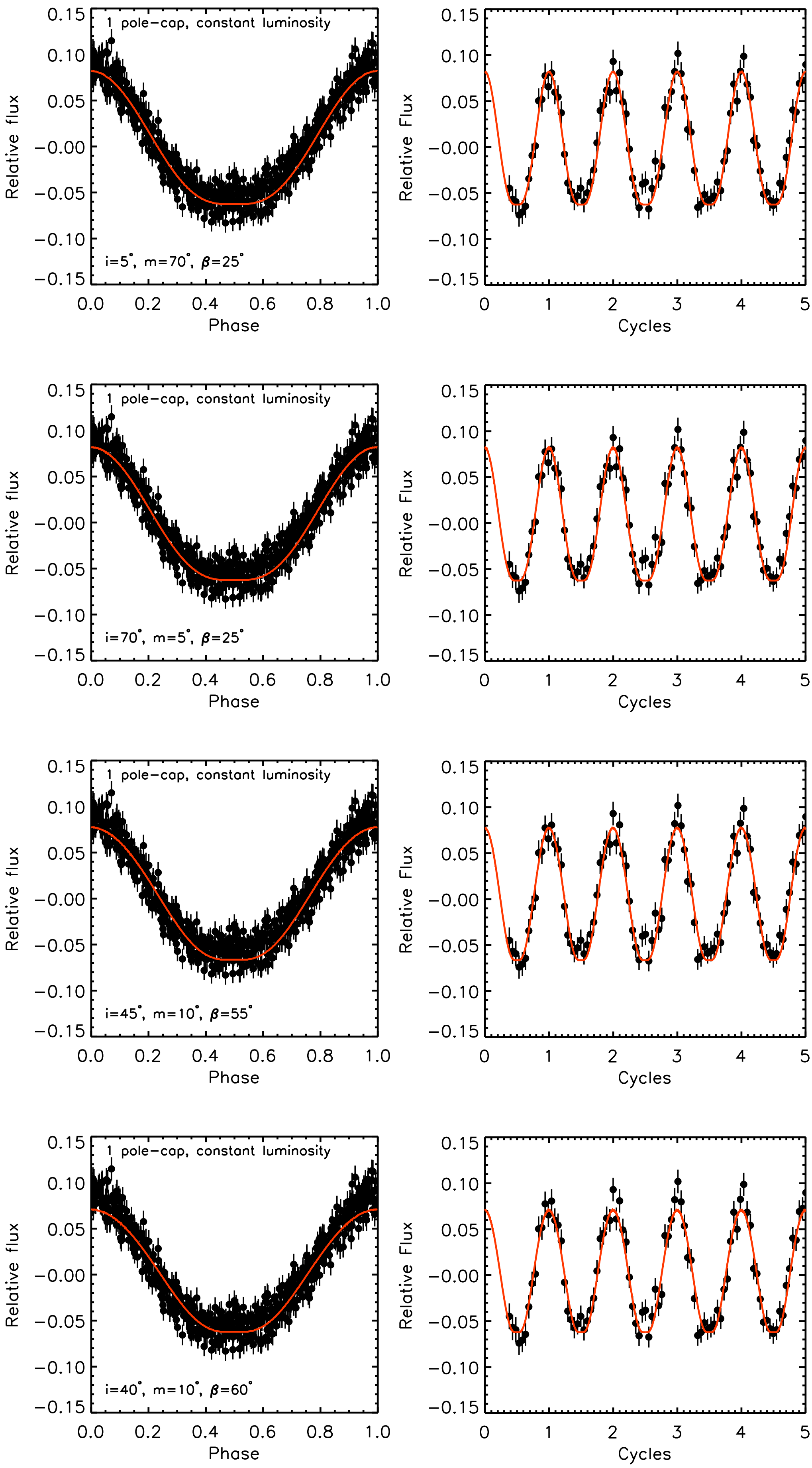

Figure 5.29: Observed light curves and models with the best-fitting parameters for one dark spot of constant luminosity.

6

Conclusions and Future Work

This chapter reviews the work presented in this thesis. The main conclusions from each chapter are summarised and the overall context is discussed. The photometric variability of magnetic white dwarfs is the common theme of this work, with the aim of determining their rotation periods on both short (minutes – days) and long timescales (months – years) to build a more comprehensive picture of the distribution of magnetic white dwarf spin periods, along with how their intrinsic physical properties relate to one another. This is extended to investigate whether the spin period of the magnetic white dwarf RE J0317-853 evolves due to magnetic dipole radiation, or from the presence of a stellar or planetary companion. To finish, some future projects are outlined that materialised from this work, such as searching for photometric variations in certain types of magnetic white dwarfs, like those with carbon-dominated atmospheres (hot DQs) or with metal-rich optical spectra (DAZs/DZs).

6.1 Conclusions

This work focuses on the photometric variability of MWDs. A search for photometric rotation periods in a variety of types of MWDs has been conducted on both short timescales (minutes – days, Chapter 2 and 3) and long timescales (months – years, Chapter 4), while a MWD rapid rotator (RE J0317-853) has been monitored over nearly 20 years to determine whether any changes occur in its spin period (Chapter 5).

In Chapter 2, a sample of 77 MWDs is studied for photometric variability on a timescale of minutes to a week. Periods of variability are determined for 12 MWDs in the sample, while modulations with poorly constrained periods are detected for a further 13 stars. The spin periods are consistent with previously known rotation periods for WDs, most of which are a few hours to days. Photometric variability is measured in four hot, low-field MWDs, caused by an unknown mechanism. Correlations are found between the spin period, magnetic field strength and effective temperature, suggesting hotter MWDs spin faster and have stronger magnetic fields. This could possibly indicate that MWDs form in mergers, where they may be expected to generate higher field strengths and be born with shorter periods and then spin down with age. The comparison between the magnetic field strength and mass for the rotating MWDs reveals two possible populations: low-field (< 1 MG), low mass ($0.5 - 0.7 M_{\odot}$) and high-field (> 1 MG), high mass ($> 0.8 M_{\odot}$) MWDs, which could potentially provide insight into the progenitors of these stars.

One of the variable MWDs, SDSS J0005-1002, identified in the variability survey is discussed in further detail in Chapter 3, along with additional data and a more thorough analysis. This particular star is a carbon-dominated atmosphere, hot DQ MWD, which exhibits long period modulations on 2.110 ± 0.045 days, with a peak-to-peak amplitude of ~11%. Previously, only modulations on short timescales (up to ~ 1000 s) have been detected in hot DQ WDs, leading to the conclusion that they are non-radial pulsators. However, no pulsation modes have periods of days, and therefore SDSS 0005-1002 is mostly likely a rotator, and not a pulsator. No evidence is found for modulations in this star on short timescales ($\lesssim 3$ hours) at an amplitude of $\lesssim \pm 0.5\%$.

Photometric variations on long timescales (months – years) have also been investigated for 10 bright, isolated MWDs previously studied by Brinkworth et al. (2013). These were found to be photometrically stable over a week, but showed modulations between observing seasons. No significant photometric variability is identified in the new light curves, although G 240-72 may exhibit variations on a timescale of months, in agreement with findings from Brinkworth et al. (2013). The survey is limited by the quality of the data in its ability to detect low-level amplitude (< few %) photometric variability on long timescales.

Finally, in Chapter 5, results are presented from a monitoring campaign over nearly 20 years which observed the massive, rapidly rotating, highly magnetic WD, RE J0317-853, to search for changes in the star's spin period using an O – C analysis. The best-fitting period for RE J0317-853 is determined as 725.727684 ± 0.000002 s, along with a rate of period change at $\dot{P} = (9.6 \pm 1.4) \times 10^{-14}$ s/s. This $\dot{P}$ estimate is consistent with the $\dot{P}$ expected, given the mass of the common proper motion WD to RE J0317-853 and the orbital separation between these two WDs, assuming a position angle in the orbit $\theta = 45 - 57°$ and orbital inclination $i = 24.7 - 56.8°$, implying the two WDs are indeed related in a wide binary. The $\dot{P}$ is much larger than expected for magnetic dipole radiation. Spin down by magnetic dipole radiation will not be observed in the majority of MWDs, as most do not have magnetic field strengths large enough for spin-down to be detectable within the cooling age of the WD. The O – C residuals appear to show a non-random scatter, but a periodicity analysis does not reveal any significant periodic signals. However, the possibility of a planetary-size companion to RE J0317-853 causing the fluctuations in the O – C residuals is discussed in more detail, including whether a planet could survive the post main-sequence evolution or if it could have perhaps formed in a dust disc as a second generation planet following a binary merger.

On the origin & evolution of MWDs

MWDs probably form through either a single star evolution, where the magnetic field is a fossil remnant from the main-sequence progenitor star, or from binary mergers, where the magnetism is generated in a dynamo-like process in the common envelope phase. Therefore, it is possible that no relationships exist between the spin period and magnetic field strength for MWDs. However, correlations between spin period and temperature and field strength are detected in this work. Stars that evolve from a single star evolution are thought to rotate more slowly as strong magnetic fields cause magnetic braking, resulting in slow rotators. In contrast, those from a binary merger origin may exhibit the opposite behaviour, where MWDs with stronger field strengths rotate faster as a result of getting spun up during the common envelope evolution. On the other hand, García-Berro et al. (2012) suggest that if MWDs form via double-degenerate mergers, then MWDs may have a variety of spin periods, since the angle between the spin axis and the magnetic axis could yield both slow rotators (if the axes are not aligned, causing the star to spin down rapidly due to magnetic dipole radiation) or rapid rotators (if the axes are near alignment). The trend in Figure 2.16 of increased spin period with decreasing magnetic field strength may simply be a coincidence due to small number statistics or it may actually indicate a physical property of the data. This will only be deciphered with a larger sample of known rotation periods for MWDs and possibly if MWDs can be separated by their plausible formation mechanism.

An increasing number of hot, low-field MWDs are showing photometric fluctuations with rotation (four from Chapter 2, and two from Brinkworth et al. 2013). These stars, in particular, need to be studied in more detail to better understand the mechanisms that cause photometric variability in all MWDs. The current understanding is that cool MWDs, with partially convective atmospheres, are capable of forming surface star spots, while hotter MWDs with radiative atmospheres are not. But this may not be the case. Effects from magnetic dichroism may be more influential at weaker field strengths than previously thought. On the other hand, in the case of BOKS 53856, the hot, weakly magnetic WD discovered in the *Kepler* field (Holberg & Howell 2011), there has been some suggestion that the photometric variability is caused by the surrounding circumstellar gas accreting onto the magnetic poles on the surface of the MWD, possibly from the tidal disruption of an asteroid or minor planet.

6.2 Future Work

6.2.1 Time-resolved spectroscopy of LHS 2534

The photometric variability survey of MWDs in Chapter 2 reveals modulations of >5% over 5 days in observations taken in the r'-band for a metal-rich cool DZ MWD, LHS 2534 (or SDSS J1214−0234, Fig. 6.1). Unfortunately, a well-constrained period of variability is not determined from the data collected, but possible periods are determined as 10.7 h, 19.1 h or 3.8 d. Observations from the Catalina Sky Survey (Drake et al. 2009) have also not constrained the period further, indicating possible periods at 5.8 d or 1.2 d, but both have high false alarm probabilities. Visually, a period of >5 days seems reasonable, although given the data sampling there could be solutions on shorter periods.

LHS 2534 is a cool ($T_{\mathrm{eff}} = 6000$ K), helium atmosphere DZ WD, with a weak magnetic field strength of ∼2 MG (Reid et al. 2001), which causes Zeeman splitting in the Na I and Mg I lines. Metal-lines in WD spectra are evidence for accretion from an external source, since elements heavier than H and He in the WD atmosphere should sink below the photosphere on the diffusion timescale (days – months). Consequently, this MWD must have accreted material at some point in its history. For example, a tentative spin period of 28–33 days was estimated by Farihi et al. (2011b) for a magnetic DAZ WD (G 77-50) from changes in the radial velocity measurements from multi-epoch spectra. They postulated that the magnetic field was perhaps generated in a common envelope, in the presence of differential rotation and convection, due to an inner giant planet merging with the WD's progenitor star during the post main-sequence evolution (similar to Tout et al. 2008 for binary star mergers). Material was then accreted onto the star from a disc formed from a tidally disrupted minor planet or asteroid.

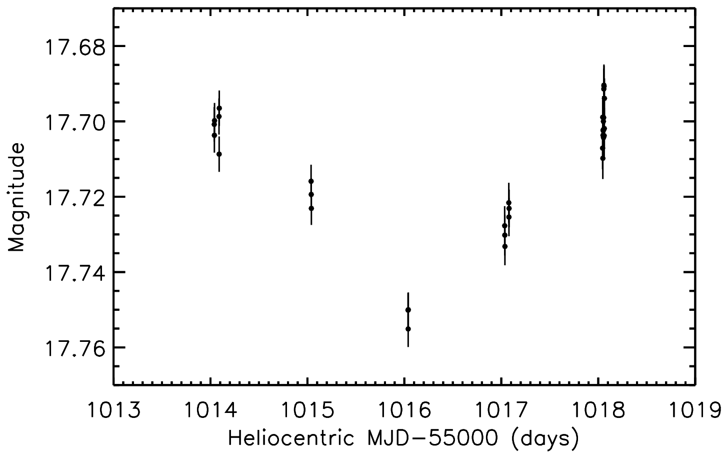

Figure 6.1: Light curve of LHS 2534 showing photometric variability over ~ 5 days with a peak-to-peak amplitude of >5%. This DZ MWD was observed with the 2.5 m INT in La Palma in March 2012 in the r'-band as part of the survey to search for photometric fluctuations in MWDs (Chapter 2).

Similarly, phase-resolved spectroscopy over the rotation period of LHS 2534 could determine whether metal abundances change as the MWD rotates and whether the accretion was confined to the magnetic poles of the star. Since the spin period is not well-constrained, approximately ten spectra could be taken at intervals over a month to adequately cover all predicted periods and unambiguously determine the rotation period. Similar to Farihi et al. (2011b), this would be achieved by measuring changes in the radial velocity of the stationary components of the Zeeman split lines. Searching for variations in the metal line strengths with phase could indicate whether the metals are uniformly distributed across the surface or concentrated at the magnetic poles, where they might be expected to have been accreted. Furthermore, since metal abundances in DZs and DAZs are normally calculated assuming a homogeneous distribution across the star's surface, this assumption could be tested, where abundance and mass estimates could be revised accordingly. Finally, the magnetic field distribution and strength across the whole star could be investigated and mapped by modelling changes in the Zeeman splitting.

Field distributions of rotating MWDs have shown they are usually highly inhomogeneous (Külebi et al. 2009).

6.2.2 Photometric variability of hot DQ WDs & DZ/DAZ MWDs

Following the discovery of photometric variations over days in a hot DQ (Chapter 3) and a metal-rich cool DZ MWD, a proposal was submitted to observe a sample of these stars with the INT in La Palma to identify further examples. We were awarded 7 nights in April 2013 to observe 12 hot DQs (including 9 new candidates from the SDSS DR7) and 19 DZ/DAZ MWDs for photometric variability on both short (minutes – hours) and long timescales (days).

Hot DQ White Dwarfs

SDSS J0005-1002 is the only hot DQ WD that has been tested for variability on long timescales of days and therefore all hot DQ WDs should be monitored for long period modulations as an indicator of rotation and magnetism. Spin periods on the order of days is consistent with the general WD population. Photometric fluctuations are expected in ~40% of MWDs, potentially indicating the presence of a previously unknown magnetic field. As suggested in Chapter 3, the photometric variability in some hot DQs, which exhibit single mode pulsations, may be rapid rotators rather than pulsators, while a hot DQ could also display both pulsations on short timescales and variations on long timescales due to rotation.

DZ/DAZ Magnetic White Dwarfs

The metals in the atmospheres of these WDs are thought to be accreted from asteroidal material. Some DAZs have debris discs, while DZs do not, since the material is long lasting in their helium atmospheres and their discs dissipated long ago (Farihi et al. 2010). Spin periods of DZ/DAZ MWDs would allow time-resolved spectroscopy to be carried out, to investigate how the metal lines vary across the surface with rotation, as outlined in §6.2.1. Since there is evidence of planetary debris at some magnetic DZs and DAZs, it is possible they formed from the merger with a giant planet (as suggested by Farihi et al. 2011b). Furthermore, by determining rotation periods due to photometric variability for many metal-rich MWDs, their rotation rates and correlations with magnetic field strength, temperature, mass and cooling age can be investigated to ascertain whether they are consistent with known merger products, which would further the argument that they formed from a merger/tidal disruption event.

6.2.3 Continual monitoring of RE J0317−853

As suggested in Chapter 5, observations of RE J0317-853 need to be continued over the following years. Figure 5.13 of RE J0317-853's O – C data, with a model of the orbital motion, illustrates that observations over ∼ 10 years could help to constrain the eccentricity of the orbit and the orbital period. A dynamical estimate for the orbital period could help constrain the total mass of the binary system, providing a model-independent estimate for the (uncertain) mass of the MWD RE J0317-853. Furthermore, observations over future years could yield a more accurate $\dot{P}$ measurement, perhaps strengthening the evidence for the rate of period change ($\dot{P}$) being caused by the reflex motion of the double-degenerate pair.

Intensive monitoring over another observing season (mid-August to January) could provide sufficient data for the O – C analysis to determine whether the fluctuations on 1.806 years (Fig. 5.14, or 0.49 years for the O – C residuals to the parabolic fit in Fig. 5.17) are significant or not. Dedicated *Spitzer* IRAC observations over the rotation period of RE J0317-853 could improve the upper limit on an unresolved planetary companion, and therefore, in conjunction with the timing results, the tentative planetary companion could be either confirmed or ruled out. The periodicity analysis of the O – C data points ($P \approx 1.806$ years) in Figure 5.14 indicate that observations over the upcoming 2013/2014 observing season should occur in a minimum of the O – C sinusoid, if the periodic signal is real and correct. Therefore, another concerted observing campaign at SAAO between August 2013 and January 2014 may help to determine whether this periodicity in the O – C data points is physical.

If this is confirmed as a bona fide planet orbiting RE J0317-853 it would be the first planet detected around a WD. The presence of an actual planet orbiting a WD would place constraints on the size and distance of planets orbiting WDs and the survival of planetary systems through the host stars' post main-sequence evolution. With theoretical models, the formation mechanism of the planet and WD could be further explored and, for example, possibly determine whether the massive, highly magnetic WD formed via a merger and if the tentative planet formed as a result of the merger or if it was orbiting one of the stars in the binary prior to merging.

6.3 Summary

In conclusion, this thesis has presented results from photometric variability surveys of MWDs to determine rotation periods on both short (minutes – days) and long timescales (months – years), to better understand the distribution of spin periods of isolated MWDs. Periods of variability measured range between hours and a few days, consistent with previously reported rotation periods. The relationships between their physical properties and rotation can provide hints into the formation mechanism of MWDs and the origin of the magnetic fields. The spin period evolution of the MWD RE J0317-853 has also been examined using nearly 20 years of observations. A rate of period change is detected which is consistent with the rate of period change expected from the orbital motion between RE J0317-853 and its non-magnetic white dwarf companion LB 9802, assuming a position angle in the orbit of $\theta = 45 - 57°$ and inclination angle of $i = 24.7 - 56.8°$. It is shown that spin-down from magnetic dipole radiation will only effect the MWDs with the strongest magnetic fields and therefore will not be detectable in the majority of the known rotating MWDs. Finally, the possibility of planets surviving the post main-sequence evolution to the WD stage is discussed, since there is tentative evidence for the presence of a planetary companion orbiting RE J0317-853 in the O – C data.

A

Chapter 2: Photometric Variability and Rotation in Magnetic White Dwarfs

A.1 Variable MWDs with well-determined periods

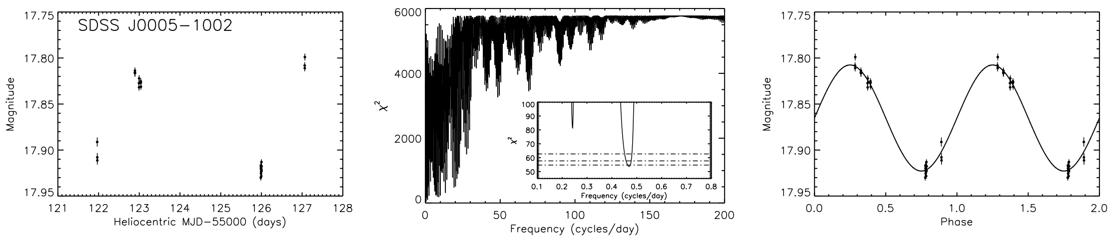

Figure A.1: SDSS J0005-1002 – light curve taken in r′ filter in October 2009, floating-mean periodogram and light curve folded on $P = 2.13 \pm 0.05$ d.

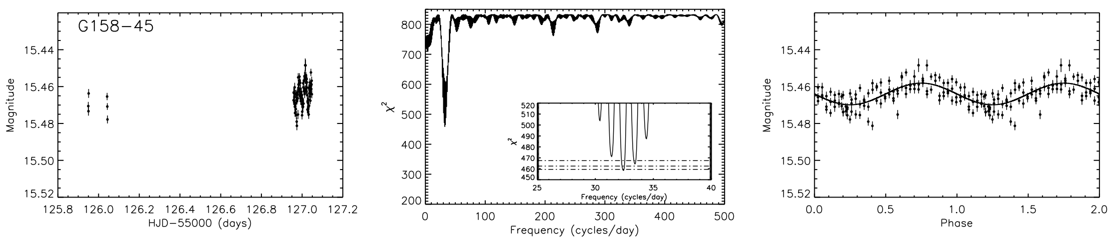

Figure A.2: G 158-45 – light curve taken in V filter in October 2009, floating-mean periodogram and light curve folded on $P = 44.43 \pm 0.12$ min.

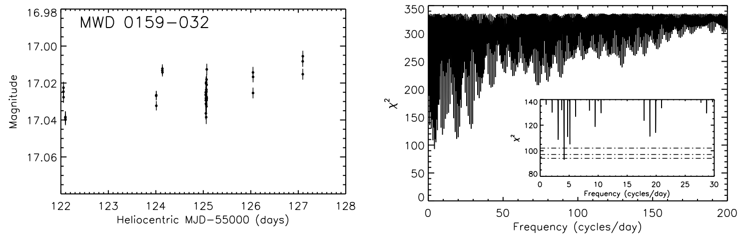

Figure A.3: MWD 0159-032 – light curve taken in V filter in October 2009, floating-mean periodogram and light curve folded on $P = 5.82 \pm 0.01$ h.

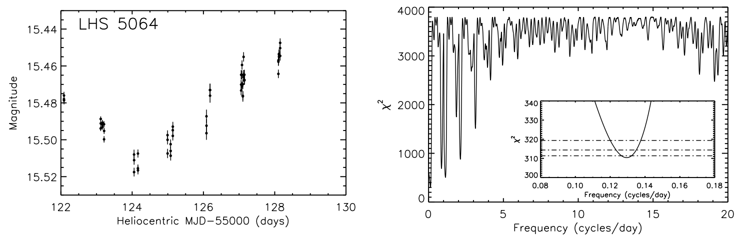

Figure A.4: LHS 5064 – light curve taken in V filter in October 2009, floating-mean periodogram and light curve folded on $P = 7.72^{+0.58}_{-0.42}$ d.

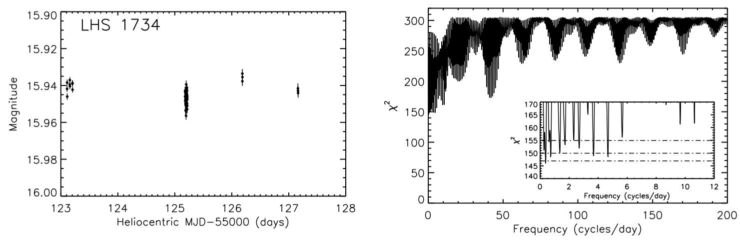

Figure A.5: LHS 1734 – light curve taken in V filter in October 2009, floating-mean periodogram and light curve folded on $P = 2.61 \pm 1.29$ d.

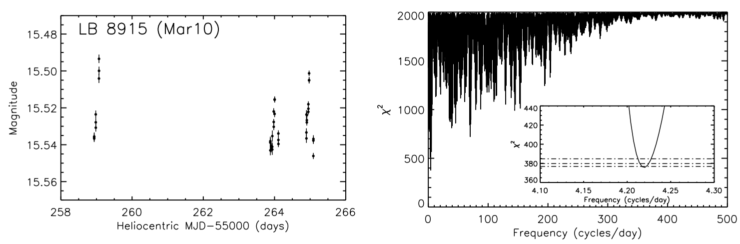

Figure A.6: LB 8915 – light curve taken in V filter in October 2009, floating-mean periodogram and light curve folded on $P = 5.694 \pm 0.006$ h.

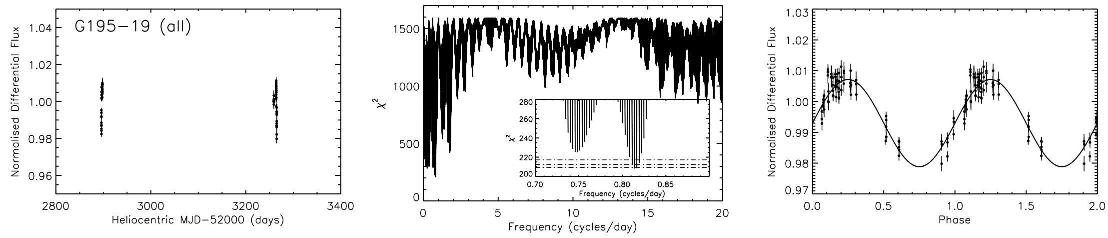

Figure A.7: G 195-19 – light curve taken in V filter of all of the data, floating-mean periodogram and light curve folded on P = 1.2285 ± 0.002 d.

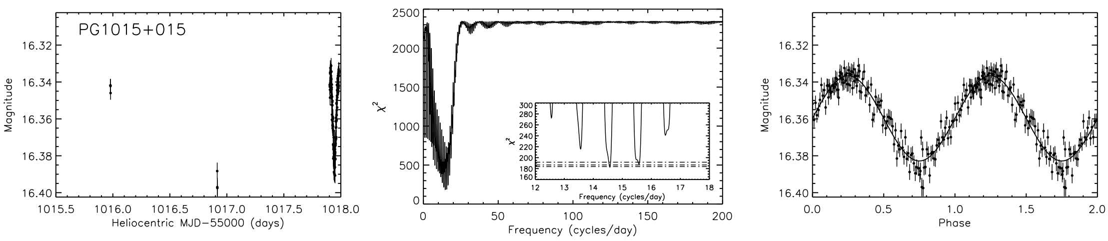

Figure A.8: PG 1015+015 – light curve taken in V filter in March 2012, floating-mean periodogram and light curve folded on $P = 98.84^{+0.14}_{-0.07}$ min.

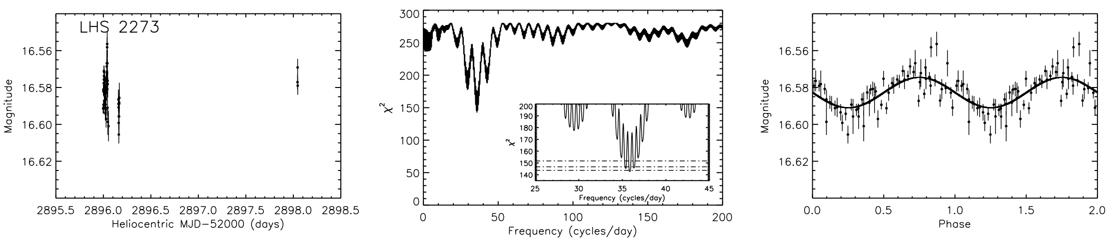

Figure A.9: LHS 2273 – light curve taken in V filter in March 2009, floating-mean periodogram and light curve folded on P = 40.14 ± 0.60 min.

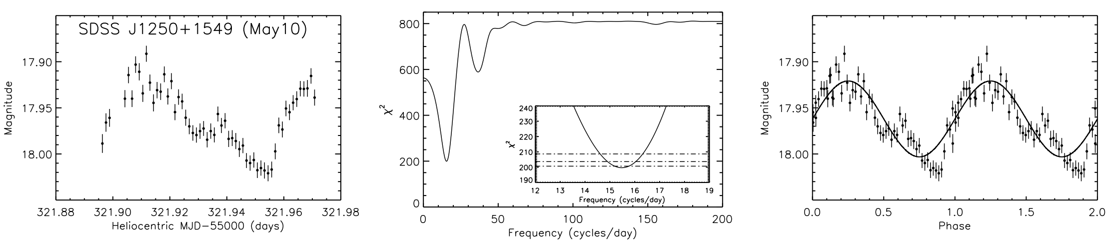

Figure A.10: SDSS J1250+1549 – light curve taken in i′-band in May 2010, floating-mean periodogram and light curve folded on P = 1.55 ± 0.06 h.

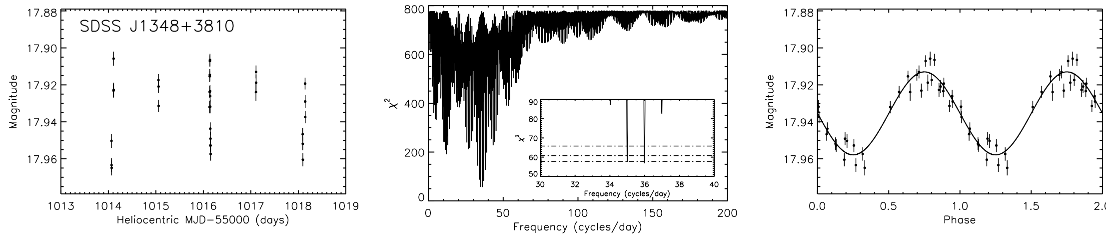

Figure A.11: SDSS J1348+3810 – light curve taken in r′ filter in March 2012, floating-mean periodogram and light curve folded on $P = 40.02^{+1.14}_{-0.02}$ min.

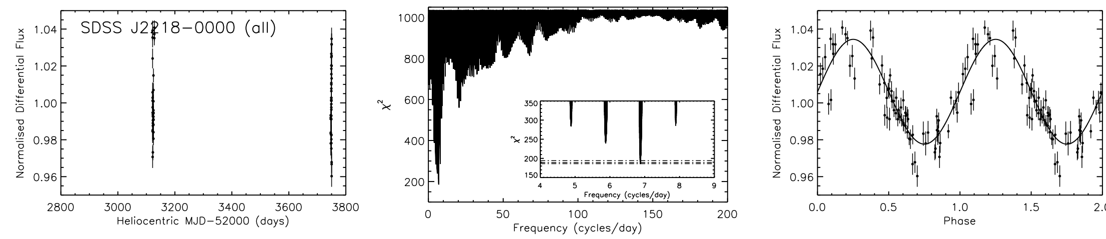

Figure A.12: SDSS J2218-0000 – light curve taken in r′ filter of all of the data, floating-mean periodogram and light curve folded on $P = 3.493 \pm 0.004$ h.

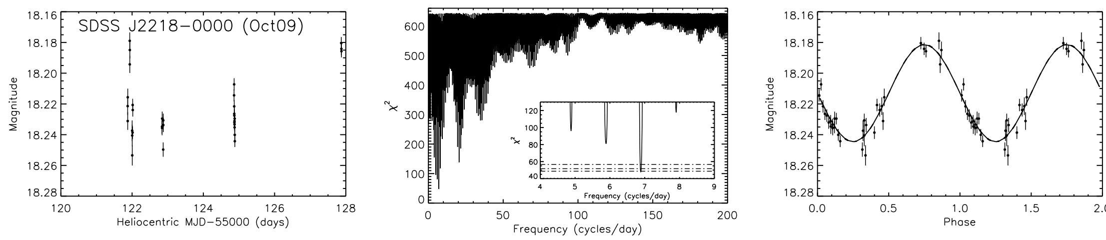

Figure A.13: SDSS J2218-0000 – light curve taken in r′ filter in October 2009, floating-mean periodogram and light curve folded on $P = 3.487 \pm 0.007$ h.

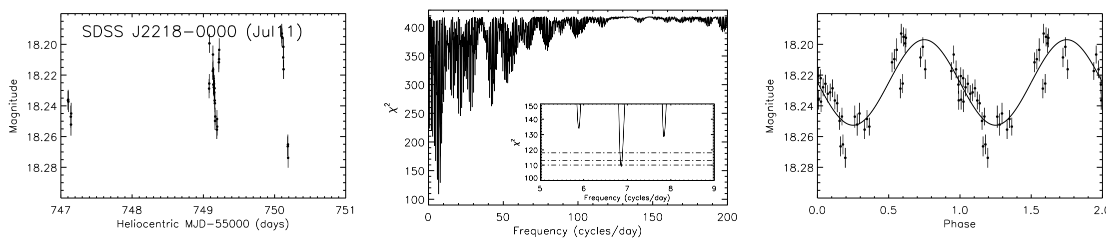

Figure A.14: SDSS J2218-0000 – light curve taken in r′ filter in July 2011, floating-mean periodogram and light curve folded on $P = 3.497 \pm 0.008$ h.

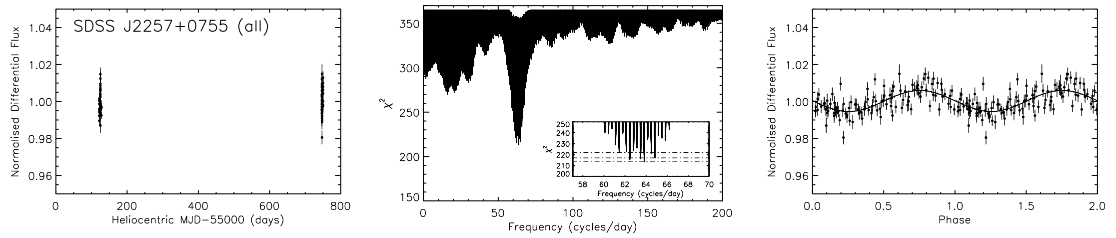

Figure A.15: SDSS J2257+0755 – light curve taken in r′ filter of all of the data, floating-mean periodogram and light curve folded on P = 22.56 ± 0.42 min.

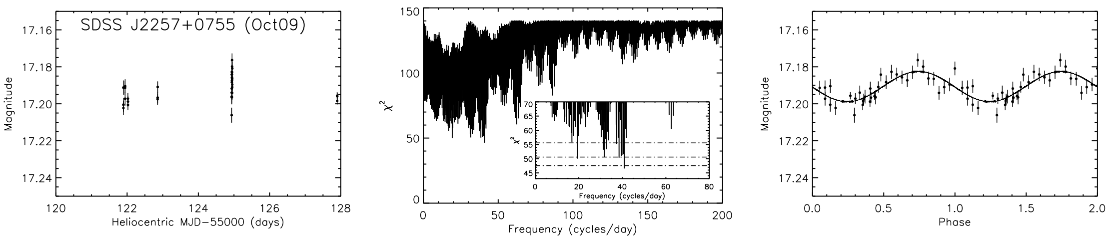

Figure A.16: SDSS J2257+0755 – light curve taken in r′ filter in October 2009, floating-mean periodogram and light curve folded on P = 35.25 ± 0.02 min.

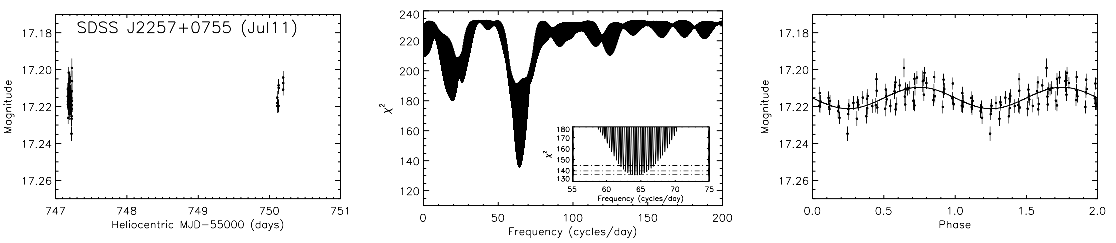

Figure A.17: SDSS J2257+0755 – light curve taken in r′ filter in July 2011, floating-mean periodogram and light curve folded on P = 22.34 ± 0.53 min.

A.2 Variable MWDs with poorly constrained periods

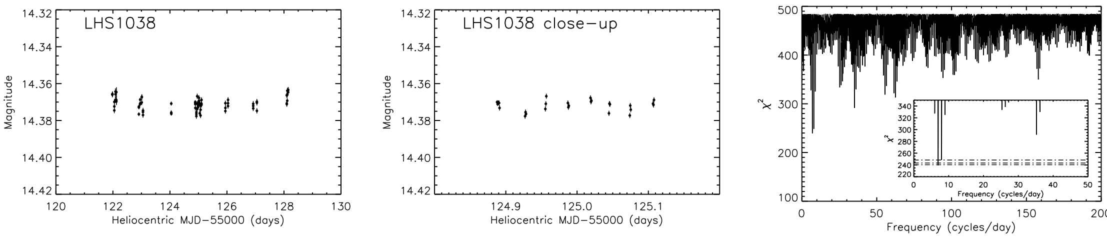

Figure A.18: LHS 1038 – light curve taken in V filter in July 2011, close-up of light curve and floating-mean periodogram, with a possible period of P = 3.438 ± 0.004 h.

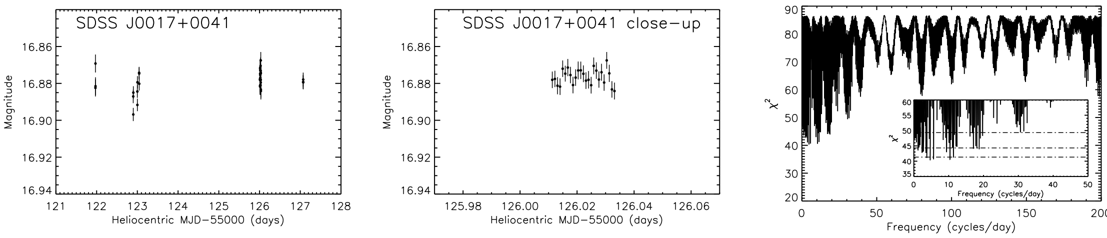

Figure A.19: SDSS 0017+0041 – light curve taken in r′ filter in July 2011, close-up of light curve and floating-mean periodogram, with a possible period between P = 1.28 – 19.44 h.

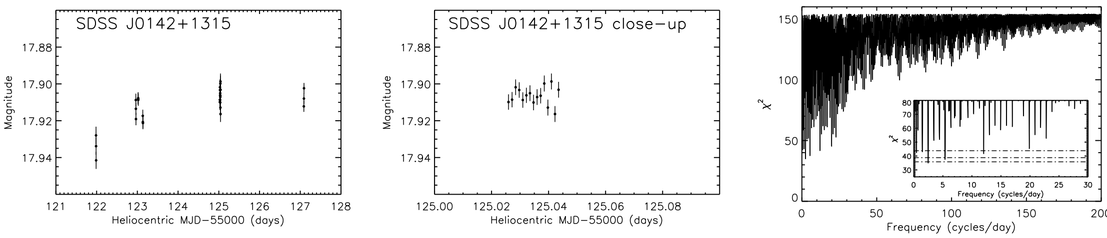

Figure A.20: SDSS J0142+1315 – light curve taken in r′ filter in July 2011, close-up of the light curve and floating-mean periodogram, with a possible period of P = 9.69 ± 2.68 h.

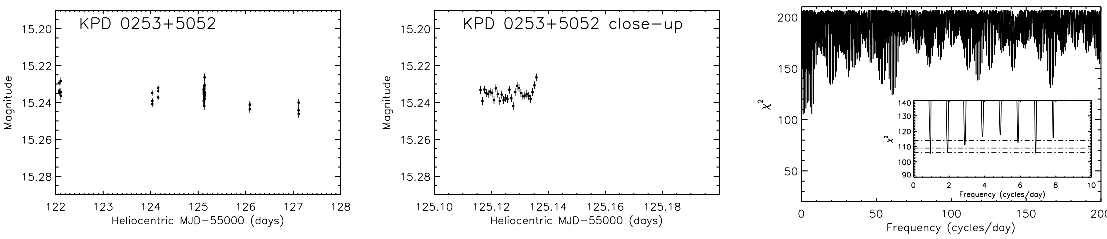

Figure A.21: KPD 0253+5052 – light curve taken in V filter in July 2011, close-up of light curve and floating-mean periodogram, with a possible period of P = 1.05 ± 0.46 d.

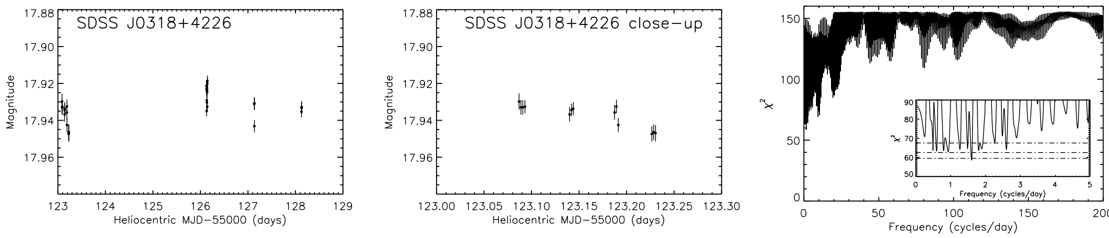

Figure A.22: SDSS J0318+4226 – light curve taken in r′ filter in July 2011, close-up of light curve and floating-mean periodogram, with a possible period of $P = 15.04 \pm 0.09$ h.

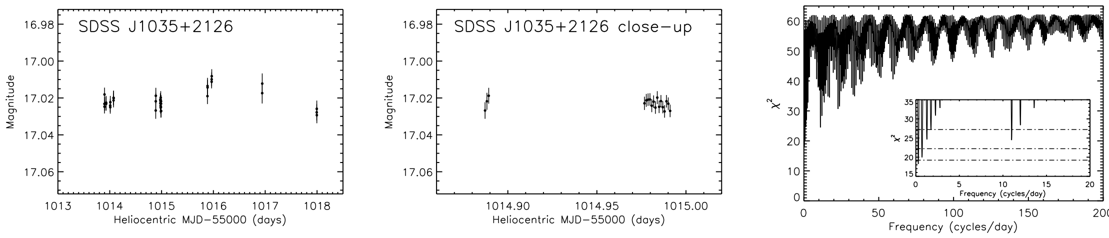

Figure A.23: SDSS J1035+2126 – light curve taken in r′ filter in July 2011, a close-up on a region of the light curve and the floating-mean periodogram, with a possible period between $P = 1.3 - 4.1$ d.

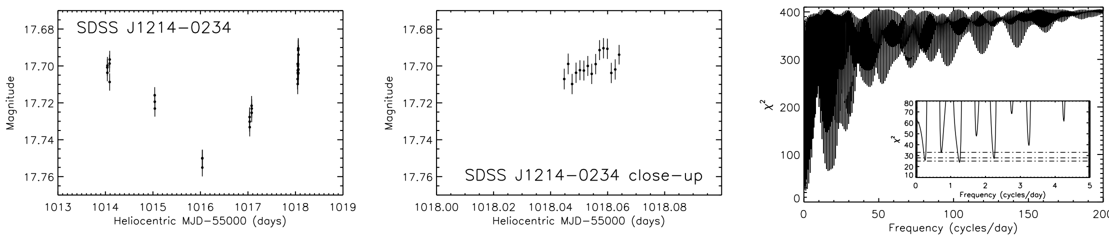

Figure A.24: SDSS J1214-0234 – light curve taken in r′ filter in July 2011, a close-up on a region of the light curve and the floating-mean periodogram, with a possible period between $P = 10.7$ h – 4.0 d.

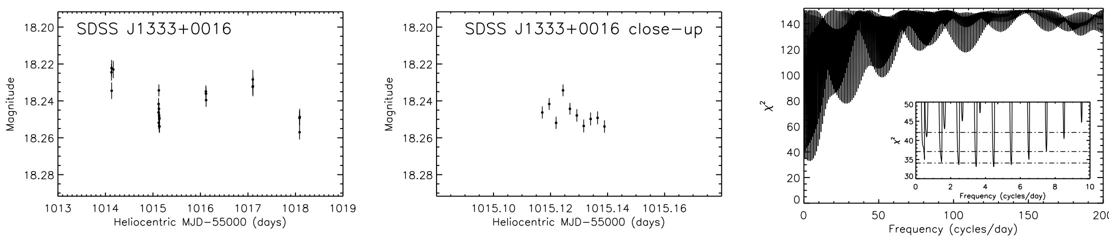

Figure A.25: SDSS J1333+0016 – light curve taken in r′ filter in July 2011, a close-up on a region of the light curve and the floating-mean periodogram, with a possible period between $P = 3.7$ h – 2.1 d.

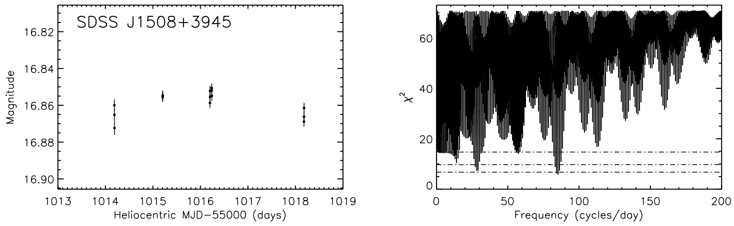

Figure A.26: SDSS J1508+3945 – light curve taken in r′ filter in July 2011 and the floating-mean periodogram, with a possible period between P = 16.7 – 53 min.

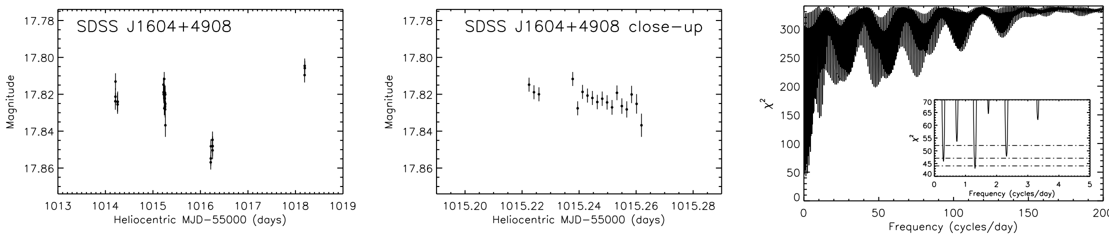

Figure A.27: SDSS J1604+4908 – light curve taken in r′ filter in July 2011, a close-up on a region of the light curve and the floating-mean periodogram, with a possible period between P = 18.2 h – 3.5 d.

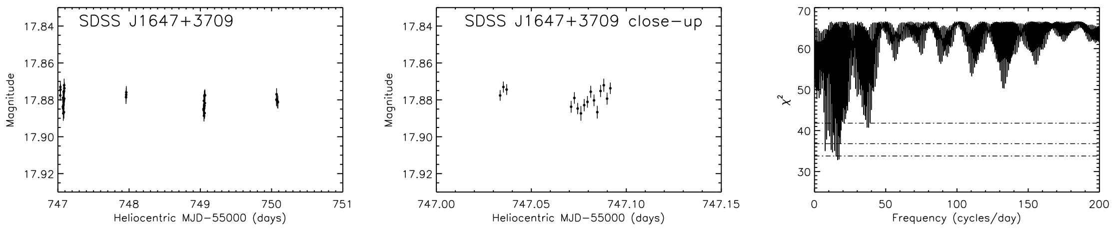

Figure A.28: SDSS J1647+3709 – light curve taken in r′ filter in July 2011, a close-up on a region of the light curve and the floating-mean periodogram, with a possible period between P = 84 – 190 min.

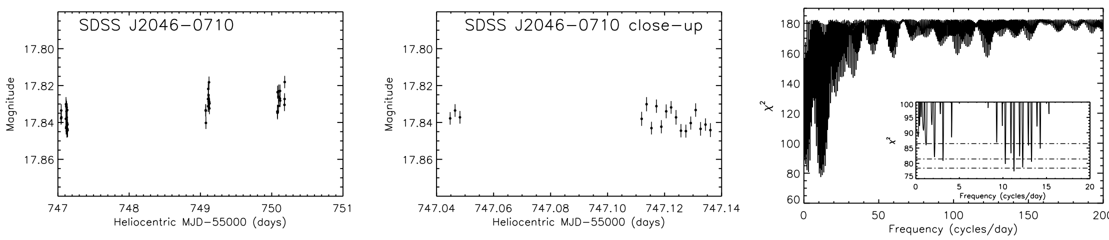

Figure A.29: SDSS J2046-0710 – light curve taken in r′ filter in July 2011, a close-up on a region of the light curve and the floating-mean periodogram, with a possible period between P = 1.8 – 7.7 h.

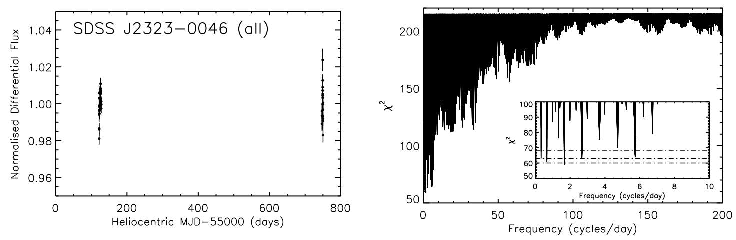

Figure A.30: SDSS J2323-0046 – light curve taken in r′ filter of all of the data and floating-mean periodogram, with a possible period between P = 14.3 h – 3.0 d.

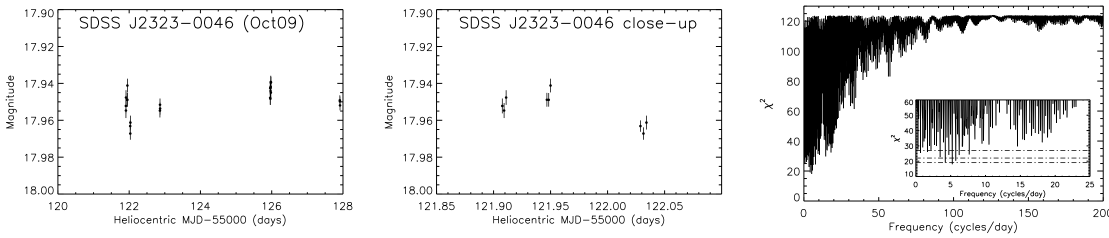

Figure A.31: SDSS J2323-0046 – light curve taken in r′ filter in October 2009, a close-up of the light curve and floating-mean periodogram, with a possible period of $P = 4.59 \pm 0.75$ h.

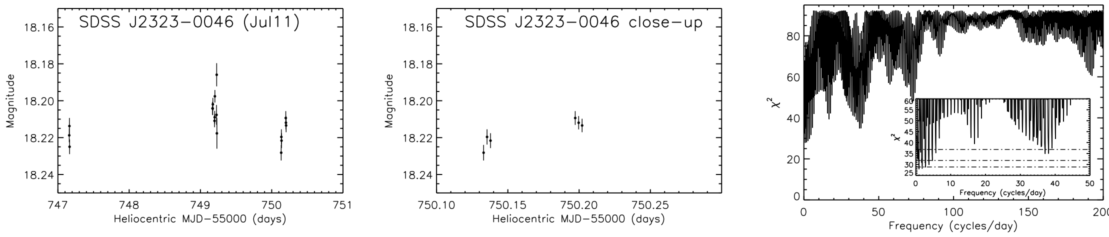

Figure A.32: SDSS J2323-0046 – light curve taken in r′ filter in July 2011, a close-up of the light curve and floating-mean periodogram, with a possible period between P = 5.1 h – 1.2 d.

A.3 MWDs where no variability is found

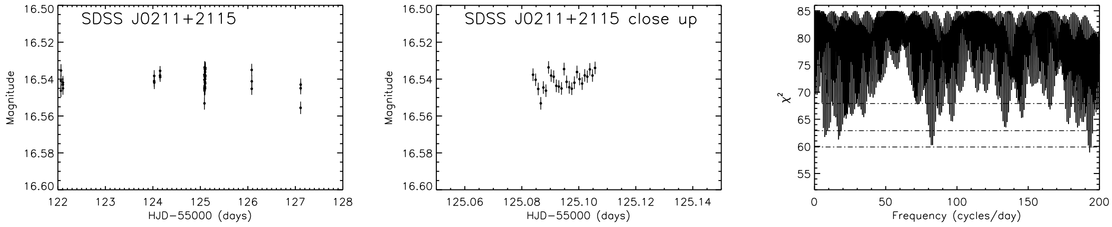

Figure A.33: SDSS J0211+2115 – light curve taken in r′ filter in October 2009, a close-up of the light curve and floating-mean periodogram.

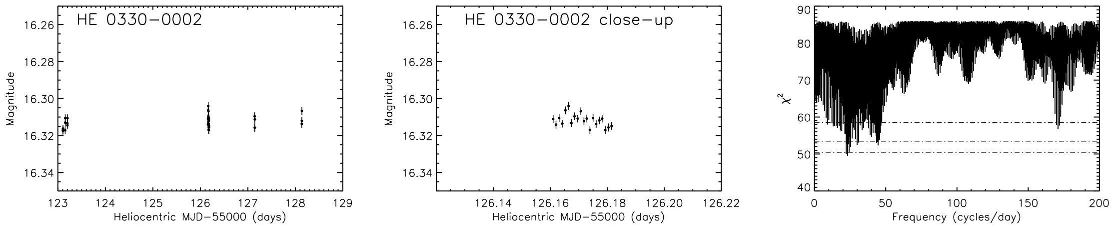

Figure A.34: HE 0330-0002 – light curve taken in r′ filter in October 2009, a close-up of the light curve and floating-mean periodogram.

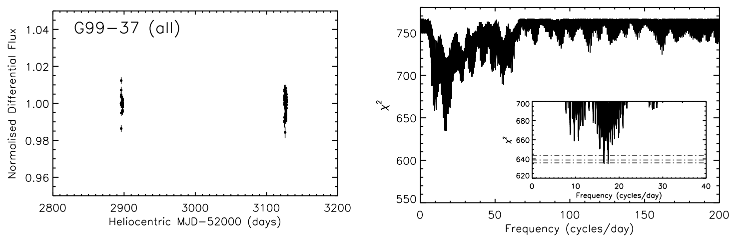

Figure A.35: G 99-37 – light curve of all of the data and floating-mean periodogram.

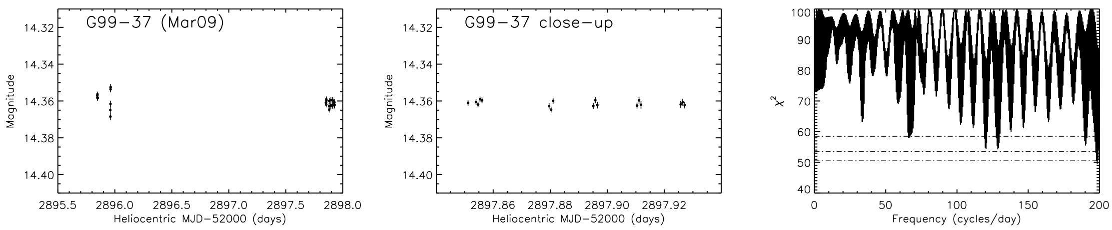

Figure A.36: G 99-37 – light curve taken in V filter in March 2009, a close-up of the light curve and the floating-mean periodogram.

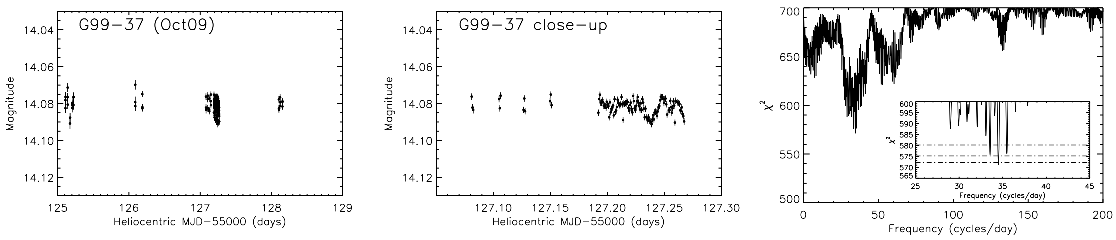

Figure A.37: G 99-37 – light curve taken in V filter in October 2009, a close-up of the light curve and the floating-mean periodogram.

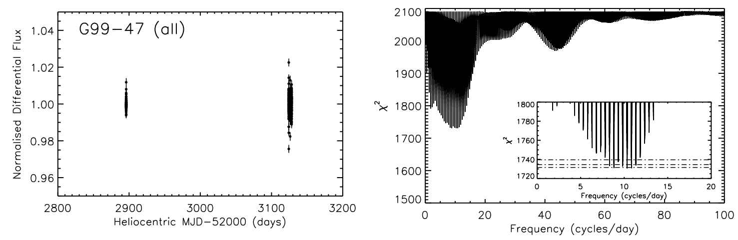

Figure A.38: G 99-47 – light curve of all of the data and floating-mean periodogram.

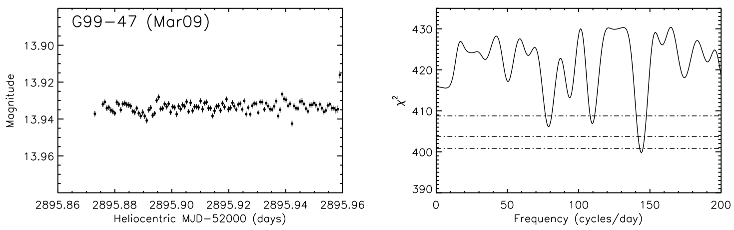

Figure A.39: G 99-47 – light curve taken in V filter in March 2009 and the floating-mean periodogram.

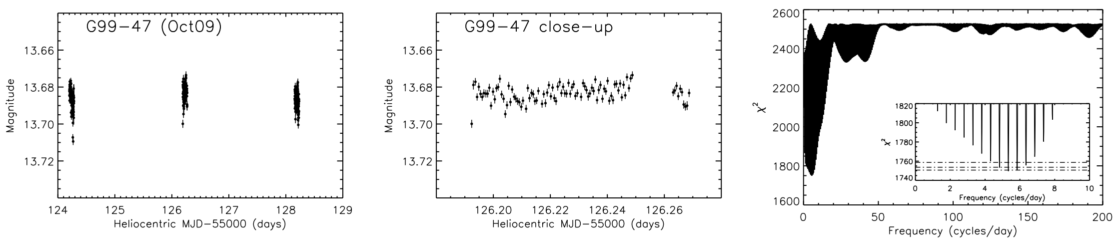

Figure A.40: G 99-47 – light curve taken in V filter in October 2009, a close-up of the light curve and the floating-mean periodogram.

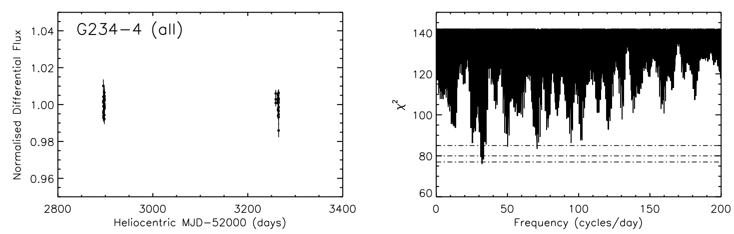

Figure A.41: G 234-4 – light curve of all of the data and floating-mean periodogram.

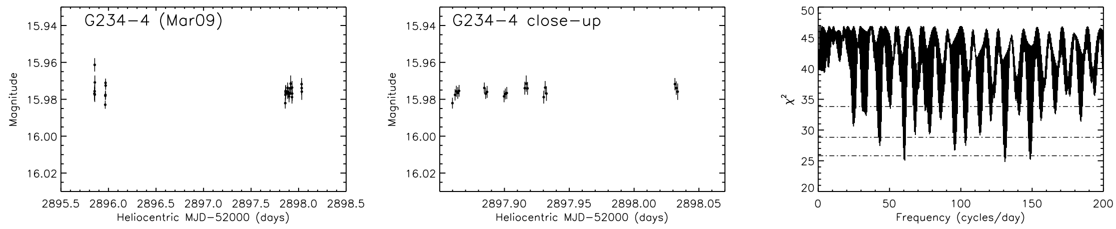

Figure A.42: G 234-4 – light curve taken in V filter in March 2009, a close-up of the light curve and floating-mean periodogram.

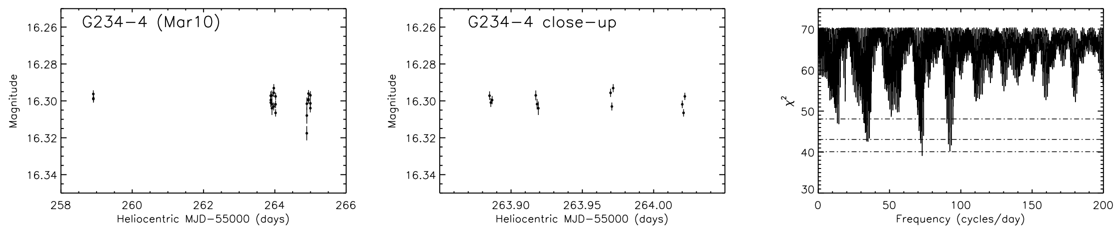

Figure A.43: G 234-4 – light curve taken in V filter in March 2010, a close-up of the light curve and floating-mean periodogram.

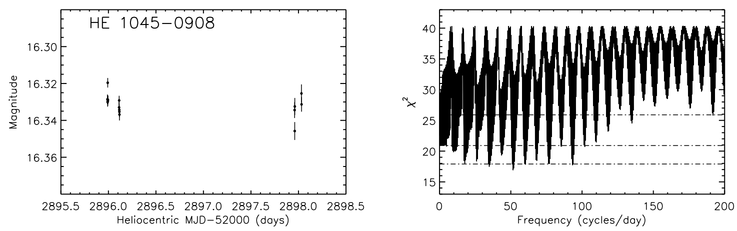

Figure A.44: HE 1045-0908 – light curve taken in V filter in March 2009 and floating-mean periodogram.

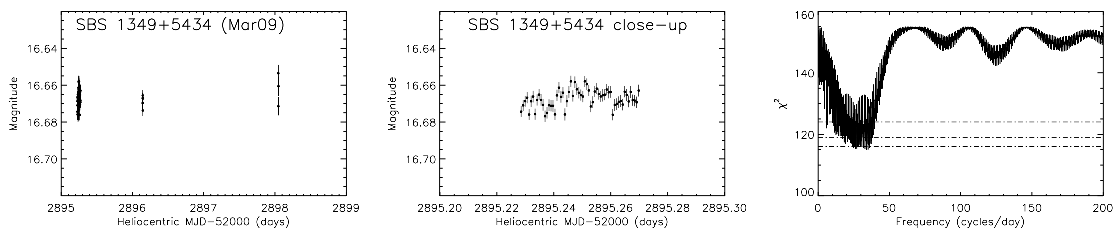

Figure A.45: SBS 1349+5434 – light curve taken in V filter in March 2009, a close-up of the light curve and floating-mean periodogram.

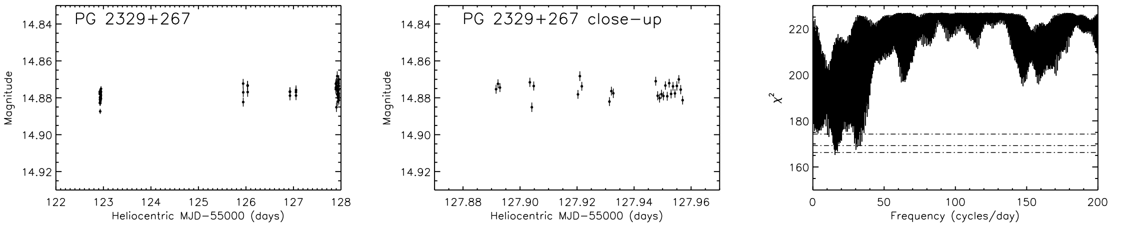

Figure A.46: PG 2329+267 – light curve taken in V filter in October 2009, a close-up of the light curve and floating-mean periodogram.

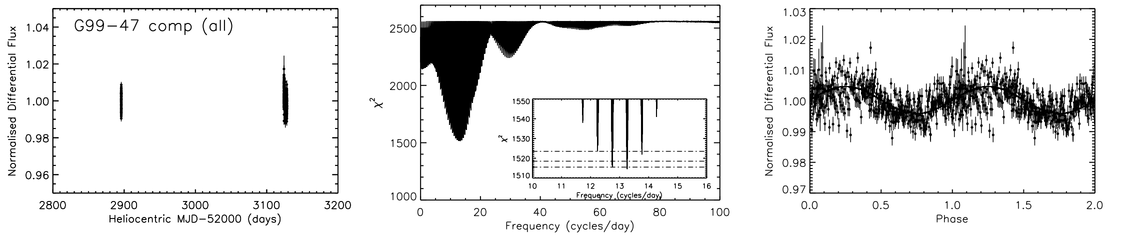

Figure A.47: G 99-47 variable comparison star – all of the data, its floating-mean periodogram and light curve folded on P = 108.57 ± 2.22 min.

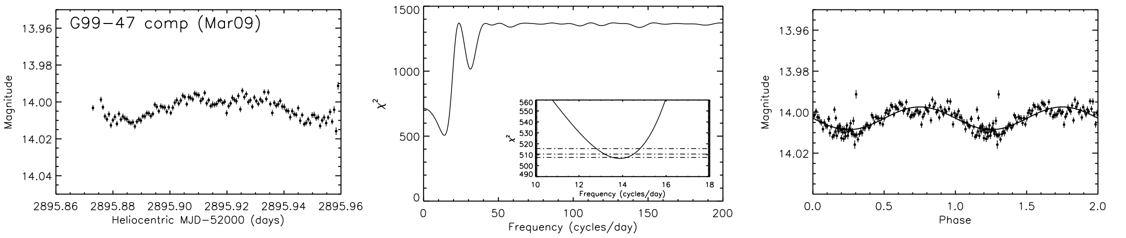

Figure A.48: G 99-47 variable comparison star – light curve taken in V filter in March 2009, floating-mean periodogram and the light curve folded on P = 103 ± 4 min.

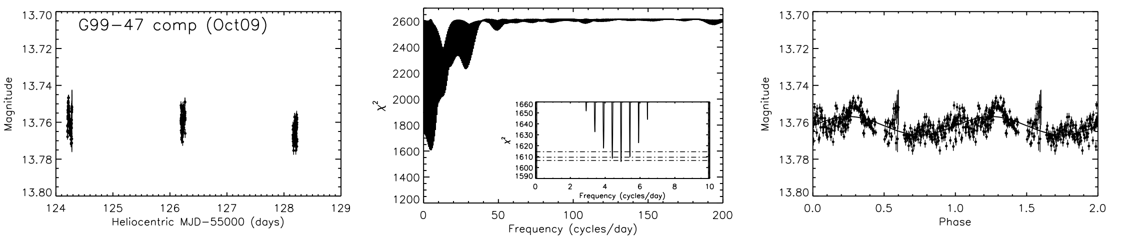

Figure A.49: G 99-47 variable comparison star – light curve taken in V filter in October 2009, its floating-mean periodogram and the light curve folded on P = 4.9 ± 0.6 h.

Table A.1: Catalogue of currently known magnetic white dwarfs.

WD	Other Names	Composition	B_p (MG)	T_{eff} (K)	M ($M_\odot$)	P_{rot}	References
0003−103	SDSS J000555.91−100213.4	C/He	1.47 [a]	19420 ± 920	$\log g = (8.0)$	2.110 ± 0.045 d	1,2,3,4
0009+501	LHS 1038	H	0.295 ± 0.006	6540 ± 150	0.74 ± 0.04	8.02 ± 0.19 h	5,6
0011−134	G 158-45	H(+He)	16.7 ± 0.6	6010 ± 120	0.71 ± 0.07	44.43 ± 0.12 min	7,8,6,4
0015+004	SDSS J001742.44+004137.4	He	8.3	15000		[c]	1
0018+147	SDSS J002129.00+150223.7	H	530.69 ± 63.56	7000			10,11
0038−084	NLTT 2219	H	~0.3 [a]	6000 ± 180	0.59 ± 0.15		5
0040+000	SDSS J004248.19+001955.3 [d]	H	2.00	11000			10,1
0041−102	Feige 7	H/He	35	20000	$\log g = (8.0)$	131.606 min	12,13,14
0051+115	HS 0051+1145	H	0.24 ± 0.01 [e]				15
0058−044	PHL 940	H	~0.32 [e]	16700 ± 62			15,16
0140+130	SDSS J014245.37+131546.4	He	4	15000		[c]	1
0155+003	SDSS J015748.15+003315.1	He (DZ)	3.7 [a]	~6000			1
0159−032	MWD 0159−032	H	6	26000	log g = (8.0)	5.81 ± 0.01 h	17,4
0208+002	SDSS J021116.34+003128.5	H	341.31 ± 54.34	9000			10,1
0209+210	SDSS J021148.22+211548.2	H	166.16 ± 7.41	12000			10,11
0231+263	SDSS J023420.62+264801.6	H	32.82 ± 6.26	13500			10
0233−083	SDSS J023609.40−080823.9	H/C	5	10000			11
0236−269	HE 0236−2656	He	?	6000 − 7000			18
0239+109	G 4-34 [d]	H	~0.70 [e]	46859 ± 569			15,16,19
0253+508	KPD 0253+5052	H	13 − 14	15000	$\log g = (8.0)$	3.79 ± 0.05 h	20,21
0257+080	LHS 5064	H	0.090 ± 0.015	6680 ± 150	0.57 ± 0.09	$7.72^{+0.58}_{-0.42}$ d	15,7,4
0301−006	SDSS J030407.40−002541.7	H	10.95 ± 0.98	15000			10,22
0307−428	MWD 0307−428	H	10	25000	$\log g = (8.0)$		17
0315−293	NLTT 10480	H (DAZ)	0.519 ± 0.004 [a]	5340 ± 190	0.58 ± 0.15		23,5
0315+422	SDSS J031824.20+422650.9	H	10.12 ± 0.10	10500		[c]	10
0321−026	KUV 03217−0240 [f]	H	?	27370:	0.92		19,24
0322−019	G 77-50	H (DAZ)	0.120	5310 ± 100	0.60 ± 0.01	28 − 33 d?	25

Table A.1: *continued*

WD	Other Names	Composition	B_p (MG)	$T_{\rm eff}$ (K)	M ($M_\odot$)	$P_{\rm rot}$	References
0325−857	EUVE J0317−855	H	180 − 800	30000 − 50000	~1.35	725 s	26,27,28,29
0323+051	SDSS J032628.17+052136.3	H	16.87 ± 2.41	25000			10
0329+005	KUV 03292+0035	H	13.13 ± 1.00	15500			10,1
0330−000	HE 0330−0002	He	849.30 ± 51.75	7000			10,1
0340−068	SDSS J034308.18−064127.3	H	9.96 ± 2.06	13000:			10,1
0342+004	SDSS J034511.11+003444.3	H	1.96 ± 0.42	8000			10,22
0350+098	1RXS J035315.5+095700 [f]	H	?	~31246:			19,30
0410−114	NLTT 12758	H	1.7 ± 0.2 [a]	7440 ± 150	0.59 ± 0.15		5
0413−077	40 Eri B	H	0.0023 ± 0.0007	16490 ± 84	0.497 ± 0.005		31,32
0416−096	NLTT 13015	H	6.0 − 7.5 [a]	5745 ± 405	0.59 ± 0.15		5
0446−789	BPM 3523	H	0.00428 ± 0.00064	23450 ± 20	0.49 ± 0.01		33
0503−174	LHS 1734	H (+He)	7.3 ± 0.2	5300 ± 120	0.37 ± 0.07	2.61±1.29 d	8,7,4
0548−001	G 99−37	He(C_2/CH)	7.3 ± 0.3	6070 ± 100	0.69 ± 0.03	4.117 h [g]	34,35,36
0553+053	G 99−47	H	20 ± 3	5790 ± 110	0.71 ± 0.03	0.97 h [g]	37,7,36
0616−649	RE J0616−649	H	14	50000	$\log g = (8.0)$		38
0637+477	GD 77	H	1.2 ± 0.2	14870 ± 120	0.69		39,40
0728+642	G 234−4	H/He?	0.0396 ± 0.0116 [b]	4500 ± 500	0.58 ± 0.18		9,41
0745+303	SDSS J074853.07+302543.5 [h]	H	11.4	21000 ± 2000	0.81 ± 0.09		42
0745+304	SDSS J074850.48+301944.8	H	6.75 ± 0.41	22000:			10,11
0746+172	SDSS J074924.91+171355.4	H	13.99 ± 1.30	20000			10
0749+173	SDSS J075234.95+172525.0	H	10.30 ± 1.23	9000			10
0755+358	SDSS J075819.57+354443.7	H	26.40 ± 3.94	22000			10,1
0756+437	G 111−49	H (C?)	220	8500 ± 500	1.07	$6.68^{+0.02}_{-0.03}$ h	43,9,44,45,46
0801+124	SDSS J080359.93+122943.9	H	40.7 ± 2.13	9000			10
0801+186	SDSS J080440.35+182731.0	H	48.47 ± 2.93	11000			10,11
0802+220	SDSS J080502.29+215320.5	H	6.11 ± 1.29	28000:			10,11
0804+397	SDSS J080743.33+393829.2	H	65.75 ± 18.52	13000			10,1

Table A.1: *continued*

WD	Other Names	Composition	B_p (MG)	$T_{\rm eff}$ (K)	M ($M_\odot$)	$P_{\rm rot}$	References
0806+376	SDSS J080938.10+373053.8	H	39.74 ± 5.41	14000			10,11
0814+043	SDSS J081648.71+041223.5	H	10.13 ± 8.03	11500			10,11
0814+201	SDSS J081716.39+200834.8	H	3.37 ± 0.44	7000			10
0816+376	GD 90	H	9	14000	$\log g$ = (8.0)		47,24
0821−252	EUVE J0823−25.4	H	2.8 − 3.5	43200 ± 1000	1.20 ± 0.04		48
0825+297	SDSS J082835.82+293448.7	H	33.40 ± 10.53	19500			10,11
0825+822	SDSS J083448.63+821059.1	H	14.44 ± 4.57	27000			10
0836+201	EG 59	H	2.83 ± 0.19	17000 ± 500	0.82 ± 0.05		49
0837+273	SDSS J084008.50+271242.7	H	10	12250			11
0839+026	SDSS J084155.74+022350.6	H	5.00 ± 0.99	7000			10,1
0843+488	SDSS J084716.21+484220.4 [d]	H	~3	19000			1
0846+830	SDSS J085550.67+824905.3	H	10.82 ± 2.99	25000			10
0848+121	SDSS J085106.12+120157.8	H	2.03 ± 0.10	11000			10
0853+163	LB 8915	H/He	0.75 − 1.0	21200 − 27700	$\log g$ = (8.0)	5.69 ± 0.01 h	50,4
0853+169	SDSS J085523.87+164058.9	H	12.6 ± 1.0	20000 ± 500	1.12 ± 0.11		49,10
0855+416	SDSS J085830.85+412635.1	H	3.38 ± 0.19	7000:			10,1
0903+083	SDSS J090632.66+080716.0	H	5.98 ± 3.02	17000:			10,11
0904+358	SDSS J090746.84+353821.5	H	22.40 ± 8.80	16500			10,11
0907+083	SDSS J091005.44+081512.2	H	1.01	25000			10
0908+422	SDSS J091124.68+420255.9	H	35.20 ± 5.83	10250			10,11
0911+059	SDSS J091437.40+054453.3	H	9.16 ± 0.77	17000			10,11
0912+536	G 195−19	He	~100	7160 ± 190	0.75 ± 0.02	1.3301 d	51,7,52
0915+211	SDSS J091833.32+205536.8	H	2.04 ± 0.10	14000			10
0922+014	SDSS J092527.47+011328.7	H	2.04	10000			10,1
	SDSS J092646.88+132134.5 [h]	H	210 ± 25.1	9500 ± 500	0.62 ± 0.10		53
0930+010	SDSS J093313.14+005135.4	He (C_2H)?	?				1
0931+105	SDSS J093356.40+102215.7	H	2.11 ± 0.49	8500			10,11

Table A.1: *continued*

WD	Other Names	Composition	B_p (MG)	$T_{\rm eff}$ (K)	M ($M_\odot$)	$P_{\rm rot}$	References
0931+394	SDSS J093409.90+392759.3	H	1.01	10000			10
0931+507	SDSS J093447.90+503312.2	H	7.35 ± 2.21	8900			10,11
0939+211	SDSS J094235.01+205208.3	H	39.21 ± 4.55	20000			10
0941+458	SDSS J094458.92+453901.2	H	15.91 ± 9.10	15500:			10,11
0945+246	LB 11146 [h]	H/He?	670	16000 ± 2000	$0.90^{+0.10}_{-0.14}$		54,55
0952+094	SDSS J095442.91+091354.4	DQ	?				11
0957+022	SDSS J100005.67+015859.2	H	19.74 ± 10.26	9000			10,1
1001+058	SDSS J100356.32+053825.6	H	672.07 ± 118.63	23000			10,11
1004+128	SDSS J100715.55+123709.5	H	5.41:	18000			10,11
1004+304	SDSS J100657.51+303338.0	H	1.00 ± 0.10	10000			10
1005+163	SDSS J100759.80+162349.6	H	19.18 ± 3.36	11000			10
1008+290	LHS 2229	He (C_2H)	∼100	4600	0.68 ± 0.01		56,103
1011+371	SDSS J101428.09+365724.4	H	11.09 ± 1.50	10500			10
1012+093	SDSS J101529.62+090703.8	H	4.09 ± 0.86	7200			10,11
1013+044	SDSS J101618.37+040920.6	H	2.01	10000			10,1
1015+014	PG 1015+014	H	99.92 ± 5.90	10000 ± 1000	1.15	$98.84^{+0.14}_{-0.07}$ min [j]	10,57,46,58
1017+367	GD 116	H	65 ± 5	16000			59
1018−103	EC 10188−1019 [f]	H	?	17720:			19
1019+200	SDSS J102239.06+194904.3	H	2.94 ± 0.71	9000			10
1019+274	SDSS J102220.69+272539.8	H	4.91 ± 0.31	11000			10
1026+117	LHS 2273 [d?]	H	18	7160 ± 170	0.59	40.14 ± 0.60 min	60,4
1031+234	PG 1031+234	H	∼200−1000	∼15000	0.93	3.53 ± 0.05 h	61,62,63,58,45,46
1031+034	HS 1031+0343	H	6.1 ± 0.3 [d]				15
1032+214	SDSS J103532.53+212603.5	H	2.96 ± 0.33	7000		[c]	10
1033+656	SDSS J103655.38+652252.0 [i]	He/C	3 [a]	15500			1,2,104
1036−204	LP 790−29	He	50	7800	$\log g = (8.0)$	24 − 28 yr	64,65
1043−050	HE 1043−0502	He	∼820	∼15000			66,18

Table A.1: *continued*

WD	Other Names	Composition	B_p (MG)	T_{eff} (K)	M ($M_\odot$)	P_{rot}	References
1045−091	HE 1045−0908	H	16	10000 ± 1000	$\log g = (8.0)$	2.7 h	67
1050+598	SDSS J105404.38+593333.3	H	17.41 ± 7.90	9500			10,1
1053+656	SDSS J105628.49+652313.5	H	29.27 ± 5.78	16500			10,1
1054+042	SDSS J105709.81+041130.3	H	2.03	8000			10
1105−048	LTT 4099	H	0.0039	15280 ± 20	0.52 ± 0.01	>3 h	33,68
1107+602	SDSS J111010.50+600141.4	H	6.37 ± 2.32	30000			10,1
1111+020	SDSS J111341.33+014641.7	He/C	?				1
1115+101	SDSS J111812.67+095241.3	H	3.38 ± 0.72	10500			10,11
1117−113	SDSS J112030.34−115051.1	H	8.90 ± 1.02	20000			10
1120+324	SDSS J112257.10+322327.7	H	11.38 ± 3.42	12500			10
1120+101	SDSS J112328.49+095619.3	H	1.21	9500			10
1126−008	SDSS J112852.88−010540.8	H	2.00	11000			10,1
1126+499	SDSS J112924.74+493931.9	H	5.31 ± 0.64	10000			10,11
1129+284	SDSS J113215.38+280934.3	H	3.01 ± 0.82	7000			10
1131+521	SDSS J113357.66+515204.8	H	8.64 ± 0.78	22000			10,1
1135+579	SDSS J113756.50+574022.4	H	5.00 ± 0.34	7800			10,11
1136−015	LBQS 1136−0132	H	22.71 ± 1.26	10500			10,1,69
1137+614	SDSS J114006.37+611008.2	H	50.19 ± 17.78	13500			10,1
1145+487	SDSS J114829.00+482731.2	H	32.47 ± 7.11	27500			10,11
1151+015	SDSS J115418.14+011711.4	H	33.47 ± 2.07	27000:			10,1
1156+619	SDSS J115917.39+613914.3	H	20.10 ± 6.70	23000			10,1
1159+619	SDSS J120150.10+614257.0	H	11.35 ± 1.53	10500			10,11
1203+085	SDSS J120609.80+081323.7	H	760.63 ± 281.66	13000			10,11
1204+444	SDSS J120728.96+440731.6	H	2.03	16750			10,11
1209+018	SDSS J121209.31+013627.7 [k]	H	10.12 ± 0.93	10000	0.60		10,1,70
1211−171	HE 1211−1707	He	50	~12000		$1.79^{+0.25}_{-0.16}$ h [b]	66,1,45,46
1212−022	LHS 2534	He (DZ)	1.92 [a]	6000			71

Table A.1: *continued*

WD	Other Names	Composition	B_p (MG)	$T_{\rm eff}$ (K)	M ($M_\odot$)	$P_{\rm rot}$	References
1214−001	SDSS J121635.37−002656.2	H	59.70 ± 10.23	15000			10,1
1219+005	SDSS J122209.44+001534.0	H	14.70 ± 4.70	14000			10,1
1220+484	SDSS J122249.14+481133.1	H	8.05 ± 2.24	9000			10,11
1220+234	PG 1220+234	H	3:	26540	0.81		58
1221+422	SDSS J122401.48+415551.9	H	22.36 ± 3.02	9500			10,11
1231+130	SDSS J123414.11+124829.6	H	4.32 ± 0.27	8200			10,11
1233−052	HE 1233−0519	H	0.61 ± 0.01 [e]	17737 ± 197	0.84		15,16
1245+413	SDSS J124806.38+410427.2	H	7.03 ± 1.19	7000			10,11
1246+296	SDSS J124836.31+294231.2	H	3.95 ± 0.25	7000			10
1246−022	SDSS J124851.31−022924.7	H	7.36 ± 2.19	13500			10,1
1248+161	SDSS J125044.42+154957.4 [l]	H	20.71 ± 3.66	10000		1.55±0.06 h	10,11,4,72
1252+564	SDSS J125416.01+561204.7	H	38.86 ± 9.03	13250			10,11
1254+345	HS 1254+3440	H	11.45 ± 0.71	8500			10
1258+592	SDSS J130033.48+590407.0	H	~6	6300 ± 300	0.54 ± 0.06		73
1309+853	G 256−7	H	4.9 ± 0.5	~5600	0.50		43,58
1312+098	PG 1312+098	H	10	~15000		5.42839 h	74,58
1317+135	SDSS J132002.48+131901.6	H	2.02	14750			10,11
1327+594	SDSS J132858.20+590851.0	H/C	18	25000			11
1328+307	G 165−7	He (DZ)	0.65 [a]	6440 ± 210	0.57 ± 0.17		75
1330+015	G 62−46 [d]	H	7.36 ± 0.11	6040	0.25		76
1331+005	SDSS J133359.86+001654.8	He (C_2H)?	?			[c]	1
1332+643	SDSS J133340.34+640627.4	H	10.71 ± 1.03	13500			10,1
1339+659	SDSS J134043.10+654349.2	H	4.32 ± 0.76	15000			19,1
1346+383	SDSS J134820.79+381017.2	H	13.65 ± 2.66	35000		$40.02^{+1.14}_{-0.07}$ min	10,4
1349+545	SBS 1349+5434	H	761.00 ± 56.42	11000			10,11
1350−090	LP 907−037	H	$\lesssim$0.3	9520 ± 140	0.83 ± 0.03		77,78
1405+501	SDSS J140716.67+495613.7	H	12.49 ± 6.20	20000			10

Table A.1: *continued*

WD	Other Names	Composition	B_p (MG)	$T_{\rm eff}$ (K)	M ($M_{\odot}$)	$P_{\rm rot}$	References
1416+256	SDSS J141906.19+254356.5	H	2.03 ± 0.10	9000			10
1425+375	SDSS J142703.40+372110.5	H	27.04 ± 3.20	19000			10,11
1424+581	SDSS J142625.71+575218.3 [i]	C/He	~1.2	19830 ± 750			79,3
1428+282	SDSS J143019.05+281100.8	H	9.34 ± 1.44	9000			10
1430+432	SDSS J143218.26+430126.7	H	1.01	24000			10,11
1430+460	SDSS J143235.46+454852.5	H	12.29 ± 6.98	16750			10,11
1440+753	EUVE J1439+75.0 [d]	H	14.8	39500	0.9 − 1.2		80
1444+592	SDSS J144614.00+590216.7	H	4.42 ± 3.79	12500			10,1
1452+435	SDSS J145415.01+432149.5	H	2.35 ± 0.88	11500			10,11
1503−070	GD 175 [d]	H	2.3	6990	0.70 ± 0.13		7
1506+522	SDSS J150746.80+520958.0 [h]	H	65.2 ± 0.3	18000 ± 1000	0.99 ± 0.05		53
1506+399	SDSS J150813.20+394504.9 [h]	H	18.9	18000 ± 2000	0.81 ± 0.09	[c]	42,10,11
1509+425	SDSS J151130.20+422023.0	H	22.40 ± 9.41	9750			10,11
1511+076	SDSS J151415.65+074446.5	H	35.34 ± 2.80	10000			10
1516+612	SDSS J151745.19+610543.6	H	13.98 ± 7.36	9500			10,1
1521+191	SDSS J152401.59+185659.2	H	11.96 ± 1.85	13500			10
1531−022	GD 185	H	0.035 ± 0.016 [e]	18620 ± 285	0.88 ± 0.03		81,78
1533+423	SDSS J153532.25+421305.6	H	5.27 ± 4.05	18500			10,1
1533−057	PG 1533−057	H	31 ± 3	20000 ± 1040	0.94 ± 0.18	1.890 ± 0.001 h	82,78,45,46
1537+532	SDSS J153829.29+530604.6	H	13.99 ± 3.82	13500			10,1
1536+085	SDSS J153843.10+084238.2	H	13.20 ± 4.34	9500			10
1539+039	SDSS J154213.48+034800.4	H	8.35 ± 2.60	8500			10,1
1541+344	SDSS J154305.67+343223.6	H	4.09 ± 2.67	25000			10
1603+492	SDSS J160437.36+490809.2	H	59.51 ± 4.64	9000		[c]	10,1
1610+330	CBS 418 [f]	H	?	~12637:			19,30
1639+537	GD 356 [m]	He	13	7510 ± 210	0.67 ± 0.07	0.0803 d	83,7,84
1641+241	SDSS J164357.02+240201.3	H	2.00	16500			10,11

Table A.1: *continued*

WD	Other Names	Composition	B_p (MG)	$T_{\rm eff}$ (K)	M ($M_\odot$)	$P_{\rm rot}$	References
1645+372	SDSS J164703.24+370910.3	H	2.10 ± 0.67	16250		[c]	10,11
1648+342	SDSS J165029.91+341125.5	H	3.38 ± 0.67	9750			10,11
1650+355	SDSS J165203.68+352815.8	H	7.37 ± 2.92	11500			10,1
1650+334	SDSS J165249.09+333444.9	H	5.07 ± 4.18	9000			10
1653+385	NLTT 43806	H (DAZ)	0.07 [a]	5900 ± 100			85
1658+440	PG 1658+441	H	2.3 ± 0.2 [a]	30510 ± 200	1.31 ± 0.02		86
1702+322	SDSS J170400.01+321328.7	H	50.11 ± 25.08	23000			10,11
1713+393	NLTT 44447	H	1.3	7000 ± 1000	0.59		87
1715+601	SDSS J171556.29+600643.9	H	2.03	13500			10,11
1719+562	SDSS J172045.37+561214.9	H	19.79 ± 5.42	22000			10,1
1722+541	SDSS J172329.14+540755.8	H	32.85 ± 3.56	10000			10,1
1728+565	SDSS J172932.48+563204.1	H	27.26 ± 7.04	10500			10,1
1743−520	BPM 25114	H	36	20000	$\log g = (8.0)$	2.84 d	88,89
1748+708	G 240−72	He	$\gtrsim$100	5590 ± 90	0.81 ± 0.01	$\gtrsim$100 yr	90,7,91,92
1814+248	G 183−35	H	~14	6500 ± 500	$\log g = (8.0)$	~50 min - few yr	43,9
1818+126	G 141−2 [d]	H	~3	6340 ± 130	0.26 ± 0.12		93,7
1820+609	G 227−28	He	$\lesssim$0.1	4780 ± 140	0.48 ± 0.05		9,7
1829+547	G 227−35	H/He?	170 − 180	6280 ± 140	0.90 ± 0.07	$\gtrsim$100 yr	37,7,92
1900+705	Grw +70°8247	He	320 ± 20	12070 ± 990	0.95 ± 0.02	$\gtrsim$100 yr	94,95,7,92
1939+401	NGC 6819−8	H	10.0 ± 1.1	19000 ± 1000	0.50 ± 0.05		49,96
1940+459	BOKS 53856 (KIC 9535405)	H	0.35 ± 0.035	32500 ± 2500	0.68 ± 0.08	6.1375 h	97
1953−011	G 92−40	H	0.095 ± 0.010	7920 ± 200	0.74 ± 0.03	1.44176 d	15,98,7,99
2010+310	GD 229	He	520	18000	≥1.0	$\gtrsim$100 yr	66,90,91,100,92
2022+130	SDSS J202501.10+131025.6	H	10.10 ± 1.76	17000			10
2039−682	GJ 2149	H	0.05 [a]	16050			81,5
2043−073	SDSS J204626.15−071037.0	H	2.03	8000		[c]	10,1
2049−004	SDSS J205233.52−001610.7	H	13.42 ± 3.73	19000			10,1

Table A.1: *continued*

WD	Other Names	Composition	B_p (MG)	$T_{\rm eff}$ (K)	M ($M_\odot$)	$P_{\rm rot}$	References
2051−208	HK 22880−134	H	0.22 − 0.29 [e]				15
2105−820	L 24−52	H (DAZ)	0.043 ± 0.01 [e]	10200 ± 290	0.75 ± 0.03		81,7
2146+005	SDSS J214900.87+004842.8	H	10.09 ± 4.71	11000			10,11
2146−077	SDSS J214930.74−072812.0	H	44.71 ± 1.92	22000:			10,1
2149+002	SDSS J215135.00+003140.5	H	~300	9000:			1
2149+126	SDSS J215148.31+125525.5	H	20.76 ± 1.39	14000			10,1
2153−512	GJ 841B	C_2/CH	1.3 ± 0.5	6100 ± 200			34
2202−000	SDSS J220435.05+001242.9	H	1.02 ± 0.10	22000			10
2215−002	SDSS J221828.59−000012.2	H	257.54 ± 48.71	15500:		3.493 ± 0.004 h	10,1,4
2245+146	SDSS J224741.46+145638.8	H	42.11 ± 2.83	18000:			10,1
2254+076	SDSS J225726.05+075541.7	H	16.17 ± 2.81	40000		22.56 ± 0.42 min	10,4
2316+123	KUV 813−14	H	45 ± 5	11000 ± 1000	$\log g$ = (8.0)	17.856 d	37,74
2317+008	SDSS J231951.73+010909.3	H	9.35:	8300			10,11
2320+003	SDSS J232248.22+003900.9	H	21.40 ± 3.36	20000:			10,1
2321−010	SDSS J232337.55−004628.2	He	4.8	15000		[c]	1
2329+267	PG 2329+267	H	2.31 ± 0.59	11730 ± 221	1.18 ± 0.03		101,78
2329−291	GD 1669 [n]	H	0.031 [a]	24000			81,5
2343+386	SDSS J234605.44+385337.6	H	798.1 ± 163.6	26000			10,11
2343−106	SDSS J234623.69−102357.0	H	9.17 ± 1.58	8500			10,11
2359−434	LTT 9857	H	0.0031 [b,o]	8570 ± 50	0.98 ± 0.04	2.695 h [p]	33,102

[a] Magnetic field strength averaged over surface, B_s.
[b] Longitudinal magnetic field strength, B_ℓ.
[c] Photometric variability may have been detected for this target in this work, see Table 2.4.
[d] Unresolved double degenerate.
[e] The magnetic field is estimated from a broadened Hα core, which could also be rotationally broadened, and therefore the magnetic field of this star is uncertain.
[f] Atmospheric parameters for this target have been determined using non-magnetic models, and therefore are rough estimates.
[g] Rotation period from polarisation measurements (Bues & Pragal 1989), but found to be photometrically stable in this work.

[h] Resolved double degenerate.
[i] Pulsator.
[j] A similar period of 98.74734 min was also derived for PG 1015+014 by Schmidt & Norsworthy (1991) using circular polarimetry.
[k] SDSS J1212+0136 is reported by Farihi, Burleigh & Hoard (2008) as a DAH with a substellar companion (possibly a late L or early T dwarf).
[l] SDSS J1250+1549 is a CV (Steele et al. 2011; Breedt et al. 2012).
[m] H emission seen in spectrum.
[n] Classified as a sdB in Gianninas et al. (2011).
[o] A larger field strength was detected by Koester et al. (2009) of 0.11 ± 0.01MG for LTT 9857, although this measurement was based on a broadened Hα core and could be rotationally broadened.
[p] Determined as part of the Pro-Am White Dwarf Monitoring (PAWM) campaign (`www.brucegary.net/WDE/WD2359-434/WD2359-434.htm`).

References. — (1) Schmidt et al. 2003; (2) Liebert et al. 2003; (3) Dufour et al. 2008b; (4) This work; (5) Kawka & Vennes 2012; (6) Valyavin et al. 2005; (7) Bergeron, Leggett & Ruiz 2001; (8) Bergeron, Ruiz & Leggett 1992; (9) Putney 1997; (10) Külebi et al. 2009; (11) Vanlandingham et al. 2005; (12) Achilleos et al. 1992; (13) Greenstein & Oke 1982; (14) Liebert et al. 1977; (15) Koester et al. 2009; (16) Koester et al. 2001; (17) Achilleos et al. 1991; (18) Schmidt et al. 2001; (19) Gianninas et al. 2011 (20) Achilleos & Wickramasinghe 1989; (21) Friedrich et al. 1997; (22) Gänsicke et al. 2002; (23) Kawka & Vennes 2011; (24) Limoges & Bergeron 2010; (25) Farihi et al. 2011b; (26) Burleigh et al. 1999; (27) Külebi et al. 2010; (28) Barstow et al. 1995; (29) Vennes et al. 2003; (30) Gianninas 2011, private communication; (31) Fabrika et al. 2003; (32) Finley et al. 1997; (33) Aznar Cuadrado et al. 2004; (34) Vornanen et al. 2010; (35) Dufour, Bergeron & Fontaine 2005; (36) Bues & Pragal 1989; (37) Putney & Jordan 1995; (38) Vennes 1999; (39) Schmidt, Stockman & Smith 1992; (40) Giovannini et al. 1998; (41) Holberg et al. 2008; (42) Dobbie et al. 2013; (43) Putney 1995; (44) Guseinov et al. 1983; (45) Brinkworth et al. 2007; (46) Brinkworth et al. 2013; (47) Angel et al. 1974; (48) Ferrario et al. 1998; (49) Külebi et al. 2013b; (50) Wesemael et al. 2001; (51) Angel 1977; (52) Angel et al. 1972; (53) Dobbie et al. 2012; (54) Glenn et al. 1994; (55) Liebert et al. 1993; (56) Schmidt et al. 1999; (57) Euchner et al. 2006; (58) Liebert, Bergeron & Holberg 2003; (59) Saffer et al. 1989; (60) Bergeron, Ruiz & Leggett 1997; (61) Latter et al. 1987; (62) Oestreicher et al. 1992; (63) Schmidt et al. 1986; (64) Bues 1999; (65) Jordan & Friedrich 2002; (66) Wickramasinghe et al. 2002; (67) Euchner et al. 2005; (68) Valyavin et al. 2006; (69) Foltz et al. 1989; (70) Farihi, Burleigh & Hoard 2008; (71) Reid et al. 2001; (72) Breedt et al. 2012; (73) Girven et al. 2010; (74) Schmidt & Norsworthy 1991; (75) Dufour et al. 2006; (76) Bergeron et al. 1993; (77) Schmidt & Smith 1994; (78) Liebert, Bergeron & Holberg 2005; (79) Dufour et al. 2008a; (80) Vennes et al. 1999; (81) Koester et al. 1998; (82) Liebert et al. 1985; (83) Ferrario et al. 1997b; (84) Brinkworth et al. 2004; (85) Zuckerman et al. 2011; (86) Schmidt et al. 1992; (87) Kawka & Vennes 2006; (88) Wickramasinghe & Martin 1979; (89) Wegner 1977; (90) Angel 1978; (91) Berdyugin & Piirola 1999; (92) West 1989; (93) Greenstein 1986; (94) Wickramasinghe & Ferrario 1988; (95) Jordan 1992; (96) Kalirai et al. 2008; (97) Holberg & Howell 2011; (98) Maxted et al. 2000; (99) Brinkworth et al. 2005; (100) Schmidt et al. 1996; (101) Moran et al. 1998; (102) Kawka et al. 2007; (103) Giammichele et al. 2012; (104) Williams et al. 2013.

B

Chapter 4: Long Term Monitoring of RE J0317−853

B.1 Spot model analysis for RE J0317–853

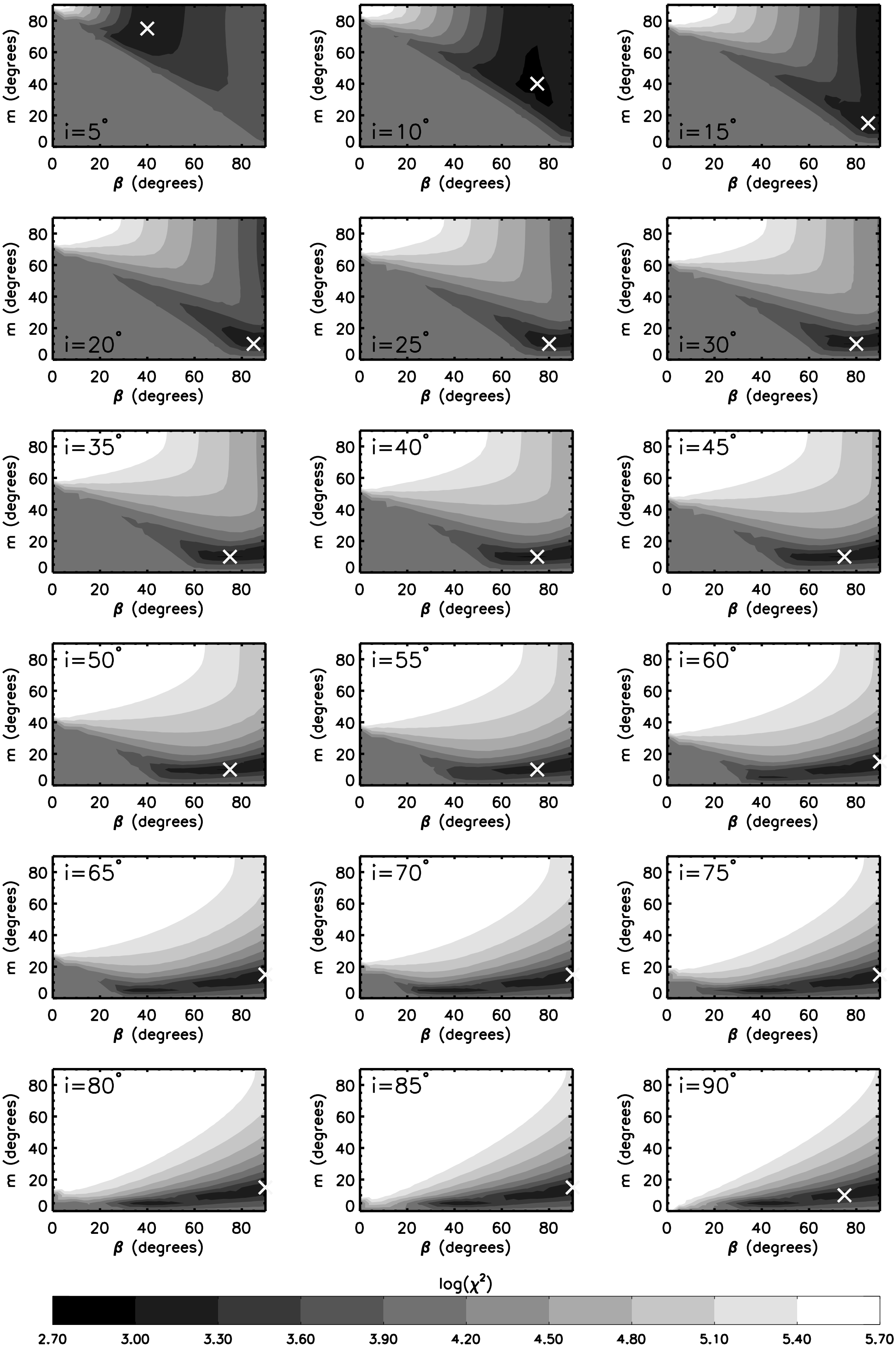

Figure B.1: Contour plots of χ^2 for the two dark spot model of constant luminosity.

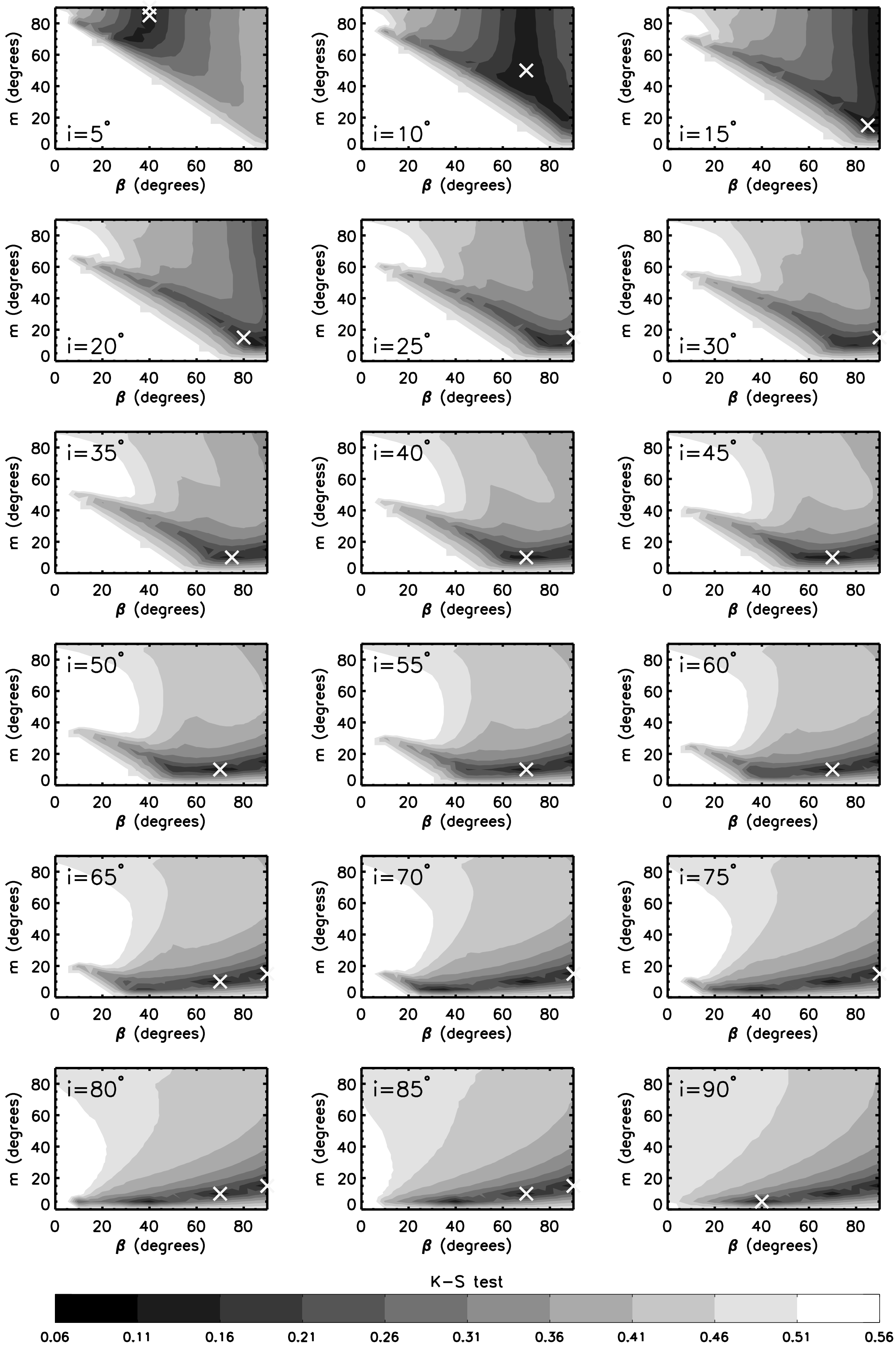

Figure B.2: Contour plots of the K-S test statistic for the two dark spot model of constant luminosity.

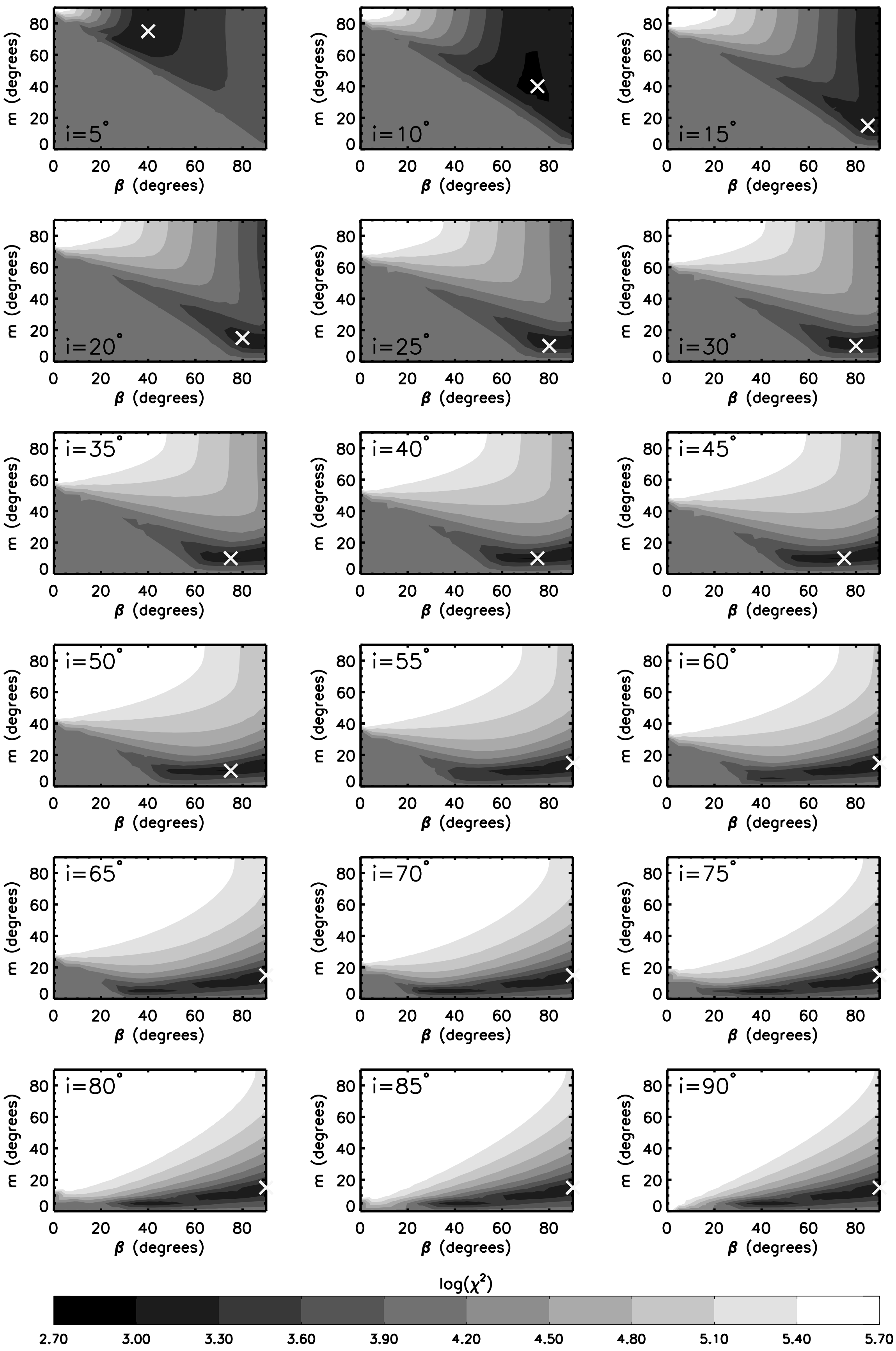

Figure B.3: Contour plots of χ^2 for the two dark spot model with a linearly changing luminosity.

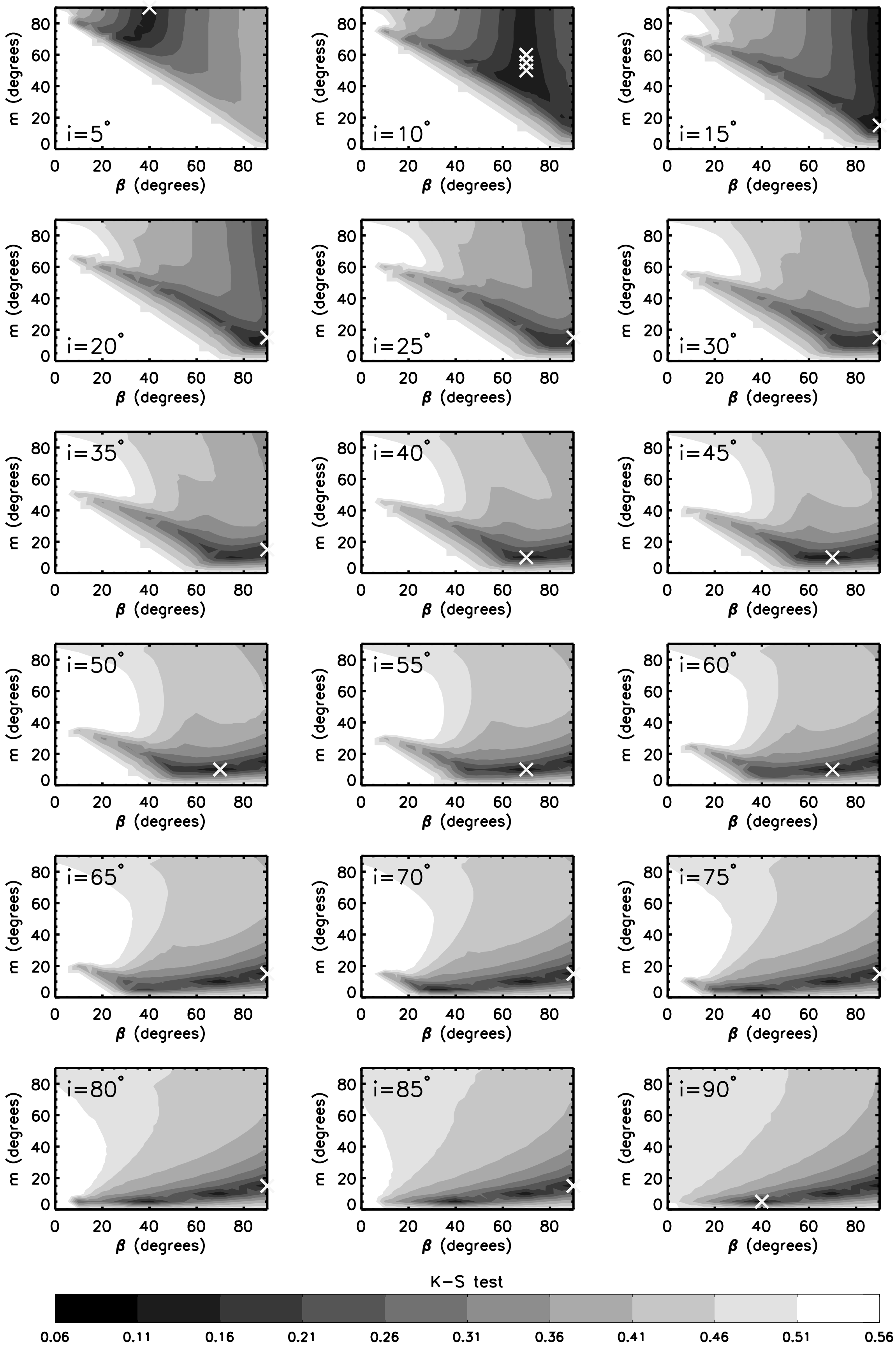

Figure B.4: Contour plots of the K-S test statistic for the two dark spot model with a linearly changing luminosity.

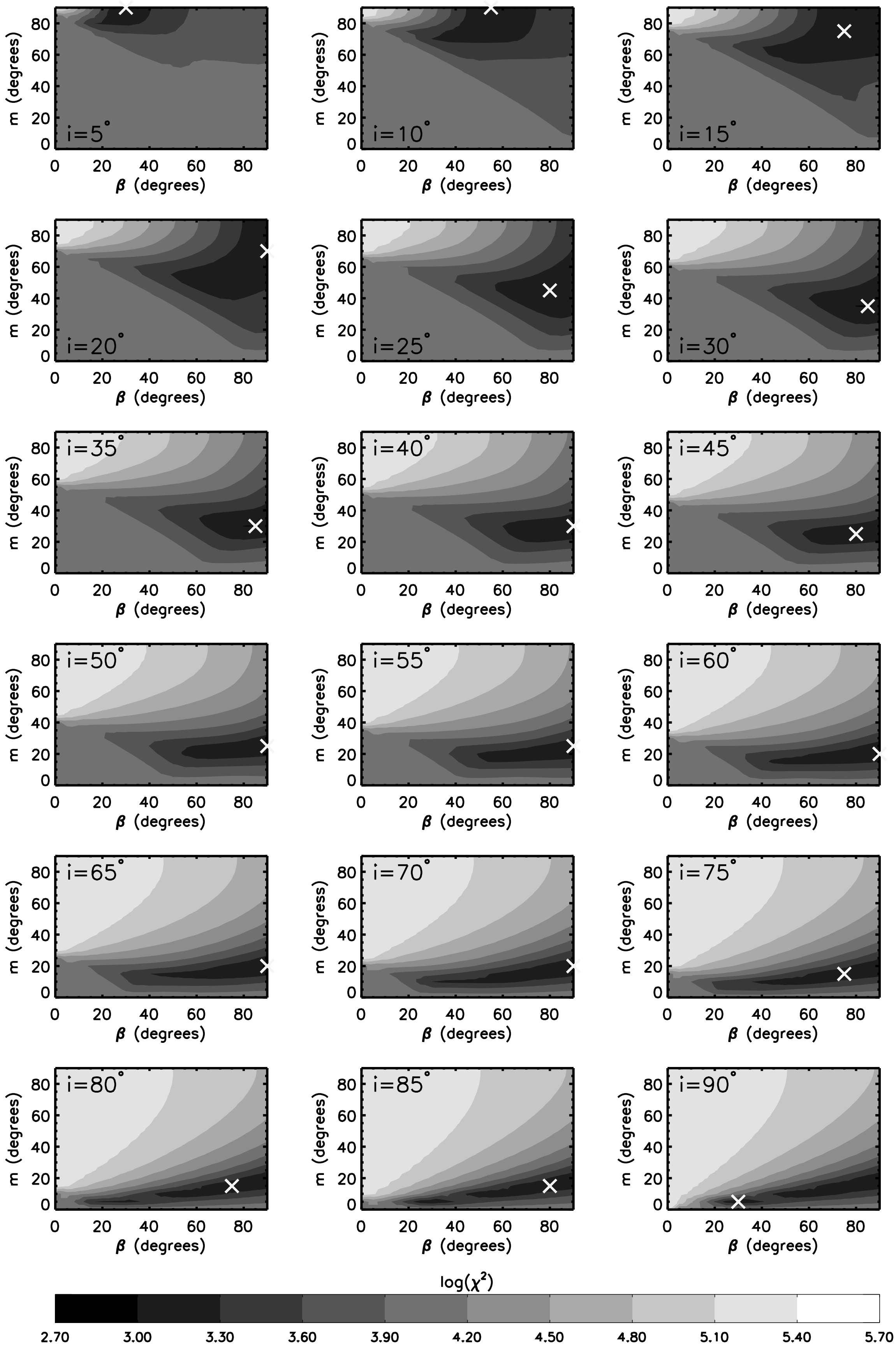

Figure B.5: Contour plots of χ^2 for the two dark spot model with an exponentially changing luminosity.

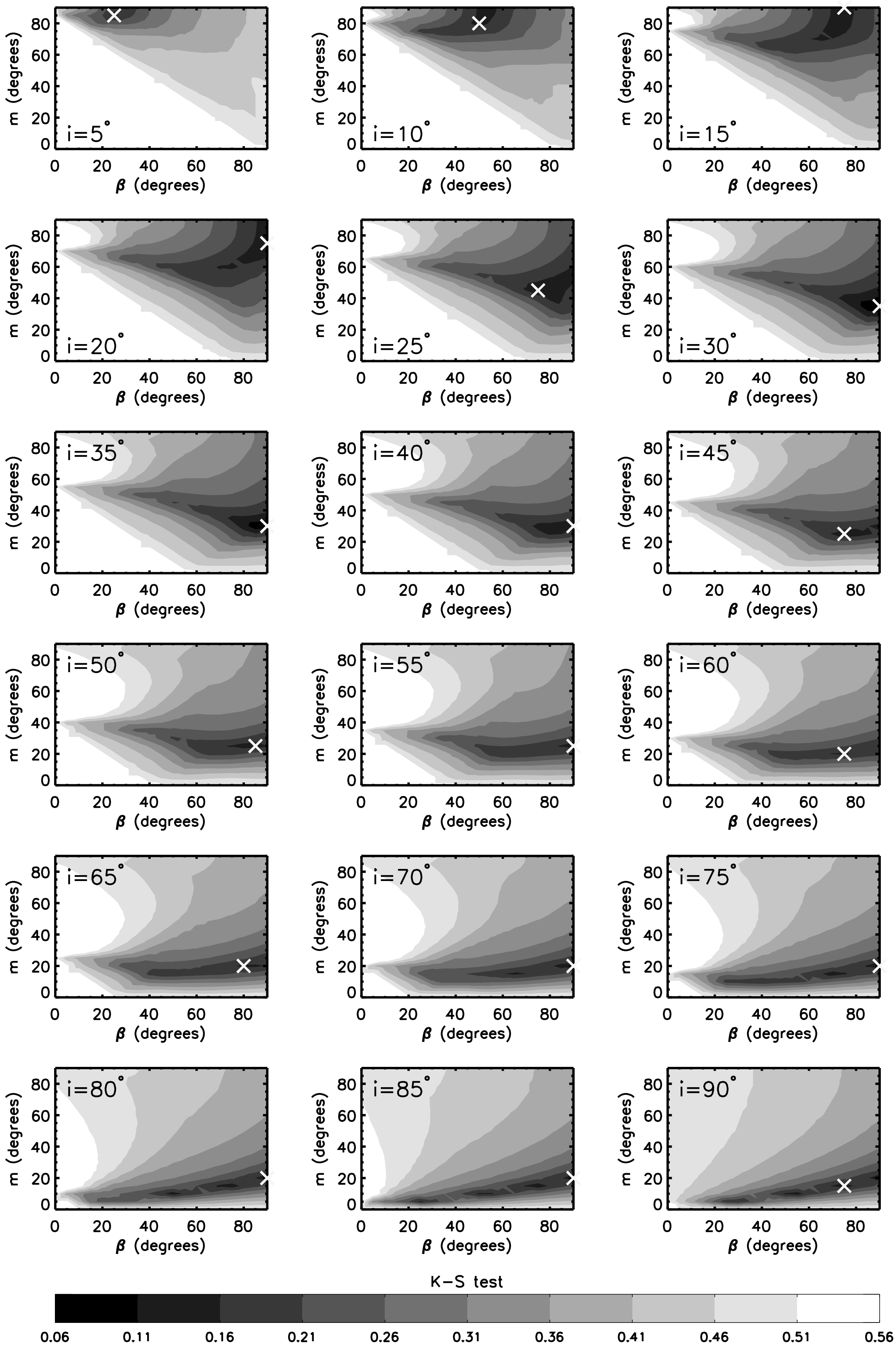

Figure B.6: Contour plots of K-S test statistic for the two dark spot model with an exponentially changing luminosity.

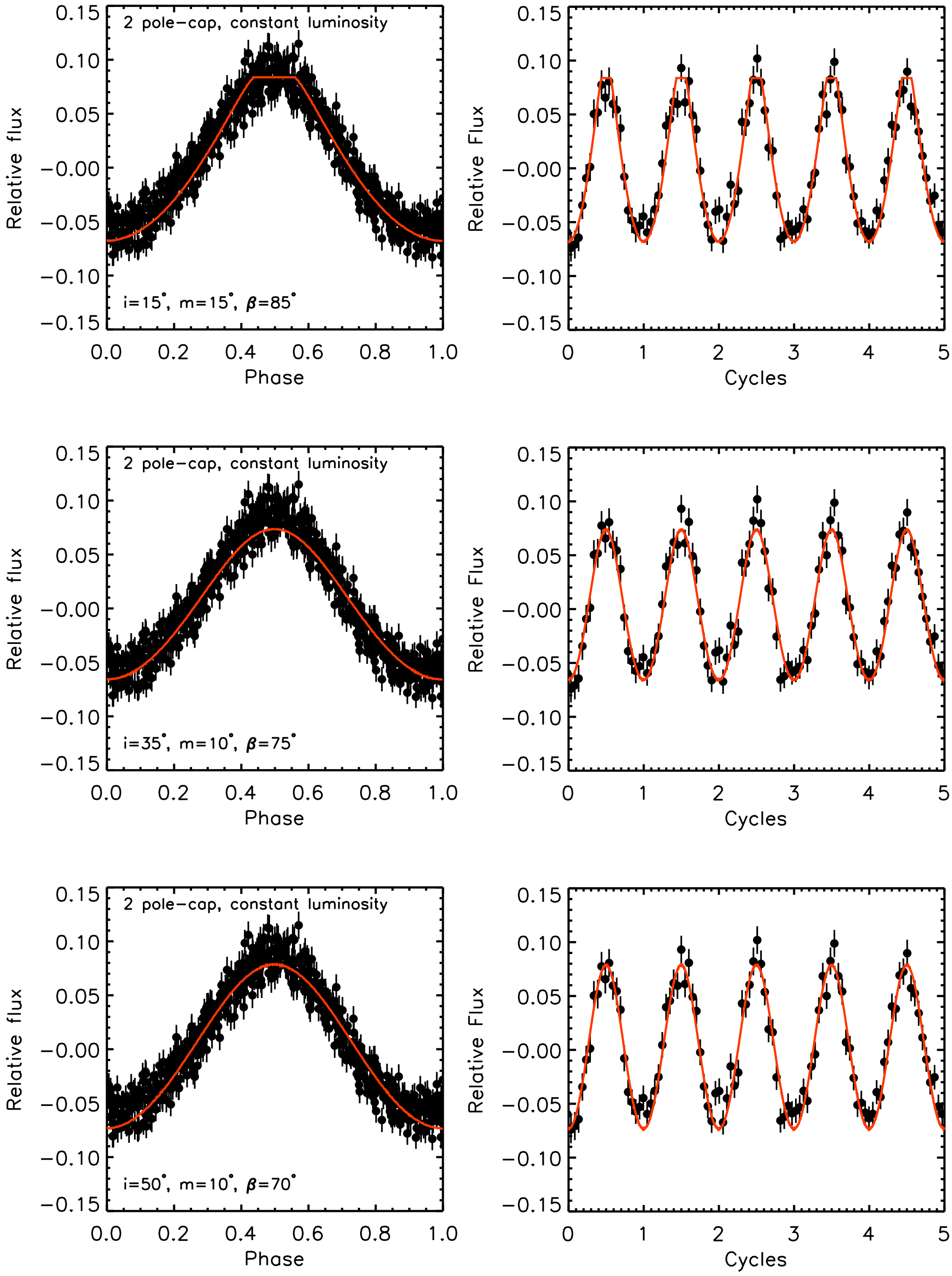

Figure B.7: Observed light curves and models with the best-fitting parameters for two symmetric dark spots of constant luminosity.

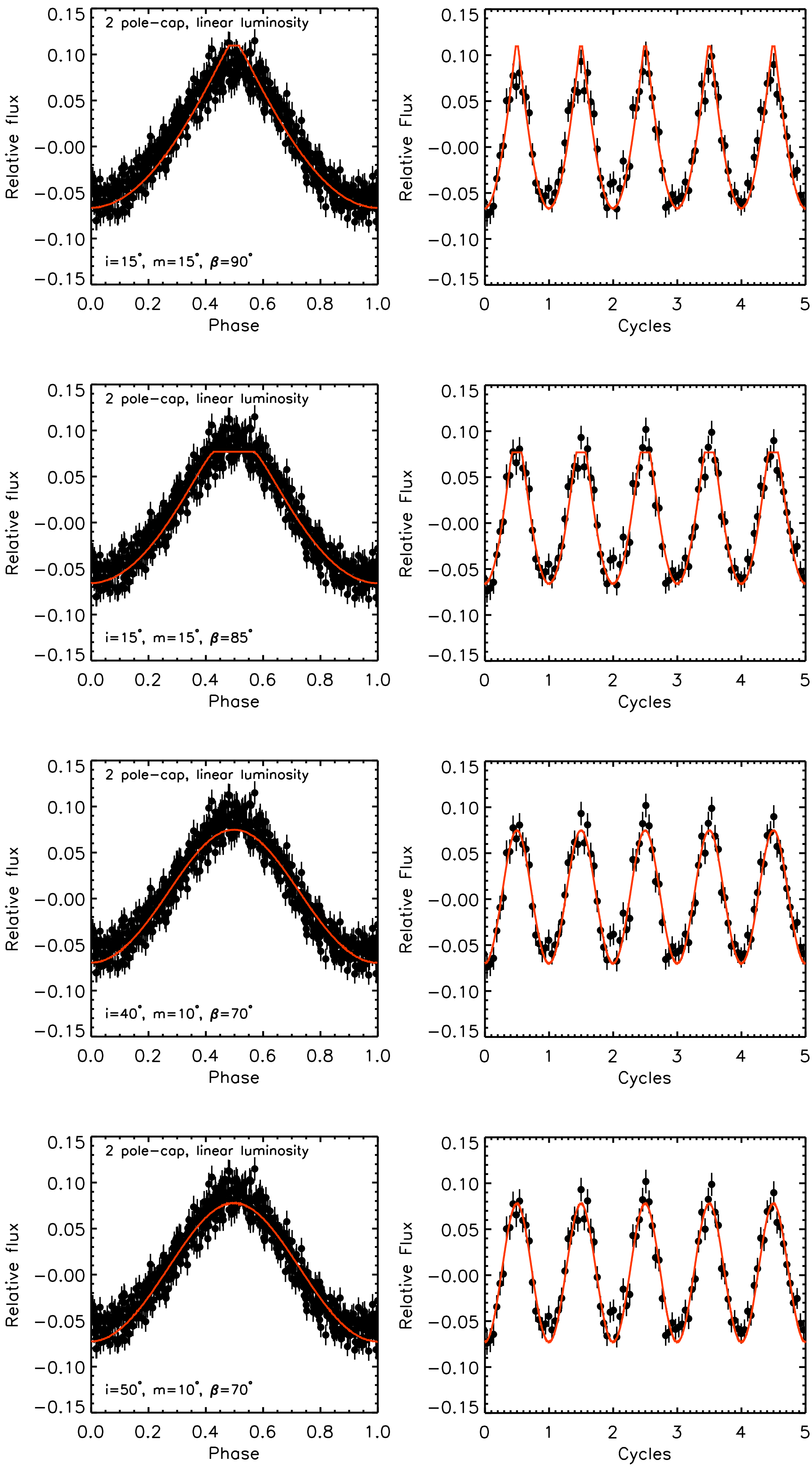

Figure B.8: Observed light curves and models with the best-fitting parameters for two symmetric dark spots of linearly changing luminosity.

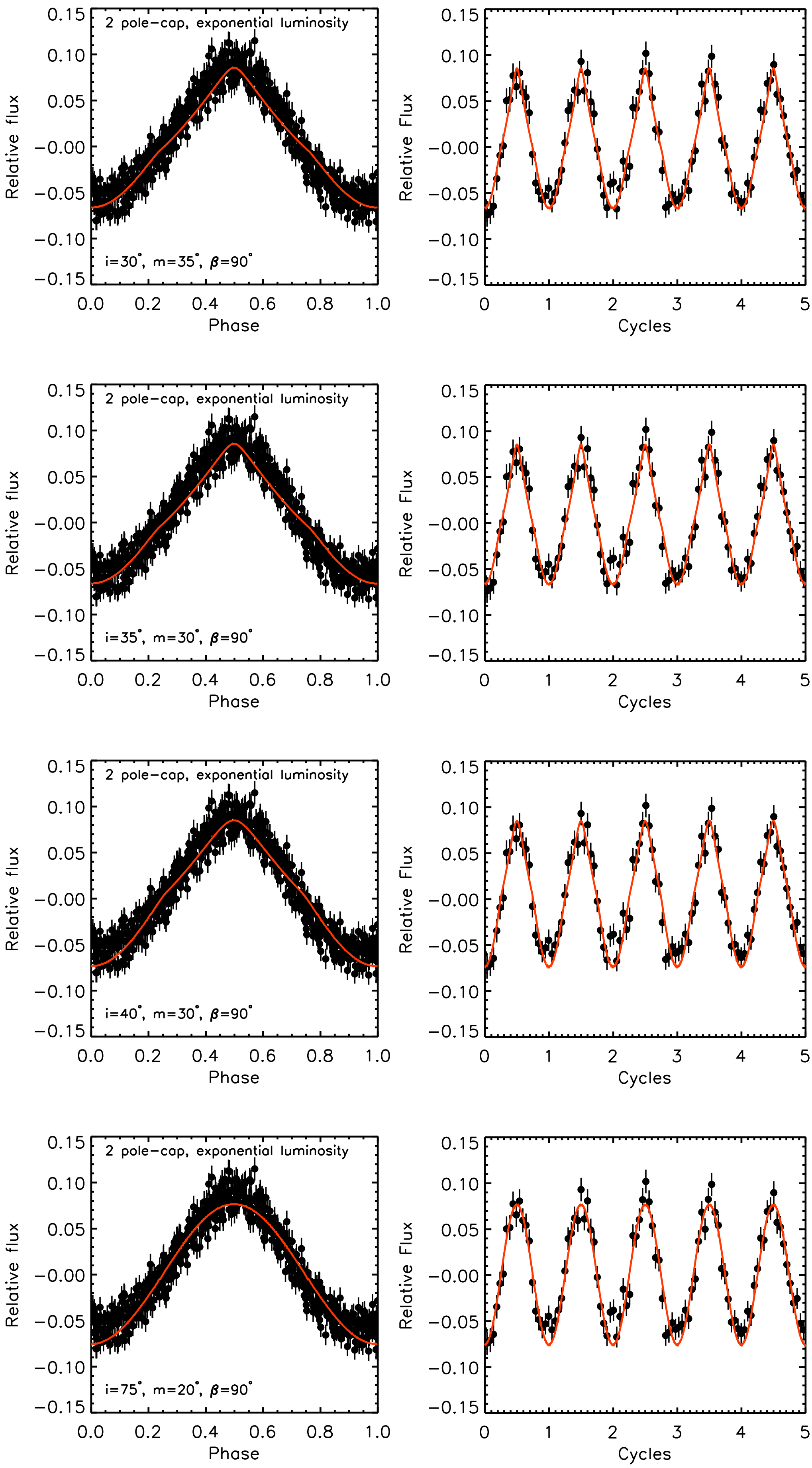

Figure B.9: Observed light curves and models with the best-fitting parameters for two symmetric dark spots of exponentially changing luminosity.

References

Achilleos N., Remillard R. A., Wickramasinghe D. T., 1991, *MNRAS*, 253, 522

Achilleos N., Wickramasinghe D. T., 1989, *ApJ*, 346, 444

Achilleos N., Wickramasinghe D. T., Liebert J., Saffer R. A., Grauer A. D., 1992, *ApJ*, 396, 273

Adams W. S., 1915, PASP, 27, 236

Alcock C., et al., 2000, *ApJ*, 542, 257

Althaus L. G., Córsico A. H., Isern J., García-Berro E., 2010, A&A Rev., 18, 471

Althaus L. G., Córsico A. H., Torres S., García-Berro E., 2009, *A&A*, 494, 1021

Angel J. R. P., 1977, *ApJ*, 216, 1

Angel J. R. P., 1978, Ann. Rev. A&A, 16, 487

Angel J. R. P., Borra E. F., Landstreet J. D., 1981, ApJS, 45, 457

Angel J. R. P., Carswell R. F., Beaver E. A., Harms R., Strittmatter P. A., 1974, *ApJL*, 194, L47

Angel J. R. P., Illing R. M. E., Landstreet J. D., 1972, *ApJL*, 175, L85+

Angel J. R. P., Landstreet J. D., 1971, *ApJL*, 165, L71

Aurière M., et al., 2007, *A&A*, 475, 1053

Aznar Cuadrado R., Jordan S., Napiwotzki R., Schmid H. M., Solanki S. K., Mathys G., 2004, *A&A*, 423, 1081

Babcock H. W., 1947, *ApJ*, 105, 105

Barlow B. N., Dunlap B. H., Clemens J. C., Reichart D. E., Ivarsen K. M., Lacluyze A. P., Haislip J. B., Nysewander M. C., 2011, *MNRAS*, 414, 3434

Barlow B. N., Dunlap B. H., Rosen R., Clemens J. C., 2008, *ApJL*, 688, L95

Barstow M. A., Jordan S., O'Donoghue D., Burleigh M. R., Napiwotzki R., Harrop-Allin M. K., 1995, *MNRAS*, 277, 971

Benvenuto O. G., García-Berro E., Isern J., 2004, PhRvD, 69, 082002

Berdyugin A. V., Piirola V., 1999, *A&A*, 352, 619

Berger L., Koester D., Napiwotzki R., Reid I. N., Zuckerman B., 2005, *A&A*, 444, 565

Bergeron P., Leggett S. K., Ruiz M. T., 2001, ApJS, 133, 413

Bergeron P., Liebert J., Greenstein J. L., 1990, *ApJ*, 361, 190

Bergeron P., Ruiz M.-T., Leggett S. K., 1992, *ApJ*, 400, 315

Bergeron P., Ruiz M.-T., Leggett S. K., 1993, *ApJ*, 407, 733

Bergeron P., Ruiz M.-T., Leggett S. K., 1997, ApJS, 108, 339

Bergeron P., Wesemael F., Lamontagne R., Fontaine G., Saffer R. A., Allard N. F., 1995, *ApJ*, 449, 258

Beuermann K., Hessman F. V., Dreizler S., Marsh T. R., Parsons S. G., Winget D. E., Miller G. F., Schreiber M. R., Kley W., Dhillon V. S., Littlefair S. P., Copperwheat C. M., Hermes J. J., 2010, *A&A*, 521, L60

Blackett P. M. S., 1947, Nat., 159, 658

Brassard P., Fontaine G., Wesemael F., Tassoul M., 1992, ApJS, 81, 747

Breedt E., Gänsicke B. T., Girven J., Drake A. J., Copperwheat C. M., Parsons S. G., Marsh T. R., 2012, *MNRAS*, p. 2885

Brinkworth C., 2005, PhD thesis, University of Southampton (United Kingdom), England

Brinkworth C. S., Burleigh M. R., Lawrie K. A., Marsh T. R., Knigge C., 2013, *ApJ in press*

Brinkworth C. S., Burleigh M. R., Marsh T. R., 2007, in R. Napiwotzki & M. R. Burleigh ed., 15th European Workshop on White Dwarfs Vol. 372 of Astronomical Society of the Pacific Conference Series, A Survey for Photometric Variability in Isolated Magnetic White Dwarfs – Measuring their Spin Periods. p. 183

Brinkworth C. S., Burleigh M. R., Wynn G. A., Marsh T. R., 2004, *MNRAS*, 348, L33

Brinkworth C. S., Marsh T. R., Morales-Rueda L., Maxted P. F. L., Burleigh M. R., Good S. A., 2005, *MNRAS*, 357, 333

Bues I., 1999, in S.-E. Solheim & E. G. Meistas ed., 11th European Workshop on White Dwarfs Vol. 169 of Astronomical Society of the Pacific Conference Series, The final model for the high-field magnetic white dwarf LHS 2293?. p. 240

Bues I., Pragal M., 1989, in G. Wegner ed., IAU Colloq. 114: White Dwarfs Vol. 328 of Lecture Notes in Physics, Berlin Springer Verlag, Phase correlated spectra of magnetic white dwarfs. pp 329–332

Burleigh M. R., Clarke F. J., Hodgkin S. T., 2002, *MNRAS*, 331, L41

Burleigh M. R., et al., 2011, in Schuh S., Drechsel H., Heber U., eds, American Institute of Physics Conference Series Vol. 1331 of American Institute of Physics Conference Series, Brown Dwarf Companions to White Dwarfs. pp 262–270

Burleigh M. R., Hogan E., Dobbie P. D., Napiwotzki R., Maxted P. F. L., 2006, *MNRAS*, 373, L55

Burleigh M. R., Jordan S., Schweizer W., 1999, *ApJL*, 510, L37

Casewell S. L., Burleigh M. R., Wynn G. A., Alexander R. D., Napiwotzki R., Lawrie K. A., Dobbie P. D., Jameson R. F., Hodgkin S. T., 2012, *ApJL*, 759, L34

Casewell S. L., Dobbie P. D., Napiwotzki R., Burleigh M. R., Barstow M. A., Jameson R. F., 2009, *MNRAS*, 395, 1795

Chandrasekhar S., 1931, *ApJ*, 74, 81

Chanmugam G., 1992, Ann. Rev. A&A, 30, 143

Chayer P., Fontaine G., Wesemael F., 1995, ApJS, 99, 189

Claver C. F., Liebert J., Bergeron P., Koester D., 2001, *ApJ*, 563, 987

Cumming A., 2004, *MNRAS*, 354, 1165

Cumming A., Marcy G. W., Butler R. P., 1999, *ApJ*, 526, 890

Currie T., Hansen B., 2007, *ApJ*, 666, 1232

Dawson R. I., Fabrycky D. C., 2010, *ApJ*, 722, 937

Debes J. H., Sigurdsson S., 2002, *ApJ*, 572, 556

Debes J. H., Walsh K. J., Stark C., 2012, *ApJ*, 747, 148

Dhillon V. S., et al., 2007, *MNRAS*, 378, 825

Diaconis P., Efron B., 1983, Sci. Am., 248, 116

Dobbie P. D., Baxter R., Külebi B., Parker Q. A., Koester D., Jordan S., Lodieu N., Euchner F., 2012, *MNRAS*, 421, 202

Dobbie P. D., Külebi B., Casewell S. L., Burleigh M. R., Parker Q. A., Baxter R., Lawrie K. A., Jordan S., Koester D., 2013, *MNRAS*, 428, L16

Dobbie P. D., Napiwotzki R., Burleigh M. R., Barstow M. A., Boyce D. D., Casewell S. L., Jameson R. F., Hubeny I., Fontaine G., 2006, *MNRAS*, 369, 383

Drake A. J., Djorgovski S. G., Mahabal A., Beshore E., Larson S., Graham M. J., Williams R., Christensen E., Catelan M., Boattini A., Gibbs A., Hill R., Kowalski R., 2009, *ApJ*, 696, 870

Dufour P., Béland S., Fontaine G., Chayer P., Bergeron P., 2011, *ApJL*, 733, L19

Dufour P., Bergeron P., Fontaine G., 2005, *ApJ*, 627, 404

Dufour P., Bergeron P., Schmidt G. D., Liebert J., Harris H. C., Knapp G. R., Anderson S. F., Schneider D. P., 2006, *ApJ*, 651, 1112

Dufour P., Fontaine G., Bergeron P., Béland S., Chayer P., Williams K. A., Liebert J., 2010a, in Werner K., Rauch T., eds, American Institute of Physics Conference Series Vol. 1273 of American Institute of Physics Conference Series, HST Observations of Hot DQ White Dwarfs. pp 64–69

Dufour P., Fontaine G., Liebert J., Schmidt G. D., Behara N., 2008b, *ApJ*, 683, 978

Dufour P., Fontaine G., Liebert J., Williams K., Lai D. K., 2008a, *ApJL*, 683, L167

Dufour P., Green E. M., Fontaine G., Brassard P., Francoeur M., Latour M., 2009, *ApJ*, 703, 240

Dufour P., Kilic M., Fontaine G., Bergeron P., Lachapelle F.-R., Kleinman S. J., Leggett S. K., 2010b, *ApJ*, 719, 803

Dufour P., Liebert J., Fontaine G., Behara N., 2007, Nature, 450, 522

Dufour P., Vornanen T., Bergeron P., Fontaine G., Berdyugin A., 2013, in 18th European White Dwarf Workshop ASP Conference Series, White Dwarfs with Carbon Dominated Atmosphere: New Observations and Analysis

Dunlap B. H., Barlow B. N., Clemens J. C., 2010, *ApJL*, 720, L159

Eastman J., Siverd R., Gaudi B. S., 2010, PASP, 122, 935

Eisenstein D. J., Liebert J., Koester D., Kleinmann S. J., Nitta A., Smith P. S., Barentine J. C., Brewington H. J., Brinkmann J., Harvanek M., Krzesiński J., Neilsen Jr. E. H., Long D., Schneider D. P., Snedden S. A., 2006, *AJ*, 132, 676

Elkin V. G., Riley J. D., Cunha M. S., Kurtz D. W., Mathys G., 2005, *MNRAS*, 358, 665

Euchner F., Jordan S., Beuermann K., Reinsch K., Gänsicke B. T., 2006, *A&A*, 451, 671

Euchner F., Reinsch K., Jordan S., Beuermann K., Gänsicke B. T., 2005, *A&A*, 442, 651

Fabrika S. N., Valyavin G. G., Burlakova T. E., 2003, Astronomy Letters, 29, 737

Fabrycky D. C., Ford E. B., Steffen J. H., et al., 2012, *ApJ*, 750, 114

Faedi F., West R. G., Burleigh M. R., Goad M. R., Hebb L., 2011, *MNRAS*, 410, 899

Farihi J., Becklin E. E., Zuckerman B., 2008, *ApJ*, 681, 1470

Farihi J., Brinkworth C. S., Gänsicke B. T., Marsh T. R., Girven J., Hoard D. W., Klein B., Koester D., 2011a, *ApJL*, 728, L8

Farihi J., Burleigh M. R., Hoard D. W., 2008, *ApJ*, 674, 421

Farihi J., Christopher M., 2004, *AJ*, 128, 1868

Farihi J., Dufour P., Napiwotzki R., Koester D., 2011b, *MNRAS*, 413, 2559

Farihi J., Jura M., Lee J.-E., Zuckerman B., 2010, *ApJ*, 714, 1386

Farihi J., Jura M., Zuckerman B., 2009, *ApJ*, 694, 805

Ferrario L., Vennes S., Wickramasinghe D. T., 1998, *MNRAS*, 299, L1

Ferrario L., Vennes S., Wickramasinghe D. T., Bailey J. A., Christian D. J., 1997a, *MNRAS*, 292, 205

Ferrario L., Wickramasinghe D. T., 2005, *MNRAS*, 356, 615

Ferrario L., Wickramasinghe D. T., Liebert J., Schmidt G. D., Bieging J. H., 1997b, *MNRAS*, 289, 105

Finley D. S., Koester D., Basri G., 1997, *ApJ*, 488, 375

Fischer D. A., Valenti J., 2005, *ApJ*, 622, 1102

Foltz C. B., Latter W. B., Hewett P. C., Weymann R. J., Morris S. L., Anderson S. F., 1989, *AJ*, 98, 665

Fontaine G., Brassard P., 2008, PASP, 120, 1043

Fontaine G., Brassard P., Dufour P., 2008, *A&A*, 483, L1

Fontaine G., Michaud G., 1979, *ApJ*, 231, 826

Fowler R. H., 1926, *MNRAS*, 87, 114

Friedrich S., Koenig M., Schweizer W., 1997, *A&A*, 326, 218

Frink S., Mitchell D. S., Quirrenbach A., Fischer D. A., Marcy G. W., Butler R. P., 2002, *ApJ*, 576, 478

Gänsicke B. T., Euchner F., Jordan S., 2002, *A&A*, 394, 957

Gänsicke B. T., Koester D., Marsh T. R., Rebassa-Mansergas A., Southworth J., 2008, *MNRAS*, 391, L103

Gänsicke B. T., Marsh T. R., Southworth J., Rebassa-Mansergas A., 2006, Science, 314, 1908

García-Berro E., Lorén-Aguilar P., Aznar-Siguán G., Torres S., Camacho J., Althaus L. G., Córsico A. H., Külebi B., Isern J., 2012, *ApJ*, 749, 25

Giammichele N., Bergeron P., Dufour P., 2012, ApJS, 199, 29

Gianninas A., Bergeron P., Ruiz M. T., 2011, *ApJ*, 743, 138

Giovannini O., Kepler S. O., Kanaan A., Wood A., Claver C. F., Koester D., 1998, Baltic Astronomy, 7, 131

Girven J., Gänsicke B. T., Külebi B., Steeghs D., Jordan S., Marsh T. R., Koester D., 2010, *MNRAS*, 404, 159

Glenn J., Liebert J., Schmidt G. D., 1994, PASP, 106, 722

Green E. M., Dufour P., Fontaine G., Brassard P., 2009, *ApJ*, 702, 1593

Green R. F., Schmidt M., Liebert J., 1986, ApJS, 61, 305

Greenstein J. L., 1986, *ApJ*, 304, 334

Greenstein J. L., Oke J. B., 1982, *ApJ*, 252, 285

Gunn J. E., Ostriker J. P., 1970, *ApJ*, 160, 979

Guseinov O. K., Novruzova K. I., Rustamov I. S., 1983, Ap&SS, 97, 305

Hansen B. M. S., Shih H.-Y., Currie T., 2009, *ApJ*, 691, 382

Hatzes A. P., Guenther E. W., Endl M., Cochran W. D., Döllinger M. P., Bedalov A., 2005, *A&A*, 437, 743

Heber U., Napiwotzki R., Reid I. N., 1997, *A&A*, 323, 819

Hermes J. J., Montgomery M. H., Winget D. E., Brown W. R., Kilic M., Kenyon S. J., 2012, *ApJL*, 750, L28

Hogan E., Burleigh M. R., Clarke F. J., 2009, *MNRAS*, 396, 2074

Holberg J. B., Bergeron P., Gianninas A., 2008, *AJ*, 135, 1239

Holberg J. B., Howell S. B., 2011, AJ, 142, 62

Holberg J. B., Sion E. M., Oswalt T., McCook G. P., Foran S., Subasavage J. P., 2008, *AJ*, 135, 1225

Holman M. J., Fabrycky D. C., Ragozzine D., et al., 2010, Science, 330, 51

Horne J. H., Baliunas S. L., 1986, *ApJ*, 302, 757

Iben Jr. I., Ritossa C., Garcia-Berro E., 1997, *ApJ*, 489, 772

Irwin J., Irwin M., Aigrain S., Hodgkin S., Hebb L., Moraux E., 2007, *MNRAS*, 375, 1449

Irwin M., Lewis J., 2001, New Astron. Rev., 45, 105

Irwin M. J., 1985, *MNRAS*, 214, 575

Jordan S., 1992, *A&A*, 265, 570

Jordan S., Aznar Cuadrado R., Napiwotzki R., Schmid H. M., Solanki S. K., 2007, *A&A*, 462, 1097

Jordan S., Friedrich S., 2002, *A&A*, 383, 519

Jura M., Farihi J., Zuckerman B., 2009, *AJ*, 137, 3191

Kalirai J. S., Hansen B. M. S., Kelson D. D., Reitzel D. B., Rich R. M., Richer H. B., 2008, *ApJ*, 676, 594

Kane S. R., Ciardi D. R., Gelino D. M., von Braun K., 2012, *MNRAS*, 425, 757

Karl C. A., Napiwotzki R., Heber U., Dreizler S., Koester D., Reid I. N., 2005, *A&A*, 434, 637

Kawaler S. D., 2004, in Maeder A., Eenens P., eds, Stellar Rotation Vol. 215 of IAU Symposium, White Dwarf Rotation: Observations and Theory (Invited Review). p. 561

Kawka A., Vennes S., 2006, *ApJ*, 643, 402

Kawka A., Vennes S., 2009, *A&A*, 506, L25

Kawka A., Vennes S., 2011, *A&A*, 532, A7

Kawka A., Vennes S., 2012, *MNRAS*, 425, 1394

Kawka A., Vennes S., Schmidt G. D., Wickramasinghe D. T., Koch R., 2007, *ApJ*, 654, 499

Kemp J. C., Swedlund J. B., Landstreet J. D., Angel J. R. P., 1970, *ApJL*, 161, L77

Kepler S. O., Costa J. E. S., Castanheira B. G., Winget D. E., Mullally F., Nather R. E., Kilic M., von Hippel T., Mukadam A. S., Sullivan D. J., 2005, *ApJ*, 634, 1311

Kepler S. O., et al., 1991, *ApJL*, 378, L45

Kepler S. O., et al., 2013, *MNRAS*, 429, 2934

Kepler S. O., Kleinman S. J., Nitta A., Koester D., Castanheira B. G., Giovannini O., Costa A. F. M., Althaus L., 2007, *MNRAS*, 375, 1315

Kilic M., Allende Prieto C., Brown W. R., Koester D., 2007, *ApJ*, 660, 1451

King A. R., Pringle J. E., Wickramasinghe D. T., 2001, *MNRAS*, 320, L45

King A. R., Shaviv G., 1984, *MNRAS*, 211, 883

Klein B., Jura M., Koester D., Zuckerman B., 2011, *ApJ*, 741, 64

Kleinman S. J., et al., 2004, *ApJ*, 607, 426

Kleinman S. J., et al., 2013, ApJS, 204, 5

Koester D., Dreizler S., Weidemann V., Allard N. F., 1998, *A&A*, 338, 612

Koester D., et al., 2001, *A&A*, 378, 556

Koester D., Voss B., Napiwotzki R., Christlieb N., Homeier D., Lisker T., Reimers D., Heber U., 2009, *A&A*, 505, 441

Konacki M., Wolszczan A., 2003, *ApJL*, 591, L147

Kovács G., Zucker S., Mazeh T., 2002, *A&A*, 391, 369

Külebi B., Ekşi K. Y., Lorén-Aguilar P., Isern J., García-Berro E., 2013, *MNRAS*, 431, 2778

Külebi B., Jordan S., Euchner F., Gänsicke B. T., Hirsch H., 2009, *A&A*, 506, 1341

Külebi B., Jordan S., Nelan E., Bastian U., Altmann M., 2010, *A&A*, 524, A36+

Külebi B., Kalirai J., Jordan S., Eucher F., 2013b, *A&A, submitted*

Kurtz D. W., 1982, *MNRAS*, 200, 807

Kurtz D. W., 1990, Ann. Rev. A&A, 28, 607

Latter W. B., Schmidt G. D., Green R. F., 1987, *ApJ*, 320, 308

Laughlin G., Bodenheimer P., Adams F. C., 1997, *ApJ*, 482, 420

Lee B.-C., Han I., Park M.-G., 2013, *A&A*, 549, A2

Lee J. W., Kim S.-L., Kim C.-H., Koch R. H., Lee C.-U., Kim H.-I., Park J.-H., 2009, *AJ*, 137, 3181

Lenz P., Breger M., 2005, Communications in Asteroseismology, 146, 53

Liebert J., Angel J. R. P., Stockman H. S., Spinrad H., Beaver E. A., 1977, *ApJ*, 214, 457

Liebert J., Bergeron P., Eisenstein D., Harris H. C., Kleinman S. J., Nitta A., Krzesinski J., 2004, *ApJL*, 606, L147

Liebert J., Bergeron P., Holberg J. B., 2003, *AJ*, 125, 348

Liebert J., Bergeron P., Holberg J. B., 2005, ApJS, 156, 47

Liebert J., Bergeron P., Schmidt G. D., Saffer R. A., 1993, *ApJ*, 418, 426

Liebert J., et al., 2003, *AJ*, 126, 2521

Liebert J., Schmidt G. D., Green R. F., Stockman H. S., McGraw J. T., 1983, *ApJ*, 264, 262

Liebert J., Schmidt G. D., Lesser M., Stepanian J. A., Lipovetsky V. A., Chaffe F. H., Foltz C. B., Bergeron P., 1994, *ApJ*, 421, 733

Liebert J., Schmidt G. D., Sion E. M., Starrfield S. G., Green R. F., Boroson T. A., 1985, PASP, 97, 158

Liebert J., Wesemael F., Hansen C. J., Fontaine G., Shipman H. L., Sion E. M., Winget D. E., Green R. F., 1986, *ApJ*, 309, 241

Liebert J., Wickramasinghe D. T., Schmidt G. D., Silvestri N. M., Hawley S. L., Szkody P., Ferrario L., Webbink R. F., Oswalt T. D., Smith J. A., Lemagie M. P., 2005, *AJ*, 129, 2376

Limoges M.-M., Bergeron P., 2010, *ApJ*, 714, 1037

Lissauer J. J., Ragozzine D., Fabrycky D. C., et al., 2011, ApJS, 197, 8

Livio M., Pringle J. E., Wood K., 2005, *ApJL*, 632, L37

Lomb N. R., 1976, Ap&SS, 39, 447

Lorén-Aguilar P., Isern J., García-Berro E., 2009, *A&A*, 500, 1193

Lorimer D. R., 2008, Living Reviews in Relativity, 11, 8

Luyten W. J., 1950, *AJ*, 55, 86

Markwardt C. B., 2009, in Bohlender D. A., Durand D., Dowler P., eds, Astronomical Data Analysis Software and Systems XVIII Vol. 411 of Astronomical Society of the Pacific Conference Series, Non-linear Least-squares Fitting in IDL with MPFIT. p. 251

Marsh M. C., 1995, PhD thesis, University of Leicester

Martin B., Wickramasinghe D. T., 1982, *MNRAS*, 200, 993

Maxted P. F. L., Ferrario L., Marsh T. R., Wickramasinghe D. T., 2000, *MNRAS*, 315, L41

Maxted P. F. L., Napiwotzki R., Dobbie P. D., Burleigh M. R., 2006, Nat., 442, 543

Mazeh T., Nachmani G., Holczer T., Fabrycky D. C., Ford E. B., Sanchis-Ojeda R., Sokol G., Rowe J. F., Agol E., Carter J. A., Lissauer J. J., Quintana E. V., Ragozzine D., Steffen J. H., Welsh W., 2013, ArXiv 1301.5499

Melis C., Farihi J., Dufour P., Zuckerman B., Burgasser A. J., Bergeron P., Bochanski J., Simcoe R., 2011, *ApJ*, 732, 90

Montgomery M. H., Williams K. A., Winget D. E., Dufour P., De Gennaro S., Liebert J., 2008, *ApJL*, 678, L51

Moran C., Marsh T. R., Dhillon V. S., 1998, *MNRAS*, 299, 218

Mullally F., Reach W. T., De Gennaro S., Burrows A., 2009, *ApJ*, 694, 327

Mullally F., Winget D. E., De Gennaro S., Jeffery E., Thompson S. E., Chandler D., Kepler S. O., 2008, *ApJ*, 676, 573

Naylor T., 1998, *MNRAS*, 296, 339

Oestreicher R., Seifert W., Friedrich S., Ruder H., Schaich M., Wolf D., Wunner G., 1992, *A&A*, 257, 353

Ostriker J. P., Gunn J. E., 1969, *ApJ*, 157, 1395

Pelletier C., Fontaine G., Wesemael F., Michaud G., Wegner G., 1986, *ApJ*, 307, 242

Perets H. B., 2010, ArXiv 1001.0581

Pollacco D. L., et al., 2006, PASP, 118, 1407

Potter A. T., Tout C. A., 2010, *MNRAS*, 402, 1072

Pringle J. E., 1975, *MNRAS*, 170, 633

Provencal J. L., Shipman H. L., Hog E., Thejll P., 1998, *ApJ*, 494, 759

Putney A., 1995, *ApJL*, 451, L67

Putney A., 1997, ApJS, 112, 527

Putney A., Jordan S., 1995, *ApJ*, 449, 863

Reach W. T., Kuchner M. J., von Hippel T., Burrows A., Mullally F., Kilic M., Winget D. E., 2005, *ApJL*, 635, L161

Rebassa-Mansergas A., Gänsicke B. T., Schreiber M. R., Koester D., Rodríguez-Gil P., 2010, *MNRAS*, 402, 620

Rebassa-Mansergas A., Nebot Gómez-Morán A., Schreiber M. R., Gänsicke B. T., Schwope A., Gallardo J., Koester D., 2012, *MNRAS*, 419, 806

Reichart D., et al., 2005, Nuovo Cimento C Geophysics Space Physics C, 28, 767

Reid I. N., Liebert J., Schmidt G. D., 2001, *ApJL*, 550, L61

Ruiter A. J., Belczynski K., Fryer C., 2009, *ApJ*, 699, 2026

Ryabchikova T., et al., 2005, *A&A*, 429, L55

Saffer R. A., Liebert J., Wagner R. M., Sion E. M., Starrfield S. G., 1989, *AJ*, 98, 668

Sato B., et al., 2003, *ApJL*, 597, L157

Scargle J. D., 1982, *ApJ*, 263, 835

Schatzman E. L., 1958, White dwarfs

Schmidt G. D., 1987, in A. G. D. Philip, D. S. Hayes, & J. W. Liebert ed., IAU Colloq. 95: Second Conference on Faint Blue Stars The observed characteristics of magnetic white dwarfs. pp 377–386

Schmidt G. D., Allen R. G., Smith P. S., Liebert J., 1996, *ApJ*, 463, 320

Schmidt G. D., Bergeron P., Liebert J., Saffer R. A., 1992, *ApJ*, 394, 603

Schmidt G. D., et al., 2003, *ApJ*, 595, 1101

Schmidt G. D., Liebert J., Harris H. C., Dahn C. C., Leggett S. K., 1999, *ApJ*, 512, 916

Schmidt G. D., Norsworthy J. E., 1991, *ApJ*, 366, 270

Schmidt G. D., Smith P. S., 1994, *ApJL*, 423, L63

Schmidt G. D., Stockman H. S., Smith P. S., 1992, *ApJL*, 398, L57

Schmidt G. D., Vennes S., Wickramasinghe D. T., Ferrario L., 2001, *MNRAS*, 328, 203

Schmidt G. D., West S. C., Liebert J., Green R. F., Stockman H. S., 1986, *ApJ*, 309, 218

Schönberg M., Chandrasekhar S., 1942, *ApJ*, 96, 161

Sigurdsson S., Richer H. B., Hansen B. M., Stairs I. H., Thorsett S. E., 2003, Science, 301, 193

Silvotti R., et al., 2007, Nat., 449, 189

Sion E. M., Greenstein J. L., Landstreet J. D., Liebert J., Shipman H. L., Wegner G. A., 1983, *ApJ*, 269, 253

Sion E. M., Holberg J. B., Oswalt T. D., McCook G. P., Wasatonic R., 2009, *AJ*, 138, 1681

Splaver E. M., Nice D. J., Stairs I. H., Lommen A. N., Backer D. C., 2005, *ApJ*, 620, 405

Spruit H. C., 1998, *A&A*, 333, 603

Spruit H. C., 2002, *A&A*, 381, 923

Steele I. A., et al., 2004, in Oschmann Jr. J. M., ed., Society of Photo-Optical Instrumentation Engineers (SPIE) Conference Series Vol. 5489 of Society of Photo-Optical Instrumentation Engineers (SPIE) Conference Series, The Liverpool Telescope: performance and first results. pp 679–692

Steele P. R., Burleigh M. R., Dobbie P. D., Jameson R. F., Barstow M. A., Satterthwaite R. P., 2011, *MNRAS*, 416, 2768

Steele P. R., Saglia R. P., Burleigh M. R., Marsh T. R., Gänsicke B. T., Lawrie K., Cappetta M., Girven J., Napiwotzki R., 2013, *MNRAS*, p. 519

Steffen J. H., Batalha N. M., Borucki W. J., et al., 2010, *ApJ*, 725, 1226

Sterken C., 2005, in Sterken C., ed., The Light-Time Effect in Astrophysics: Causes and cures of the O-C diagram Vol. 335 of Astronomical Society of the Pacific Conference Series, The O-C Diagram: Basic Procedures. p. 3

Swedlund J. B., Wolstencroft R. D., Michalsky Jr. J. J., Kemp J. C., 1974, *ApJL*, 187, L121

Tout C. A., Pringle J. E., 1992, *MNRAS*, 256, 269

Tout C. A., Wickramasinghe D. T., Liebert J., Ferrario L., Pringle J. E., 2008, *MNRAS*, 387, 897

Valyavin G., Bagnulo S., Fabrika S., Reisenegger A., Wade G. A., Han I., Monin D., 2006, ApJ, 648, 559

Valyavin G., Bagnulo S., Monin D., Fabrika S., Lee B.-C., Galazutdinov G., Wade G. A., Burlakova T., 2005, A&A, 439, 1099

Vanlandingham K. M., Schmidt G. D., Eisenstein D. J., Harris H. C., Anderson S. F., Hall P. B., Liebert J., Schneider D. P., Silvestri N. M., Stinson G. S., Wolfe M. A., 2005, *AJ*, 130, 734

Vennes S., 1999, *ApJ*, 525, 995

Vennes S., Ferrario L., Wickramasinghe D. T., 1999, *MNRAS*, 302, L49

Vennes S., Kawka A., 2008, *MNRAS*, 389, 1367

Vennes S., Schmidt G. D., Ferrario L., Christian D. J., Wickramasinghe D. T., Kawka A., 2003, *ApJ*, 593, 1040

Vennes S., Thejll P. A., Galvan R. G., Dupuis J., 1997, *ApJ*, 480, 714

Verbiest J. P. W., Bailes M., van Straten W., Hobbs G. B., Edwards R. T., Manchester R. N., Bhat N. D. R., Sarkissian J. M., Jacoby B. A., Kulkarni S. R., 2008, *ApJ*, 679, 675

Villaver E., Livio M., 2007, *ApJ*, 661, 1192

Vornanen T., Berdyugina S. V., Berdyugin A. V., Piirola V., 2010, ApJL, 720, L52

Wegner G., 1977, Mem. Soc. Astron. Italiana, 48, 27

Weidemann V., Koester D., 1983, *A&A*, 121, 77

Wesemael F., Liebert J., Schmidt G. D., Beauchamp A., Bergeron P., Fontaine G., 2001, *ApJ*, 554, 1118

West S. C., 1989, *ApJ*, 345, 511

Wickramasinghe D. T., Cropper M., 1988, *MNRAS*, 235, 1451

Wickramasinghe D. T., Farihi J., Tout C. A., Ferrario L., Stancliffe R. J., 2010, *MNRAS*, 404, 1984

Wickramasinghe D. T., Ferrario L., 1988, *ApJ*, 327, 222

Wickramasinghe D. T., Ferrario L., 2000, PASP, 112, 873

Wickramasinghe D. T., Ferrario L., 2005, *MNRAS*, 356, 1576

Wickramasinghe D. T., Martin B., 1979, *MNRAS*, 188, 165

Wickramasinghe D. T., Schmidt G., Ferrario L., Vennes S., 2002, *MNRAS*, 332, 29

Williams K. A., Winget D. E., Montgomery M. H., Dufour P., Kepler S. O., Hermes J. J., Falcon R. E., Winget K. I., Bolte M., Rubin K. H. R., Liebert J., 2013, *ApJ*, 769, 123

Winget D. E., Kepler S. O., 2008, Ann. Rev. A&A, 46, 157

Wolszczan A., 1994, Science, 264, 538

Wolszczan A., 1997, Celestial Mechanics and Dynamical Astronomy, 68, 13

Wolszczan A., Frail D. A., 1992, Nat., 355, 145

Wood M. A., 1992, *ApJ*, 386, 539

Wynn G. A., King A. R., 1992, *MNRAS*, 255, 83

Zechmeister M., Kürster M., 2009, *A&A*, 496, 577

Zuckerman B., Koester D., Dufour P., Melis C., Klein B., Jura M., 2011, *ApJ*, 739, 101

Zuckerman B., Koester D., Melis C., Hansen B. M., Jura M., 2007, *ApJ*, 671, 872

Zuckerman B., Melis C., Klein B., Koester D., Jura M., 2010, *ApJ*, 722, 725